

Translating nonclinical findings to prioritize multi-drug regimens for the treatment of tuberculosis

by
Jacqueline Ernest

DISSERTATION

Submitted in partial satisfaction of the requirements for degree of
DOCTOR OF PHILOSOPHY

in

Pharmaceutical Sciences and Pharmacogenomics

in the

GRADUATE DIVISION

of the

UNIVERSITY OF CALIFORNIA, SAN FRANCISCO

Approved:

DocuSigned by:

Deanna Kroetz

Deanna Kroetz

0611A116B51E4AA...

Chair

DocuSigned by:

Radojka Savic

Radojka Savic

DocuSigned by:

Veronique Dartois

Veronique Dartois

B4BFA27530C942B...

Committee Members

Dedication

To my mom and dad, Malu and Jim

Acknowledgments

There are many people to thank. I would first like to thank and acknowledge the bench scientists, animal technicians, and assistants responsible for generating the database of in vitro, ex vivo, and animal experiments presented in this dissertation. The patience, persistence, and diligence to execute these experiments are found in few. Without your contributions to the field, analyses, including ones found in this dissertation, would not be possible.

To my advisor, Dr. Rada Savic – thank you for being an exceptional example of a leader and scientist. Thank you for creating a lab environment that has been fundamental to my growth as a scientist and person. Since I first joined the lab, you have invested your time in me, trusted me, and believed in my success. I am so grateful and proud to be a part of your incredible team and among your graduate student alumni. I look forward to the next chapter.

To Dr. Véronique Dartois – thank you for serving as a brilliant and reliable second advisor and mentor. Although we have still yet to meet in person, working with you over the course of my PhD has been a joy. Thank you for always thinking through problems critically and thoroughly. Thank you for showing me how to think independently, how to be an exceptional mentor and writer, and how to be generous with knowledge and expertise. I look forward to continuing to work with you.

To my program mentor and thesis chair, Dr. Deanna Kroetz – thank you for your thoughtful comments and questions that made this dissertation dramatically better. Thank you for always prioritizing students and their progress. Thank you for leading and improving our program, Pharmaceutical Sciences and Pharmacogenomics (PSPG). The program will always be my academic home. I would like to thank the classmates and friends that I have had the pleasure of learning from. You are some of the most committed, hardworking people I know.

To the members of the Savic Lab – thank you for helping me grow as a modeler, data scientist, and pharmacometrician. I would especially like to thank the original Translational TB Team – Dr. Natasha Strydom, Dr. Qianwen (Chores) Wang, and Dr. Nan Zhang – for your

support and encouragement through my rotation and in the early days of my time in the lab when I needed it most. Thank you to the current Translational TB Team – Anna Fochesato, Lorenzo Flori, Janice Goh, Dr. Marjorie Imperial, Anu Patel, Hoang-Anh Vu, Dr. Rob Christiaan van Wijk, and Dr. Michael Zastrozhin – for your support as I finish this chapter in my scientific career. It has been an honor to work with you all.

To my PSPG classmates who joined the Savic Lab before or with me – Drs. Marjorie Imperial, Emma Hughes, Kendra Radtke, and Vincent Chang – thank you for demonstrating effortlessly how to succeed in the Savic Lab. Thank you to the incoming PhD students – Anu Patel, Hoang-Anh Vu, and Ava Xu, who have given me the opportunity to mentor and to share my passion. And thank you to the rotation students and visiting scholars – Joana Cabrera, Lorenzo Flori, Anna Fochesato, Michelle Jin, Amy Lyden, and Veronika Westergren – who have equally helped me learn and mentor and who have contributed to projects.

To the additional mentors that played a role in my development including Eric Nuermberger, Payam Nahid, Kathy Giacomini, and Sulggi Lee – thank you for serving on committees, for being excellent collaborators, and helpful mentors. I would like to thank Rebecca Dawson for all she does behind the scenes for PSPG. I would like to thank funders including the ARCS Foundation and the National Institutes of Health Training Grant T32 GM007175 for their support.

I would like to thank those who have supported me outside of the lab, especially Michelle Folan. Thank you for your constant support and compassion. You make daily life so fun and full of adventures. I can't wait for more to come. Thank you to my sister, Madeline Huertas, for everything. Thank you to my friends – Juliana Joseph, Amy Czyz, Gina Bradley, Sara Loewel, Jesse Clurman, Kara Natividad, Emma Kruse, Olivia DeFelice, Katie Kelly, and Mary O'Connor – for making my life so full.

I would like to gratefully acknowledge my family including the Alvarez family, the Bulos family, the Escano family, and the Ernest family. Without the foundation of our family, the pursuit

of education or career would be impossible and meaningless. I am filled with gratitude and pride to be a member of our family.

Finally, to my parents, Malu and Jim – thank you for the wonderful childhood and life you have given me. Thank you for demonstrating how to work for what you believe in, for always encouraging me, and for supporting my ambition. I am deeply indebted to you for all your love, support, and encouragement throughout my life. This dissertation is dedicated to you.

Contributions

Several chapters in this dissertation have been previously published. In all cases, they have been edited and may not fully represent their published form. Author affiliations can be found in the original publication.

Chapter 1 was written by a team including Natasha Strydom, Qianwen Wang, Nan Zhang, Eric Nuernberger, Véronique Dartois, Rada Savic, and me. It was originally published in *Annual Reviews of Pharmacology and Toxicology*. The work was funded by grants awarded by the Bill and Melinda Gates Foundation and Critical Path Institute (OPP1174780, OPP1031105-MS05, and INV-002483).

Chapter 2 was originally published in *Antimicrobial Agents and Chemotherapy*. Jansy Sarathy and I equally contributed as first author. Other authors include Ning Wang, Firat Kaya, Matthew D. Zimmerman, Natasha Strydom, Han Wang, Min Xie, Martin Gengenbacher, Laura E. Via, Clifton E. Barry III, Claire L. Carter, Rada M. Savic. Véronique Dartois is the senior corresponding author. Natasha Strydom, Rada Savic, and I analyzed the pharmacokinetic and tissue penetration data, built the pharmacokinetic-pharmacodynamic model and performed simulations. Jansy Sarathy, Ning Wang, Firat Kaya, Matthew Zimmerman, Han Wang, Min Xie, Martin Gengenbacher, Laura Via, and Claire Carter performed all experiments with contributions from the animal technical teams of the Public Health Research Institute at Rutgers University, the Center for Discovery and Innovation at Hackensack Meridian Health, and the Tuberculosis Research Section of the National Institute of Allergy and Infectious Diseases. Véronique Dartois, Rada Savic, and Clifton E. Barry III designed selected parts of the study. Jansy Sarathy, Claire Carter, and Véronique Dartois and I drafted the manuscript. All authors read and edited the manuscript. The studies were funded in part by NIH grants S10OD023524 and S10OD018072 to Véronique Dartois and grant INV-002483 from the Bill and Melinda Gates Foundation to Rada Savic and Véronique Dartois, and in part by the Division of Intramural Research of the NIAID, NIH. The content does not necessarily reflect the views or policies of the

Department of Health and Human Services, nor does the mention of trade names, commercial products, or organizations imply endorsement by the U.S. Government.

Chapter 3 was originally published in *Antimicrobial Agents and Chemotherapy*. Firat Kaya and I equally contributed as first authors. Other authors include Katherine LoMauro, Martin Gengenbacher, Abdeldjalil Madani, Wassihun Wedajo Aragaw, Matthew D. Zimmerman, Jansy P. Sarathy, Nadine Alvarez, Isaac Daudelin, Han Wang, Danielle Weiner, Laura E. Via, Clifton E. Barry, Kenneth Olivier, Thomas Dick, Brendan K. Podell, and Rada M. Savic. The senior corresponding author is Véronique Dartois.

Chapter 4 was authored by Marjorie Imperial, Firat Kaya, Véronique Dartois, Rada Savic, and me. It was first presented as an oral presentation at the PAGE conference in June 2022 in Ljubljana, Slovenia. The work was funded by the Bill and Melinda Gates Foundation under grant (INV-0002483). TB Alliance provided clinical data on TBAJ-587. The Center for Discovery and Innovation at Hackensack Meridian Health and the National Institute of Health provided rabbit data.

Chapter 5 is one piece of a larger work currently in preparation for publication. Co-first authors on the larger work are Janice Goh, Natasha Strydom, Rob Christiaan van Wijk, Qianwen Wang, Nan Zhang, and me. Other authors are Amelia Dietchman and Eric Nuermberger. Rada Savic is the senior corresponding author.

Chapter 6 was originally published in *Antimicrobial Agents and Chemotherapy*. Kendra K. Radtke and I equally contributed as first authors. Other authors include Nan Zhang, Nicole C. Ammerman, Eric Nuermberger, Robert Belknap, Rosanna Boyd, and Timothy R. Sterling. The senior corresponding author Rada Savic. This work was supported by TB Trials Consortium of the Centers for Disease Control and Prevention (CDC 09FED07950 to Timothy R. Sterling, Rada Savic, and Robert Belknap). The high-dose rifapentine PK and PK-PD studies in mice and subsequent modeling were funded by the U.S. Food and Drug Administration (U18-FD004004 to Eric Nuermberger), the National Institutes of Health (R01-AI111992 to Eric Nuermberger).

The low-dose rifapentine PK and PK-PD studies in mice were funded by a 2019 developmental grant from the Johns Hopkins University Center for AIDS Research, an NIH funded program (1P30AI094189 to Eric Nuermberger and Nicole C. Ammerman), which is supported by the following NIH Co-Funding and Participating Institutes and Centers: NIAID, NCI, NICHD, NHLBI, NIDA, NIA, NIGMS, NIDDK, NIMHD.

Translating nonclinical findings to prioritize sterilizing multidrug regimens for tuberculosis

Jacqueline P. Ernest

Abstract

Tuberculosis (TB) is second only to COVID-19 as the most lethal infectious disease in the world, claiming 1.6 million lives per year. Novel, potent, and safe drug combinations are needed to shorten treatment durations, improve outcomes, and combat resistance against available therapeutics. While the TB drug development pipeline is rich with new and repurposed drug classes with novel mechanisms of action and novel drug combinations, there is no consensus on how best to prioritize multidrug regimens for clinical trials and no *modus operandi* for nonclinical-clinical translation of TB therapeutics. An increasingly applied solution for the accurate translation and integration of nonclinical findings and emerging clinical data is through model-based approaches. The work presented in this dissertation aims to develop data-driven models integrating a compendium of experimental data to predict clinical efficacy and to contribute toward development of model-based translation methods.

In the first half of this dissertation, site-of-action models to predict lesion-centric pharmacokinetics (PK) and pharmacodynamics (PD) in patients were developed for three drugs. Kanamycin and amikacin do not reach therapeutic concentration at the site-of-action, highlighting their limited clinical utility. Clarithromycin accumulates in all tissues compared to plasma; however, its lack of bactericidal activity limits its utility in nontuberculous mycobacteria pulmonary disease (NTM-PD). The approach establishes a platform for future lesion penetration investigations for both TB and NTM-PD. In the second half of this work, semi-mechanistic models based on murine PK-PD data were developed to predict early bactericidal activity in active TB. Our predictive tool, built using nine approved drugs, can predict first-in-patient trials and de-risks entrance into clinical development. The approach was extended to compare efficacy of rifapentine alone and in combination in patients with latent TB infection. Our results

suggest that ultra-short course therapy of six weeks with rifapentine is equivalent to approved latent TB regimens.

The findings in this dissertation demonstrate model-based translational approaches to predict PK-PD at the site of action and to translate murine drug response in active and latent TB. The model-based tools developed and implemented in this dissertation contribute to regimen development – one of the greatest challenges in TB clinical development – and establish a basis for nonclinical-clinical translation in TB drug development.

Table of Contents

Chapter 1: Development of new tuberculosis drugs: Translation to regimen composition for drug-sensitive and multidrug-resistant tuberculosis.....	1
Abstract.....	1
Introduction	2
Data available for modeling	4
Translational approaches: Importance, advantages, and disadvantages	9
Translational toolbox.....	17
Conclusion	27
References.....	28
 Chapter 2: Lesion Penetration and Activity Limit the Utility of Second-Line Injectable Agents in Pulmonary Tuberculosis	45
Abstract.....	45
Introduction	46
Methods	49
Results	58
Discussion.....	72
References.....	75
Supplementary Material.....	86
 Chapter 3: A Rabbit Model to Study Antibiotic Penetration at the Site of Infection for Nontuberculous Mycobacterial Lung Disease: Macrolide Case Study.....	97
Abstract.....	97
Introduction	99
Methods	103

Results	111
Discussion.....	125
References.....	130
Supplementary Material.....	141
Chapter 4: Spatially and temporally resolved diffusion kinetics of bedaquiline and TBAJ-587 in hard-to-treat sites of tuberculosis disease	147
Abstract.....	147
Introduction	148
Methods	150
Results	152
Discussion.....	157
References.....	158
Chapter 5: Translational predictions of phase 2a first-in-patient efficacy studies for bedaquiline and rifapentine	159
Abstract.....	159
Introduction	160
Methods	163
Results	169
Discussion.....	176
References.....	179
Chapter 6: Comparative efficacy of rifapentine alone and in combination with isoniazid for latent tuberculosis infection: a translational pharmacokinetic-pharmacodynamic modelling study	181
Abstract.....	181

Introduction	182
Methods	184
Results	187
Discussion.....	194
References.....	198
Supplementary Material.....	202
Chapter 7: Conclusions	210

List of Figures

Figure 1.1 Examples of empirical and mechanistic models.....	10
Figure 1.2. Pathway to translating nonclinical to clinical outcomes for tuberculosis (TB).....	12
Figure 1.3. Modeling tools important for a translational platform.....	14
Figure 2.1. Distribution of KAN and AMK in lung, necrotic lesions and cavities.	60
Figure 2.2. KAN distribution in human lung lesions.	62
Figure 2.3. Model structure and visual predictive checks (VPC) for plasma-to-tissue distribution of AMK and KAN.	64
Figure 2.4. Potency of aminoglycosides against typical Mtb subpopulations found in lesions. ..	68
Figure 2.5. Clinical plasma and site-of-action PK simulations for a 24-hour steady-state profile in a typical TB patient.	71
Figure 3.1. Comparative histopathology of human clinical NTM infection, human clinical Mtb infection and Mtb infection in the rabbit model.....	112
Figure 3.2. Distribution of clarithromycin from plasma into major pulmonary lesion compartments.	117
Figure 3.3. Visual predictive check of clarithromycin rabbit plasma-to-tissue multicompartment model.	118
Figure 3.4. Clinical simulations of clarithromycin PK-PD coverage in plasma and four lung compartments.	122
Figure 3.5. Predicted target attainment expressed as AUC/potency across compartments against M. abscessus and M. avium disease.....	124
Figure 4.1. Representative images of caseous lesions from TB-infected rabbits.	149
Figure 4.2. Model structure of parent-metabolite plasma-lesion multicompartment model.	151
Figure 4.3. Spatial data available for BDQ, TBAJ-587, and their metabolites.	152
Figure 4.4. Visual predictive check of BDQ and TBAJ-587 spatial model.....	154

Figure 4.5. Clinical simulations at varying depths into lesions.	155
Figure 4.6. Predicted clinical lesion coverage.	156
Figure 5.1. The translational pharmacology approach to predicting early bactericidal efficacy in patients.	162
Figure 5.2. Mouse pharmacokinetic and pharmacodynamic data available for rifapentine and bedaquiline.	164
Figure 5.3. Visual predictive check of bedaquiline and rifapentine pharmacokinetics in mice.	171
Figure 5.4 Visual predictive check of bedaquiline and rifapentine PKPD models in mice.	172
Figure 5.5. Clinical simulations using translational PKPD model and clinical observations.	174
Figure 5.6. Model-based prediction of daily change in log ₁₀ CFU/mL correlates well with clinically observed daily change in log ₁₀ CFU/mL for nine TB drugs at multiple dose levels of monotherapy treatment between day 0 to 2 (left) and day 2 to 14 (right).	175
Figure 6.1. Predicted rifapentine exposure in patients.	187
Figure 6.2. Steady state rifapentine pharmacokinetics in mice and humans.	189
Figure 6.3. Concentration-response relationship of rifapentine-containing regimens.	191
Figure 6.4. Predicted bacterial load over time in humans following LTBI treatment with rifapentine-containing regimens.	192
Figure 6.5. Kaplan-Meier plot.	193

List of Tables

Table 2.1. Final parameter estimates for the rabbit plasma-to-lesion PK model.	65
Table 2.2. In vitro lesion PK properties of the aminoglycosides.	67
Table 2.3. Summary of in vitro potency of the aminoglycosides in relevant assays.	69
Table 3.1. In vitro lesion pharmacokinetic profiling of macrolides, clarithromycin and azithromycin.	114
Table 3.2. Clarithromycin plasma pharmacokinetic parameters in rabbits compared to human at the clinical dose.	115
Table 3.3. Plasma-to-tissue model parameters.	119
Table 3.4. In vitro potency of clarithromycin in representative growth inhibitory and bactericidal assays.	120
Table 4.1. Final model parameter estimates.	153
Table 5.1. Mouse PKPD data available for bedaquiline and rifapentine.	163
Table 5.2. Published population PK models and EBA trial information.	165
Table 5.3. Mouse PK and PKPD parameter estimates.	170
Table 6.1. PK/PD indices for rifapentine-containing LTBI regimens.	188
Table 6.2. Pharmacological parameters of rifapentine-containing regimens in latent TB mouse study.	190

Chapter 1: Development of new tuberculosis drugs: Translation to regimen composition for drug-sensitive and multidrug-resistant tuberculosis*

Abstract

Tuberculosis (TB) kills more people than any other infectious disease. Challenges for developing better treatments include the complex pathology due to within-host immune dynamics, interpatient variability in disease severity and drug pharmacokinetics-pharmacodynamics (PK-PD), and the growing emergence of resistance. Model-informed drug development using quantitative and translational pharmacology has become increasingly recognized as a method capable of drug prioritization and regimen optimization to efficiently progress compounds through TB drug development phases. In this review, we examine translational models and tools, including plasma PK scaling, site-of-disease lesion PK, host-immune and bacteria interplay, combination PK-PD models of multidrug regimens, resistance formation, and integration of data across nonclinical and clinical phases. We propose a workflow that integrates these tools with computational platforms to identify drug combinations that have the potential to accelerate sterilization, reduce relapse rates, and limit the emergence of resistance.

* Modified from the publication: Ernest JP, *et al. Annual Reviews of Pharmacology and Toxicology*. 2021. 61:495–516

Introduction

With over 1.4 million deaths in 2018, tuberculosis (TB) claimed more lives than any other infectious disease. In addition, 10 million new cases of TB were estimated globally. Though the incidence rate has declined, the cumulative reduction in incidence rate from 2015 to 2018 was only 6.3%, noticeably short of the 20% milestone set by the End TB Strategy for 2020 (1).

First-line treatment can be highly effective against drug-susceptible tuberculosis (DS-TB). In clinical trials, the standard 4-drug, 6-month regimen produces cure rates of over 95% (2–4). However, in practice, this complex regimen often fails to meet these cure rates due to the lengthy duration of therapy, excessive toxicity, and general lack of adherence (5). Furthermore, drug-resistant TB remains a major threat (roughly 500,000 new cases in 2018) (1), highlighting the need for more treatment options.

Fortunately, recent successes in TB drug discovery and development have produced a number of new drug approvals, late-stage drug candidates, and new compounds entering the clinical phases of development (6, 7). This progress has resulted in a new challenge in TB drug development: With many possible combinations, how do development teams prioritize regimens to test in resource- and cost-intensive clinical trials?

Rational selection of new drugs is challenging for several reasons, including the need for multidrug regimens, the challenges inherent in translating nonclinical results into predictions of clinical outcomes, and the lack of consistent biomarkers across development phases (8–15). Large, late-phase clinical trial failures emphasize the need for better tools in the nonclinical and early clinical spaces to address these challenges. Although there is no consensus on a definitive TB drug development pathway, it is clear that efforts spanning all levels of research provide new and distinct insights (8). It is not the lack of data but a lack of data integration across these platforms that remains the greatest challenge in constructing a rationally designed treatment regimen (9).

Quantitative pharmacology and model-informed drug development are recognized as methods to overcome the limitations of individual models and single experiments and combine data derived from multiple platforms (15–19). This review focuses on current approaches to translate nonclinical experiments into safer, shorter treatment for DS-TB and multidrug-resistant tuberculosis (MDR-TB). Specifically, we focus on computational methods spanning empirical, pharmacokinetic-pharmacodynamic (PK-PD), and systems approaches that complement experimental models to strengthen clinical predictions. We discuss tools that are being implemented to address unique challenges in translating between species, and we summarize previous work that uses computational approaches to predict clinical outcome.

Data available for modeling

Nonclinical data form the cornerstone of rational drug selection. Here, we highlight experimental models that are used to inform translational modeling. These experimental models have been extensively reviewed elsewhere (10, 19–21).

In Vitro

Most TB drug discovery and development programs rely on potency metrics obtained through in vitro assays. In vitro assays are the most rapid approach to determine drug efficacy, and assay parameters can be easily adjusted to test efficacy in different conditions. Traditionally, fixed drug concentrations are tested, but assays that use changing, or dynamic, drug concentrations such as the hollow fiber system (HFS) have also been developed.

Fixed concentration assays.

Static concentration growth inhibitory and time-kill assays obtained from high-throughput screening in early discovery are used to calculate PK-PD target calculations in late preclinical development and clinical trial simulations (19). Today, the field is evolving rapidly to design more sophisticated assays that, while still resorting to static concentrations, integrate a variety of growth media and assay conditions to partially recapitulate the microenvironment found at sites of active TB disease (13, 14) and to specifically target persisters (22). The major limitations of static concentration assays are the relatively short testing period, compound instability, and the absence of the dynamic drug exposures seen in vivo. Despite these limitations, one could argue that the two latest additions to the TB drug arsenal, bedaquiline (BDQ) and delamanid, were developed using these potency metrics to support in vivo dose finding and efficacy studies. While these assays have thus proven useful and effective, optimizing new regimens will require more refined approaches and PK-PD translational tools.

Dynamic concentration using the hollow fiber system.

The HFS has been used extensively to test the activity of antibiotics under conditions that simulate a desired PK profile (23). The HFS adds a critical dynamic layer to the in vitro assessment of drug activity, since the shape of the concentration-time profile influences microbial kill rates and resistance emergence (19, 20, 24). Outputs include colony-forming unit (CFU) counts as well as time to positivity (TTP) in the Mycobacteria Growth Indicator Tube culture system, but the model is also amenable to sampling bacterial and host cell products useful for profiling metabolites or gene or protein expression (20). The HFS has recently been qualified by the European Medicines Agency as a predictive nonclinical model for TB drug development (24, 25) and endorsed by the US Food and Drug Administration.

The major limitation of the HFS is the absence of components of the immune response, although it has been adapted to assess the response of *Mycobacterium tuberculosis* (Mtb) to fluctuating drug concentrations inside of macrophages (26). Additional challenges relate to reproducing drug exposures at the various sites of infection, accounting for highly protein-bound and/or tissue-avid drugs and the tendency of some drugs to bind to system components (19). These issues are particularly relevant to modeling TB treatment, given the heterogeneous pathology and bacterial phenotypes observed and the recent trend toward advancing TB drug candidates with high lipophilicity and other challenging physicochemical and pharmacological traits. For these reasons, the outputs from the HFS and other in vitro systems are best utilized in tandem with outputs from in vivo infection models.

In Vivo

In vivo models allow assessment of drug efficacy within a complex system that includes the presence of an immune system and physiological processes that contribute to drug exposure. In vivo models can be adapted for longer testing periods than in vitro models, can study multiple bacterial subpopulations at one time, and have more relevant outputs like relapse

rates. Here, we discuss three commonly used in vivo models in TB research: mouse, rabbit, and nonhuman primate models.

Mouse models.

Typically, mouse models are used for the first test of efficacy in vivo due to the relatively low logistical requirements, including low costs and ease of handling (10). Although several different inbred and outbred strains are available, experiments using BALB/c mice have provided the largest database for in vivo efficacy studies of TB drugs (27). Data outputs such as bacterial burden (most commonly reported as CFU counts) over time in whole-lung homogenates and the proportion of relapse over time have shown predictive value for determining the efficacy of drug regimens and quantifying exposure-response relationships (14, 15). Comprehensive data sets exist for drugs used as monotherapy and in combination with others (27–33).

In mouse infection models, parameters such as the size of the infectious dose and the length of the incubation period prior to treatment can be modulated to establish distinct infection models with varying bacterial burdens, replication rates, and host immune effects (27, 34). Genetically immune-deficient athymic nude mice, which do not develop an effective adaptive immune response to *Mtb* infection, have been used to estimate the effect of the adaptive immune response on bacterial number and drug activity. Athymic nude mice require longer treatment durations and are more prone to resistance emergence, suggesting that there is utility in modeling treatment outcomes in the context of advanced immune-compromising conditions (35, 36). As such, the type of infection model (e.g., the inoculum size and incubation period) and the underlying development of the adaptive immune response (e.g., host genetic background) are essential factors determining bacterial burden, survival, and drug response, which in turn can affect the interpretation of the drug's effect (10, 14, 34).

Despite the spectrum of experimental controls of infection, most mouse strains fail to

show caseation necrosis, a hallmark of human TB pathology (20). Therefore, mouse infection models using BALB/c, C57BL/6, Swiss, athymic nude, and other commonly used strains are principally models of intracellular infection. Certain mouse strains have shown a propensity to develop caseating lung lesions upon Mtb infection (e.g., C3HeB/FeJ, *Nos2^{-/-}*) and now enable studies of large populations of bacteria residing extracellularly in the necrotic centers of these lesions (37–39) and lesion drug distribution (33, 40). Thus, C3HeB/FeJ and other similar mouse strains provide an economic way to generate lesion-level PK-PD data.

Rabbit model.

The rabbit model of active TB presents multiple pulmonary lesion types, each taking different trajectories over time in response to immune pressure and drug treatment, thus reproducing the dynamic pathology observed in humans (41–43). These aspects allow the rabbit model to be useful in PK-PD and target attainment investigations in plasma and at the site of the disease. Recent technological advances have improved the quantification of lesion-level TB drugs (44–46). Specifically, laser-capture microdissection followed by drug quantitation combines the fully quantitative feature of LCMS (liquid chromatography coupled to mass spectrometry) analysis of tissue homogenate with the high spatial resolution (up to 30–50 μ m) of MALDI (matrix-assisted laser desorption/ionization) mass spectrometry imaging. For example, drug levels can be measured in uninvolved lung, the outer cellular rim rich in lymphocytes, the inner cellular rim rich in foamy macrophages, the outer edge of the necrotic core or caseum, and the center of the caseum. Measured drug concentrations can be related to the concentrations required to inhibit growth or kill resident bacterial populations. Extensive plasma and lesion PK data sets are available for rifampin (RIF), isoniazid (INH), pyrazinamide (PZA) (47, 48), and several fluoroquinolones (47, 49–51). Comprehensive data sets, including plasma PK, lesion PK, potency against persisters in caseum, and lesion-centric efficacy measured by CFU counts and chromosome equivalents, are available for PZA (43, 47, 48, 52)

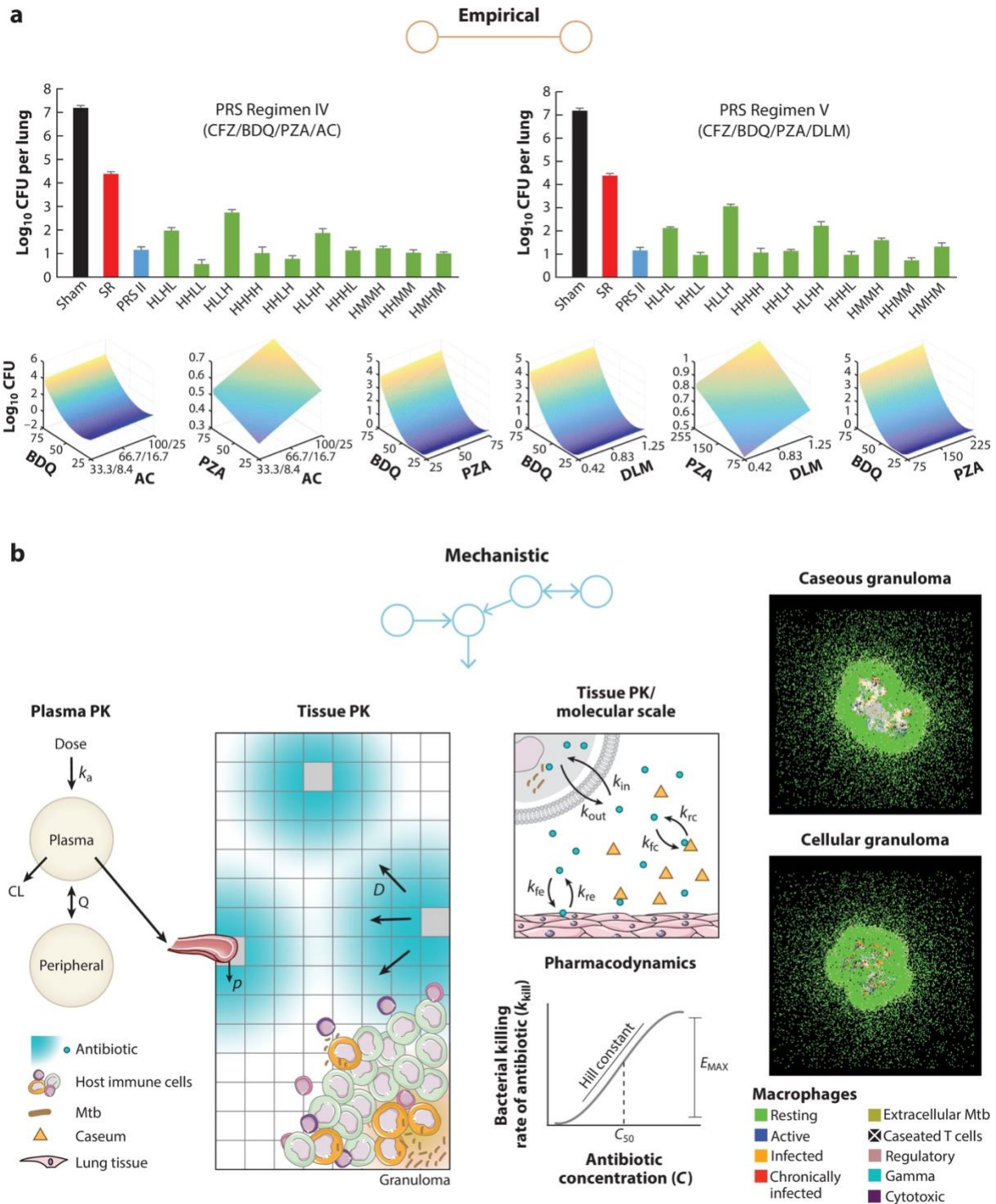
and three fluoroquinolones (46).

Nonhuman primate model.

Compared with other animal models, nonhuman primates (NHPs) often closely recapitulate the plasma PK and metabolism of small-molecule drugs in humans. In addition, NHP models best capture most of the disease pathologies seen in human TB. FDG-PET/CT (fluorodeoxyglucose positron emission tomography/computed tomography) has been used to track longitudinal lesion-level responses to immune pressure and drug treatment within the same animal (53–55). When combined with measurements of bacterial burden and drug concentrations in plasma and lesions, PET-CT imaging is a powerful tool for generating plasma-based and lesion-centric PK-PD models. PK and efficacy studies in rhesus and cynomolgus macaques, as well as in marmosets, have delivered comprehensive data sets for metronidazole, RIF and INH (56), several oxazolidinones (57), and the standard four-drug regimen compared to a combination of INH and streptomycin (58). Most live births in marmosets are twins, thus comparison of results from siblings treated with different drugs or regimens allows for direct comparisons that exclude host factors as a source of variability in drug response (59).

Translational approaches: Importance, advantages, and disadvantages

Translational approaches can be divided into two broad categories: empirical and mechanistic (Figure 0.1). Empirical methods build relationships between variables and outcomes without the need for or an explanation of the mechanism. Conversely, mechanistic models approximate biological phenomena. In drug discovery and development, mechanistic and semi-mechanistic models include integration of relevant physiological and pharmacological relationships between the host, the drug(s), and the bacteria (17, 27). Here, we summarize the approaches and reflect on the potential advantages and disadvantages of each approach.



Ernest JP, et al. 2021
Annu. Rev. Pharmacol. Toxicol. 61:495–516

Figure 0.1 Examples of empirical and mechanistic models.

(a) Empirical models use a top-down approach to link predictive variables to outcomes. Clemens et al. (64) use in vivo dose-response data and a parabolic response surface to empirically predict effective

drug-dose combinations. (b) Mechanistic models use a bottom-up or middle-out approach to recapitulate biological processes. Pienaar et al. (80) simulate host-drug-bacteria dynamics at a molecular level to compare efficacies of fluoroquinolones. Figure adapted with permission from References 64 and 80.

Empirical (Nonpharmacological) Approach

Empirical models are considered to be simpler models, as they are easier to implement than mechanistic models (60). The era of big data has led to increasing artificial intelligence techniques that provide predictive algorithms and has made empirical approaches highly efficient (61).

A challenge in selecting the best TB drug regimen is the number of experiments required as the number of drugs increases. Using machine learning, Horwitz and colleagues (62) were able to show that multidrug-dose relationships from in vitro assays can be described by a parabolic surface using stepwise regression, which was further optimized by machine-learning algorithms and tested in BALB/c mice (63, 64) (Figure 0.1). This approach reduced a theoretical 30.5 billion experiments needed to test 14 drugs to only three phases of 85–155 drug-dose combinations at each phase. Although only a narrow range of combinations was tested in mice, one of the selected regimens (clofazimine, BDQ, and PZA) prevented relapse in mice after only 3 weeks of treatment (64), confirming prior evidence of its rapid sterilizing activity in mice (65). Regression analysis methods could also be applied to increasing amounts of in vivo data in efforts to evaluate the predictive accuracy of nonclinical models and to validate an optimized approach to better translate clinical outcomes from nonclinical data.

A limitation to this approach is that extrapolation of nonclinical efficacy data to the human system of disease and clinical outcomes is not straightforward, and drug targets or pathways that are important to translation could be missed. Additionally, a layer of data is lost, as continuous data are not utilized. Integrating changes over time that are essential to describing disease progression and drug cure would require a mechanistic approach.

Mechanistic (Pharmacological) Approach

Mechanistic approaches that examine drugs at a pharmacological level and may improve the translation of TB drugs are summarized in Figure 0.2.

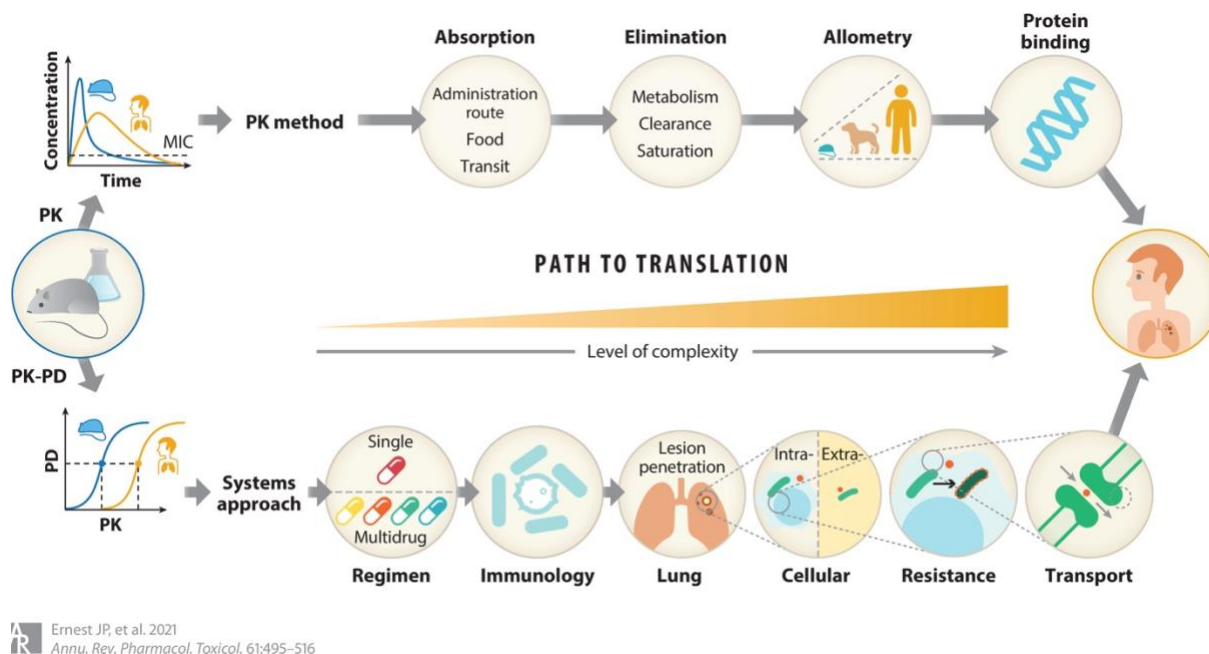


Figure 0.2. Pathway to translating nonclinical to clinical outcomes for tuberculosis (TB).

Different pathways exist to translate preclinical to clinical outcomes. Two methods reviewed here include a pharmacokinetic (PK) approach and a systems approach. The PK approach can be used to predict equivalent drug exposure between nonclinical models and humans. Here, the assumption is that the outcomes will be comparable between species if drug exposure is matched. However, with the complexity of TB disease, a more systems-like approach may be necessary, as species differences in disease pathology do not capture the full spectrum of outcomes in patients. This approach therefore incorporates host-specific differences and models host-bacteria-drug dynamics at the site of action to make more accurate predictions in patients.

Pharmacokinetics-pharmacodynamics.

Traditionally, PK-PD translation involves identifying the human dose that produces the exposure with demonstrated efficacy in an animal model (13). While this approach gives a broad idea of a safe and effective dose, it relies on strong assumptions, including (a) that scaling between species is predictable and reliable, (b) that the antibacterial effects of the host immune system are equivalent between species, and (c) that drug exposures and effects are

not impacted by other drugs through drug-drug interactions. Thus, PK-PD approaches are an attractive option to refine predictions and incorporate additional knowledge.

In general, the purpose of PK-PD studies is to define a relationship between dose and response. With this, PK-PD models can identify the optimal dose and dosing schedule and can simulate alternate regimens. PK-PD modeling has evolved from empirical, descriptive approaches to mechanistic approaches that include properties such as host antimicrobial effects, disease progression, and target site drug distribution (66). The movement toward models with more biological plausibility has improved the predictive accuracy and our ability to extrapolate from them. Mechanism-based PK-PD methods consider time, unlike time-collapsed methods/measures such as AUC, C_{\max} , or time relative to minimum inhibitory concentration (MIC), and reflect gradual killing effects, with changes in concentration as opposed to a binary kill–no kill measure assumed by MIC.

In addition to the time course of drug concentration and response, PK-PD models can include submodels that describe the underlying biological system (66–68). The biological system is the setting in which the drug-bacteria interplay takes place. The primary effect of the biological system is often attributed to the adaptive immune system of the host organism, which can combat the infection and limit growth or reduce bacterial burden without drugs (27, 34). Thus, capturing its effect in a model is critical to establish an uninflated and translatable drug effect (28). Additionally, the heterogeneous lesions of active TB are primarily driven by the immune response (69). These structures add an additional obstacle for drug movement to the site of the disease. Therefore, the time delay for distribution into the site of action is an important component in a PK-PD model.

PK-PD modeling and simulation can substantially reduce uncertainty, time, and cost in high-level decision-making in all phases of development (11, 12, 70). Section 4 of this review highlights both addressable and ongoing challenges in TB drug development that PK-PD modeling can improve, including site-of-disease or lesion PK, immunology, and combination

regimens. The translational toolbox is composed of key components that we believe must be implemented in order to accurately translate from nonclinical experiments to clinical outcomes (Figure 0.3).

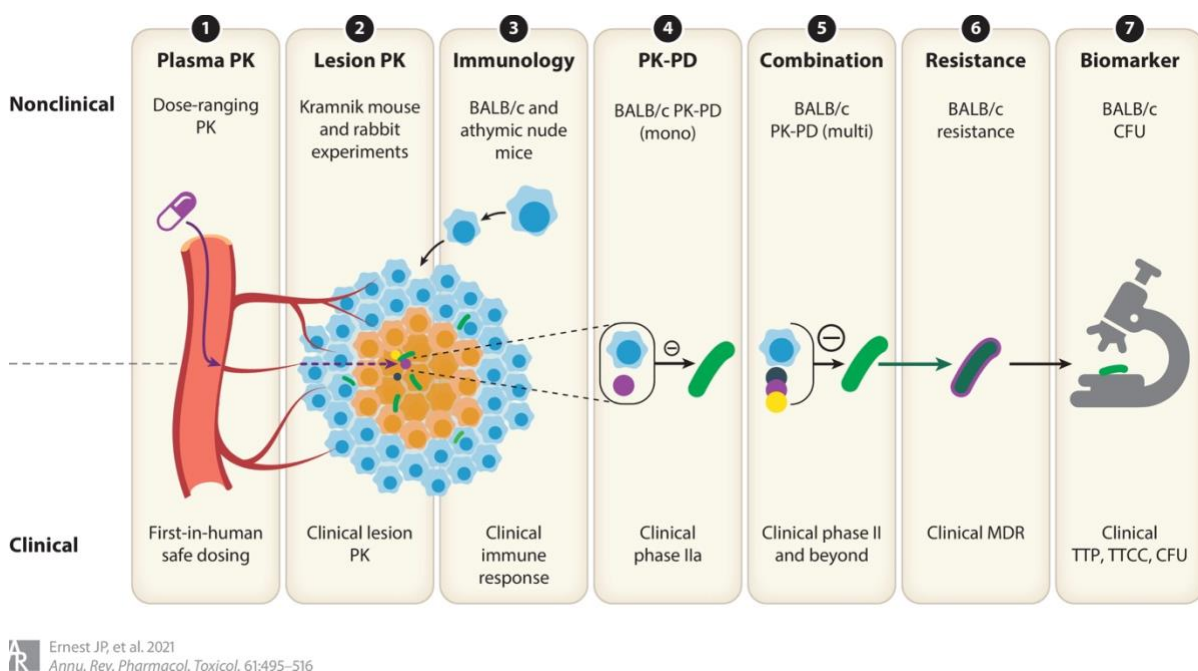


Figure 0.3. Modeling tools important for a translational platform.

Each modeling tool listed is an essential component for predicting clinical outcomes. (①) Plasma pharmacokinetics (PK) studies are a cornerstone to translation. Efficacy, safety, and tissue distribution parameters can be linked to plasma concentration, and plasma PK can inform first-in-human dosing. (②) Lesion PK studies can determine whether a new drug is likely to reach the site of action, including heterogeneous lesions. Mechanistic PK models can simulate predicted levels in patient lesions. (③) Comparing and modeling responses in immune-competent and immune-compromised animal models can predict anticipated differences in host immune response and natural disease progression. (④,⑤) Monotherapy and combination pharmacokinetics-pharmacodynamics (PK-PD) models link drug concentration to drug effect and are a cornerstone of defining optimal drug combinations. (⑥) Resistance models incorporate mechanisms related to the emergence of resistance to therapy over time. (⑦) Biomarkers of disease progression and treatment response in different species should be aligned using statistical models to link nonclinical and clinical readouts that determine outcome.

Systems pharmacology.

Systems pharmacology models use a bottom-up approach to characterize networks of pharmacology, pathology, and biological systems. The increase in nonclinical data available to TB researchers ranges from in vitro assays to unique animal models, making a quantitative systems pharmacology (QSP) approach useful for integrating data and uncovering optimal therapeutics. Differing time scales, specific sites of disease compartments, immune considerations (71), population PK (72), drug resistance (73), and bacterial dynamics, including intracellular survival and metabolomic changes in bacteria (74), can be integrated using QSP methodology.

Existing systems pharmacology models of TB have focused on the host-bacteria relationship. Kirschner et al. (71) have become the leading group in describing within-host infection, which is summarized in their review. Their systems pharmacology models are capable of describing the spectrum of latent to active TB and account for how patients move between these states (75, 76). These models aim to reconstruct the immune response involved in forming granulomas and has culminated in GranSim, an agent-based model that provides two- and three-dimensional spatial models of the lung parenchyma, immune cells, and their interaction over time (73, 77–81) (Figure 0.2). This work has further been expanded by other groups to include oxygen dynamics and antibiotic treatment within granulomas and the modeling of the access of drugs and oxygen to bacteria in relation to their distance from blood vessels (82). A multiscale, whole-lung and lymphatic model has been built based on these principles that can integrate heterogeneity similar to that found in patients, potentially leading to the opportunity to consider a cure across multiple sites of infection within the same patient (83).

This work has provided a scaffold to examine factors that limit the efficacy of antimycobacterial drugs and how systems pharmacology models can guide optimization for current and future drugs. Importantly, when building a systems model, care is needed to reduce the model to its essential parts. Large systems models can cause a loss of confidence when

they become unwieldy and contain pathways and networks that may not offer real insights.

Translational toolbox

The translational toolbox refers to the essential components for translating nonclinical data to clinical outcomes (Figure 0.3). In this section, we summarize seven essential components and highlight published work.

Plasma Pharmacokinetics

Before testing in vivo efficacy of a new compound, developers test oral bioavailability through PK studies (14). Animal plasma PK is essential to determine the potential of a compound to attain reasonable exposures in vivo and, later, to establish PK-PD indices in efficacy studies and determine first-in-human dosing projections. Dose-ranging and dose fractionation studies establish human-equivalent doses, drivers of efficacy, and important nonlinearities in absorption and clearance. Allometric scaling is a weight-based empirical approach to extrapolate animal PK to humans (84). However, protein binding, metabolic pathways, and transport may be species-specific and thus limit the utility of allometric scaling (though renally excreted drugs are generally well predicted). Physiologically based PK modeling (models using parameters based on physiology) improves scaling between species but is much more complex (85). Additional absorption, distribution, metabolism, and excretion studies like human hepatocyte studies to identify drug-drug interactions and investigation of maximal tolerated dose and food effects add insight to drug behavior in patients.

Lesion Pharmacokinetics

Drug distribution to the site of action has become increasingly appreciated as a core PK-PD determinant (9, 66). Pulmonary lesions begin as cellular granulomas, organized structures made of various immune cell types, and evolve to necrotizing granulomas as a result of host cell and bacterial lysis. Thus, TB lesions are primarily made of two major compartments: cellular and

necrotic, the latter being devoid of vascular supply (86). Drugs vary greatly in the manner in which they partition into cellular and necrotic portions of lesions, which can create stark differences in drug exposures between intracellular and extracellular sites of infection (and even into foamy and non-foamy macrophages) in the same lesion and alter PK-PD relationships based on plasma exposure. Differential vascularization and vascular efficiency (87), immune cell types (51), protein binding (88), drug physicochemical properties (89), and interindividual PK variability (90) all affect tissue distribution. In addition, the microenvironments and bacterial phenotypes differ at these sites of infection, which can further alter PK-PD relationships (33, 91, 92). Bacterial populations exhibit differential persistence in the face of immune pressure (93) and drug exposure (52), due to various metabolic and physiologic adaptations to the local environment (22). Mtb isolated from caseum in rabbit lung lesions is profoundly drug tolerant compared to bacteria grown in laboratory media (52).

PK modeling of lesion compartments implements an effect compartment to describe drug distribution from plasma (66),

$$\frac{dC_{\text{lesion}}}{dt} = K_{\text{pl-lesion}} (R_{\text{pl-lesion}} \times C_{\text{plasma}} - C_{\text{lesion}}), \quad 1.$$

and has been used to model PK in rabbits (47) as well as in patients undergoing lung resection (90). Moxifloxacin (MFX) was predicted to be the most efficacious fluoroquinolone (80) using these methods, and PZA was demonstrated to be active against Mtb residing in difficult-to-sterilize necrotic lesions (33, 43, 94). Incorporation of differential drug exposure and drug susceptibility in the calculation of lesion-centric PK-PD parameters can improve translation to PK-PD models. Taking lesion-centric PK-PD parameters into consideration could lead to the rational design of combination regimens made of agents that together reach and kill all bacterial populations.

Immune System Quantification/Bacterial Growth Dynamics

Due to the important role of the host adaptive immune response on impacting treatment effect, various mathematical models have been developed to describe bacterial infection and the resulting immunological responses in animal models of TB (71, 73, 81, 83, 95–98). The enormous amount of data from mouse models of TB has provided great advantages in modeling the bacterial infection and the underlying development of immune responses. In a bacterial growth submodel, the net change in bacterial number (B) over time on growth is described by a one-compartment model with one first-order rate for bacterial replication (K_g) and one first-order rate for natural death (K_d):

$$\frac{dB}{dt} = K_g \times B - K_d \times B \quad 2.$$

In addition, a logistic function can describe a growth plateau as it approaches a maximum population (B_{\max}) (99–101):

$$\frac{dB}{dt} = K_g \times B \times \left(1 - \frac{B}{B_{\max}}\right) \quad 3.$$

The decrease of bacterial replication rate and plateau of bacterial burden are believed to be mainly caused by the onset and development of the adaptive immune response. The impact of the adaptive immune response on bacterial replication was previously described as a nonlinear (sigmoidal) function of bacterial load, with maximal immune effect (K_B) and a bacterial load that stimulates half of the maximal effect (B_{50}) (102–105):

$$\frac{dB}{dt} = K_g \times B \times \left(1 - \frac{B}{B_{\max}}\right) - \frac{K_B \times B}{B_{50} + B} \times B \quad 4.$$

This effect has also been described using a sigmoidal function of time of incubation with

maximal immune effect (K_T) and incubation time that stimulates half of the maximal effect (T_{50}) (28):

$$\frac{dB}{dt} = K_g \times B \times \left(1 - \frac{B}{B_{\max}}\right) - \frac{K_T \times t}{T_{50} + t} \times B \quad 5.$$

The effect has been further described by two sigmoidal functions depending on both bacterial number and time of incubation in order to differentiate the immune effect at the same incubation time but with different bacterial load or the effect with the same bacterial load but at different incubation time (27). Considering the evolution of bacterial populations in vivo from actively replicating bacilli to nonreplicating bacilli, this adaptive immune effect is added onto the bacterial growth as an inhibitory effect to slow bacterial replication (27):

$$\frac{dB}{dt} = K_g \times B \times \left(1 - \frac{K_B \times B^{\gamma_B}}{B_{50}^{\gamma_B} + B^{\gamma_B}}\right) \times \left(1 - \frac{K_T \times t^{\gamma_T}}{T_{50}^{\gamma_T} + t^{\gamma_T}}\right) - K_d \times B \quad 6.$$

Incorporation of the immune system is a critical step in PK-PD modeling. Without it, the drug effect becomes inflated, and the efficacy predictions can be overshoot or overly optimistic.

Pharmacokinetics-Pharmacodynamics

As previously discussed, static MIC does not consider the change in drug exposures over time or in different lesions, while a PK-PD approach does so and can therefore provide better predictions. Clewe et al. (106) developed a multistate tuberculosis pharmacometric (MTP) model based on in vitro time-kill studies. The MTP model consists of three bacterial growth states (fast, slow, and nonmultiplying) and could serve as a framework for accurate characterization of drug effects on different bacterial states. The model was extended by Wicha et al. (107) to successfully predict treatment outcomes in an HFS model, a mouse TB model, and a human phase IIa study.

Establishing PK-PD relationships from in vivo experiments requires integrating the contribution of the immune system. Using BALB/c mouse data, we modeled the interplay between bacterial growth, the adaptive immune response, lung pathology, and TB drugs (28). Our translational model platform includes a quantitative model of the interplay of bacterial growth and immune response, allowing the characterization of the net exposure-response relationships of rifapentine (RPT), RIF, and MFX. This translational PK-PD model adequately predicted long-term outcomes observed in recent clinical trials, including REMox-TB (4) and RIFAQUIN (2). In addition, this model showed that it had the ability to be applied to ongoing trials, in which it predicted minimal risk of relapse at 1 year following 4 months of treatment with high-dose, RPT-containing regimens in TBTC study 31 (ClinicalTrials.gov identifier NCT02410772) and with high-dose, RIF-containing regimens in the RIFASHORT trial (ClinicalTrials.gov identifier NCT02581527). These works illustrate that experimental data, when combined with appropriate considerations of differential bacterial states and the immune system, can improve predictions of clinical outcomes.

Combination Regimens

Combination therapies are the cornerstone for TB treatment, based on superior efficacy and reduced risk of drug resistance (108). With multiple diverse sites of infection and bacterial subpopulations, it is unlikely that a single drug will ever replace combination therapy.

Much effort has been devoted to exploring the interaction between drug pairs. The most commonly used methods can be summarized as effect based and dose-effect based. Effect-based methods compare the effect resulting from the combination of two drugs (E_{AB}) directly to the effects of its individual components (E_A , E_B). The Bliss independence model is one of the most popular effect-based methods. It quantifies interaction with a combination index (CI), where the combination effect can be less than ($CI > 1$), similar to ($CI = 1$) or greater than ($CI < 1$) the expected additive effect from individual agents (109–111):

$$CI = \frac{E_A + E_B - E_A E_B}{E_{AB}} \quad 7.$$

Alternatively, dose-effect-based methods compare the amount or concentration of each drug that produces the same effect (112) and are based on the mathematical framework known as Loewe additivity (113). Under the assumption that the mathematical relation of single dose A and B to reach the combination effect by pair of doses (a, b) is

$$\frac{a}{A} + \frac{b}{B} = 1, \quad 8.$$

CI could be defined as

$$\frac{a}{A} + \frac{b}{B} = CI, \quad 9.$$

where $CI > 1$ indicates an effect produced by the dose pair (a, b) that is less than the expected effect from additivity. Graphical approaches such as isobologram and response surface analysis are also widely utilized, as they are conceptually straightforward, but crucial drawbacks include difficulties in quantitative interpretation and the inability to use graphical analysis for longitudinal data.

As combinations of three or more drugs are typically administered for TB, an urgent task is to develop an analytical framework for when drug pair analysis cannot be applied. Wood et al. (114) developed a simple equation for drug combinations in *Escherichia coli* and *Staphylococcus aureus*, and Zimmer et al. (115) have extended the Bliss independence model in which the effects of all drugs in the mixture are the product of their effective doses (calculated by the model) rather than true doses (dose administered). CI could be evaluated using the ratio of effective and true doses for individual drugs. The general pharmacodynamic interaction (GPDI) model was built on this work and developed for the analysis of TB drug combinations

(116). The GPDI model was adapted from a competitive inhibition model (117); however, it uses an estimable interaction term (INT) that allows both positive and negative shift of the PD parameter (EC_{50}):

$$E_A = \frac{E_{\max A} \times C_A}{\left(EC_{50 A} \times \left(1 + \frac{INT_{AB} \times C_B^{H_{INT,AB}}}{EC_{50 INT,AB}^{H_{INT,AB}} + C_B^{H_{INT,AB}}} \right) \right) + C_A} \quad 10.$$

The GPDI model considers that two drugs could simultaneously be both a perpetrator and victim drug, and thus both positive and negative shifts of EC_{50} are allowed by the value INT, which could be between -1 and ∞ . One of the highlights of the GPDI model is that, for the first time, PD interactions are considered a function of concentration, which could be bidirectional with a change in time. Such a model has been implemented in three- and four-drug combinations (118, 119).

A major limitation to studying drug combinations is the number of experiments required to capture all possible combinations at multiple dose levels. Diagonal measurement of N -way drug interactions (DiaMOND) was recently proposed to address this problem (120). DiaMOND assumes that in a checkerboard assay, only regions with the most information about the shape of the contour are needed. Therefore, for a triplet drug interaction, only dose responses of single drugs and the combination 1:1:1 mixtures are required to be sampled for analysis of interactions within the combination, making the DiaMOND method a more efficient method to inform experimental design of drug combinations.

Using these approaches, synergy and antagonism can be established early in development to evaluate the efficacy of novel regimens.

Drug Resistance Models

Resistance to TB drugs has been an inevitable consequence of clinical usage. Resistance to the new TB drugs BDQ and delamanid has already occurred (121–123). New regimens that are designed to prevent resistance before reaching patients are required.

Two resistance mechanisms can be considered in modeling approaches, namely genetic resistance and phenotypic resistance (drug tolerance). The Mtb genome mutates spontaneously at random, with frequencies ranging between 10^{-6} and 10^{-10} per generation for standard drugs (124). Genetic resistance due to chromosomal mutations leads to acquired MDR-TB and extensively drug-resistant TB. Phenotypic resistance can occur due to epigenetics, protein modification, and metabolic and physiologic reversible adaptations in the presence of drugs and can lead to prolonged treatment and relapse (125, 126). Phenotypic resistance can ultimately promote genetic resistance (121).

To model resistance, in vitro methods can predict the minimum selection concentration of drugs, explained as the minimum concentration at which resistant bacteria are selected for but not killed (127). This work follows the mutant selection window paradigm that hypothesizes that drug-resistant mutants are selected within a window that spans from the MIC of wild-type growth and the upper boundary of concentration-inhibiting growth for the most resistant strains (128, 129). These windows of resistance selection may be pronounced in heterogeneous lesions like granulomas (90, 130, 131), in which differential drug distribution into lesion compartments may result in low drug exposures.

Mechanistic PK-PD models can quantify longitudinal wild-type and resistant bacteria data using genetic and phenotypic principles (102). To model genetic resistance, a preexisting subpopulation model can be used, whereby the resistant compartment is initiated with an estimated fraction of already-resistant bacteria that may have a fitness cost modeled through slower growth (132, 133). Drugs preferentially kill the more drug-sensitive, wild-type bacteria,

leading to an increase of the less susceptible bacteria. Different EC_{50} or E_{max} values can be estimated for the two subpopulations (134). Alternatively, the appearance of new mutants can be modeled with a first-order rate constant (99, 135). Expansion of this model has included sequential mutations in which bacteria mutate with a relative loss in fitness and then mutate again to regain fitness (136). A similar approach in the GranSim platform is used to model mono-resistance in heterogeneous granulomas (137).

Phenotypic resistance models include adaptive and persister models. For adaptive modeling, changes in E_{max} , EC_{50} , or growth rate are modeled over time in discrete populations, allowing for a gradually increasing resistant subpopulation that changes the initial mixed population to a homogeneous population that is more difficult to kill (101). Variants of this model include on-off binding to increase or decrease this process in the presence of drugs (138). The persister model uses phenotype switching between a normal-growing population and a slow-growing persister population that is assumed to be responsible for poor outcomes (139).

Multidrug-resistant models likely require additional mechanisms of resistance. The mutation rate of INH+RIF-resistant bacteria has been estimated to be 1,000-fold higher than the respective mono-resistant rates, which suggests that with each resistant generation, bacteria are primed for further resistance (140).

Biomarkers

While there are many new biomarkers under investigation, animal models of TB and in vitro assays measure bacterial burden by counting CFUs. CFU counts are the gold standard of bacterial burden and are used across historical data to measure and compare new drug performance in clinical development programs (141). Translation of preclinical solid-culture CFU counts to clinically used liquid culture TTP, time to culture conversion (TTCC), and sputum smear tests is necessary to accurately predict patient outcomes in clinical trials.

Animal models study the total population of Mtb in the lung, including bacteria in closed

lesions (142), whereas clinical measures use sputum samples from patients that reveal only those bacteria at the surface of lung and cavities and are often discrete or binary measures. A translational model to consolidate these different data types, from different infection sites and possibly measuring different bacterial subpopulations, is required.

Diacon et al. (143) showed that CFU counts can be replaced by faster and less laborious TTP measures to assess early bactericidal activity (144). Models to describe liquid-culture CFU and TTP measurements have revealed negative correlations with a gradient shift to higher bacterial burden in TTP compared to CFU counts at later time points, showing that, over time, the increase in TTP is inflated compared to the decrease of CFU counts (145). Therefore, TTP seems to be able to account for a subpopulation of bacteria not reflected in CFU counts (145, 146). This relationship between CFU counts and TTP in patients was modeled using machine learning with a Gompertz model, which was reported to be the best fit:

$$\log(CFU) = \frac{TTP - (562.318e^{-0.789e^{-0.195t}})}{-64.111e^{-1.002e^{-0.248t}}}. \quad 11.$$

This model was included in the MTP model discussed under PK-PD tools (106). CFU and TTP values are made available at early clinical trial stages (phase IIa), and TTCC has become an important end point for later-stage trials. Several studies showed that TTCC could be an early predictor of treatment success in drug-resistant TB patients after the first 2 months (147–150). To our knowledge, no study has reported a mathematical relationship between CFU/TTP and TTCC. As one of the most important end points and a potential predictor for resistance, filling the gap between CFU/TTP and TTCC could serve as a powerful translational tool.

Conclusion

The arsenal of new drugs in the pipeline imposes new challenges for the TB community, and quantitative tools are needed to refine results and predict clinical outcomes with higher confidence. In the wake of clinical trial failures, TB drug developers must utilize lessons learned and find new ways to provide safe, novel regimens for testing in TB patients. Importantly, the growing body of technological and methodological advances should be implemented and integrated. As an essential component to modern drug development, translational modeling serves as a platform to connect experimental data and create networks of knowledge. We believe that the use of the translational tools presented here can build confidence into deciding which regimens should be tested; fill in the gaps of experimental uncertainty; and ultimately produce safe, effective, and novel regimens for testing in TB clinical trials.

References

1. WHO (World Health Organ.). 2019. Global tuberculosis report: executive summary. Rep., WHO, Geneva
2. Jindani A, Harrison TS, Nunn AJ, Phillips PP, Churchyard GJ, et al. 2014. High-dose rifapentine with moxifloxacin for pulmonary tuberculosis. *N. Engl. J. Med.* 371:1599–608
3. Merle CS, Fielding K, Sow OB, Gninafon M, Lo MB, et al. 2014. A four-month gatifloxacin-containing regimen for treating tuberculosis. *N. Engl. J. Med.* 371:1588–98
4. Gillespie SH, Crook AM, McHugh TD, Mendel CM, Meredith SK, et al. 2014. Four-month moxifloxacin-based regimens for drug-sensitive tuberculosis. *N. Engl. J. Med.* 371:1577–87
5. Vernon A, Fielding K, Savic R, Dodd L, Nahid P. 2019. The importance of adherence in tuberculosis treatment clinical trials and its relevance in explanatory and pragmatic trials. *PLOS Med.* 16:e1002884
6. Eisinger RW, Embry AC, Read SW, Fauci AS. 2020. 2019: A banner year for tuberculosis research. *J. Infect. Dis.* In press
7. Tornheim JA, Dooley KE. 2019. The global landscape of tuberculosis therapeutics. *Annu. Rev. Med.* 70:105–20
8. Nuermberger E, Sizemore C, Romero K, Hanna D. 2016. Toward an evidence-based nonclinical road map for evaluating the efficacy of new tuberculosis (TB) drug regimens: Proceedings of a Critical Path to TB Drug Regimens-National Institute of Allergy and Infectious Diseases In Vivo Pharmacology Workshop for TB Drug Development. *Antimicrob. Agents Chemother.* 60:1177–82
9. Dooley KE, Hanna D, Mave V, Eisenach K, Savic RM. 2019. Advancing the development of new tuberculosis treatment regimens: the essential role of translational and clinical pharmacology and microbiology. *PLOS Med.* 16:e1002842

10. Nuermberger EL. 2017. Preclinical efficacy testing of new drug candidates. *Microbiol. Spectr.* 5(3):TBTB2-0034-2017
11. Miller R, Ewy W, Corrigan BW, Ouellet D, Hermann D, et al. 2005. How modeling and simulation have enhanced decision making in new drug development. *J. Pharmacokinet. Pharmacodyn.* 32:185–97
12. Tuntland T, Ethell B, Kosaka T, Blasco F, Zang RX, et al. 2014. Implementation of pharmacokinetic and pharmacodynamic strategies in early research phases of drug discovery and development at Novartis Institute of Biomedical Research. *Front. Pharmacol.* 5:174
13. Dartois V, Barry CE 3rd. 2013. A medicinal chemists' guide to the unique difficulties of lead optimization for tuberculosis. *Bioorg. Med. Chem. Lett.* 23:4741–50
14. Franzblau SG, DeGroot MA, Cho SH, Andries K, Nuermberger E, et al. 2012. Comprehensive analysis of methods used for the evaluation of compounds against *Mycobacterium tuberculosis*. *Tuberculosis* 92:453–88
15. Lanoix JP, Chaisson RE, Nuermberger EL. 2016. Shortening tuberculosis treatment with fluoroquinolones: lost in translation? *Clin. Infect. Dis* 62:484–90
16. Gumbo T, Angulo-Barturen I, Ferrer-Bazaga S. 2015. Pharmacokinetic-pharmacodynamic and dose-response relationships of antituberculosis drugs: recommendations and standards for industry and academia. *J. Infect. Dis.* 211(Suppl. 3):S96–106
17. Brill MJE, Kristoffersson AN, Zhao C, Nielsen EI, Friberg LE. 2018. Semi-mechanistic pharmacokinetic-pharmacodynamic modelling of antibiotic drug combinations. *Clin. Microbiol. Infect.* 24:697–706
18. Drusano GL. 2016. From lead optimization to NDA approval for a new antimicrobial: use of pre-clinical effect models and pharmacokinetic/pharmacodynamic mathematical modeling. *Bioorg. Med. Chem.* 24:6401–8

19. Bulitta JB, Hope WW, Eakin AE, Guina T, Tam VH, et al. 2019. Generating robust and informative nonclinical in vitro and in vivo bacterial infection model efficacy data to support translation to humans. *Antimicrob. Agents Chemother.* 63:e02307–18
20. Gumbo T, Lenaerts AJ, Hanna D, Romero K, Nuermberger E. 2015. Nonclinical models for antituberculosis drug development: a landscape analysis. *J. Infect. Dis.* 211(Suppl. 3):S83–95
21. Yasinskaya Y, Sacks L. 2011. Models and approaches for anti-TB drug testing. *Expert Rev. Anti. Infect. Ther.* 9:823–31
22. Gold B, Nathan C. 2017. Targeting phenotypically tolerant *Mycobacterium tuberculosis*. *Microbiol. Spectr.* 5(1):TBTB2-0031-2016
23. Ambrose PG, Bhavnani SM, Rubino CM, Louie A, Gumbo T, et al. 2007. Pharmacokinetics-pharmacodynamics of antimicrobial therapy: It's not just for mice anymore. *Clin. Infect. Dis.* 44:79–86
24. Gumbo T, Pasipanodya JG, Romero K, Hanna D, Nuermberger E. 2015. Forecasting accuracy of the hollow fiber model of tuberculosis for clinical therapeutic outcomes. *Clin. Infect. Dis.* 61(Suppl. 1):S25–31
25. Gumbo T, Pasipanodya JG, Nuermberger E, Romero K, Hanna D. 2015. Correlations between the hollow fiber model of tuberculosis and therapeutic events in tuberculosis patients: learn and confirm. *Clin. Infect. Dis.* 61(Suppl. 1):S18–24
26. Deshpande D, Gumbo T. 2011. Pharmacokinetic/pharmacodynamic-based treatment of disseminated *Mycobacterium avium*. *Future Microbiol.* 6:433–39
27. Zhang N, Strydom N, Tyagi S, Soni H, Tasneen R, et al. 2020. Mechanistic modeling of *Mycobacterium tuberculosis* infection in murine models for drug and vaccine efficacy studies. *Antimicrob. Agents Chemother.* 64(3):e01727-19

28. Bartelink IH, Zhang N, Keizer RJ, Strydom N, Converse PJ, et al. 2017. New paradigm for translational modeling to predict long-term tuberculosis treatment response. *Clin. Transl. Sci.* 10:366–79
29. Almeida D, Nuermberger E, Tasneen R, Rosenthal I, Tyagi S, et al. 2009. Paradoxical effect of isoniazid on the activity of rifampin-pyrazinamide combination in a mouse model of tuberculosis. *Antimicrob. Agents Chemother.* 53:4178–84
30. Rosenthal IM, Tasneen R, Peloquin CA, Zhang M, Almeida D, et al. 2012. Dose-ranging comparison of rifampin and rifapentine in two pathologically distinct murine models of tuberculosis. *Antimicrob. Agents Chemother.* 56:4331–40
31. de Steenwinkel JE, Aarnoutse RE, de Knecht GJ, ten Kate MT, Teulen M, et al. 2013. Optimization of the rifampin dosage to improve the therapeutic efficacy in tuberculosis treatment using a murine model. *Am. J. Respir. Crit. Care Med.* 187:1127–34
32. Rouan MC, Lounis N, Gevers T, Dillen L, Gilissen R, et al. 2012. Pharmacokinetics and pharmacodynamics of TMC207 and its N-desmethyl metabolite in a murine model of tuberculosis. *Antimicrob. Agents Chemother.* 56:1444–51
33. Lanoix JP, Ioerger T, Ormond A, Kaya F, Sacchettini J, et al. 2016. Selective inactivity of pyrazinamide against tuberculosis in C3HeB/FeJ mice is best explained by neutral pH of caseum. *Antimicrob. Agents Chemother.* 60:735–43
34. Cooper AM. 2009. Cell-mediated immune responses in tuberculosis. *Annu. Rev. Immunol.* 27:393–422
35. Park SW, Tasneen R, Converse PJ, Nuermberger EL. 2017. Immunodeficiency and intermittent dosing promote acquired rifamycin monoresistance in murine tuberculosis. *Antimicrob. Agents Chemother.* 61:e01502-17
36. Xu J, Li SY, Almeida DV, Tasneen R, Barnes-Boyle K, et al. 2019. Contribution of pretomanid to novel regimens containing bedaquiline with either linezolid or moxifloxacin

- and pyrazinamide in murine models of tuberculosis. *Antimicrob. Agents Chemother.* 63(5):e00021-19
37. Irwin SM, Driver E, Lyon E, Schrupp C, Ryan G, et al. 2015. Presence of multiple lesion types with vastly different microenvironments in C3HeB/FeJ mice following aerosol infection with *Mycobacterium tuberculosis*. *Dis. Model. Mech.* 8:591–602
38. Lanoix JP, Lenaerts AJ, Nuermberger EL. 2015. Heterogeneous disease progression and treatment response in a C3HeB/FeJ mouse model of tuberculosis. *Dis. Model. Mech.* 8:603–10
39. Gengenbacher M, Duque-Correa MA, Kaiser P, Schuerer S, Lazar D, et al. 2017. NOS2-deficient mice with hypoxic necrotizing lung lesions predict outcomes of tuberculosis chemotherapy in humans. *Sci. Rep.* 7:8853
40. Robertson GT, Eknitphong VA, Scherman MS, McNeil MB, Dennison D, et al. 2019. Efficacy and improved resistance potential of a cofactor-independent InhA inhibitor of *Mycobacterium tuberculosis* in the C3HeB/FeJ mouse model. *Antimicrob. Agents Chemother.* 63(4):e02071-18
41. Subbian S, Tsenova L, Yang G, O'Brien P, Parsons S, et al. 2011. Chronic pulmonary cavitary tuberculosis in rabbits: a failed host immune response. *Open Biol.* 1:110016
42. Via LE, Schimel D, Weiner DM, Dartois V, Dayao E, et al. 2012. Infection dynamics and response to chemotherapy in a rabbit model of tuberculosis using [(1)(8)F]2-fluoro-deoxy-D-glucose positron emission tomography and computed tomography. *Antimicrob. Agents Chemother.* 56:4391–402
43. Blanc L, Sarathy JP, Alvarez Cabrera N, O'Brien P, Dias-Freedman I, et al. 2018. Impact of immunopathology on the antituberculous activity of pyrazinamide. *J. Exp. Med.* 215:1975–86
44. Prideaux B, Lenaerts A, Dartois V. 2018. Imaging and spatially resolved quantification of drug distribution in tissues by mass spectrometry. *Curr. Opin. Chem. Biol.* 44:93–100

45. Zimmerman M, Blanc L, Chen PY, Dartois V, Prideaux B. 2018. Spatial quantification of drugs in pulmonary tuberculosis lesions by laser capture microdissection liquid chromatography mass spectrometry (LCM-LC/MS). *J. Vis. Exp.* 134:e57402
46. Sarathy J, Blanc L, Alvarez-Cabrera N, O'Brien P, Dias-Freedman I, et al. 2019. Fluoroquinolone efficacy against tuberculosis is driven by penetration into lesions and activity against resident bacterial populations. *Antimicrob. Agents Chemother.* 63(5):e02516-18
47. Kjellsson MC, Via LE, Goh A, Weiner D, Low KM, et al. 2012. Pharmacokinetic evaluation of the penetration of antituberculosis agents in rabbit pulmonary lesions. *Antimicrob. Agents Chemother.* 56:446–57
48. Via LE, Savic R, Weiner DM, Zimmerman MD, Prideaux B, et al. 2015. Host-mediated bioactivation of pyrazinamide: implications for efficacy, resistance, and therapeutic alternatives. *ACS Infect. Dis.* 1:203–14
49. Prideaux B, Dartois V, Staab D, Weiner DM, Goh A, et al. 2011. High-sensitivity MALDI-MRM-MS imaging of moxifloxacin distribution in tuberculosis-infected rabbit lungs and granulomatous lesions. *Anal. Chem.* 83:2112–18
50. Prideaux B, ElNaggar MS, Zimmerman M, Wiseman JM, Li X, Dartois V. 2015. Mass spectrometry imaging of levofloxacin distribution in TB-infected pulmonary lesions by MALDI-MSI and continuous liquid microjunction surface sampling. *Int. J. Mass Spectrom.* 377:699–708
51. Blanc L, Daudelin IB, Podell BK, Chen PY, Zimmerman M, et al. 2018. High-resolution mapping of fluoroquinolones in TB rabbit lesions reveals specific distribution in immune cell types. *eLife* 7:e41115
52. Sarathy JP, Via LE, Weiner D, Blanc L, Boshoff H, et al. 2018. Extreme drug tolerance of *Mycobacterium tuberculosis* in caseum. *Antimicrob. Agents Chemother.* 62(2):e02266-17

53. White AG, Maiello P, Coleman MT, Tomko JA, Frye LJ, et al. 2017. Analysis of 18FDG PET/CT imaging as a tool for studying *Mycobacterium tuberculosis* infection and treatment in non-human primates. *J. Vis. Exp.* 127:e56375
54. Martin CJ, Cadena AM, Leung VW, Lin PL, Maiello P, et al. 2017. Digitally barcoding *Mycobacterium tuberculosis* reveals in vivo infection dynamics in the macaque model of tuberculosis. *mBio* 8(3):e00312-17
55. Lin PL, Ford CB, Coleman MT, Myers AJ, Gawande R, et al. 2014. Sterilization of granulomas is common in active and latent tuberculosis despite within-host variability in bacterial killing. *Nat. Med.* 20:75–79
56. Lin PL, Dartois V, Johnston PJ, Janssen C, Via L, et al. 2012. Metronidazole prevents reactivation of latent *Mycobacterium tuberculosis* infection in macaques. *PNAS* 109:14188–93
57. Coleman MT, Chen RY, Lee M, Lin PL, Dodd LE, et al. 2014. PET/CT imaging reveals a therapeutic response to oxazolidinones in macaques and humans with tuberculosis. *Sci. Transl. Med.* 6:265ra167
58. Via LE, England K, Weiner DM, Schimel D, Zimmerman MD, et al. 2015. A sterilizing tuberculosis treatment regimen is associated with faster clearance of bacteria in cavitary lesions in marmosets. *Antimicrob. Agents Chemother.* 59:4181–89
59. Via LE, Weiner DM, Schimel D, Lin PL, Dayao E, et al. 2013. Differential virulence and disease progression following *Mycobacterium tuberculosis* complex infection of the common marmoset (*Callithrix jacchus*). *Infect. Immun.* 81:2909–19
60. Benson N. 2019. Quantitative systems pharmacology and empirical models: friends or foes? *CPT Pharmacometrics Syst. Pharmacol.* 8:135–37
61. Shah P, Kendall F, Khozin S, Goosen R, Hu J, et al. 2019. Artificial intelligence and machine learning in clinical development: a translational perspective. *NPJ Digit. Med.* 2:69

62. Silva A, Lee BY, Clemens DL, Kee T, Ding X, et al. 2016. Output-driven feedback system control platform optimizes combinatorial therapy of tuberculosis using a macrophage cell culture model. *PNAS* 113:E2172–79
63. Al-Shyoukh I, Yu F, Feng J, Yan K, Dubinett S, et al. 2011. Systematic quantitative characterization of cellular responses induced by multiple signals. *BMC Syst. Biol.* 5:88
64. Clemens DL, Lee BY, Silva A, Dillon BJ, Maslesa-Galic S, et al. 2019. Artificial intelligence enabled parabolic response surface platform identifies ultra-rapid near-universal TB drug treatment regimens comprising approved drugs. *PLOS ONE* 14:e0215607
65. Williams K, Minkowski A, Amoabeng O, Peloquin CA, Taylor D, et al. 2012. Sterilizing activities of novel combinations lacking first- and second-line drugs in a murine model of tuberculosis. *Antimicrob. Agents Chemother.* 56:3114–20
66. Danhof M, de Jongh J, De Lange EC, Della Pasqua O, Ploeger BA, Voskuyl RA. 2007. Mechanism-based pharmacokinetic-pharmacodynamic modeling: biophase distribution, receptor theory, and dynamical systems analysis. *Annu. Rev. Pharmacol. Toxicol.* 47:357–400
67. Danhof M, de Lange EC, Della Pasqua OE, Ploeger BA, Voskuyl RA. 2008. Mechanism-based pharmacokinetic-pharmacodynamic (PK-PD) modeling in translational drug research. *Trends Pharmacol. Sci.* 29:186–91
68. Rathi C, Lee RE, Meibohm B. 2016. Translational PK/PD of anti-infective therapeutics. *Drug Discov. Today Technol.* 21–22:41–49
69. Lenaerts A, Barry CE 3rd, Dartois V. 2015. Heterogeneity in tuberculosis pathology, microenvironments and therapeutic responses. *Immunol. Rev.* 264:288–307
70. Drusano GL. 2004. Antimicrobial pharmacodynamics: critical interactions of ‘bug and drug’. *Nat. Rev. Microbiol.* 2:289–300

71. Kirschner D, Pienaar E, Marino S, Linderman JJ. 2017. A review of computational and mathematical modeling contributions to our understanding of *Mycobacterium tuberculosis* within-host infection and treatment. *Curr. Opin. Syst. Biol.* 3:170–85
72. Lyons MA, Lenaerts AJ. 2015. Computational pharmacokinetics/pharmacodynamics of rifampin in a mouse tuberculosis infection model. *J. Pharmacokinet. Pharmacodyn.* 42:375–89
73. Pienaar E, Cilfone NA, Lin PL, Dartois V, Mattila JT, et al. 2015. A computational tool integrating host immunity with antibiotic dynamics to study tuberculosis treatment. *J. Theor. Biol.* 367:166–79
74. Boshoff HI, Lun DS. 2010. Systems biology approaches to understanding mycobacterial survival mechanisms. *Drug Discov. Today Dis. Mech.* 7:e75–82
75. Marino S, Gideon HP, Gong C, Mankad S, McCrone JT, et al. 2016. Computational and empirical studies predict *Mycobacterium tuberculosis*-specific T cells as a biomarker for infection outcome. *PLOS Comput. Biol.* 12:e1004804
76. Young D, Stark J, Kirschner D. 2008. Systems biology of persistent infection: tuberculosis as a case study. *Nat. Rev. Microbiol.* 6:520–28
77. Sershen CL, Plimpton SJ, May EE. 2016. Oxygen modulates the effectiveness of granuloma mediated host response to *Mycobacterium tuberculosis*: a multiscale computational biology approach. *Front. Cell Infect. Microbiol.* 6:6
78. Cicchese JM, Evans S, Hult C, Joslyn LR, Wessler T, et al. 2018. Dynamic balance of pro- and anti-inflammatory signals controls disease and limits pathology. *Immunol. Rev.* 285:147–67
79. Marino S, Hult C, Wolberg P, Linderman JJ, Kirschner DE. 2018. The role of dimensionality in understanding granuloma formation. *Computation* 6(4):58

80. Pienaar E, Sarathy J, Prideaux B, Dietzold J, Dartois V, et al. 2017. Comparing efficacies of moxifloxacin, levofloxacin and gatifloxacin in tuberculosis granulomas using a multi-scale systems pharmacology approach. *PLOS Comput. Biol.* 13:e1005650
81. Cilfone NA, Perry CR, Kirschner DE, Linderman JJ. 2013. Multi-scale modeling predicts a balance of tumor necrosis factor- α and interleukin-10 controls the granuloma environment during *Mycobacterium tuberculosis* infection. *PLOS ONE* 8:e68680
82. Bowness R, Chaplain MAJ, Powathil GG, Gillespie SH. 2018. Modelling the effects of bacterial cell state and spatial location on tuberculosis treatment: insights from a hybrid multiscale cellular automaton model. *J. Theor. Biol.* 446:87–100
83. Pitcher MJ, Bowness R, Dobson S, Gillespie SH. 2018. A spatially heterogeneous network-based metapopulation software model applied to the simulation of a pulmonary tuberculosis infection. *Appl. Netw. Sci.* 3:33
84. Huh Y, Smith DE, Feng MR. 2011. Interspecies scaling and prediction of human clearance: comparison of small- and macro-molecule drugs. *Xenobiotica* 41:972–87
85. Jones H, Rowland-Yeo K. 2013. Basic concepts in physiologically based pharmacokinetic modeling in drug discovery and development. *CPT Pharmacometrics Syst. Pharmacol.* 2:e63
86. Dartois V. 2014. The path of anti-tuberculosis drugs: from blood to lesions to mycobacterial cells. *Nat. Rev. Microbiol.* 12:159–67
87. Datta M, Via LE, Kamoun WS, Liu C, Chen W, et al. 2015. Anti-vascular endothelial growth factor treatment normalizes tuberculosis granuloma vasculature and improves small molecule delivery. *PNAS* 112:1827–32
88. Smith DA, Rowland M. 2019. Intracellular and intraorgan concentrations of small molecule drugs: theory, uncertainties in infectious diseases and oncology, and promise. *Drug Metab. Dispos.* 47:665–72

89. Sarathy JP, Zuccotto F, Hsinpin H, Sandberg L, Via LE, et al. 2016. Prediction of drug penetration in tuberculosis lesions. *ACS Infect. Dis.* 2:552–63
90. Strydom N, Gupta SV, Fox WS, Via LE, Bang H, et al. 2019. Tuberculosis drugs' distribution and emergence of resistance in patient's lung lesions: a mechanistic model and tool for regimen and dose optimization. *PLOS Med.* 16:e1002773
91. Irwin SM, Gruppo V, Brooks E, Gilliland J, Scherman M, et al. 2014. Limited activity of clofazimine as a single drug in a mouse model of tuberculosis exhibiting caseous necrotic granulomas. *Antimicrob. Agents Chemother.* 58:4026–34
92. Via LE, Lin PL, Ray SM, Carrillo J, Allen SS, et al. 2008. Tuberculous granulomas are hypoxic in guinea pigs, rabbits, and nonhuman primates. *Infect. Immun.* 76:2333–40
93. Ganchua SKC, Cadena AM, Maiello P, Gideon HP, Myers AJ, et al. 2018. Lymph nodes are sites of prolonged bacterial persistence during *Mycobacterium tuberculosis* infection in macaques. *PLOS Pathog.* 14:e1007337
94. Kempker RR, Heinrichs MT, Nikolaishvili K, Sabulua I, Bablishvili N, et al. 2017. Lung tissue concentrations of pyrazinamide among patients with drug-resistant pulmonary tuberculosis. *Antimicrob. Agents Chemother.* 61(6):e00226-17
95. Fallahi-Sichani M, El-Kebir M, Marino S, Kirschner DE, Linderman JJ. 2011. Multiscale computational modeling reveals a critical role for TNF- α receptor 1 dynamics in tuberculosis granuloma formation. *J. Immunol.* 186:3472–83
96. Ganguli S, Gammack D, Kirschner DE. 2005. A metapopulation model of granuloma formation in the lung during infection with *mycobacterium tuberculosis*. *Math. Biosci. Eng.* 2:535–60
97. Marino S, El-Kebir M, Kirschner D. 2011. A hybrid multi-compartment model of granuloma formation and T cell priming in tuberculosis. *J. Theor. Biol.* 280:50–62
98. Eftimie R, Gillard JJ, Cantrell DA. 2016. Mathematical models for immunology: current state of the art and future research directions. *Bull. Math. Biol.* 78:2091–134

99. Champion JJ, Chung P, McNamara PJ, Titlow WB, Evans ME. 2005. Pharmacodynamic modeling of the evolution of levofloxacin resistance in *Staphylococcus aureus*. *Antimicrob. Agents Chemother.* 49:2189–99
100. Mouton JW, Vinks AA. 2005. Pharmacokinetic/pharmacodynamic modelling of antibacterials in vitro and in vivo using bacterial growth and kill kinetics: the minimum inhibitory concentration versus stationary concentration. *Clin. Pharmacokinet.* 44:201–10
101. Tam VH, Schilling AN, Nikolaou M. 2005. Modelling time-kill studies to discern the pharmacodynamics of meropenem. *J. Antimicrob. Chemother.* 55:699–706
102. Nielsen EI, Friberg LE. 2013. Pharmacokinetic-pharmacodynamic modeling of antibacterial drugs. *Pharmacol. Rev.* 65:1053–90
103. Drusano GL, Fregeau C, Liu W, Brown DL, Louie A. 2010. Impact of burden on granulocyte clearance of bacteria in a mouse thigh infection model. *Antimicrob. Agents Chemother.* 54:4368–72
104. Drusano GL, Liu W, Kulawy R, Louie A. 2011. Impact of granulocytes on the antimicrobial effect of tedizolid in a mouse thigh infection model. *Antimicrob. Agents Chemother.* 55:5300–5
105. Drusano GL, Vanscoy B, Liu W, Fikes S, Brown D, Louie A. 2011. Saturability of granulocyte kill of *Pseudomonas aeruginosa* in a murine model of pneumonia. *Antimicrob. Agents Chemother.* 55:2693–95
106. Clewe O, Aulin L, Hu Y, Coates AR, Simonsson US. 2016. A multistate tuberculosis pharmacometric model: a framework for studying anti-tubercular drug effects in vitro. *J. Antimicrob. Chemother.* 71:964–74
107. Wicha SG, Clewe O, Svensson RJ, Gillespie SH, Hu Y, et al. 2018. Forecasting clinical dose-response from preclinical studies in tuberculosis research: translational predictions with rifampicin. *Clin. Pharmacol. Ther.* 104:1208–18

108. Foucquier J, Guedj M. 2015. Analysis of drug combinations: current methodological landscape. *Pharmacol. Res. Perspect.* 3:e00149
109. Bliss CI. 1939. The toxicity of poisons applied jointly. *Ann. Appl. Biol.* 26:585–615
110. Greco WR, Bravo G, Parsons JC. 1995. The search for synergy: a critical review from a response surface perspective. *Pharmacol. Rev.* 47:331–85
111. Geary N. 2013. Understanding synergy. *Am. J. Physiol. Endocrinol. Metab.* 304:E237–53
112. Berenbaum MC. 1978. A method for testing for synergy with any number of agents. *J. Infect. Dis.* 137:122–30
113. Loewe S. 1953. The problem of synergism and antagonism of combined drugs. *Arzneimittelforschung* 3:285–90
114. Wood K, Nishida S, Sontag ED, Cluzel P. 2012. Mechanism-independent method for predicting response to multidrug combinations in bacteria. *PNAS* 109:12254–59
115. Zimmer A, Katzir I, Dekel E, Mayo AE, Alon U. 2016. Prediction of multidimensional drug dose responses based on measurements of drug pairs. *PNAS* 113:10442–47
116. Wicha SG, Chen C, Clewe O, Simonsson USH. 2017. A general pharmacodynamic interaction model identifies perpetrators and victims in drug interactions. *Nat. Commun.* 8:2129
117. Ariens EJ, Van Rossum JM, Simonis AM. 1957. Affinity, intrinsic activity and drug interactions. *Pharmacol. Rev.* 9:218–36
118. Clewe O, Wicha SG, de Vogel CP, de Steenwinkel JEM, Simonsson USH. 2018. A model-informed preclinical approach for prediction of clinical pharmacodynamic interactions of anti-TB drug combinations. *J. Antimicrob. Chemother.* 73:437–47
119. Chen C, Wicha SG, de Knecht GJ, Ortega F, Alameda L, et al. 2017. Assessing pharmacodynamic interactions in mice using the multistate tuberculosis pharmacometric and general pharmacodynamic interaction models. *CPT Pharmacometrics Syst. Pharmacol.* 6:787–97

120. Cokol M, Kuru N, Bicak E, Larkins-Ford J, Aldridge BB. 2017. Efficient measurement and factorization of high-order drug interactions in *Mycobacterium tuberculosis*. *Sci. Adv.* 3(10):e1701881
121. Zhang Y, Yew WW. 2015. Mechanisms of drug resistance in *Mycobacterium tuberculosis*: update 2015. *Int. J. Tuberc. Lung. Dis.* 19:1276–89
122. Veziris N, Bernard C, Guglielmetti L, Le Du D, Marigot-Outtandy D, et al. 2017. Rapid emergence of *Mycobacterium tuberculosis* bedaquiline resistance: lessons to avoid repeating past errors. *Eur. Respir. J.* 49(3):1601719
123. Fujiwara M, Kawasaki M, Hariguchi N, Liu Y, Matsumoto M. 2018. Mechanisms of resistance to delamanid, a drug for *Mycobacterium tuberculosis*. *Tuberculosis* 108:186–94
124. David HL. 1970. Probability distribution of drug-resistant mutants in unselected populations of *Mycobacterium tuberculosis*. *Appl. Microbiol.* 20:810–14
125. Zhang Y, Yew WW, Barer MR. 2012. Targeting persisters for tuberculosis control. *Antimicrob. Agents Chemother.* 56:2223–30
126. Zhang Y. 2014. Persisters, persistent infections and the Yin-Yang model. *Emerg. Microbes Infect.* 3:e3
127. Greenfield BK, Shaked S, Marrs CF, Nelson P, Raxter I, et al. 2018. Modeling the emergence of antibiotic resistance in the environment: an analytical solution for the minimum selection concentration. *Antimicrob. Agents Chemother.* 62(3):e01686-17
128. Zhao X, Drlica K. 2002. Restricting the selection of antibiotic-resistant mutant bacteria: measurement and potential use of the mutant selection window. *J. Infect. Dis.* 185:561–65
129. Drlica K, Zhao X. 2007. Mutant selection window hypothesis updated. *Clin. Infect. Dis.* 44:681–88

130. Elliott AM, Berning SE, Iseman MD, Peloquin CA. 1995. Failure of drug penetration and acquisition of drug resistance in chronic tuberculous empyema. *Tuber. Lung Dis.* 76:463–67
131. Dheda K, Lenders L, Magombedze G, Srivastava S, Raj P, et al. 2018. Drug-penetration gradients associated with acquired drug resistance in patients with tuberculosis. *Am. J. Respir. Crit. Care Med.* 198:1208–19
132. Mouton JW, Vinks AA, Punt NC. 1997. Pharmacokinetic-pharmacodynamic modeling of activity of ceftazidime during continuous and intermittent infusion. *Antimicrob. Agents Chemother.* 41:733–38
133. Meagher AK, Forrest A, Dalhoff A, Stass H, Schentag JJ. 2004. Novel pharmacokinetic-pharmacodynamic model for prediction of outcomes with an extended-release formulation of ciprofloxacin. *Antimicrob. Agents Chemother.* 48:2061–68
134. Tam VH, Louie A, Deziel MR, Liu W, Leary R, Drusano GL. 2005. Bacterial-population responses to drug-selective pressure: examination of garenoxacin's effect on *Pseudomonas aeruginosa*. *J. Infect. Dis.* 192:420–28
135. Li RC, Nix DE, Schentag JJ. 1994. Pharmacodynamic modeling of bacterial kinetics: β -lactam antibiotics against *Escherichia coli*. *J. Pharm. Sci.* 83:970–75
136. Wu B, Derendorf H. 2010. Pharmacokinetic/pharmacodynamic model-based combination therapy approach to target antibiotic resistant populations emerged from ciprofloxacin exposure. *Pharmazie* 65:417–20
137. Pienaar E, Linderman JJ, Kirschner DE. 2018. Emergence and selection of isoniazid and rifampin resistance in tuberculosis granulomas. *PLOS ONE* 13:e0196322
138. Mohamed AF, Nielsen EI, Cars O, Friberg LE. 2012. Pharmacokinetic-pharmacodynamic model for gentamicin and its adaptive resistance with predictions of dosing schedules in newborn infants. *Antimicrob. Agents Chemother.* 56:179–88

139. Nielsen EI, Viberg A, Lowdin E, Cars O, Karlsson MO, Sandstrom M. 2007. Semimechanistic pharmacokinetic/pharmacodynamic model for assessment of activity of antibacterial agents from time-kill curve experiments. *Antimicrob. Agents Chemother.* 51:128–36
140. Colijn C, Cohen T, Ganesh A, Murray M. 2011. Spontaneous emergence of multiple drug resistance in tuberculosis before and during therapy. *PLOS ONE* 6:e18327
141. Reed JL, Basu D, Butzler MA, McFall SM. 2017. XtracTB Assay, a *Mycobacterium tuberculosis* molecular screening test with sensitivity approaching culture. *Sci. Rep.* 7:3653
142. Kramnik I, Beamer G. 2016. Mouse models of human TB pathology: roles in the analysis of necrosis and the development of host-directed therapies. *Semin. Immunopathol.* 38:221–37
143. Diacon AH, Maritz JS, Venter A, van Helden PD, Dawson R, Donald PR. 2012. Time to liquid culture positivity can substitute for colony counting on agar plates in early bactericidal activity studies of antituberculosis agents. *Clin. Microbiol. Infect.* 18:711–17
144. Bark CM, Okwera A, Joloba ML, Thiel BA, Nakibali JG, et al. 2011. Time to detection of *Mycobacterium tuberculosis* as an alternative to quantitative cultures. *Tuberculosis* 91:257–59
145. Bowness R, Boeree MJ, Aarnoutse R, Dawson R, Diacon A, et al. 2015. The relationship between *Mycobacterium tuberculosis* MGIT time to positivity and cfu in sputum samples demonstrates changing bacterial phenotypes potentially reflecting the impact of chemotherapy on critical sub-populations. *J. Antimicrob. Chemother.* 70:448–55
146. de Knegt GJ, Dickinson L, Pertinez H, Evangelopoulos D, McHugh TD, et al. 2017. Assessment of treatment response by colony forming units, time to culture positivity and the molecular bacterial load assay compared in a mouse tuberculosis model. *Tuberculosis* 105:113–18

147. Bizzi G. 1965. Use of a new antitussive preparation (1-N-phenyl-4-N-(2,3-dihydroxypropyl-diethylene-diamine) in pediatric practice. *Gazz. Med. Ital.* 124:240–44
148. Basit A, Ahmad N, Khan AH, Javaid A, Syed Sulaiman SA, et al. 2014. Predictors of two months culture conversion in multidrug-resistant tuberculosis: findings from a retrospective cohort study. *PLOS ONE* 9:e93206
149. Singla R, Sarin R, Khalid UK, Mathuria K, Singla N, et al. 2009. Seven-year DOTS-Plus pilot experience in India: results, constraints and issues. *Int. J. Tuberc. Lung. Dis.* 13:976–81
150. Bojorquez-Chapela I, Backer CE, Orejel I, Lopez A, Diaz-Quinonez A, et al. 2013. Drug resistance in Mexico: results from the National Survey on Drug-Resistant Tuberculosis. *Int. J. Tuberc. Lung. Dis.* 17:514–19

Chapter 2: Lesion Penetration and Activity Limit the Utility of Second-Line Injectable Agents in Pulmonary Tuberculosis*

Abstract

Amikacin and kanamycin are second-line injectables used in the treatment of multidrug resistant tuberculosis (MDR-TB), based on the clinical utility of streptomycin, another aminoglycoside and first line anti-TB drug. While streptomycin was tested as a single agent in the first controlled TB clinical trial, introduction of amikacin and kanamycin into MDR-TB regimens was not preceded by randomized controlled trials. A recent large retrospective meta-analysis revealed that compared with regimens without any injectable drug, amikacin provided modest benefits, and kanamycin was associated with worse outcomes. Although their long-term use can cause irreversible ototoxicity, they remain part of MDR-TB regimens because they have a role in preventing emergence of resistance to other drugs. To quantify the contribution of amikacin and kanamycin to second-line regimens, we applied 2-dimensional MALDI mass spectrometry imaging in large lung lesions, quantified drug exposure in lung and lesions of rabbits with active TB, and measured the concentrations required to kill or inhibit growth of the resident bacterial populations. Using these metrics, we applied site-of-action pharmacokinetic and pharmacodynamic (PK-PD) concepts and simulated drug coverage in patients' lung lesions. The results provide a pharmacological explanation for the limited clinical utility of both agents and reveal better PK-PD lesion coverage for amikacin than kanamycin, consistent with retrospective data of contribution to treatment success. Together with recent mechanistic studies dissecting antibacterial activity from aminoglycoside ototoxicity, the limited but rapid penetration of streptomycin, amikacin and kanamycin to the sites of TB disease supports the development of analogs with improved efficacy and tolerability.

* Modified from the publication: Ernest JP, *et al.* Lesion Penetration and Activity Limit the Utility of Second-Line Injectable Agents in Pulmonary Tuberculosis. *Antimicrobial Agents and Chemotherapy*. 2021. 65:10

Introduction

Kanamycin (KAN) and amikacin (AMK) are injectable aminoglycoside antibiotics discovered in the 1950-70's and were among the first agents approved to treat gram-negative and gram-positive bacterial infections (1). They were repurposed to treat multi-drug resistant tuberculosis (MDR-TB) based on the clinical utility of streptomycin (SM), an earlier injectable aminoglycoside tested as a single agent in the first controlled clinical trial with TB patients in 1946 (2). In recent years, however, large retrospective studies and meta-analyses provided limited evidence that use of second-line injectable aminoglycosides KAN and AMK is associated with an increased likelihood of treatment success (3; 4). Consistent with these observations, unfavorable outcomes were similar in patients susceptible versus resistant to KAN and AMK (5). Prospective observational studies and randomized placebo-controlled trials were lacking at the time of their introduction in MDR-TB regimens. The results of early bactericidal activity (EBA) trials with AMK and liposomal AMK were published in 2001, showing barely detectable and negligible effect, respectively (6-8).

Second-line injectables can cause serious and irreversible ototoxicity, resulting in permanent hearing loss in 3% to more than 60% of the patients across studies (4; 9-12). This comes in addition to the logistical challenge and pain associated with daily injections for many months. Since the risks of severe ototoxic and nephrotoxic reactions are sharply increased in patients who receive prolonged therapy (12), aminoglycosides are only recommended for short-term treatment of severe infections, not to exceed 7 to 10 days, except in the case of TB and nontuberculous mycobacterial infections.

Given the limited evidence of clinical utility and irreversible side effects, why were KAN and AMK introduced and kept in MDR-TB regimens? SM was the first antibiotic approved to treat TB and remained in use as a first-line agent in resource-limited countries until 2019 (13). Since KAN and AMK exhibit in vitro potency four- and two-fold lower than SM against

Mycobacterium tuberculosis, respectively (14), it was assumed they may achieve similar or minimally reduced efficacy. In mice and guinea pigs, high doses of AMK and KAN provided limited efficacy compared to SM and isoniazid (15). Efficacy was slightly improved when animals received high infectious doses via the intravenous or intracardial route and treatment started immediately for up to 90 days (16; 17), and in γ -IFN knockout mice (18). When AMK and KAN were tested side by side, AMK appeared more efficacious at comparable doses (17). Intrapulmonary delivery did not provide any benefit compared to subcutaneous injection of AMK (19). Liposomal formulation of AMK showed improved activity compared to free AMK in mice during the acute phase (20), which has been attributed to the liposomes favoring drug penetration into macrophages and retarding its clearance from the site of action (21). The predictive value of these efficacy studies is limited by the lack of a pharmacological rationale to select a dose that reproduces the pharmacokinetic-pharmacodynamic (PK-PD) target of aminoglycosides in TB patients (8; 22). While peak plasma concentration relative to minimum inhibitory concentration (C_{\max}/MIC) is considered the PK-PD driver of efficacy for aminoglycosides against most bacterial infections (23), no systematic in vivo studies have been conducted to confirm this for TB and establish PK-PD targets of efficacy (8). Based on PK-PD threshold of efficacy versus toxicity in patients (24), dose fractionation studies in the hollow fiber system (25) and PK-PD targets in other bacterial infections (26), the WHO recommends doses that achieve C_{\max}/MIC of 10 for KAN and AMK (27; 28). Because most animal efficacy studies described above were performed in the “pre-PK” era, there were no PK data reported to assess PK-PD parameters. However, PK data from other studies ((29) and our unpublished results) indicate that C_{\max}/MIC must have been in excess of the WHO-recommended target and may have exceeded KAN and AMK exposures that are tolerated in humans. Despite the disappointing EBA trials, AMK and KAN were kept in MDR-TB regimens because they were believed to have a role in preventing emergence of resistance to other drugs (6). They are

therefore considered 'companion drugs', used to avert treatment failure due to acquired resistance against core drugs (30-32).

To provide a pharmacological rationale for the limited contribution of AMK and KAN to second-line regimens, we applied site-of-disease PK-PD concepts and measured drug exposure at the site of infection in rabbits with active TB, relative to concentrations required to kill or inhibit growth of the resident bacterial populations. Using these metrics for assessing lesion PK-PD coverage in patients, we provide a pharmacological explanation for the limited clinical utility of both agents and the slightly more favorable contribution of AMK to MDR-TB regimens in retrospective studies, compared to KAN.

Methods

In vivo pharmacokinetics in naïve and TB infected rabbits

All animal studies were performed in Biosafety Level 2 and Biosafety Level 3 (BSL3) facilities and approved by the Institutional Animal Care and Use Committee of the New Jersey Medical School, Rutgers University, Newark, NJ; Hackensack Meridian Health, NJ, or the National Institute of Allergy and Infection Disease, NIH, Bethesda, MD (LCIM-3). All studies followed the guidelines and basic principles in the United States Public Health Service Policy on Humane Care and Use of Laboratory Animals. All samples collected from *M. tuberculosis* infected animals were handled and processed in the BSL3 in compliance with protocols approved by the Institutional Biosafety Committee of the New Jersey Medical School, Rutgers University, Newark, NJ, and Hackensack Meridian Health, NJ.

For pharmacokinetic studies in rabbits, female New Zealand White (NZW) rabbits (Charles River Laboratories, Canada), weighing 2.2 to 2.6 kg, were maintained under specific pathogen-free conditions and fed water and chow *ad libitum*. In dose finding pharmacokinetic studies in uninfected animals, rabbits received a single 60 mg/kg dose of AMK formulated in 0.9% saline administered via the intramuscular route.

For plasma and tissue pharmacokinetics in TB infected animals, NZW rabbits were infected with a high inoculum of *M. tuberculosis* HN878, using a nose-only aerosol exposure system as described (33). Approximately 1,000 to 3,000 CFU were recovered from 2 rabbits analyzed 3 h post infection. At 14 to 20 weeks post infection, once mature cellular and necrotic lesions had developed, rabbits received three daily doses of AMK or KAN at 25 mg/kg, or a single 20 mg/kg dose of SM. Blood was collected from the central ear artery of each rabbit pre-dose, and at several time points between drug administration and necropsy (typically 0.5, 1, 2, 4, and 6 h following drug administration, until the time of euthanasia). Groups of 3 to 6 rabbits were euthanized 2 h (selected as the earliest time point allowing for distribution from plasma to

tissue) and 6 h (the latest practical time point that minimizes the risk of plasma or tissue levels falling below the limit of quantitation) post-dose for AMK and KAN. For SM, a single time point was selected at 3 h post-dose for SM. Due to the rapid clearance of AMK and KAN, and the analytically challenging nature of the aminoglycosides, plasma and lesions collected at 24 h post dose could have delivered a large percentage of BLOQ data points. All blood samples were centrifuged at 4,000 rpm for 5 min and the supernatants (plasma) were transferred and stored at -80°C until analyzed by high-pressure liquid chromatography coupled to tandem mass spectrometry (LC/MS-MS).

Collection of human tubercular tissues

Patients undergoing elective resection surgery to debulk MDR or XDR *M. tuberculosis* infected lung segments were recruited into a previously reported multicenter clinical study (ClinicalTrials.gov identifier NCT00816426, (34; 35)) with written consent. The institutional review boards of the National Institute of Allergy and Infectious Disease, National Institutes of Health, Bethesda, Maryland USA and the Asan Medical Center, Seoul, ROK, approved the study. All procedures were in accordance with the ethical standards of the Helsinki Declaration. The patients received a single dose of 1,000 mg KAN if the drug was not part of their current drug regimen at specific times prior to surgery and subsequent tissue removal. During surgery, the exact time of pulmonary artery ligation was recorded and used to calculate the time of drug administration relative to surgery (Supplementary Table 2.2). Upon lung resection, the tissue was immediately dissected into individual tubercular lesions that were snap frozen in liquid nitrogen vapor for sectioning and laser capture microdissection and stored at -80°C until analyzed.

Lesion dissection and processing

From each lung lobe, individual granulomas, mediastinal lymph nodes and uninvolved (non-diseased) lung tissue areas were dissected, sized, weighed, and recorded. Special care was taken to remove the uninvolved lung tissue surrounding each granuloma. The samples were classified as lymph node, uninvolved lung (devoid of macroscopically visible lesions, though known to be infiltrated with various immune cell types and may contain cellular micro-lesions), cellular granuloma (appears opaque and feels hard to the touch), necrotic granuloma (shows a white/yellow center under the cellular rim and feels soft to the touch) or cavity (presents a large open and opaque ring with a central air pocket and variable amounts of caseum remaining). When necrotic granulomas were greater than 7mm, they were dissected so that the lesion wall and the caseous material within could be stored and analyzed separately. Lesions collected for laser-capture microdissection and MALDI mass spectrometry imaging were left embedded in the surrounding tissue, and snap-frozen in liquid nitrogen vapor as described previously (36). All samples were stored in individual 2 mL tubes at -80°C.

Prior to drug quantitation by LC-MS/MS, all tissue samples were homogenized in approximately, but accurately recorded, 5 volumes of phosphate buffered saline (PBS). Homogenization of tissue samples was achieved using a FastPrep-24 instrument (MP Biomedicals) and 1.4mm zirconium oxide beads (Precellys). Lung and lesion homogenates were stored at -80°C prior to KAN, AMK and SM quantitation by LC-MS/MS analysis.

In vitro pharmacokinetic assays

Caseum binding assay

The caseum binding assay was carried out by rapid equilibrium dialysis using a disposable rapid equilibrium dialysis (RED) device (ThermoFisher Scientific, MA) as previously described (37; 38). Briefly, caseum was diluted 10-fold in PBS, homogenized, and spiked at a

final incubation concentration of 5 μ M. An aliquot (200 μ L) of the spiked matrix was placed in the sample chambers and the buffer chambers were filled with 350 μ L of PBS. The plates were then covered with adhesive seals and incubated at 37°C for 4 h on an orbital shaker set at 300 rpm. Following incubation, samples were removed from both chambers and extracted with water containing 33% trichloroacetic acid prior to LC-MS/MS quantitation. The fraction unbound (f_u) in diluted caseum was calculated as the ratio between free (buffer chamber) and total (sample chamber) drug concentrations.

Macrophage uptake assay

Aminoglycoside uptake assays in THP-1 cells were performed as previously reported (39). Briefly, THP-1 cells (ATCC TIB-202), grown in RPMI 1640 medium supplemented with 10% fetal bovine serum and 2 mM L-glutamine in a CO₂ incubator, were seeded into wells of a 96-well tissue culture-treated plate at 5×10^4 cells / well. THP-1 monocytes were differentiated overnight to macrophages with 100 nM phorbol 12-myristate 13-acetate (PMA). Culture medium was carefully removed and media containing 5 μ M of AMK, KAN or SM was added. After 30 min at 37°C, the cells were gently washed twice with ice-cold PBS to remove extracellular drug. Cells were lysed with deionized water for 1 h at 37°C. The drug content of cell lysates was analyzed by LC/MS-MS, and subsequently normalized to (i) the number of cells per well after drug treatment and washing of dead (non-adherent) cells if any and (ii) the average cellular volume to calculate the intracellular concentration of each aminoglycoside. The drug accumulation factor is expressed as a ratio between the intracellular concentration and extracellular concentration (IC/EC).

In vitro pharmacodynamic assays

Intracellular M. tuberculosis potency assay in THP-1 derived macrophages

To measure aminoglycoside activity against intracellular bacteria, THP-1 monocytes were cultured as mentioned above, differentiated to macrophages with PMA on 24-well cell culture-treated plates seeded with 5×10^5 cells / well. The macrophages were infected with the Erdman strain of *M. tuberculosis* at a multiplicity of infection of 1:1. After 4 h of infection, the wells were washed three times with PBS to remove extracellular bacteria. Fresh media containing 1, 5, 20, 50 or 100 μM of each study drug was added, with vehicle-only wells included as controls. After 1, 2 and 3 days at 37°C and 5% CO_2 , the THP-1 macrophages were detached with 5 mM ethylenediaminetetraacetic acid (EDTA), lysed with 0.05% sodium dodecyl sulfate (SDS), and serial dilutions of the lysates were plated on Middlebrook 7H11 agar for CFU enumeration.

Caseum minimum bactericidal concentration assay

The minimum bactericidal concentration assay against *M. tuberculosis* found in rabbit caseum (MBC_{90} in ex vivo caseum) was performed as described previously (40). Briefly, rabbit caseum was homogenized and incubated with SM, AMK or KAN at concentrations ranging from 0.03125 to 512 μM for 7 days and then plated on Middlebrook 7H11 agar for CFU enumeration, including no-drug controls. The MBC in caseum or casMBC_{90} is defined as the minimum concentration that kills 90% of endogenous bacteria residing in caseum.

Analytical methods for quantitation and imaging of AMK, KAN and SM

LC-MS/MS method for quantitation of aminoglycosides in plasma and tissue homogenates

KAN, AMK and SM internal standards were purchased from Sigma Aldrich. Drug free K_2EDTA plasma and lungs from NZW rabbits were obtained from BioIVT for use as blank matrices to build standard curves. Neat 1 mg/mL Milli-Q stocks were serially diluted in water

containing 1% formic acid to create neat standards. Control tissue and study sample homogenates were created by adding 9-parts PBS buffer to 1-part tissue (10x dilution) and shaking the samples using a Fisher Bead Mill for 1 minute at 6,000 g with zirconia beads. Standard, quality control, and study samples were extracted by combining 10 μ L of tissue homogenate or plasma, 10 μ L of 500 ng/mL internal standard, and 100 μ L of water containing 33% trichloroacetic acid. AMK was used as internal standard for SM sample analysis, and SM was used for AMK and KAN sample analysis. Extracts were vortexed for 5 minutes and centrifuged at 4,000 rpm for 5 minutes. An aliquot (100 μ L) of supernatant was transferred to a 96-well plate for LC-MS/MS analysis. LC-MS/MS analysis was performed on a Sciex Applied Biosystems Qtrap 6500+ triple-quadrupole mass spectrometer coupled to a Shimadzu Nexera X2 UHPLC system to quantify each drug in plasma. Chromatography was performed on an Agilent Zorbax SB-C8 column (2.1x30 mm; particle size, 3.5 μ m) using a reverse phase gradient elution with aqueous. Milli-Q deionized water with 0.1% formic acid (FA) and 0.1% heptafluorobutyric acid (HFBA) was used for the aqueous mobile phase and 0.1% FA and 0.1% HFBA in ACN for the organic mobile phase. Representative chromatograms are shown in Supplementary Figure 2.5. Multiple-reaction monitoring (MRM) of precursor/fragment transitions in electrospray positive-ionization mode was used to quantify the analytes. MRM transitions of 586.70/163.20, 485.40/163.00, and 582.30/263.30 were used for AMK, KAN and SM respectively. Sample analysis was accepted if the concentrations of the quality control samples were within 20% of the nominal concentration. Data processing was performed using Analyst software (version 1.6.2; Applied Biosystems Sciex).

Laser-capture microdissection

Laser-capture microdissection (LCM) was carried out as previously described (36). Briefly, γ -irradiated frozen lung biopsies were sectioned at 10 μ m for histology and 25 μ m for LCM using a CM1810 cryostat (Leica). Sections for histological analysis were taken immediately

adjacent to those taken for LCM and data were correlated. LCM sections were thaw-mounted onto 1.4 μm thick PET membrane slides (Leica). Regions of necrotic caseum, their corresponding cellular rim and normal lung tissue, were dissected using a LMD7 scope (Leica) until an area of 3 million μm^2 had been collected for each region. Dissected regions of interest were stored at -80°C until analysis.

LC-MS/MS method for quantitation of AMK and KAN in laser capture microdissected samples

Laser-capture microdissection (LCM) sample quantification was carried out according to a previously published protocol (36). Briefly, neat 1 mg/mL Milli-Q stocks of AMK and KAN were serially diluted in water containing 1% formic acid to create neat standards. Control tissue homogenate was created by adding 25.6 parts PBS buffer to 1-part tissue (26.7x dilution) and shaking the samples using a Fisher Bead Mill for 1 minute at 6,000 rpm with zirconia beads. Standard, quality control, and control samples were extracted by adding 2 μL of blank homogenate, 10 μL of neat standard, 5 μL of 500 ng/mL SM as internal standard, and 50 μL of water containing 33% trichloroacetic acid. LCM study samples were extracted identical to standards using 2 μL of PBS in place of tissue homogenate. Extracts were bath sonicated 10 minutes and centrifuged at 4,000 rpm for 5 minutes. An aliquot (50 μL) of supernatant was transferred to a 96-well plate for HPLC-MS/MS analysis. HPLC-MS/MS analysis was performed as described in the whole tissue analysis methods.

MALDI mass spectrometry imaging

Sample Preparation and Data Acquisition

Mass spectrometry imaging experiments were carried out on 10 μm sections taken adjacent to those used for histological registration of the LCM sections, as described above. Tissue washing was carried out prior to matrix deposition by submerging the slides in chloroform for 15 s at -20°C as previously published (41). The slides were then allowed to air-

dry for 10 min prior to matrix deposition. The DHB matrix solution (20 mg/mL in 50% methanol, 5 mM sodium chloride and 0.1% trifluoroacetic acid) was deposited over the tissue sections using the HTX M5 sprayer (HTX Technologies LLC, Chapel Hill, NC, USA) using the following parameters: 60°C nozzle temperature, 50 μ L/min flow rate, 900 velocity, 8 p.s.i, 26 passes and crisscross spray pattern. Data acquisition was carried out using a Bruker solarix 7 Tesla FT-ICR mass spectrometer (Bruker Daltonics, Billerica, MA, USA), equipped with a dual ESI/MALDI ion source and Smartbeam II Nd:YAG (355 nm) laser. The instrument was operated in the positive ion mode within the mass range of m/z 150-3,000, utilizing the continuous accumulation of selected ions (CASI) function, in which the quadrupole mass was set to m/z 550 with an isolation window of 200. Images were acquired at 50 μ m resolution using the small laser setting and 200 laser shots per pixel. The transient length was 0.7340, which resulted in an estimated resolving power of 99,000 at m/z 400 (full width at half maximum). Following data acquisition, the slides were washed with 70% ethanol to remove the matrix and stained with hematoxylin and eosin (H&E). The stained sections were then co-registered with the MSI data for analysis.

Data Analysis

Data analysis was carried out using the SCiLS Lab MVS, version 2020a Pro (Bruker Daltonics, Billerica, MA, USA). The data files for the 2- and 6-hour post-dose time-points were combined and imported into a single file for each drug compound to enable comparison across time-points and for statistical analysis. MS images of KAN and AMK were processed using the weak denoising function and presented using the rainbow scale color scheme. Regions of interest (ROIs) were drawn around the different histologically identifiable areas of TB infected lung tissue, these included inner and outer caseum, the cellular layer and normal tissue lung parenchyma. From each of these regions ~350 spectra were acquired from individual pixels (50x50 μ m) used to create relative pixel intensity plots of KAN and AMK ion abundance in each

region. The spectral data obtained from the polygonal ROIs in SCiLS Lab were exported and further analyzed in GraphPad Prism (GraphPad Software, San Diego, CA, USA).

Pharmacokinetic-pharmacodynamic modelling and simulations

Data from a single dose of 60 mg/kg AMK in uninfected rabbits were used to develop a plasma PK model. Simulations were performed to match exposure in rabbits predicted to be equivalent to a 1,000 mg dose in humans. To describe the movement of drug from plasma to sites of action, nonlinear mixed effects models were built for KAN and AMK using available rabbit data (Supplementary Table 2.1). Tissue density was assumed to be 1 g/mL of homogenate. Plasma and lesions were modeled sequentially, where plasma data were modeled first. The plasma parameters were fixed, and effect compartments were added for each distinct tissue. Samples quantified by both homogenate/LCMS and LCM/LCMS methods were pooled together and treated equally. A rate ($k_{pl-lesion}$), ratio ($PC_{pl-lesion}$), and residual error were estimated for each lesion type. Model building was guided by goodness of fit plots, objective function value, and visual predictive checks. One thousand simulations using inter-individual variability and residual error as variability were performed to confirm model fit to raw data. NONMEM version 7.4.2, R software version 3.6.1, and the R packages ggplot2, xpose4, and PKPDsim were used for model building, data visualization, and simulations. A translational model was developed by linking lesion parameters estimated in rabbits to previously published clinical plasma PK models (35; 42). Clinical simulations were compared to in vitro targets and unbound C_{max} , AUC, and time relative to in vitro targets were quantified. Fraction unbound was assumed to be > 0.99 for KAN (43) and 0.9 for AMK (44).

Results

AMK and KAN penetrate major TB lesion compartments to similar extents

To build a translational model of lesion penetration for second line injectables AMK and KAN, we first identified a rabbit dose that achieves exposure comparable to that of TB patients receiving a 1,000 mg intramuscular dose (42; 45-49). The AMK concentration time profile was established in naïve (uninfected) rabbits following a single intramuscular 60 mg/kg dose (Supplementary Table 2.1A). The ratio between peak plasma concentration (C_{max}) and MIC is considered the primary PK-PD parameter driving antibacterial effect of the aminoglycosides (50), though a recent review and reappraisal of available literature and updated guidelines suggest that the area under the concentration-time curve (AUC)/MIC ratio may be a more reliable indicator of bacterial killing and clinical efficacy for these agents (51; 52). Overall, rabbits clear AMK faster than humans, leading to higher C_{max} at human equivalent AUC. To achieve a compromise between matching human C_{max} and human AUC, a dose of 25 mg/kg was selected, given daily for three days to reach steady state (Supplementary Figure 2.1 and Supplementary Table 2.1). Since AMK and KAN display similar PK profile and exposure in patients (26; 53; 54) and in rabbits (45; 55-57), the same dose of 25 mg/kg was selected for both agents. Next, the PK profile of AMK and KAN was obtained in TB infected rabbits following three daily doses of 25 mg/kg, confirming identical exposure of AMK and KAN and reaching a compromise between matching C_{max} and AUC of TB patients receiving a daily dose of 1,000 mg (Supplementary Figure 2.2 and Supplementary Table 2.1).

To visualize the partitioning of AMK and KAN in necrotic lesions and surrounding lung tissue, we generated drug heat maps using MALDI mass spectrometry imaging (MSI) in thin tissue sections collected 2 h and 6 h after the third dose (Figure 0.1A). Sections imaged by MALDI MSI were washed and subsequently stained with hematoxylin and eosin (H&E) to reveal the underlying lesion structure and cellular composition. At 2 h post-dose, penetration of both

drugs was homogeneous throughout uninvolved lung, cellular and necrotic lesion compartments, with apparent higher abundance in denser tissue areas. Given the rapid clearance of aminoglycosides, plasma levels had fallen below 1 mg/mL at 6 h post dose (Supplementary Figure 2.1A). This was reflected by the low drug concentrations in uninvolved lung and cellular lesion areas, which are well vascularized. In contrast, AMK and KAN were partially retained within caseous foci at 6 h, leading to highest signal intensity in the center of the necrotic cores. Lesions collected at 6 h post-dose are larger than at 2 h due to inter-animal variability in pathology. To obtain semi-quantitative data from these drug ion maps, individual pixel intensities were plotted in regions of interest (ROI) manually delineated based on immunopathology staining by H&E: uninvolved lung, cellular rim and caseum. Outer and inner caseum were sampled separately when large necrotic lesions were present. The data confirmed the partitioning of AMK and KAN visualized by MALDI MSI (Figure 0.1B). To measure absolute drug concentrations in defined lung and lesion areas, we collected samples in adjacent tissue sections by laser-capture microdissection (LCM) (36) in 5 to 9 lesions per drug at 2 and 6 h post-dose. AMK and KAN concentrations were measured in microdissected areas and concomitantly collected plasma by conventional mass spectrometry. As anticipated based on MALDI MSI images and pixel intensities, we found higher AMK and KAN concentrations in caseum than in cellular lesion rims. Both drugs were higher in plasma than in tissues at 2 h post dose, while the opposite was observed at 6 h. Absolute drug levels decreased in all compartments between 2 and 6 h post-dose (Figure 0.1C and Supplementary Figure 2.3).

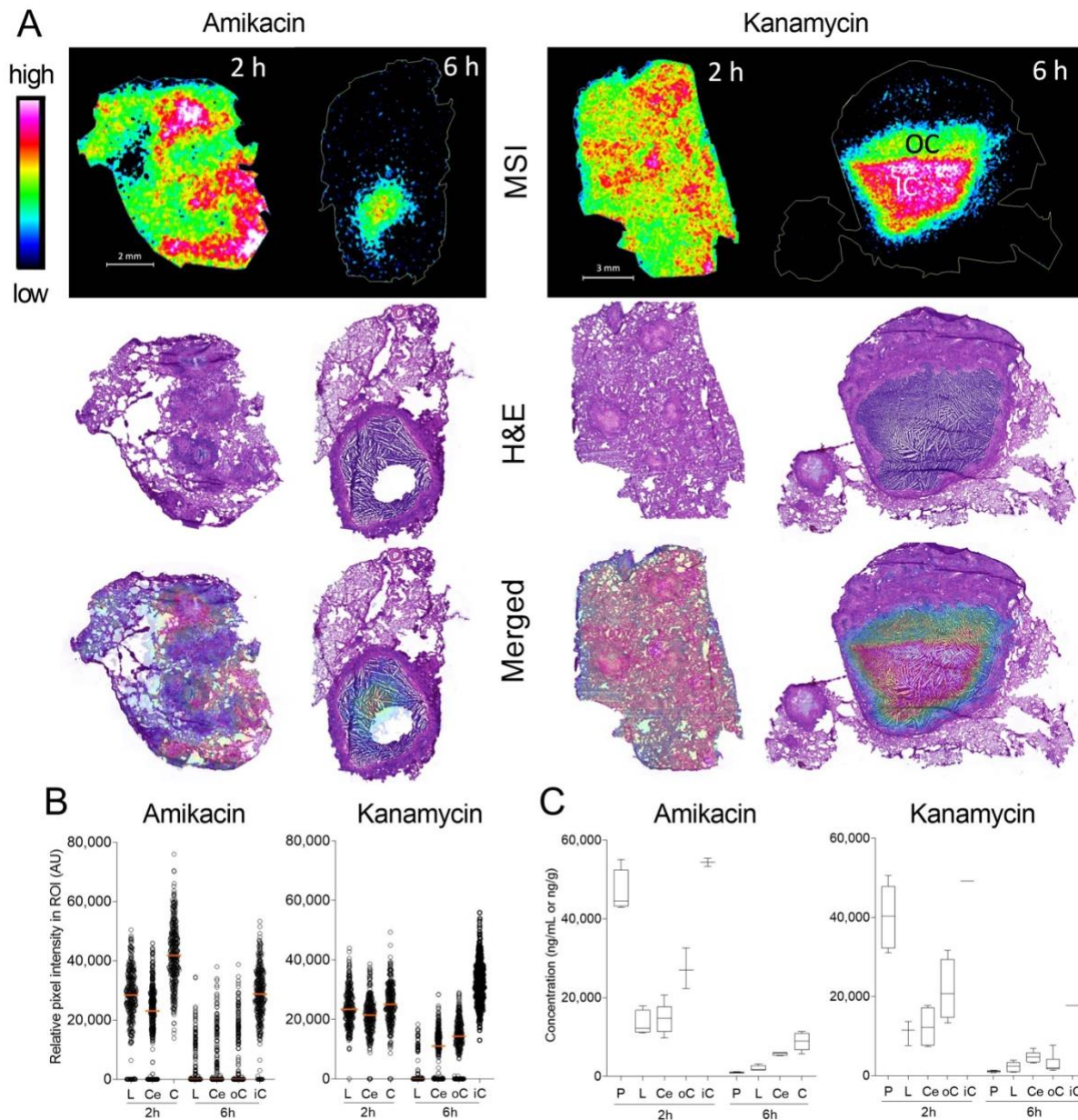


Figure 0.1. Distribution of KAN and AMK in lung, necrotic lesions and cavities.

(A) MALDI mass spectrometry (MS) ion maps of AMK and KAN in representative rabbit lung tissues collected 2 and 6 h post-dose at steady state. MS images of AMK and KAN distribution are displayed in the top panel. The hematoxylin and eosin (H&E) stains of the sections used for MSI are shown in the middle panel, and merged H&E and MS images in the bottom panel. Scale bar = 3 mm. **(B)** Scatter plots of relative pixel (50x50 mm) intensities within regions of interest (ROI) drawn to encompass approximately 350 pixels within lung and lesion compartments as indicated; L: uninvolved lung; Ce: cellular rim; oC: outer caseum; iC: inner caseum. **(C)** Absolute concentrations of AMK and KAN in plasma and infected lung regions determined by laser-capture microdissection and LC/MS-MS. P: plasma; L: uninvolved lung; Ce: cellular rim; C: caseum; oC: outer caseum; iC: inner caseum.

To complement the rabbit dataset and determine whether the partitioning of KAN between uninvolved lung, cellular and caseous rabbit lesion compartments extends to humans, we applied LCM to 20 large necrotic lesions and cavities collected in a previous clinical study from 10 subjects who had received 1,000 mg KAN by intramuscular injection (34; 35). TB patients who undergo lung resection usually present with drug refractory cavitary disease, thus enabling lesion PK investigations in a wider spectrum of lesion type and size (34). These subjects had MDR- or XDR-TB and either received KAN as part of their optimized drug regimen or received a single dose of KAN in addition to their background regimen on the day of scheduled lung resection (Supplementary Table 2.2). Although within-subject and across subject variability was higher than in rabbits as expected, we observed similarly rapid diffusion into caseum in all subjects, both following a single dose and at steady state (Figure 0.1). KAN concentrations were higher in caseum than surrounding cellular and lung tissue in a minority of lesions, which did not appear to be associated with steady state (Supplementary Table 2.2). There was no trend of increased partitioning into caseum relative to the surrounding tissue at steady state, regardless of the time point post dose. Overall, KAN concentrations decreased rapidly over the course of the dosing interval, as seen in rabbits.

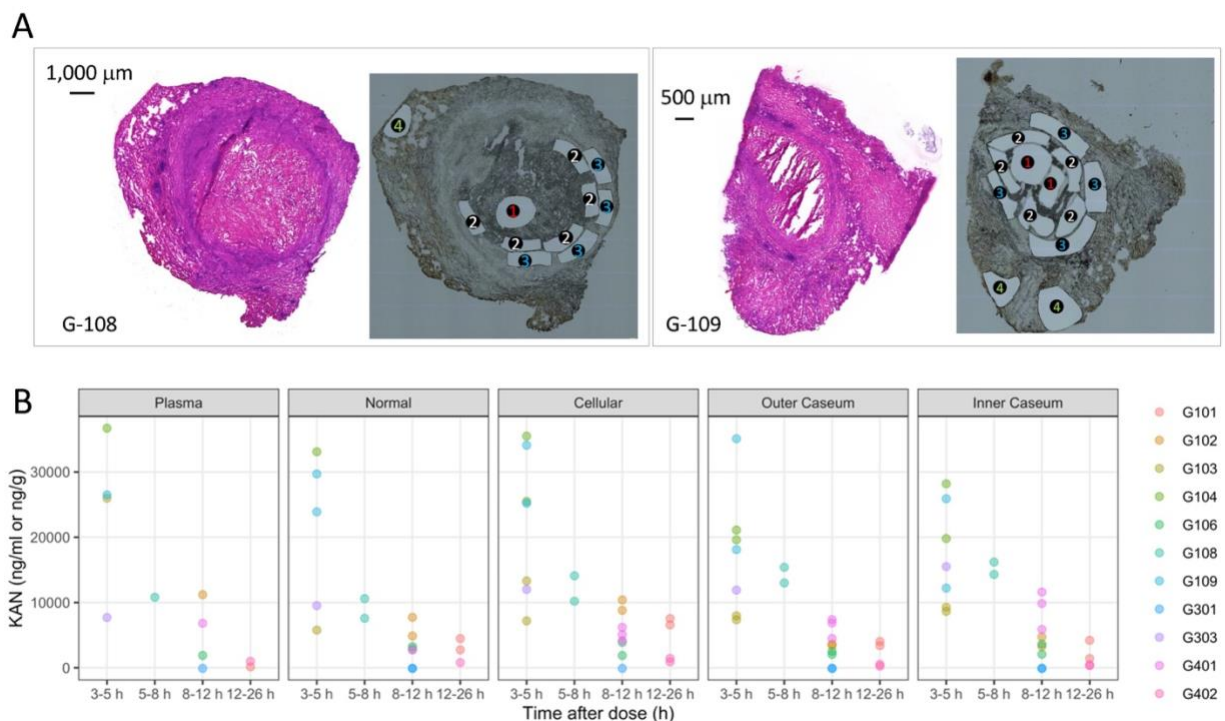


Figure 0.2. KAN distribution in human lung lesions.

(A) Typical examples of histology staining and laser-capture microdissection (LCM) of thin human lesions sections. Two large necrotic lesions were collected from the resected lung tissue of human subject G-108 and G-109. Adjacent lesion sections were used for hematoxylin and eosin (H&E) staining (left) to guide LCM sample collection (right): 1. Inner caseum; 2. Outer caseum; 3. Cellular rim; 4. Uninvolved lung. Laser-dissected pieces belonging to the same tissue compartment were pooled for quantitation by LC-MS/MS. **(B)** Concentrations of KAN in plasma and 20 resected human lesions from 10 subjects, collected at various times from 3 to 26 h after a single or multiple doses of 1,000 mg KAN injected intramuscularly (35). Concentrations were determined in thin section samples collected by LCM, analyzed by LC/MS-MS (36). Each color corresponds to one subject.

To build a translational model of AMK and KAN penetration at the site of TB disease, we measured drug concentrations in serial blood samples and whole lung and lesion homogenates in groups of three TB infected rabbits dosed with 25 mg/kg of AMK or KAN and analyzed at 2 and 6 h after the third daily dose. The total number of observations and the concentrations of AMK and KAN data in plasma, uninvolved lung, cellular and necrotic lesions are shown in Supplementary Figure 2.1B and Supplementary Table 2.3.

KAN plasma PK in rabbits were best described by a one-compartment model with inter-individual variability on bioavailability. Clearance (CL) was estimated to be 0.45 liters/hour and

volume of distribution (V) was estimated to be 0.5 liters, indicating rapid elimination (elimination half-life of 47 minutes). Bioavailability was fixed to one while the rate of absorption after intramuscular injection was estimated to be 2.94 (absorption half-life of 14 minutes). A slope-intercept model best described the residual error with a proportional error of 9.23 percent and additive error of 0.034 mg/L. The model structure of rabbit plasma and site-of-action PK, and scatter visual predictive check of AMK and KAN distribution from plasma to infected lung tissues are shown in Figure 0.3. KAN exposure was greater in plasma than in any tissue compartment. Estimated plasma-to-lesion partition coefficients were 0.338, 0.454, 0.476, 0.497 for uninvolved lung, cellular lesions, caseous lesions, and caseum, respectively, indicating that all lesion compartments have AMK and KAN exposure less than half the exposure measured in plasma. Of tissue compartments, caseum had the highest exposure followed by caseous lesions, cellular lesions, and uninvolved lung. The residual error in tissue compartments was best described by a proportional error model. Final model parameters are listed in Table 0.1.

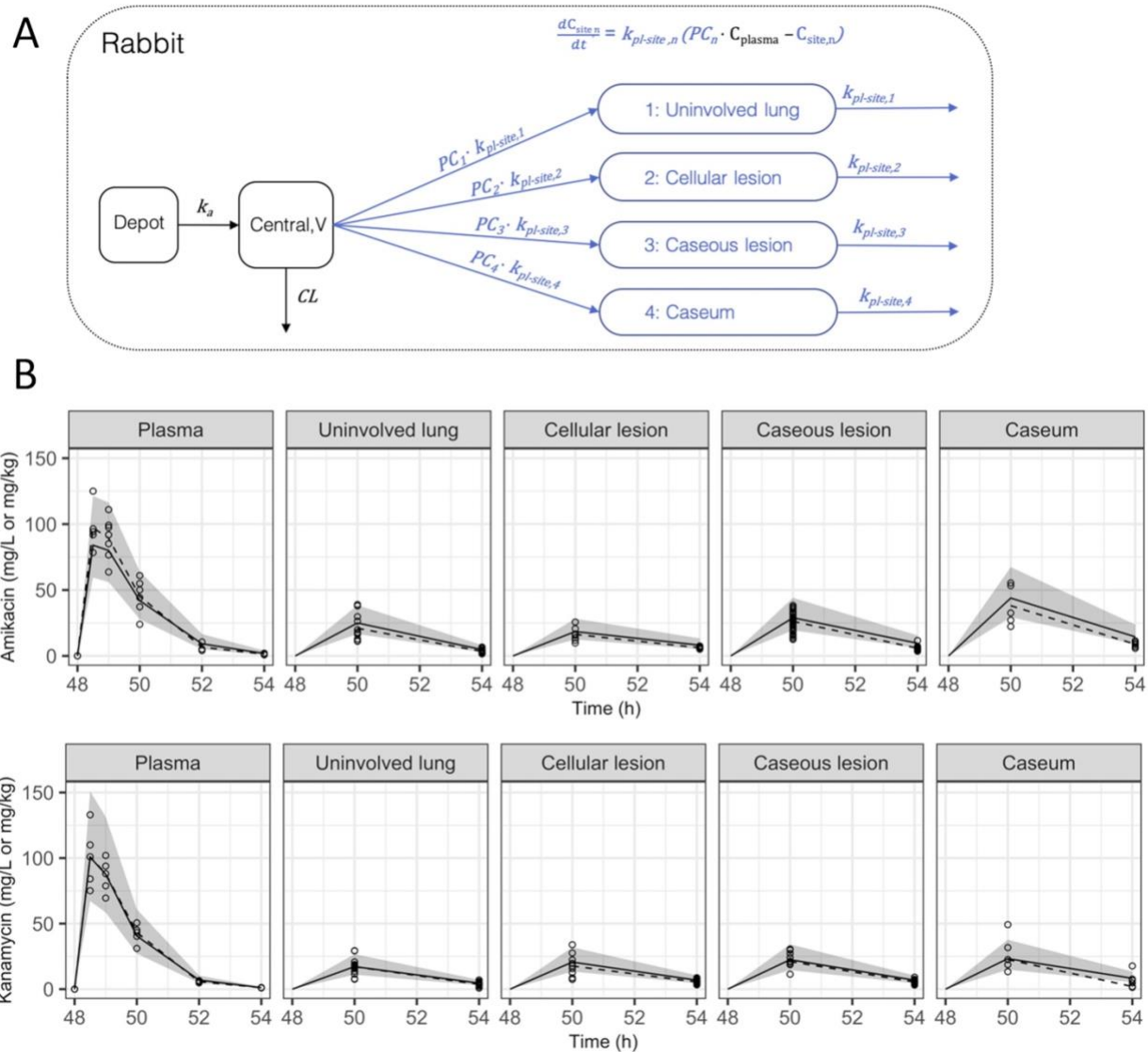


Figure 0.3. Model structure and visual predictive checks (VPC) for plasma-to-tissue distribution of AMK and KAN.

(A) Model structure for the rabbit plasma and site-of-action PK. **(B)** Scatter VPC of rabbit plasma-to-tissue model for AMK and KAN. Points and dashed lines represent observed data points and median of observed data, respectively. Shaded area and solid lines represent the 90% prediction interval and the median of 1,000 simulations, respectively. k_a , absorption rate constant; V , central volume of distribution; CL , clearance; PC , partition coefficient or the ratio of drug at site compared to plasma; $k_{\text{pl-site}}$, distribution rate constant; C_{plasma} , concentration in plasma; C_{site} , concentration at site-of-action.

Table 0.1. Final parameter estimates for the rabbit plasma-to-lesion PK model.

Compartment	Parameter	AMK Value, RSE (%)	KAN Value, RSE (%)
Plasma	k_a (1/h)	2.51 (14.7)	2.94 (10.2)
	CL (L/h)	0.461 (8.0)	0.447 (9.8)
	V (L)	0.572 (8.3)	0.502 (9.8)
	F1	1 FIX	1 FIX
	IIV F1 (CV %)	19.8 (23.3)	21.5 (10.1)
	IIV CL (CV %)	10.4 (18.5)	-
	Proportional Error (CV %)	16.4 (17.2)	9.23 (11.6)
	Additive Error (mg/L)	0.0568 (23.1)	0.0335 (22.0)
Uninvolved lung	Rate ($k_{pl-site,1}$) (1/h)	0.716 (5.8)	0.493 (10.3)
	Partition coefficient (PC_1)	0.437 (5.0)	0.338 (3.1)
	Proportional Error (CV %)	37.8 (10.6)	44.5 (21.0)
Cellular lesions	Rate ($k_{pl-site,2}$) (1/h)	0.385 (10.0)	0.419 (9.0)
	Partition coefficient (PC_2)	0.462 (7.3)	0.454 (6.1)
	Proportional Error (CV %)	25.0 (13.4)	34.7 (7.1)
Caseous lesions	Rate ($k_{pl-site,3}$) (1/h)	0.490 (7.9)	0.448 (15.1)
	Partition coefficient (PC_3)	0.618 (6.7)	0.476 (9.9)
	Proportional Error (CV %)	29.6 (8.2)	32.7 (12.8)
Caseum	Rate ($k_{pl-site,4}$) (1/h)	0.496 (8.1)	0.395 (22.6)
	Partition coefficient (PC_4)	0.927 (8.0)	0.497 (21.3)
	Proportional Error (CV %)	31.5 (14.8)	87.9 (18.6)

k_a , absorption rate constant; 1/h, per hour; CL, clearance; V, central volume of distribution; F1, bioavailability; IIV, inter-individual variability; CV, coefficient of variance; RSE, relative standard error; $k_{pl-site}$, distribution rate constant (See Figure 2.2A for rate constant and partition coefficient description).

AMK plasma PK were similarly described by a one-compartment model with inter-individual variability on bioavailability and CL. CL and V were estimated to be 0.461 L/h and 0.572 L (elimination half-life of 52 minutes). Bioavailability was fixed to one while the absorption rate constant after intramuscular injection was estimated to be 2.51 h⁻¹ (absorption half-life of 17 minutes). A slope-intercept model best described the residual error with a proportional error of 16.4 percent and additive error of 0.057 mg/L. AMK exposure was greater in plasma than in any tissue compartment. Plasma-to-lesion partitioning were 0.437, 0.462, 0.618, and 0.927 for uninvolved lung, cellular lesions, caseous lesions, and caseum, respectively, indicating highest exposure in caseum (Table 0.1). Overall, KAN and AMK presented similar plasma PK profiles and showed modest but comparable penetration at all sites of pulmonary disease, with higher partitioning in caseum than other lung areas. Interestingly, all partition coefficients were greater for AMK than KAN in lung and lesions, particularly in caseum. A similar trend was observed in a limited dataset of streptomycin (SM) distribution in rabbit lung and lesions, showing lung-to-plasma and cellular lesion-to-plasma concentration ratios ranging from 0.3 to 0.5, and cavity caseum-to-plasma concentration ratios of 1.0 to 1.5 (Supplementary Figure 2.4). Thus, the three injectable aminoglycosides used in the treatment of TB have similar distribution patterns into lung lesions.

To further understand the higher retention of AMK, KAN and SM in caseum than in vascularized cellular compartments, we measured the non-specific binding of AMK, KAN and SM in ex vivo caseum and found moderate to high binding and free fractions ranging from 4 to 10% (caseum f_u) for all three drugs, in stark contrast with their low protein binding and high unbound fraction in plasma (plasma f_u), reported in the literature (Table 2.2). This pattern is unique to the aminoglycosides and is consistent with rapid distribution from plasma to caseum and slightly prolonged retention in caseum given the low plasma and high caseum binding. In contrast, most TB drugs exhibit only slightly higher non-specific binding in caseum than in plasma (38), and achieve higher concentrations in cellular than in necrotic and caseous lesion

areas. To determine what contributes to their rapid and moderate distribution in cellular lesion areas, we measured the uptake of AMK, KAN and SM in THP-1 derived macrophages in vitro. We found intracellular to extracellular concentration ratios between 2 and 3, similar to linezolid and falling in the 'low uptake' category compared to other TB drugs (Table 2.2) (34; 58; 59). Thus, the high caseum binding and modest uptake in macrophages is consistent with the partitioning patterns of aminoglycosides in the cellular and necrotic regions of TB lesions.

Table 0.2. In vitro lesion PK properties of the aminoglycosides.

	AMK	KAN	SM	BDQ	MXF	LZD	references
IC/EC ratio in THP-1 macrophages	3.6 ± 0.2	3.8 ± 2.9	2.1 ± 0.7	176.5 ± 164.4	8.8 ± 4.5	2.3 ± 0.9	This work
caseum f_u (%)	3.6 ± 0.3	4.8 ± 1.4	10.5 ± 1.9	< 0.01	16.8 ± 1.8	27.9 ± 2.2	This work
Plasma f_u (%)	> 90	~ 100	65	< 0.1	50 - 60	70	(43; 60)

IC/EC: intracellular to extracellular concentration ratio after 30 minutes of incubation; f_u : fraction unbound; BDQ: bedaquiline, MXF: moxifloxacin; LZD: linezolid

AMK and KAN are weakly active against *M. tuberculosis* populations found in lesions

The MIC of AMK, KAN and SM against a panel of clinical Mtb isolates have been reported in the literature. MIC distributions against a large panel of susceptible isolates center around 0.5 mg/L for SM, 1 mg/L for AMK and 2 mg/L for KAN (14). To place the lesion concentrations of AMK and KAN into pharmacodynamic context at the site of disease, we measured (i) the concentrations required for growth inhibition and killing of intracellular Mtb in macrophages, and (ii) the concentrations required to kill non-replicating Mtb in ex vivo caseum (40). SM was included in all assays as a first line reference aminoglycoside tested as a single agent in early clinical trials (61). In infected THP-1 derived macrophages treated for 3 days, 90% growth inhibition of intracellular Mtb was achieved between 13 and 40 mM or 7.6, 13.6 and 23.3 mg/L for AMK KAN and SM, respectively. No bacterial kill was observed up to 100 mM, all three drugs exerted static effect only (Figure 0.4A). Against non-replicating persisters in caseum, both AMK and SM achieved a 1-log kill around 32 mM (19 mg/L). KAN was inactive up

to 512 mM (Figure 0.4B). Overall, potency was low against intracellular and non-replicating Mtb compared to standard MIC values, and KAN was less potent than AMK, consistent with reported MIC and MBC (Table 0.3).

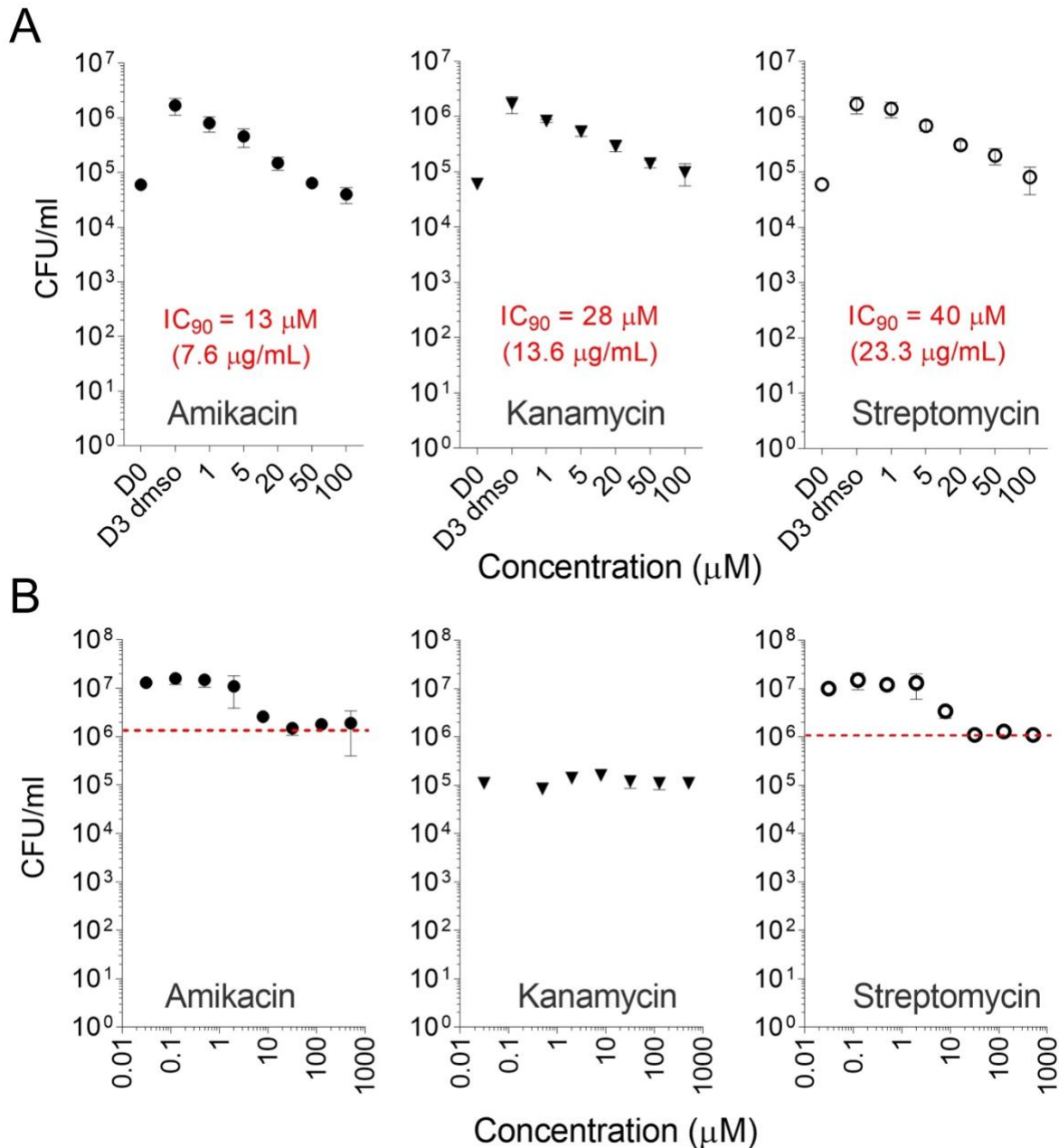


Figure 0.4. Potency of aminoglycosides against typical Mtb subpopulations found in lesions.
(A) Aminoglycoside growth inhibitory activity against intracellular Mtb in THP-1 derived macrophages. Intracellular bacterial burden is shown for treated and drug-free control samples after 3 days of

incubation, at the concentrations indicated. D0: bacterial burden prior to drug treatment; D3 dms0: drug-free control on Day 3. The experiment was carried out twice with technical triplicates; one representative experiment is shown. **(B)** Bactericidal activity of aminoglycosides against non-replicating Mtb persists in ex vivo rabbit caseum (40). The red dotted line indicates the 1-log kill mark, or caseum MBC₉₀.

Table 0.3. Summary of in vitro potency of the aminoglycosides in relevant assays.

	AMK	KAN	SM	Reference
MIC (mg/L)	1	2	0.5	(14; 62)
MBC (mg/L)	1.0 – 8.0	3.0 – 32.0	0.5 – 8.0	(62; 63)
MaIC₉₀ (mg/L)	13	28	40	This work
casMBC₉₀ (mg/L)	19	> 248	19	This work

MIC, minimum inhibitory concentration; MaIC₉₀, concentration at which 90% of bacterial growth is inhibited in THP-1 derived macrophages; casMBC₉₀, concentration at which 90% of bacteria are killed in ex-vivo caseum.

Simulation of lesion pharmacokinetic-pharmacodynamic reveals poor lesion coverage

Aminoglycosides exert concentration dependent activity in vivo, with both C_{max}/MIC and AUC/MIC driving antibacterial effect (50-52). While these PK-PD drivers were established for bacterial infections other than TB, they are generally recognized as a property of the class. The long post-antibiotic effect of aminoglycosides provides a rational explanation for C_{max}/MIC driven killing (26). Given the limited evidence that use of KAN and AMK is associated with an increased likelihood of treatment success (3; 4; 64), we hypothesized that lesion-centric PK-PD parameters are better predictors of efficacy than conventional plasma C_{max}/MIC or AUC/MIC, as observed for other TB drugs (65; 66).

First, lung and lesion penetration coefficients measured in rabbits were applied to clinical plasma concentrations of AMK and KAN to simulate exposure in infected lung compartments. Using published clinical plasma PK models, daily intramuscular injections of 1,000 mg of either AMK or KAN were simulated to steady state (Figure 0.5) (35; 42). Plasma $fAUC/MIC$ (294.1 and 108.5 for AMK and KAN, respectively) and plasma fC_{max}/MIC (44.6 and 13 for AMK and KAN,

respectively) appeared favorable based on PK-PD studies in patients with gram-negative and gram-positive infections (51; 67). In these patient populations, a C_{\max}/MIC ratio of 8–10 and AUC/MIC of 80 to 100 have been associated with effective treatment and prevention of resistance (26; 51; 68). Corresponding thresholds have not been established for TB and would be challenging to validate given the intrinsic multidrug nature of TB treatment. Regardless, the plasma PK-PD parameters of AMK and KAN obtained in our simulations comfortably meet these thresholds. This was true whether total or free drug concentrations in plasma were used since aminoglycoside free fraction is high.

Next, we applied lesion penetration coefficients measured in rabbits to the clinical plasma PK models, then calculated PK-PD parameters in TB lesion compartments using MIC as the denominator (Supplementary Table 2.4). While these remained within the desirable range in lesions, their relevance is limited given (i) the disconnect between replicating Mtb drug susceptibility in broth compared to susceptibility of intracellular and extracellular Mtb at the site of disease, and (ii) the fact that free drug fraction is unknown in tissues. To overcome this caveat, we assessed PK-PD coverage in lesions using potency values against the two major bacterial populations as measured in the previous section, intracellular IC_{90} in macrophages and MBC_{90} in ex vivo caseum (Figure 0.5 and Supplementary Table 2.4). Unlike MIC, these two assays better reproduce the lesion environment and thus measure free drug potency. In contrast to coverage based on plasma PK and MIC, these simulations revealed poor lesion coverage and poor target attainment at the sites of disease. C_{\max}/MBC_{90} in caseum or caseous lesions was 1.7 for AMK and around 0.04 for KAN. In uninvolved lung and cellular lesions where Mtb is mostly intracellular, neither drug achieved the intramacrophage IC_{90} (Figure 0.5). Thus, PK-PD parameters that integrate drug concentrations in cellular and caseous TB lesions versus potency against intracellular Mtb and non-replicating persisters in caseum show that potency

targets are not achieved by the second line aminoglycosides at the site of disease. This may explain their limited contribution to treatment success in MDR-TB patients (3).

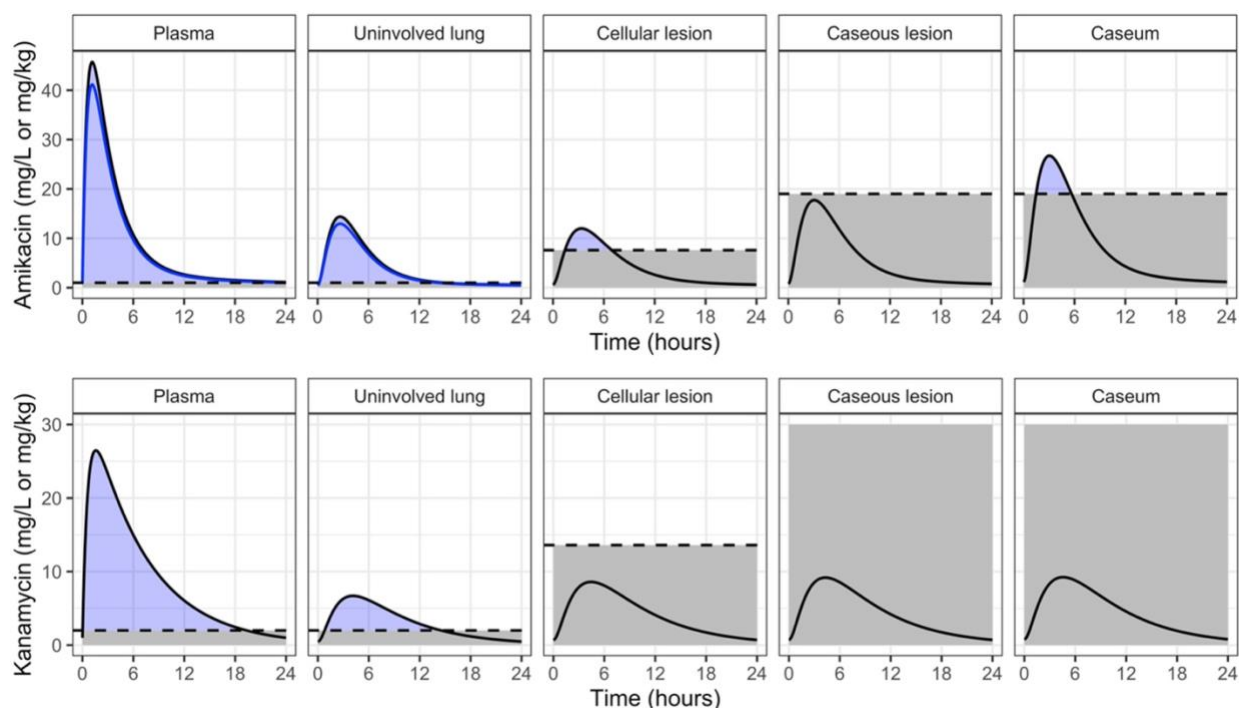


Figure 0.5. Clinical plasma and site-of-action PK simulations for a 24-hour steady-state profile in a typical TB patient.

Dashed lines indicate in vitro target relevant for each compartment. Plasma and uninvolved lung are relative to MIC (1 mg/L, 2 mg/L for AMK and KAN, respectively). Cellular lesion is relative to Macrophage IC_{90} (7.6 mg/L, 13.6 mg/L for AMK and KAN, respectively). Caseous lesion and caseum are relative to caseum MBC_{90} (19 mg/L, 248.1 mg/L for AMK and KAN, respectively). Blue lines for AMK in plasma and uninvolved lung represent the free fraction (KAN plasma protein binding is negligible).

Discussion

The efficacy of second line injectables AMK and KAN has not been evaluated in placebo controlled randomized trials that would measure their contribution to MDR-TB regimens. Our knowledge therefore largely relies on meta-analyses that retrospectively assess the benefits of AMK and KAN inclusion in second line regimens. In the context of newer MDR-TB regimens that include linezolid, bedaquiline and clofazimine, these analyses indicate that AMK provides modest benefits compared to regimens without injectables, while KAN was associated with worse outcomes (3; 4). Both drugs appeared to have modest benefits in past studies that compared weaker drugs and regimens (64). These meta-analyses also showed that aminoglycosides were associated with highest incidence of adverse events leading to permanent drug discontinuation (69). However, use of second line injectables is justified by their potential to prevent emergence of resistance to companion drugs (31; 32).

To help quantify the contribution of AMK and KAN to relapse free cure and rationalize their use against MDR-TB, we measured and modeled drug concentrations at the site of infection in rabbits with active TB, applied lesion penetration coefficients to clinical plasma PK models, measured concentrations required to kill or inhibit growth of intramacrophage and caseum Mtb, and simulated lesion PK-PD coverage of both agents in key lesion compartments. The simulations show that potency targets are not achieved by KAN in cellular and necrotic lesions, and that AMK reaches caseum MBC_{90} for a few hours but with a low caseum $C_{max}/caseum\ MBC_{90}$ of 1.7. These results are consistent with the modest benefits of AMK and worse outcomes associated with KAN use (3), and support recent WHO recommendations that “kanamycin be replaced by amikacin, based on evidence from the comparative effectiveness.” (13). SM, which presents (i) similar plasma PK in patients (22) , (ii) similar penetration in rabbit lung lesions, and (iii) the same caseum MBC as AMK, was deemed very weakly bactericidal in

cavities in which the great majority of bacilli are present in smear-positive pulmonary TB, based on outcomes of an early bactericidal activity trial (70).

Our findings also support WHO recommendations to replace second line injectables with newly approved agents bedaquiline and delamanid when available, given the irreversible toxicity induced by long term aminoglycoside use. Interestingly, bedaquiline containing regimens are more cost effective based on cost-per-treatment success compared with injectable containing regimens (71). However, recent studies advocate for the maintenance of second line injectables owing to their acquired resistance-preventing activity (31) and the rising rate of acquired resistance to bedaquiline (30). In plasma and major sites of disease, AMK but not KAN achieved recommended targets of C_{max} and AUC relative to MIC. This may translate into controlling emergence of resistance in compartments that are permissive to Mtb replication where MIC may partially represent drug potency. However, Mtb also replicates intracellularly in the cellular rim of lesions, where PK-PD coverage is critically low for AMK and below the threshold across the dosing interval for KAN (Figure 0.5). This raises the concern of acquired resistance to these second line injectables while on therapy (72; 73). Whereas a thrice weekly dosing scheme has been proposed to limit AMK toxicity (8; 30), a study that compared the incidence of ototoxicity and nephrotoxicity in patients receiving either 25 mg/kg thrice weekly or 15 mg/kg daily did not detect any difference in outcome (12). In addition, the 3-times weekly dosing scheme may also decrease the already modest lesion coverage despite the long post-antibiotic effect of aminoglycosides, and further open the door for acquired resistance.

This study has a few limitations. (1) A compromise between matching clinical C_{max} and AUC in rabbits was adopted due to the high aminoglycoside clearance in rabbits. Because we selected a dose on the higher side of this compromise (~3-fold higher C_{max} and ~10-20% lower AUC in rabbits than in TB patients), and since KAN and AMK do not or barely reach the target potency at this high C_{max} , putting a stronger emphasis on matching clinical C_{max} – even if the clearance were artificially decreased to ‘humanize’ the rabbit model – would likely reinforce the

conclusions of the study. (2) TB patients who received KAN also received multiple 1st and 2nd line drugs. While aminoglycosides are largely excreted unchanged in the urine and thus not prone to metabolic drug-drug interactions, we cannot exclude drug-drug interactions at the level of transport and efflux in and out of tissues, lesions, and immune cells. (3) KAN but not AMK was included in the clinical lesion PK study. Because the two drugs display similar physicochemical properties, similar in vitro PK parameters known to influence lesion penetration (caseum binding, macrophage uptake, plasma protein binding), and similar plasma and lesion PK in rabbits, we leveraged the favorable rabbit-to-human translation of the KAN findings to extend the AMK distribution patterns from rabbits to humans. AMK, KAN and SM all exhibit attractive physicochemical properties that translate into favorable and rapid penetration into necrotic nodules and cavities, as well as good retention in non-vascularized cavity caseum. This highlights the potential of the class if one could discover analogs with improved toxicity profiles and potency against non-replicating persisters. Recent progress with apramycin, a veterinary drug currently in clinical trials, indicate that dissociation between antibacterial activity and ototoxicity is achievable (18; 74). A formulation that maximizes pulmonary delivery relative to systemic drug concentrations and/or promotes slow release to minimize the frequency of injections would further improve their clinical utility. In addition, aminoglycosides were shown to synergize with cell-wall-active agents such as β -lactams (75), a class of antibiotics that has generated renewed interest against MDR-TB (76; 77).

In conclusion, the pharmacological profiling of AMK and KAN in pulmonary TB provides an explanation for their limited contribution to MDR-TB regimens, and a rationale for the WHO recommendation to replace KAN with AMK. Together with recent mechanistic studies dissecting antibacterial activity from aminoglycoside ototoxicity, the rapid penetration of SM, AMK and KAN to the sites of TB disease supports the development of analogs with improved efficacy and tolerability.

References

1. Krause KM, Serio AW, Kane TR, Connolly LE. 2016. Aminoglycosides: An Overview. Cold Spring Harb Perspect Med 6.
2. Fisher MW, Fishburn GW, Wallace JB. 1947. Streptomycin and bed-rest in the treatment of pulmonary tuberculosis. Am Rev Tuberc 56:534-9.
3. Ahmad N, Ahuja SD, Akkerman OW, Alffenaar JC, Anderson LF, Baghaei P, Bang D, Barry PM, Bastos ML, Behera D, Benedetti A, Bisson GP, Boeree MJ, Bonnet M, Brode SK, Brust JCM, Cai Y, Caumes E, Cegielski JP, Centis R, Chan PC, Chan ED, Chang KC, Charles M, Cirule A, Dalcolmo MP, D'Ambrosio L, de Vries G, Dheda K, Esmail A, Flood J, Fox GJ, Frechet-Jachym M, Fregona G, Gayoso R, Gegia M, Gler MT, Gu S, Guglielmetti L, Holtz TH, Hughes J, Isaakidis P, Jarlsberg L, Kempker RR, Keshavjee S, Khan FA, Kipiani M, Koenig SP, Koh WJ, Kritski A, et al. 2018. Treatment correlates of successful outcomes in pulmonary multidrug-resistant tuberculosis: an individual patient data meta-analysis. Lancet 392:821-834.
4. Reuter A, Tisile P, von Delft D, Cox H, Cox V, Ditiu L, Garcia-Prats A, Koenig S, Lessem E, Nathavitharana R, Seddon JA, Stillo J, von Delft A, Furin J. 2017. The devil we know: is the use of injectable agents for the treatment of MDR-TB justified? Int J Tuberc Lung Dis 21:1114-1126.
5. Migliori GB, Lange C, Centis R, Sotgiu G, Mutterlein R, Hoffmann H, Kliiman K, De Iaco G, Lauria FN, Richardson MD, Spanevello A, Cirillo DM, Group TS. 2008. Resistance to second-line injectables and treatment outcomes in multidrug-resistant and extensively drug-resistant tuberculosis cases. Eur Respir J 31:1155-9.
6. Donald PR, Sirgel FA, Venter A, Smit E, Parkin DP, Van de Wal BW, Mitchison DA. 2001. The early bactericidal activity of amikacin in pulmonary tuberculosis. Int J Tuberc Lung Dis 5:533-8.

7. Donald PR, Sirgel FA, Venter A, Smit E, Parkin DP, Van de Wal BW, Mitchison DA. 2001. The early bactericidal activity of a low-clearance liposomal amikacin in pulmonary tuberculosis. *J Antimicrob Chemother* 48:877-80.
8. Sturkenboom MGG, Simbar N, Akkerman OW, Ghimire S, Bolhuis MS, Alffenaar JC. 2018. Amikacin Dosing for MDR Tuberculosis: A Systematic Review to Establish or Revise the Current Recommended Dose for Tuberculosis Treatment. *Clin Infect Dis* 67:S303-S307.
9. Arnold A, Cooke GS, Kon OM, Dedicoat M, Lipman M, Loyse A, Chis Ster I, Harrison TS. 2017. Adverse Effects and Choice between the Injectable Agents Amikacin and Capreomycin in Multidrug-Resistant Tuberculosis. *Antimicrob Agents Chemother* 61.
10. Seddon JA, Thee S, Jacobs K, Ebrahim A, Hesselning AC, Schaaf HS. 2013. Hearing loss in children treated for multidrug-resistant tuberculosis. *J Infect* 66:320-9.
11. Petersen L, Rogers C. 2015. Aminoglycoside-induced hearing deficits – a review of cochlear ototoxicity. *South African Family Practice* 57:77-82.
12. Peloquin CA, Berning SE, Nitta AT, Simone PM, Goble M, Huitt GA, Iseman MD, Cook JL, Curran-Everett D. 2004. Aminoglycoside toxicity: daily versus thrice-weekly dosing for treatment of mycobacterial diseases. *Clin Infect Dis* 38:1538-44.
13. WHO. 2019. WHO consolidated guidelines on drug-resistant tuberculosis treatment. World Health Organization, Geneva, Switzerland.
14. Jureen P, Angeby K, Sturegard E, Chryssanthou E, Giske CG, Werngren J, Nordvall M, Johansson A, Kahlmeter G, Hoffner S, Schon T. 2010. Wild-type MIC distributions for aminoglycoside and cyclic polypeptide antibiotics used for treatment of *Mycobacterium tuberculosis* infections. *J Clin Microbiol* 48:1853-8.
15. Lounis N, Ji B, Truffot-Pernot C, Grosset J. 1997. Which aminoglycoside or fluoroquinolone is more active against *Mycobacterium tuberculosis* in mice? *Antimicrob Agents Chemother* 41:607-10.

16. Steenken W, Jr., Montalbino V, Thurston JR. 1958. The antituberculous activity of kanamycin in vitro and in the experimental animal (guinea pig). *Ann N Y Acad Sci* 76:103-8.
17. Sanders WE, Jr., Hartwig C, Schneider N, Cacciatore R, Valdez H. 1982. Activity of amikacin against Mycobacteria in vitro and in murine tuberculosis. *Tubercle* 63:201-8.
18. Meyer M, Freihofer P, Scherman M, Teague J, Lenaerts A, Bottger EC. 2014. In vivo efficacy of apramycin in murine infection models. *Antimicrob Agents Chemother* 58:6938-41.
19. Gonzalez-Juarrero M, Woolhiser LK, Brooks E, DeGroot MA, Lenaerts AJ. 2012. Mouse model for efficacy testing of antituberculosis agents via intrapulmonary delivery. *Antimicrob Agents Chemother* 56:3957-9.
20. Dhillon J, Fielding R, Adler-Moore J, Goodall RL, Mitchison D. 2001. The activity of low-clearance liposomal amikacin in experimental murine tuberculosis. *J Antimicrob Chemother* 48:869-76.
21. Ortega V, Giorgio S, de Paula E. 2017. Liposomal formulations in the pharmacological treatment of leishmaniasis: a review. *J Liposome Res* 27:234-248.
22. Zhu M, Burman WJ, Jaresko GS, Berning SE, Jelliffe RW, Peloquin CA. 2001. Population pharmacokinetics of intravenous and intramuscular streptomycin in patients with tuberculosis. *Pharmacotherapy* 21:1037-45.
23. Scaglione F, Paraboni L. 2006. Influence of pharmacokinetics/pharmacodynamics of antibacterials in their dosing regimen selection. *Expert Rev Anti Infect Ther* 4:479-90.
24. van Altena R, Dijkstra JA, van der Meer ME, Borjas Howard JF, Kosterink JG, van Soolingen D, van der Werf TS, Alffenaar JW. 2017. Reduced Chance of Hearing Loss Associated with Therapeutic Drug Monitoring of Aminoglycosides in the Treatment of Multidrug-Resistant Tuberculosis. *Antimicrob Agents Chemother* 61.

25. Srivastava S, Modongo C, Siyambalapitiyage Dona CW, Pasipanodya JG, Deshpande D, Gumbo T. 2016. Amikacin Optimal Exposure Targets in the Hollow-Fiber System Model of Tuberculosis. *Antimicrob Agents Chemother* 60:5922-7.
26. Lacy MK, Nicolau DP, Nightingale CH, Quintiliani R. 1998. The pharmacodynamics of aminoglycosides. *Clin Infect Dis* 27:23-7.
27. Organization WH. 2016. WHO treatment guidelines for drug-resistant tuberculosis, 2016 update (WHO/HTM/TB/2016.4). Geneva.
28. Organization WH. 2018. Technical report on the pharmacokinetics and pharmacodynamics (PK/PD) of medicines used in the treatment of drug-resistant tuberculosis. Geneva.
29. Craig WA, Redington J, Ebert SC. 1991. Pharmacodynamics of amikacin in vitro and in mouse thigh and lung infections. *J Antimicrob Chemother* 27 Suppl C:29-40.
30. Tahseen S, vanDeun A, de Jong BC, Decroo T. 2020. Second-line injectable drugs for rifampicin-resistant tuberculosis: better the devil we know? *J Antimicrob Chemother* doi:10.1093/jac/dkaa489.
31. Van Deun A, Decroo T, Piubello A, de Jong BC, Lynen L, Rieder HL. 2018. Principles for constructing a tuberculosis treatment regimen: the role and definition of core and companion drugs. *Int J Tuberc Lung Dis* 22:239-245.
32. Decroo T, Maug AKJ, Hossain MA, Uwizeye C, Gumusboga M, Demeulenaere T, Ortuno-Gutierrez N, de Jong BC, Van Deun A. 2020. Injectables' key role in rifampicin-resistant tuberculosis shorter treatment regimen outcomes. *PLoS One* 15:e0238016.
33. Bayer AS, Crowell DJ, Yih J, Bradley DW, Norman DC. 1988. Comparative pharmacokinetics and pharmacodynamics of amikacin and ceftazidime in tricuspid and aortic vegetations in experimental *Pseudomonas* endocarditis. *J Infect Dis* 158:355-9.
34. Bugnon D, Potel G, Xiong YQ, Caillon J, Kergueris MF, Le Conte P, Baron D, Drugeon H. 1996. In vivo antibacterial effects of simulated human serum profiles of once-daily

- versus thrice-daily dosing of amikacin in a *Serratia marcescens* endocarditis experimental model. *Antimicrob Agents Chemother* 40:1164-9.
35. Illamola SM, Huynh HQ, Liu X, Bhakta ZN, Sherwin CM, Liou TG, Carveth H, Young DC. 2018. Population Pharmacokinetics of Amikacin in Adult Patients with Cystic Fibrosis. *Antimicrob Agents Chemother* 62.
 36. Kato H, Hagihara M, Hirai J, Sakanashi D, Suematsu H, Nishiyama N, Koizumi Y, Yamagishi Y, Matsuura K, Mikamo H. 2017. Evaluation of Amikacin Pharmacokinetics and Pharmacodynamics for Optimal Initial Dosing Regimen. *Drugs R D* 17:177-187.
 37. Modongo C, Pasipanodya JG, Zetola NM, Williams SM, Sirugo G, Gumbo T. 2015. Amikacin Concentrations Predictive of Ototoxicity in Multidrug-Resistant Tuberculosis Patients. *Antimicrob Agents Chemother* 59:6337-43.
 38. Peloquin C. 1991. Antituberculosis drugs: pharmacokinetics, p p. 89–122. In H L (ed), *Drug susceptibility in the chemotherapy of mycobacterial infections* CRC Press, Boca Raton, FL.
 39. Moore RD, Lietman PS, Smith CR. 1987. Clinical response to aminoglycoside therapy: importance of the ratio of peak concentration to minimal inhibitory concentration. *J Infect Dis* 155:93-9.
 40. Bland CM, Pai MP, Lodise TP. 2018. Reappraisal of Contemporary Pharmacokinetic and Pharmacodynamic Principles for Informing Aminoglycoside Dosing. *Pharmacotherapy* 38:1229-1238.
 41. Ambrose PG, Bhavnani SM, Jones RN. 2019. USCAST, The National Antimicrobial Susceptibility Testing Committee for the United States. Aminoglycoside In Vitro Susceptibility Test Interpretive Criteria Evaluations. Version 1.3, 2019.
 42. Doluisio JT, Dittert LW, Lapiana JC. 1973. Pharmacokinetics of Kanamycin Following Intramuscular Administration. *Journal of Pharmacokinetics and Biopharmaceutics* 1:253-265.

43. Kunin CM. 1966. Absorption, distribution, excretion and fate of kanamycin. *Ann N Y Acad Sci* 132:811-8.
44. Mayers M, Rush D, Madu A, Motyl M, Miller MH. 1991. Pharmacokinetics of amikacin and chloramphenicol in the aqueous humor of rabbits. *Antimicrob Agents Chemother* 35:1791-8.
45. Staneva M, Markova B, Atanasova I, Terziivanov D. 1994. Pharmacokinetic and pharmacodynamic approach for comparing two therapeutic regimens using amikacin. *Antimicrob Agents Chemother* 38:981-5.
46. Lashev LD, Pashov DA, Marinkov TN. 1992. Interspecies differences in the pharmacokinetics of kanamycin and apramycin. *Vet Res Commun* 16:293-300.
47. Zimmerman M, Blanc L, Chen PY, Dartois V, Prideaux B. 2018. Spatial Quantification of Drugs in Pulmonary Tuberculosis Lesions by Laser Capture Microdissection Liquid Chromatography Mass Spectrometry (LCM-LC/MS). *J Vis Exp* 134: e57402.
48. Prideaux B, Via LE, Zimmerman MD, Eum S, Sarathy J, O'Brien P, Chen C, Kaya F, Weiner DM, Chen PY, Song T, Lee M, Shim TS, Cho JS, Kim W, Cho SN, Olivier KN, Barry CE, 3rd, Dartois V. 2015. The association between sterilizing activity and drug distribution into tuberculosis lesions. *Nat Med* 21:1223-7.
49. Strydom N, Gupta SV, Fox WS, Via LE, Bang H, Lee M, Eum S, Shim T, Barry CE, 3rd, Zimmerman M, Dartois V, Savic RM. 2019. Tuberculosis drugs' distribution and emergence of resistance in patient's lung lesions: A mechanistic model and tool for regimen and dose optimization. *PLoS Med* 16:e1002773.
50. Sarathy JP, Zuccotto F, Hsinpin H, Sandberg L, Via LE, Marriner GA, Masquelin T, Wyatt P, Ray P, Dartois V. 2016. Prediction of Drug Penetration in Tuberculosis Lesions. *ACS Infect Dis* 2:552-63.
51. Johnson JD, Hand WL, Francis JB, King-Thompson N, Corwin RW. 1980. Antibiotic uptake by alveolar macrophages. *J Lab Clin Med* 95:429-39.

52. Hand WL, Corwin RW, Steinberg TH, Grossman GD. 1984. Uptake of antibiotics by human alveolar macrophages. *Am Rev Respir Dis* 129:933-7.
53. Sarathy JP, Via LE, Weiner D, Blanc L, Boshoff H, Eugenin EA, Barry CE, 3rd, Dartois VA. 2018. Extreme Drug Tolerance of *Mycobacterium tuberculosis* in Caseum. *Antimicrob Agents Chemother* 62.
54. Fox W, Ellard GA, Mitchison DA. 1999. Studies on the treatment of tuberculosis undertaken by the British Medical Research Council tuberculosis units, 1946-1986, with relevant subsequent publications. *Int J Tuberc Lung Dis* 3:S231-79.
55. Ahuja SD, Ashkin D, Avendano M, Banerjee R, Bauer M, Bayona JN, Becerra MC, Benedetti A, Burgos M, Centis R, Chan ED, Chiang CY, Cox H, D'Ambrosio L, DeRiemer K, Dung NH, Enarson D, Falzon D, Flanagan K, Flood J, Garcia-Garcia ML, Gandhi N, Granich RM, Hollm-Delgado MG, Holtz TH, Iseman MD, Jarlsberg LG, Keshavjee S, Kim HR, Koh WJ, Lancaster J, Lange C, de Lange WC, Leimane V, Leung CC, Li J, Menzies D, Migliori GB, Mishustin SP, Mitnick CD, Narita M, O'Riordan P, Pai M, Palmero D, Park SK, Pasvol G, Pena J, Perez-Guzman C, Quelapio MI, Ponce-de-Leon A, et al. 2012. Multidrug resistant pulmonary tuberculosis treatment regimens and patient outcomes: an individual patient data meta-analysis of 9,153 patients. *PLoS Med* 9:e1001300.
56. Sarathy J, Blanc L, Alvarez-Cabrera N, O'Brien P, Dias-Freedman I, Mina M, Zimmerman M, Kaya F, Ho Liang HP, Prideaux B, Dietzold J, Salgame P, Savic RM, Linderman J, Kirschner D, Pienaar E, Dartois V. 2019. Fluoroquinolone Efficacy against Tuberculosis Is Driven by Penetration into Lesions and Activity against Resident Bacterial Populations. *Antimicrob Agents Chemother* 63.
57. Zimmerman M, Lestner J, Prideaux B, O'Brien P, Dias-Freedman I, Chen C, Dietzold J, Daudelin I, Kaya F, Blanc L, Chen PY, Park S, Salgame P, Sarathy J, Dartois V. 2017.

- Ethambutol Partitioning in Tuberculous Pulmonary Lesions Explains Its Clinical Efficacy. *Antimicrob Agents Chemother* 61.
58. Burgess DS. 2005. Use of pharmacokinetics and pharmacodynamics to optimize antimicrobial treatment of *Pseudomonas aeruginosa* infections. *Clin Infect Dis* 40 Suppl 2:S99-104.
 59. Kashuba AD, Nafziger AN, Drusano GL, Bertino JS, Jr. 1999. Optimizing aminoglycoside therapy for nosocomial pneumonia caused by gram-negative bacteria. *Antimicrob Agents Chemother* 43:623-9.
 60. Lan Z, Ahmad N, Baghaei P, Barkane L, Benedetti A, Brode SK, Brust JCM, Campbell JR, Chang VWL, Falzon D, Guglielmetti L, Isaakidis P, Kempker RR, Kipiani M, Kuksa L, Lange C, Laniado-Laborin R, Nahid P, Rodrigues D, Singla R, Udwadia ZF, Menzies D, Collaborative Group for the Meta-Analysis of Individual Patient Data in MDRTbT. 2020. Drug-associated adverse events in the treatment of multidrug-resistant tuberculosis: an individual patient data meta-analysis. *Lancet Respir Med* 8:383-394.
 61. Donald PR, Sirgel FA, Venter A, Smit E, Parkin DP, Van de Wal BW, Dore CJ, Mitchison DA. 2002. The early bactericidal activity of streptomycin. *Int J Tuberc Lung Dis* 6:693-8.
 62. Ionescu AM, Mpobela Agnarson A, Kambili C, Metz L, Kfoury J, Wang S, Williams A, Singh V, Thomas A. 2018. Bedaquiline- versus injectable-containing drug-resistant tuberculosis regimens: a cost-effectiveness analysis. *Expert Rev Pharmacoecon Outcomes Res* 18:677-689.
 63. Ershova JV, Kurbatova EV, Moonan PK, Cegielski JP. 2012. Acquired resistance to second-line drugs among persons with tuberculosis in the United States. *Clin Infect Dis* 55:1600-7.
 64. Chen Y, Yuan Z, Shen X, Wu J, Wu Z, Xu B. 2016. Resistance to Second-Line Antituberculosis Drugs and Delay in Drug Susceptibility Testing among Multidrug-Resistant Tuberculosis Patients in Shanghai. *Biomed Res Int* 2016:2628913.

65. Matt T, Ng CL, Lang K, Sha SH, Akbergenov R, Shcherbakov D, Meyer M, Duscha S, Xie J, Dubbaka SR, Perez-Fernandez D, Vasella A, Ramakrishnan V, Schacht J, Bottger EC. 2012. Dissociation of antibacterial activity and aminoglycoside ototoxicity in the 4-monosubstituted 2-deoxystreptamine apramycin. *Proc Natl Acad Sci U S A* 109:10984-9.
66. Eliopoulos GM, Eliopoulos CT. 1988. Antibiotic combinations: should they be tested? *Clin Microbiol Rev* 1:139-56.
67. Diacon AH, van der Merwe L, Barnard M, von Groote-Bidlingmaier F, Lange C, Garcia-Basteiro AL, Sevene E, Ballell L, Barros-Aguirre D. 2016. beta-Lactams against Tuberculosis--New Trick for an Old Dog? *N Engl J Med* 375:393-4.
68. de Jager VR, Vanker N, van der Merwe L, van Brakel E, Muliaditan M, Diacon AH. 2020. Optimizing beta-Lactams against Tuberculosis. *Am J Respir Crit Care Med* 201:1155-1157.
69. Subbian S, Tsenova L, Yang G, O'Brien P, Parsons S, Peixoto B, Taylor L, Fallows D, Kaplan G. 2011. Chronic pulmonary cavitary tuberculosis in rabbits: a failed host immune response. *Open Biol* 1.
70. Sarathy JP, Liang HH, Weiner D, Gonzales J, Via LE, Dartois V. 2017. An In Vitro Caseum Binding Assay that Predicts Drug Penetration in Tuberculosis Lesions. *J Vis Exp* doi:10.3791/55559.
71. Chen C, Gardete S, Jansen RS, Shetty A, Dick T, Rhee KY, Dartois V. 2018. Verapamil Targets Membrane Energetics in Mycobacterium tuberculosis. *Antimicrob Agents Chemother* 62.
72. Wang N, Dartois V, Carter CL. 2021. An optimized method for the detection and spatial distribution of aminoglycoside and vancomycin antibiotics in tissue sections by mass spectrometry imaging. *J Mass Spectrom* in press.
73. Gordon RC, Regamey C, Kirby WM. 1972. Serum protein binding of the aminoglycoside antibiotics. *Antimicrob Agents Chemother* 2:214-6.

74. Alhadab AA, Ahmed MA, Brundage RC. 2018. Amikacin Pharmacokinetic-Pharmacodynamic Analysis in Pediatric Cancer Patients. *Antimicrob Agents Chemother* 62.
75. MacGowan AP. 2003. Pharmacokinetic and pharmacodynamic profile of linezolid in healthy volunteers and patients with Gram-positive infections. *J Antimicrob Chemother* 51 Suppl 2:ii17-25.
76. Ho YI, Chan CY, Cheng AF. 1997. In-vitro activities of aminoglycoside-aminocyclitols against mycobacteria. *J Antimicrob Chemother* 40:27-32.
77. Heifets L, Lindholm-Levy P. 1989. Comparison of bactericidal activities of streptomycin, amikacin, kanamycin, and capreomycin against *Mycobacterium avium* and *M. tuberculosis*. *Antimicrob Agents Chemother* 33:1298-301.
78. Sadeghi K, Hamishehkar H, Najmeddin F, Ahmadi A, Hazrati E, Honarmand H, Mojtahedzadeh M. 2018. High-dose amikacin for achieving serum target levels in critically ill elderly patients. *Infect Drug Resist* 11:223-228.
79. Arechiga-Alvarado NA, Medellin-Garibay SE, Milan-Segovia RDC, Ortiz-Alvarez A, Magana-Aquino M, Romano-Moreno S. 2020. Population Pharmacokinetics of Amikacin Administered Once Daily in Patients with Different Renal Functions. *Antimicrob Agents Chemother* 64.
80. Park SI, Oh J, Jang K, Yoon J, Moon SJ, Park JS, Lee JH, Song J, Jang IJ, Yu KS, Chung JY. 2015. Pharmacokinetics of Second-Line Antituberculosis Drugs after Multiple Administrations in Healthy Volunteers. *Antimicrob Agents Chemother* 59:4429-35.
81. Tod M, Lortholary O, Seytre D, Semaoun R, Uzzan B, Guillevin L, Casassus P, Petitjean O. 1998. Population pharmacokinetic study of amikacin administered once or twice daily to febrile, severely neutropenic adults. *Antimicrob Agents Chemother* 42:849-56.

82. Yew WW, Cheung SW, Chau CH, Chan CY, Leung CK, Cheng AF, Wong CF. 1999. Serum pharmacokinetics of antimycobacterial drugs in patients with multidrug-resistant tuberculosis during therapy. *Int J Clin Pharmacol Res* 19:65-71.
83. Holdiness MR. 1984. Clinical pharmacokinetics of the antituberculosis drugs. *Clin Pharmacokinet* 9:511-44.

Supplementary Material

Supplementary Table 0.1. Comparative pharmacokinetic parameters of AMK and KAN at 1,000 mg in human subjects and 25 mg/kg in New Zealand White rabbits.

	AMK	KAN
C_{max} rabbits (25 mg/kg) (mg/L)	90 (75 – 110)	101 (75 – 133)
C_{max} clinical (1,000 mg or 15 mg/kg) (mg/L)	33 (20 – 60)*	35 (20 – 50)†
AUC rabbits (25 mg/kg) (mg*h/L)	178 (140 – 250)	178 (147 – 213)
AUC clinical (1,000 mg or 15 mg/kg) (mg*h/L)	225‡	190§

* Values from: Kato H, Hagihara M, Hirai J, Sakanashi D, Suematsu H, Nishiyama N, Koizumi Y, Yamagishi Y, Matsuura K, Mikamo H. 2017. Evaluation of Amikacin Pharmacokinetics and Pharmacodynamics for Optimal Initial Dosing Regimen. *Drugs R D* 17:177-187; Sadeghi K, Hamishehkar H, Najmeddin F, Ahmadi A, Hazrati E, Honarmand H, Mojtahedzadeh M. 2018. High-dose amikacin for achieving serum target levels in critically ill elderly patients. *Infect Drug Resist* 11:223-228; Arechiga-Alvarado NA, Medellin-Garibay SE, Milan-Segovia RDC, Ortiz-Alvarez A, Magana-Aquino M, Romano-Moreno S. 2020. Population Pharmacokinetics of Amikacin Administered Once Daily in Patients with Different Renal Functions. *Antimicrob Agents Chemother* 64.

† Values from: Park SI, Oh J, Jang K, Yoon J, Moon SJ, Park JS, Lee JH, Song J, Jang IJ, Yu KS, Chung JY. 2015. Pharmacokinetics of Second-Line Antituberculosis Drugs after Multiple Administrations in Healthy Volunteers. *Antimicrob Agents Chemother* 59:4429-35.

‡ Value from: Tod M, Lortholary O, Seytre D, Semaoun R, Uzzan B, Guillemin L, Casassus P, Petitjean O. 1998. Population pharmacokinetic study of amikacin administered once or twice daily to febrile, severely neutropenic adults. *Antimicrob Agents Chemother* 42:849-56.

Yew WW, Cheung SW, Chau CH, Chan CY, Leung CK, Cheng AF, Wong CF. 1999. Serum pharmacokinetics of antimycobacterial drugs in patients with multidrug-resistant tuberculosis during therapy. *Int J Clin Pharmacol Res* 19:65-71.

§ Values from: Holdiness MR. 1984. Clinical pharmacokinetics of the antituberculosis drugs. *Clin Pharmacokinet* 9:511-44.

Supplementary Table 0.3. Description of human subject characteristics (ClinicalTrials.gov identifier NCT00816426).

Subject	Gender	Age (years)	BMI	Weight (kg)	Prior TB episodes ^(a)	Study drugs single dose	Study drugs at steady state	Cavitary disease	Other anti-TB agents at steady state ^(b)	Time of surgery post-study drugs
G101	Male	27	24	74	2	INH, RIF, PZA	MXF, KAN	Yes	LZD, AUG, CLA	25h 20min
G402	Male	40	17	57	2	RIF, PZA, KAN	INH, MXF	Yes	EMB	24h 20min
G105	Male	54	29	84	2	INH, RIF, PZA, MXF, KAN		Yes	LZD, AMK, PAS, CFZ, PIP	12h 35min
G106	Female	48	22	54	1	INH, RIF, PZA, KAN	MXF	Yes	LZD, CS, AMX, PTH, PAS	11h 00min
G102	Male	43	27	80	2	INH, RIF, PZA	MXF, KAN	Yes	LZD, PAS, AUG	11h 12min
G103	Female	23	19	50	2	INH, RIF, PZA, MXF, KAN		No	LZD, CS, CFZ	4h 56min
G108	Male	47	19	58	1	RIF, PZA, MXF, KAN	INH	No	LZD, CS, AUG, PTH, STM	5h 41min
G303	Male	39	22	66	4	INH, RIF, MXF, KAN	PZA	Yes	CS, LFX, PTH, STM	4h 23min
G109	Female	58	21	62	1	INH, RIF, PZA, MXF	KAN	?	LZD, CS, PAS	21h 55min
G104	Female	27	20	53	1	INH, RIF, MXF, KAN	PZA	No	LZD, CS, AUG, STM	3h 18min
G401	Male	44	24	58	1	RIF, MXF, KAN	INH, PZA	Yes	EMB, LFX	8h 30min

(a) all subjects had either MDR- or XDR-TB

(b) AMK, amikacin; AUG, amoxicillin/clavulanate; CFZ, clofazimine; CLA, clarithromycin; CS, cycloserine; EMB, ethambutol; LFX, levofloxacin; LZD, linezolid; PAS, para-aminosalicylate; PTH, prothionamide; STM, streptomycin; PIP: piperacillin/tazobactam.

Supplementary Table 0.4. Number of observations of KAN or AMK concentration in rabbit plasma and tissue including uninvolved lung and tubercular lesions. Samples were analyzed via LCMS or LCM. n, number of samples; N, number of subjects, LCMS, liquid chromatography mass spectrometry; LCM, laser capture microdissection.

	AMK	KAN
Observations, total (n, N)	169, 9	144, 5
Plasma (LCMS, LCM)	45, 0	26, 0
Uninvolved lung (LCMS, LCM)	23, 11	29, 12
Cellular lesions (LCMS, LCM)	9, 11	26, 12
Caseous lesions (LCMS, LCM)	59, 0	24, 0
Caseum (LCMS, LCM)	0, 11	1, 14

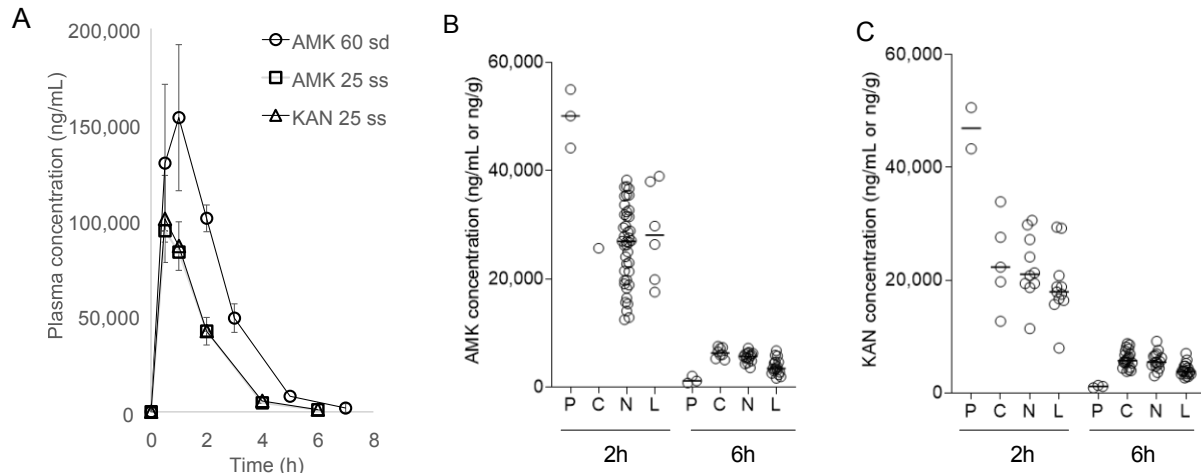
Supplementary Table 0.5 Model-based clinical predictions of C_{\max} , AUC, and time relative to MIC per lesion for (A.) AMK and (B.) KAN. C_{\max} and unbound C_{\max} relative to MIC, MacIC_{90} , and casMBC_{90} . Values in mg/L (plasma) or mg/kg (lung and lesions). AUC and unbound AUC relative to MIC. Values in mg*h/L (plasma) or mg*h/kg (lung and lesions). Time above MIC, Macrophage IC_{90} , or caseum MBC_{90} within a 24-hour period of once daily dosing at steady-state. Values are hours above target with a maximum of 24.

A. AMK

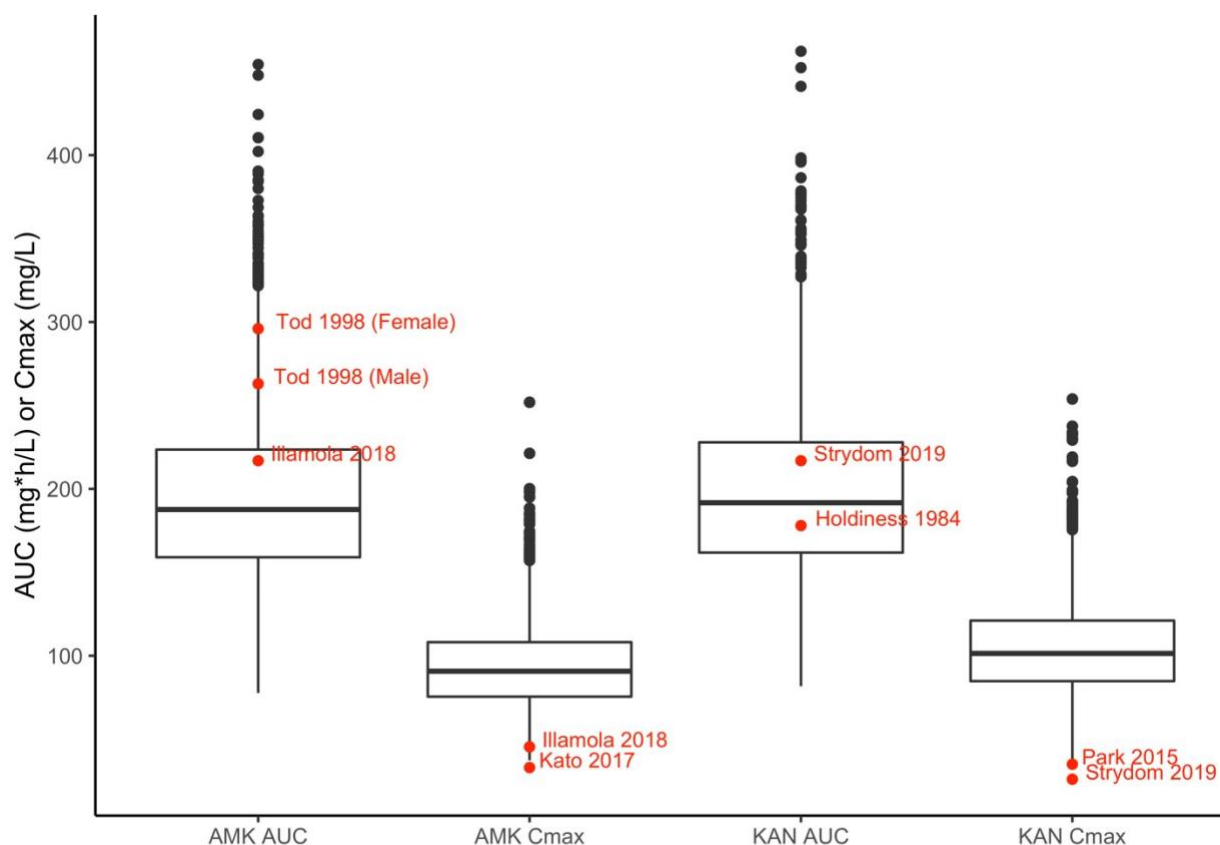
	Plasma	Uninvolved lung	Cellular lesion	Caseous lesion	Caseum
C_{\max}	45.7	14.4	12.0	17.7	26.7
fC_{\max}	41.1	12.9	10.8	16.0	24.1
fC_{\max}/MIC	41.1	12.9	10.8	16.0	24.1
$C_{\max}/\text{MacIC}_{90}$	6.0	1.9	1.6	2.3	3.5
$C_{\max}/\text{casMBC}_{90}$	2.4	0.8	0.6	0.9	1.4
AUC	216.9	94.8	100.2	134.1	201.1
$f\text{AUC}/\text{MIC}$	195.2	85.3	90.2	120.7	181.0
Time above MIC	24	14	17	19	24
Time above MacIC_{90}	7	6	5	7	9
Time above casMBC_{90}	4	0	0	0	4

B. KAN

	Plasma	Uninvolved lung	Cellular lesion	Caseous lesion	Caseum
C_{\max}	26.5	6.7	8.6	9.2	9.2
fC_{\max}	26.5	6.7	8.6	9.2	9.2
fC_{\max}/MIC	13.2	3.4	4.3	4.6	4.6
$C_{\max}/\text{MacIC}_{90}$	1.9	0.5	0.6	0.7	0.7
$C_{\max}/\text{casMBC}_{90}$	0.1	0.0	0.0	0.0	0.0
AUC	216.9	73.3	98.5	103.3	107.8
$f\text{AUC}/\text{MIC}$	108.5	36.7	49.2	51.6	53.9
Time above MIC	19	14	16	17	17
Time above MacIC_{90}	6	0	0	0	0
Time above casMBC_{90}	0	0	0	0	0



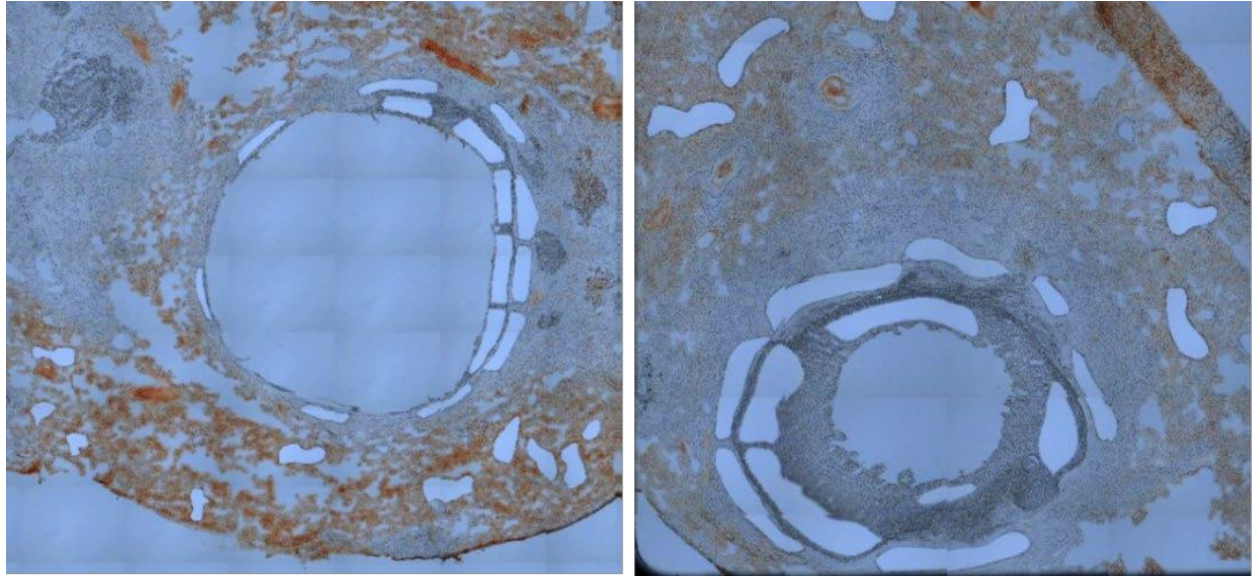
Supplementary Figure 0.1. Rabbit pharmacokinetics of AMK and KAN. (A) Plasma concentration-time profiles in uninfected rabbits and rabbits with active TB. In a dose finding study, three uninfected rabbits received a single 60 mg/kg dose (sd) of AMK administered via the intramuscular route; in tissue and lesion distribution studies, groups of 5 or 6 rabbits received 3 daily doses (steady state or ss) of AMK or KAN administered via the intramuscular route, as indicated. (B) Drug concentrations in lung and lesion homogenates of TB infected rabbits following three daily doses of 25 mg/kg AMK and KAN. P: plasma; C: cellular lesion; N: necrotic (caseous) lesion; L: uninvolved lung. A sample size of 3 animals per drug treatment and time point was selected based on historic ability to build PK models that deliver adequate fit. Animals that did not present adequate pathology or adequate number of evaluable lesions were replaced until we reached N=3. For LCMS quantitation in homogenized tissue/lesions, the following number of lesions per animal were collected: (i) 6 pieces of uninvolved lung with the exception of 2 rabbits at the 2 h AMK time point, which had extensive pathology to the extent that it was difficult to locate uninvolved lung (3 pieces were collected in these rabbits), (ii) 5 to 10 cellular lesions with the exception of the same 2 rabbits where all but one lesion were necrotic, (iii) 3 to 26 necrotic lesions (more necrotic lesions were collected when cellular lesions could not be found).



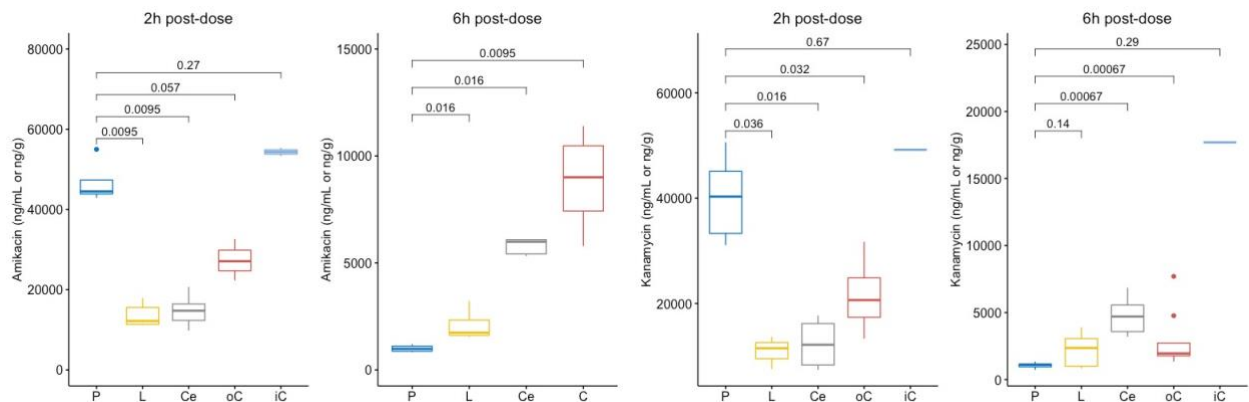
Supplementary Figure 0.2. Comparison of steady state AUC (area under the concentration-time curve) and C_{max} (peak plasma concentration) in rabbits after three 25 mg/kg intramuscular doses (black box and whisker plots) and in TB patients receiving 1,000 mg daily (red dots retrieved from published studies). Emphasis was placed on matching AUC since it is considered the driver of aminoglycoside efficacy.*

* References: Holdiness MR. 1984. Clinical pharmacokinetics of the antituberculosis drugs. Clin Pharmacokinet 9:511-44; Illamola SM, Huynh HQ, Liu X, Bhakta ZN, Sherwin CM, Liou TG, Carveth H, Young DC. 2018. Population Pharmacokinetics of Amikacin in Adult Patients with Cystic Fibrosis. Antimicrob Agents Chemother 62; Kato H, Hagihara M, Hirai J, Sakanashi D, Suematsu H, Nishiyama N, Koizumi Y, Yamagishi Y, Matsuura K, Mikamo H. 2017. Evaluation of Amikacin Pharmacokinetics and Pharmacodynamics for Optimal Initial Dosing Regimen. Drugs R D 17:177-187; Park SI, Oh J, Jang K, Yoon J, Moon SJ, Park JS, Lee JH, Song J, Jang IJ, Yu KS, Chung JY. 2015. Pharmacokinetics of Second-Line Antituberculosis Drugs after Multiple Administrations in Healthy Volunteers. Antimicrob Agents Chemother 59:4429-35; Strydom N, Gupta SV, Fox WS, Via LE, Bang H, Lee M, Eum S, Shim T, Barry CE, 3rd, Zimmerman M, Dartois V, Savic RM. 2019. Tuberculosis drugs' distribution and emergence of resistance in patient's lung lesions: A mechanistic model and tool for regimen and dose optimization. PLoS Med 16:e1002773; Tod M, Lortholary O, Seytre D, Semaoun R, Uzzan B, Guillemin L, Casassus P, Petitjean O. 1998. Population pharmacokinetic study of amikacin administered once or twice daily to febrile, severely neutropenic adults. Antimicrob Agents Chemother 42:849-56

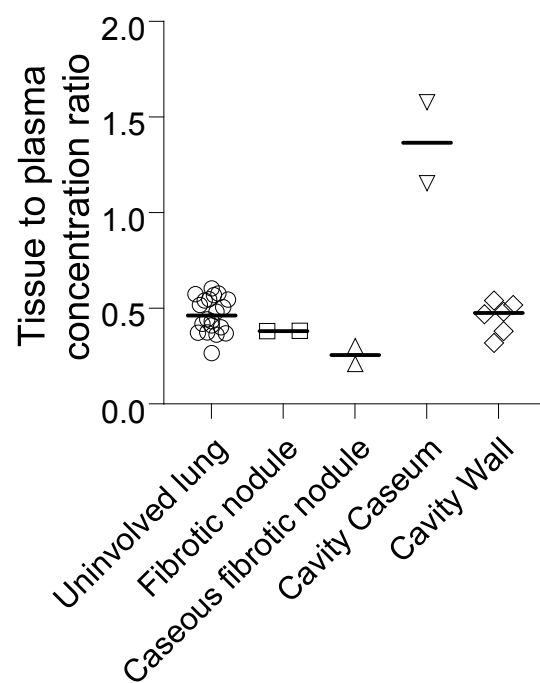
A.



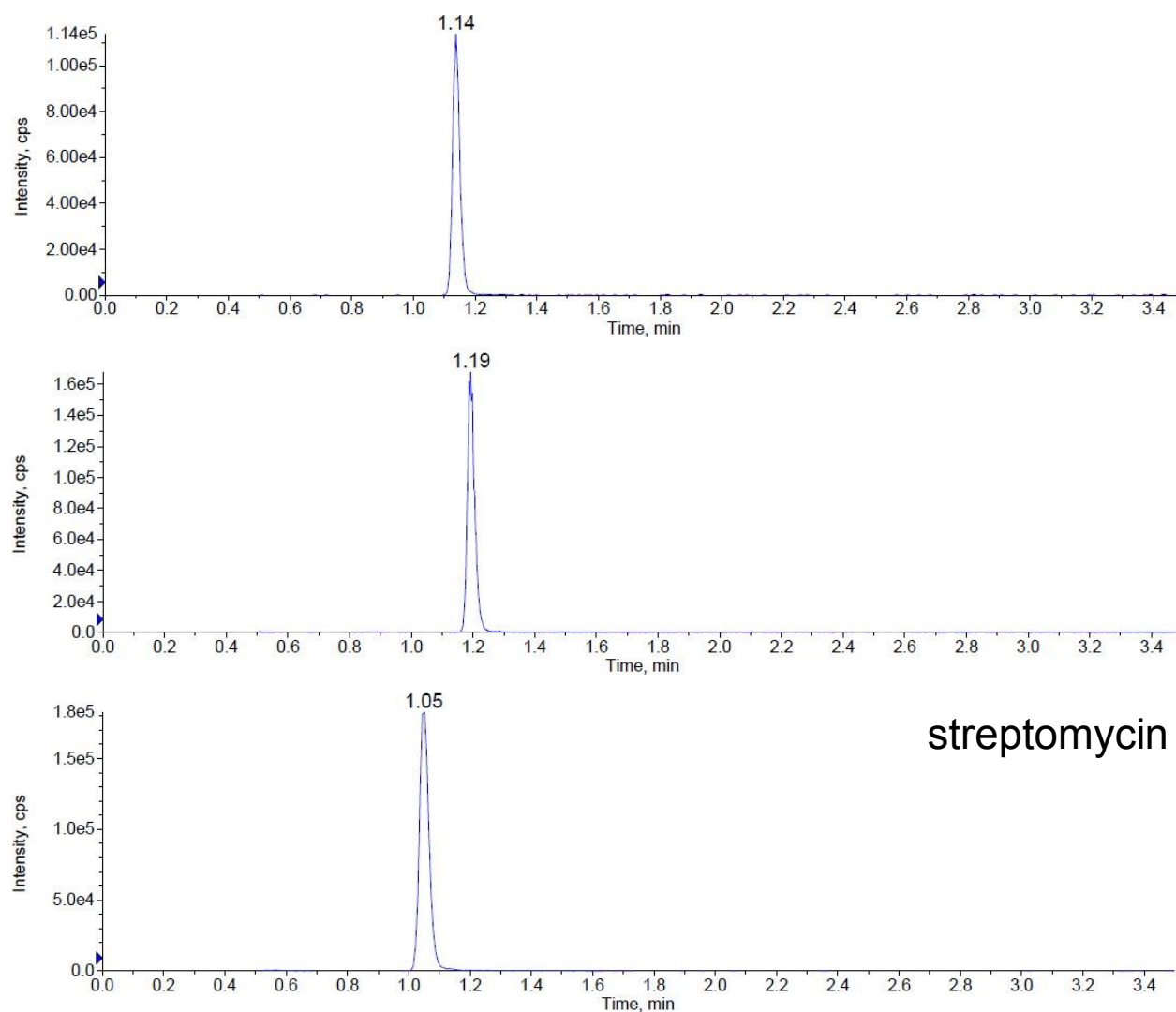
B.



Supplementary Figure 0.3. Sample size and statistical analysis of data shown in Figure 2.1C. For drug quantitation by laser capture microdissection, large necrotic lesions and cavities were collected with the surrounding uninvolved lung, as follows: AMK 2 h: 6 lesions; AMK 6 h: 6 lesions; KAN 2 h: 4 lesions; KAN 6 h: 8 lesions. (A) Representative large cavities collected from the AMK rabbits analyzed 6 h post dose, from which the inner caseum is missing, either because it emptied prior to lesion removal at the time of euthanasia, or because it fell apart at the time of cryosectioning. Consequently, only “caseum” (C) is reported in Figure 1C for AMK at 6 h post dose. (B) Box-and-whisker plots and statistical analysis of absolute concentrations of AMK and KAN in plasma and infected lung regions determined by laser-capture microdissection and LC/MS-MS. P: plasma; L: uninvolved lung; Ce: cellular rim; C: caseum; oC: outer caseum; iC: inner caseum. The horizontal bar is the median, the hinges are the interquartile range (IQR), the whiskers extend to 1.5*IQR, and dots are outliers. Drug concentrations in tissue compartments were compared to plasma concentrations using the Wilcoxon test.



Supplementary Figure 0.4. Partitioning of streptomycin in rabbit lung and lesion compartments 3h after a single 20 mg/kg dose. Concentrations were measured in tissue homogenates and normalized to plasma concentrations at the time of necropsy.



Supplementary Figure 0.5. HPLC-MS/MS chromatograms for three aminoglycosides. Typical plasma standard HPLC-MS/MS chromatograms for amikacin, kanamycin, and the internal standard streptomycin, at 5000 ng/mL.

Model Code

```
$PROBLEM      KAN PK from plasma to caseum in rabbits
$INPUT          ID OLDID=DROP SAMPLEID TIME TAD LESIONNAME=DROP LESION
                NGG DV METHOD LESIONWT EVID MDV AMT II ADDL WT DOSE iF1 CMT
$DATA          dataset.csv          IGNORE=@

$SUBROUTINE    ADVAN13 TOL=6
$MODEL        NCOMP = 5
                COMP  = (ABS,DEFD0SE)
                COMP  = (CENTRAL, DEFOBS)
                COMP  = (AUC)
                COMP  = (CASEUM)
                COMP  = (CASEUMAUC)

$PK

CL      = THETA(1)
V       = THETA(2)
KA      = THETA(3)

KE      = CL/V
S2      = V

F1      = iF1 ; use individual parameter estimates from final plasma model

K4      = THETA(4) * EXP(ETA(1))
PC4     = THETA(5) * EXP(ETA(2))

$DES
DADT(1) = - KA*A(1)
DADT(2) =  KA*A(1) - KE*A(2)
DADT(3) =  A(2)/V ; AUC of plasma

DADT(4) =  K4 * ( PC4 * A(2)/V - A(4) )
DADT(5) =  A(4) ; AUC of caseum

$ERROR

CP      = A(2)/V ; Concentration in plasma
AUC     = A(3) ; AUC in plasma
A4      = A(4) ; Concentration in caseum
A5      = A(5) ; AUC in caseum

IPRED = A(4)

W       = IPRED
IRES    = DV - IPRED
IWRES   = IRES / W
Y       = IPRED + W * EPS(1)
```

\$THETA

0.376 FIX ; 1 CL L/h

0.422 FIX ; 2 V L

2.940 FIX ; 3 KA 1/h

0.840 FIX ; 4 F1

(0, 0.3952) ; 5 K4

(0, 0.4968) ; 6 PC4

\$OMEGA

0 FIX ; 1 IIV K4

0 FIX ; 2 IIV PC4

\$SIGMA

0.772 ; Proportional Error

\$ESTIMATION METHOD=1 INTERACTION PRINT=5 NSIG=3 SIGL=9 MAXEVAL=9999 NOABORT

\$COVARIANCE UNCONDITIONAL

\$TABLE ID TIME TAD IPRED PRED DV AMT LESION CMT WT CP AUC A4 A5 DOSE WRES

IWRES CWRES EVID FILE=sdtabXXX NOPRINT ONEHEADER

\$TABLE ID CL V KA KE F1 K4 PC4 FILE=patabXXX NOPRINT ONEHEADER

Chapter 3: A Rabbit Model to Study Antibiotic Penetration at the Site of Infection for Nontuberculous Mycobacterial Lung Disease: Macrolide Case Study*

Abstract

Nontuberculous mycobacterial pulmonary disease (NTM-PD) is a potentially fatal infectious disease requiring long treatment duration with multiple antibiotics and against which there is no reliable cure. Among the factors that have hampered the development of adequate drug regimens is the lack of an animal model that reproduces the NTM lung pathology required for studying antibiotic penetration and efficacy. Given the well-documented similarities between tuberculosis and NTM immunopathology in patients, we first determined that the rabbit model of active tuberculosis reproduces key features of human NTM-PD and provides an acceptable surrogate model to study lesion penetration. We focused on clarithromycin, a macrolide and pillar of NTM-PD treatment, and explored the underlying causes of the disconnect between its favorable potency and pharmacokinetics, and variable clinical outcome. To quantify pharmacokinetic-pharmacodynamic target attainment at the site of disease, we developed a translational model describing clarithromycin distribution from plasma to lung lesions, including the spatial quantitation of clarithromycin and azithromycin in mycobacterial lesions of two patients on long-term macrolide therapy. Through clinical simulations, we visualized the coverage of clarithromycin in plasma and four disease compartments, revealing heterogeneous bacteriostatic and bactericidal target attainment depending on the compartment and the corresponding potency against nontuberculous mycobacteria in clinically relevant assays. Overall, clarithromycin's favorable tissue penetration and lack of bactericidal activity indicated that its clinical activity is limited by pharmacodynamic rather than pharmacokinetic factors. Our results pave the way towards the simulation of lesion pharmacokinetic-pharmacodynamic

* Modified from the publication: Kaya F, Ernest JP, *et al.* A Rabbit Model to Study Antibiotic Penetration at the Site of Infection for Nontuberculous Mycobacterial Lung Disease: Macrolide Case Study. *Antimicrobial Agents and Chemotherapy*. 2022. 66:3

coverage by multi-drug combinations, to enable the prioritization of promising regimens for clinical trials.

Introduction

Non-tuberculous mycobacteria (NTM) are environmental mycobacteria related to *Mycobacterium tuberculosis* and can cause progressive, fatal pulmonary disease (NTM-PD) (1). NTM-PD occurs in patients with immunodeficiencies, structural lung damage, or both. The immunopathology that develops in NTM-PD patients is partially driven by these pre-existing conditions (2). In immunocompromised patients – where the cause of immunosuppression is either genetic or induced by drug treatment or HIV infection – disease manifestations include extrathoracic disease, poorly formed granulomatous structures, diffuse consolidation and miliary disease, all consistent with systemic immune dysfunction and reminiscent of tuberculosis (TB)-HIV (2-4). In immunocompetent patients with bronchiectatic conditions – chronic obstructive pulmonary disease (COPD) and cystic fibrosis (CF) being the most common – nodular or cavitory pathology, necrosis and worsening bronchiectasis are frequently seen (5-7). These presentations bear key similarities with TB in immunocompetent subjects (8), where the most common microscopic finding is necrotizing granulomas and cavities, characterized by a central zone of necrosis surrounded by a variably thick rim of macrophages, neutrophils, lymphocytes and fibroblasts. As seen in TB, necrotic lesions have also been found in the lymph nodes of NTM-PD patients, particularly in those with HIV (9). Cavities in NTM-PD are similar to pulmonary TB cavities with subtle differences such as a thinner fibrotic wall as detected by computed tomography (10-12) and enhanced associated pleural thickening (13). Although cavitory disease is overall less frequent in NTM-PD than TB patients (14), the presence of large cavities is associated with disease progression leading to respiratory failure and high mortality rate (15). There is consensus in the clinical field that differentiating NTM-PD from pulmonary TB solely based on radiologic findings is not recommended due to considerable overlap in the clinical and radiographic features of pulmonary TB and NTM-PD (16, 17). Histologic feature

similarities between TB and NTM disease, and their relative frequencies, have been extensively reviewed by Jain et al. (18).

Surgical resections, which have been practiced since the 1960s until today when disease is localized, show gross and histopathologic findings identical to the manifestation usually associated with typical *M. tuberculosis* infection (13, 19). Histology and acid-fast stains of resected cavities have revealed bacterial aggregates or heaps along the inner wall of cavities (8, 20, 21). More recently, scanning electron microscopy of the inner wall of a resected cavity demonstrated bacilli embedded within a matrix (20). High bacterial burden ($> 10^7$ colony forming units) were enumerated in a 0.5 g sample from the lung cavity, a significant fraction of which were in biofilm-like structures (6).

Clarithromycin and azithromycin, broad-spectrum macrolides, are the pillar of NTM treatment and are used prophylactically in HIV patients with CD4 counts lower than 50, i.e. at high risk of opportunistic infections (3). Most NTM-PD patients are treated with a macrolide-containing multidrug regimen until they remain sputum-negative for 12 consecutive months (22). Despite such intensive therapy and the adequate potency of clarithromycin against susceptible NTM strains, treatment failures and relapse rates are high, particularly for *M. abscessus* disease (23, 24). Understanding the underlying causes of such disconnects is important if we are to optimize existing drug regimens and develop more effective ones.

Macrolide antibiotics accumulate in phagocytic cells (25) and preferentially distribute in tissues where populations of these cells reside (26). A beneficial consequence of high uptake in host cells is increased activity against intracellular pathogens (27). In addition, phagocytes may serve as a vehicle that transports macrolides to the site of infection (tissue-directed pharmacokinetics) (28, 29). Indeed, tissue and intracellular concentrations may be more useful for assessing the antibacterial activity of macrolides than plasma concentrations (30). Accordingly, tissue pharmacokinetic-pharmacodynamic (PK-PD) concepts have been proposed for macrolides (31), and therapeutic drug monitoring in plasma is not recommended (32). While

accumulation in phagocytes positively contributes to bacterial eradication, the heterogeneous sites of NTM-PD disease in patient populations with diverse manifestations (18) may provide the ground for subtherapeutic clarithromycin coverage of poorly vascularized compartments where the pathogen resides, as seen for some TB drugs (33). In vitro, clarithromycin is used as the representative macrolide in drug susceptibility assays, due to higher *erm41*–mediated induction of macrolide resistance in *M. abscessus* than azithromycin (34), though this remains a matter of debate (35, 36). Clarithromycin is mostly bacteriostatic against replicating NTM cultures and intracellular bacteria in macrophages (37), although longer incubation times have delivered bactericidal activity at 16 mg/L and above against replicating *M. abscessus* in cation-adjusted Muller-Hinton broth (38). It lacks bactericidal activity against NTM in biofilms (37), slow-replicating or non-replicating persisters (39). Thus, there is a potential disconnect between clarithromycin growth inhibitory activity (MIC) measured in clinical practice and activity against mycobacterial subpopulations at the sites of disease. Collectively, pharmacokinetic and pharmacodynamic observations suggest heterogeneous coverage of the sites of disease and bacterial populations in macrolide-susceptible NTM-PD.

Despite significant efforts dedicated to the development of animal models of NTM disease (40-42), we still lack an immunocompetent model that presents organized cellular and necrotic lesions and reasonably reproduces the human lung pathology required for studying antibiotic penetration (43). Here we first determine that the rabbit model of active TB disease provides an acceptable surrogate for studying pharmacokinetics at the site of NTM-PD. Taking advantage of TB and NTM-PD pathology similarities, we quantify the distribution of clarithromycin in mycobacterial lesion compartments following multiple human-equivalent oral doses to rabbits with active TB. We compare these results to a limited dataset of clarithromycin and azithromycin in mycobacterial lung lesions from patients on long-term macrolide therapy. To assess the potential efficacy of clarithromycin at the sites of disease in immuno-competent and -compromised patients, we relate these concentrations to those required to inhibit growth of or

kill nontuberculous mycobacteria in standard culture media, biofilms and macrophages. Future studies of similar design with other NTM drugs could help rationalize differential clinical responses of patients with a spectrum of disease presentation and immunopathology.

Methods

Clinical research study design and human subjects

One adult with pulmonary MDR-TB scheduled for elective lung resection surgery was asked to participate in the study “Pharmacokinetics of Standard First and Second Line anti-TB Drugs in the Lung and Lesions of Subjects Elected for Resection Surgery” (www.ClinicalTrials.gov identifier NCT00816426; also in Chapter 2: Supplementary Table 2.2). The subject had received 1,000 mg daily doses of clarithromycin for 5 weeks (subject 1 in (44)). The institutional review boards of the National Institute of Allergy and Infection Disease, National Institutes of Health, Bethesda, Maryland USA and the Asan Medical Center, Seoul, ROK, approved the study. All procedures were in accordance with the ethical standards of the Helsinki Declaration. During the surgery, the exact time of pulmonary artery ligation was recorded and used to calculate the time of drug administration relative to surgery, or 31h.

One adult with chronic *Mycobacterium abscessus* infection scheduled for elective surgery at the NIH Clinical Center gave written consent to participate under NIAID study “Study of Mycobacterial Infections” (www.ClinicalTrials.gov identifier NCT00018044). This participant had pulmonary nontuberculous mycobacterial disease presenting with cavitary lesions, well-organized necrotizing granulomas, and non-necrotizing granulomas similar to those described previously in lung disease caused by non-TB mycobacteria and *M. tuberculosis*. This 73-year-old female participant received 250 mg azithromycin (AZI), 600 mg RIF, 100 mg CFZ and 900 mg ethambutol as part of her standard drug regimen for two years prior to lung resection. Vessel ligation occurred 26 h after the last AZI dose. Upon lung resection, tissues were either fixed in 4% paraformaldehyde for histopathology staining, weighed and rapidly frozen at -80°C for homogenization and drug quantitation, or snap frozen in liquid nitrogen vapor for sectioning and laser capture microdissection (44).

Pharmacokinetic studies in naïve rabbits

Pharmacokinetic studies in uninfected New Zealand White rabbits were performed in Biosafety Level 2 facilities and approved by the Institutional Animal Care and Use Committee of the New Jersey Medical School, Rutgers University, Newark, NJ. Groups of four rabbits received a single or three daily doses of clarithromycin formulated in 0.5% CMC and 0.5% Tween 80, by oral gavage. Blood was collected in K₂-EDTA coated tubes from the central ear artery of each rabbit pre-dose, and at several time points between drug administration and necropsy (typically 0.5, 1, 2, 4, 6, 8 and 24 h following drug administration). Blood samples were centrifuged at 6,000 rpm for 5 min and plasma supernatants were transferred and stored at -80°C until analyzed by high-pressure liquid chromatography coupled to tandem mass spectrometry (LC/MS-MS).

Rabbit infection, drug administration and blood collection

All rabbit infection studies were performed in Biosafety Level 3 facilities and approved by the Institutional Animal Care and Use Committee of the New Jersey Medical School, Rutgers University, Newark, NJ, and of the Center for Discovery and Innovation, Hackensack Meridian Health, Nutley, NJ. Female New Zealand White (NZW) rabbits (Charles River Laboratories), weighing 2.2 to 2.6 kg, were maintained under specific pathogen-free conditions and fed water and chow ad libitum. The rabbits were infected with *M. tuberculosis* HN878, using a nose-only aerosol exposure system as described (45). At defined time points from 12 to 16 weeks post-infection (at which point rabbits harbor a spectrum of cellular and necrotic lesions representative of human pathology), rabbits received three daily doses of 200 mg/kg clarithromycin formulated in 0.5% CMC and 0.5% Tween 80, by oral gavage. Blood was collected from the central ear artery of each rabbit pre-dose, and at several time points between drug administration and necropsy (typically 0.5, 1, 2, 4, 6, and 24 h or until the time of necropsy). Groups of 3 rabbits were euthanized at 6 and 24 h post-dose. These time points were selected based on the

plasma PK profile to capture the end of the distribution phase (6 h) and the trough or C_{\min} (24 h). Plasma was prepared as described above and stored at -80°C until analyzed by LC/MS-MS.

Lesion dissection and processing

The right and left lungs were removed and weighed for analytical drug measurement and histopathology. From each lung lobe, individual granulomas and uninvolved (non-diseased) lung tissue sections were dissected, sized, weighed, and recorded. Lesions weighing less than 5 mg were pooled. Special care was taken to remove the uninvolved lung tissue surrounding each granuloma. The samples collected from each rabbit were classified as uninvolved lung, necrotic or cellular granulomas, cavity wall or cavity caseum. When feasible, cavity caseum was separated from the cavity wall, to be stored and analyzed separately. Lesions collected for laser-capture microdissection were left embedded in the surrounding tissue, and snap-frozen in liquid nitrogen vapor as described previously (46). All samples were stored in individual 2ml tubes at -80°C .

Prior to drug quantitation by LC/MS-MS, all tissue samples were homogenized in 9 volumes of phosphate buffered saline (PBS). Homogenization of all tissue samples was achieved using a FastPrep-24 instrument (MP Biomedicals) and 1.4mm zirconium oxide beads (Precellys).

Analytical method for macrolide quantitation

Azithromycin and clarithromycin were purchased from Sigma Aldrich. Azithromycin-d5 and clarithromycin-d4 internal standards were purchased from Toronto Research Chemicals. Drug free K_2EDTA plasma and lungs from NZW rabbits were obtained from BioIVT for use as blank matrices to build standard curves. Neat 1 mg/mL DMSO stocks for clarithromycin and azithromycin were serial diluted in 50/50 acetonitrile water to create standard curves and quality control spiking solutions. Spiked matrix standards and QCs were created by adding 10 μL of spiking solutions to 90 μL of drug free plasma or control lung homogenate. Extraction was performed for standards, QCs, and study samples by adding 200 μL of 1:1 acetonitrile

(ACN)/methanol (MeOH) containing 10 ng/mL stable labeled clarithromycin-d4 and azithromycin-d5 to 20 µl of plasma or homogenized tissue sample and 20 µl of 1:1 ACN:H₂O.

LC/MS-MS analysis was performed on a Sciex Qtrap 6500+ triple-quadrupole mass spectrometer coupled to a Shimadzu Nexera X2 UHPLC system to quantify each drug in plasma. Chromatography was performed on an Agilent Zorbax SB-C8 column (2.1x30 mm; particle size, 3.5 µm) using a reverse phase gradient elution with aqueous. Milli-Q deionized water with 0.1% formic acid (FA) was used for the aqueous mobile phase and 0.1% FA in ACN for the organic mobile phase. Multiple-reaction monitoring (MRM) of precursor/fragment transitions in electrospray positive-ionization mode was used to quantify the analytes. MRM transitions of 749.38/591.30, 754.37/596.30, 748.32/590.30 and 752.33/162.10 were used for azithromycin, azithromycin-d5, clarithromycin and clarithromycin-d4 respectively. Sample analysis was accepted if the concentrations of the quality control samples were within 20% of the nominal concentration. Data processing was performed using Analyst software (version 1.6.3; Sciex).

Laser-capture microdissection of rabbit and human lesion sections

Twenty-five µm thick tissue sections were cut from γ -irradiated rabbit lung biopsies using a Leica CM 1860UV (Buffalo Grove, IL) and thaw-mounted onto 1.4 µm thick Leica PET-Membrane FrameSlides (Buffalo Grove, IL) for laser capture microdissection. Tissue sections were immediately stored in sealed containers at -80°C. Adjacent 10 µm thick tissue sections were thaw-mounted onto standard glass microscopy slides for H&E and Ziehl-Neelsen staining. Cellular, necrotic (caseum), and uninvolved lung lesion areas totaling 3 million µm² were dissected from between 3 to 5 serial lung biopsy tissue sections using a Leica LMD7 system (Buffalo Grove, IL). The total tissue volume of each pooled sample was determined based on the surface area of the pooled sections and the 25 µm tissue thickness. Areas of cellular and caseous lesion were identified optically from the brightfield image scan and by comparison to

the adjacent H&E reference tissue. Pooled dissected lesion tissues were collected into 0.25 mL standard PCR tubes and immediately transferred to -80°C.

Neat 1 mg/mL DMSO stocks for all compounds were diluted serially in 50/50 ACN:H₂O to create standard curves and quality control spiking solutions. An aliquot of (2 µL) of neat spiking solutions were added to 2 µL of lesion homogenate were combined prior to extraction. Equal volumes (2 µL) of ACN:H₂O and PBS were added to the dissected study samples. Extraction was performed by adding 50 µL of extraction solution ACN/MeOH (1/1) with 5 ng/mL Clarithromycin-d₄ and Azithromycin-d₅. Extracts were vortexed for 5 minutes and centrifuged at 10,000 rpm for 5 minutes. An aliquot (40 µL) of supernatant was transferred for LC/MS-MS analysis and diluted with an additional 40 µL of MilliQ water. See HPLC-mass spectrometry section for LC-MS parameters.

Drug potency assays

Minimum inhibitory and bactericidal concentrations were measured as previously described (47). For growth inhibition and bactericidal assays against intracellular bacteria, we used the protocol of Lefebvre et al.(48) with minor modifications. THP-1 cells were obtained from the American Type Culture Collection (ATCC) and cultured in RPMI 1640 medium supplemented with 10% fetal bovine serum (FBS, GIBCO) at 37°C in a humidified CO₂ incubator. THP-1 (10⁵ cells per well) were seeded into 96-well plates and differentiated for 24 h by adding 500 ng/ml of phorbol-12-myristate-13-acetate (PMA). The resulting macrophages were washed three times with PBS and infected with *M. abscessus* ATCC 19977 or *M. avium* 11 (49) at a multiplicity of infection (MOI) of 10 for 3h. The infected macrophages were washed three times with PBS to remove extracellular mycobacteria and treated with clarithromycin as indicated for three (*M. abscessus*) or four (*M. avium*) days. To enumerate intracellular surviving bacteria, cells were washed three times with PBS then lysed with PBS 0.1% Triton 100X. Tenfold serial dilutions were performed using 96-well plates containing 180 µL of PBS and each dilution was plated onto 7H10 agar. CFU were counted after four days of incubation.

Macrophage viability was assessed by trypan blue exclusion test. Each experiment included technical duplicates and the experiments were performed twice independently.

Macrophage uptake and caseum binding assays

Human monocytes were isolated from fresh packed leucocytes (New York Blood Center), purified, activated and differentiated into foamy macrophages as described previously (124). Uptake of clarithromycin, azithromycin and erythromycin in primary non-foamy and foamy macrophages was carried out as described (50), and the incubation concentration was 20 mM for all three drugs. Nonspecific drug binding in cavity caseum was measured as previously described (51; 52).

Modeling of tissue distribution and PK-PD simulations

Data from 100 and 300 mg/kg single doses of CLA in uninfected rabbits were used to develop a plasma PK model. Simulations were performed to match exposure in rabbits predicted to be equivalent to a 200 mg/kg dose in humans. To describe the movement of drug from plasma to the sites of action, a population approach using nonlinear mixed effects modeling in NONMEM was used. A population plasma PK model was built using data from both infected and uninfected rabbits (Figure 3.2). One- and two-compartment distribution compartments were tested. Saturated clearance was tested using the Michaelis-Menten kinetics equation (Equation 3.1).

$$\text{Rate of elimination} = -\frac{V_{max} * C_{plasma}}{k_m + C_{plasma}} \quad \text{Eq. 3.1}$$

First-order, zero-order, transit compartment, Weibull function (53), flip-flop, and first-order with a lag period were tested to fit the absorption phase. Replacing first-order absorption with Weibull absorption function significantly improved model fit (delta Objective Function Value or dOFV = -52.743). Interindividual variability was added to F1 (dOFV= -82.377). The Weibull absorption is defined by Equation 3.2 and 3.3, where K_w is the absorption rate constant, T_w is time after dose, and λ is the shape parameter.

$$WB = \left(1 - e^{-K_w \cdot T_w^\lambda}\right) \quad \text{Eq. 3.2}$$

$$\frac{dA_{abs}}{dt} = -WB \times A_{abs} \quad \text{Eq. 3.3}$$

Infection status and weight were tested as covariates. Interindividual variability was tested on bioavailability, volume of distribution, and clearance. To estimate extent of partitioning to the sites of action, the parameters of the final plasma model were fixed, and effect compartments were added for each tissue type as previously described (33; 54; 55). For the plasma-to-lesion model, the plasma-to-uninvolved lung rate constant was fixed at 10/h given the rapid equilibration half-life of 4 min. Fixing the rate to higher values did not change the other parameter estimates (partition coefficient) significantly. Tissue density was assumed to be 1 g/mL of homogenate. Data obtained with tissue samples processed as homogenates and samples collected by laser-capture microdissection were pooled and treated as equal. Data for the two cavity caseum samples were merged with outer caseum data points based on gross pathology and histology data, because no data was available at or near C_{max} for this compartment. A rate constant ($k_{pl-lesion}$), a coefficient of penetration ($PC_{pl-lesion}$), and residual error were estimated for each lesion type. The structural model is shown in Equation 3.4.

$$\frac{dC_{lesion}}{dt} = k_{pl-lesion} (PC_{pl-lesion} \times C_{plasma} - C_{lesion}) \quad \text{Eq. 3.4}$$

Model building was guided by goodness-of-fit plots, objective function value, and visual predictive checks. One thousand simulations, using interindividual variability and residual error as variability, were performed to confirm model fit. NONMEM version 7.4.2, R software version 4.0.5, and the R packages ggplot2 and xpose4 were used for model building, data visualization, and simulations.

A rabbit-to-human translational model was developed by linking lesion parameters estimated in rabbits to a previously published clinical plasma PK model (56). Clinical simulations were integrated with in vitro PD targets to derive unbound C_{max} , AUC and fraction of the dosing

interval relative to targets. Fraction unbound was assumed to be 0.3 (57). Model diagnostic plots are shown in Figure 0.3.

Results

The rabbit model of active TB reproduces major histopathology features of clinical NTM-PD

Given the lack of NTM animal models with pathological features comparable to human clinical NTM disease, we assessed the histopathological similarities between the rabbit model of active TB, clinical NTM disease, and clinical TB disease in a human patient (Figure 0.1) to evaluate the suitability of the rabbit TB model for lesion penetration of NTM drugs. Key pulmonary sites of infection where drugs show differential partitioning are the cellular and necrotic regions of granulomas and cavities.

Similar to the rabbit model of TB, human clinical NTM infection develops structured granulomas including central caseous necrosis with a pauci-cellular inner caseum and greater neutrophil composition at the outer caseum margin. The central necrosis is surrounded by a macrophage layer and an outer cellular layer composed of greater lymphocyte composition, fibrosis, and pulmonary epithelium (Figure 0.1A-B). These features are all similarly represented in both the rabbit model of TB (Figure 0.1C-D) and in human clinical TB (Figure 0.1E-F). Collectively, the pulmonary tissue from human clinical NTM infection demonstrated a heterogeneous profile of lesions over chronic disease and lengthy antimicrobial treatment (Supplementary Figure 3.1). Aside from an abundance of granuloma lesions similar to the rabbit TB model, these features also included fibrosis in peri-lesional lung, pleural, and alveolar interstitium, and the presence of secondary lymphoid follicles. Several heterogeneous and/or occasional features of clinical NTM-PD such as coalescing non-necrotic granulomas, cavitary necrotic lesions with abundant caseum, and bronchioles filled with necrotic caseum containing neutrophils – indicative of bronchogenic spread as seen in human TB (58; 59) – were also observed in rabbits with active TB (Supplementary Figure 3.2). Comparable immunohistopathology of NTM and TB lung disease has been reported by others (12; 18). Thus, the

rabbit model of active TB reproduces key pathological features of clinical NTM-PD and is a useful tool for evaluating drug penetration at key pulmonary sites of mycobacterial infection.

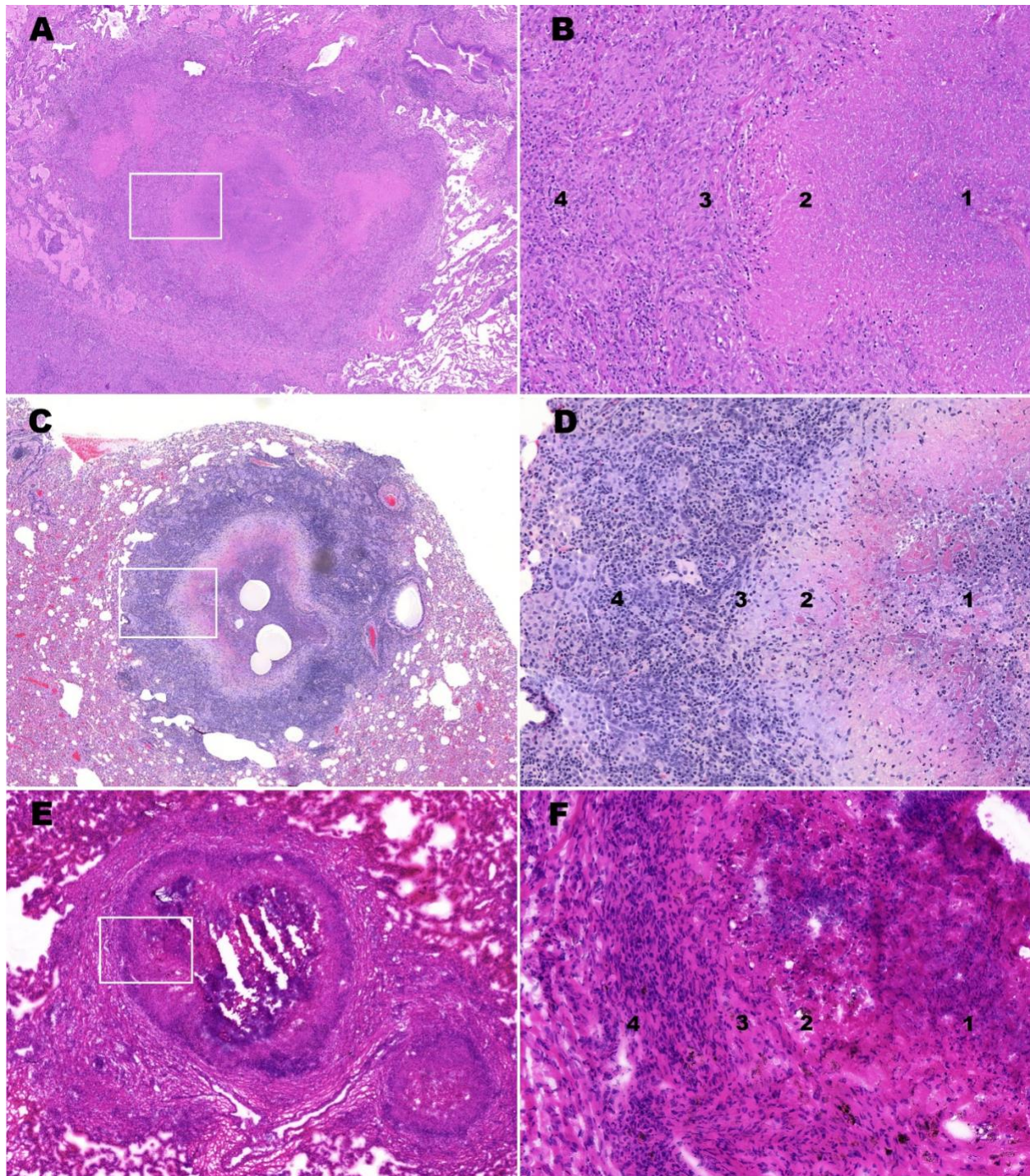


Figure 0.1. Comparative histopathology of human clinical NTM infection, human clinical Mtb infection and Mtb infection in the rabbit model.

(A) H&E-stained image of representative NTM granuloma lesion in the lung of human patient with clinical NTM infection caused by *M. abscessus*. (B) higher magnification of inset region in (A) demonstrating

microenvironmental locations, labeled 1-4. (C) H&E-stained image of representative granuloma lesion in the lung of an *M. tuberculosis* infected rabbit. (D) higher magnification of inset region in (C) demonstrating microenvironmental locations, labeled 1-4. (E) H&E-stained image of representative TB granuloma lesion in the lung of a human patient with clinical *M. tuberculosis* infection. (F) higher magnification of inset region in (A) demonstrating microenvironmental locations, labeled 1-4. 1, Inner Caseum; 2, Outer Caseum and Neutrophil rim; 3, Macrophage layer; and 4, Lymphocyte-rich cellular and collagen rim.

In vitro prediction of macrolide partitioning in cellular and necrotic lesion areas

Previous work by our group indicated that drug penetration in cellular granulomas and partitioning between the cellular rim and necrotic core of lung lesions is a function of (i) uptake into immune cells in vitro (50) and (ii) binding to caseum macromolecules (44; 52). The fate of drug molecules at the outer edge of caseum is a balance between uptake into the bordering macrophages, binding to macromolecules and effective diffusion into non-vascularized caseum. In necrotizing granulomas, intracellular Mtb is found in macrophages (12; 18; 60). In response to infection and low oxygen tension caused by decreased vascular efficiency (61; 62), macrophages accumulate lipid bodies and become foamy. These foamy infected macrophages necrotize and release their bacterial and cellular contents into the central caseum.

To predict the distribution of clarithromycin and azithromycin in cellular and necrotic lesion compartments, we measured drug binding in ex vivo caseum and uptake into primary human macrophages – foamy and non-foamy – derived from blood monocytes. The average unbound fraction in caseum (f_u -caseum) was 3 to 5%, thus moderate-to-low for both drugs (Table 0.1). Intracellular uptake was measured in primary human macrophages, including macrophages where the foamy phenotype was induced by infection with irradiated *M. tuberculosis* (50). We observed high intracellular accumulation in blood derived macrophages, and similar accumulation in foamy and non-foamy macrophages (Table 0.1), indicative of favorable penetration and higher concentrations in cellular lesions than in plasma. Together with the relatively low f_u -caseum, high intracellular uptake predicted limited or slow passive diffusion through non-vascularized caseum. To confirm these predictions, we measured clarithromycin

concentrations at the site of mycobacterial disease in the rabbit model of active TB, which presents with cellular granulomas, necrotic lesions, and cavities.

Table 0.1. In vitro lesion pharmacokinetic profiling of macrolides, clarithromycin and azithromycin.

azithromycin.						
	Clarithromycin			Azithromycin		
Free caseum fraction ⁽¹⁾						
	3.9 ± 0.1%			5.4 ± 0.4%		
Uptake in primary human macrophages (Intracellular to extracellular concentration ratio) ⁽¹⁾						
	Donor 1	Donor 2	Donor 3	Donor 1	Donor 2	Donor 3
Standard differentiated macrophages	95.0 ± 13.3	38.6 ± 16.9	106.2 ± 7.2	75.6 ± 3.0	46.8 ± 14.9	114.6 ± 14.3
Foamy macrophages	98.5 ± 2.8	32.2 ± 7.0	89.8 ± 19.5	86.5 ± 10.0	37.7 ± 8.1	95.8 ± 12.6

⁽¹⁾ mean ± SD, n = 3 replicates

Clarithromycin exhibits differential penetration into mycobacterial lung lesions

Clarithromycin was selected as a representative macrolide used to treat NTM-PD. To study and model the penetration of clarithromycin in lung lesions, we first identified a rabbit dose that achieves exposure comparable to that of NTM patients receiving 500 mg daily (56; 63-67). The concentration time profile was established in naïve (uninfected) rabbits following single oral doses of 100 mg/kg and 300 mg/kg, and three daily doses of 300 mg/kg (Table 0.2 and Supplementary Figure 3.3A). The area under the concentration-time curve (AUC)/MIC ratio is considered the primary PK-PD parameter driving antibacterial effect of clarithromycin and azithromycin (68-70). To reproduce the AUC achieved in humans following repeated oral daily doses of 500 mg, we selected 200 mg/kg for subsequent tissue and lesion penetration studies in rabbits (Supplementary Figure 3.3B and Table 0.2).

Table 0.2. Clarithromycin plasma pharmacokinetic parameters in rabbits compared to human at the clinical dose.

Dose (number of doses)	C_{max} (ng/mL)	t_{max} (h)	AUC_[0-24] (ng*h/mL)	Target human PK parameters (500 mg at steady state)
100 mg/kg (single dose)	427 ± 286	3 ± 1	3,762 ± 3,365	C _{max} (ug/mL) = 2.5 – 3.0 AUC _[0-24] (ug*h/mL) = 18 – 20 T _{max} (h) = 2 – 3 (135-137; 139)
300 mg/kg (single dose)	2,828 ± 1,001	4 ± 1.5	28,409 ± 12,317	
300 mg/kg (3 daily doses)	4,158 ± 916	1.4 ± 0.8	28,543 ± 8,790	
200 mg/kg (3 daily doses in infected rabbits)	1,938 ± 1,073	1.50 ± 0.55	11,709 ± 4,922	

C_{max}: peak plasma concentration; t_{max}: time of peak plasma concentration; AUC_[0-24]: area under the concentration-time curve from 0 to 24 h; AUC_{inf}: area under the concentration-time curve from 0 to infinity.

To build a translational model of clarithromycin penetration at the site of mycobacterial lung disease, we measured drug concentrations in serial blood samples, uninvolved lung tissue and lesion homogenates in groups of 3 infected rabbits following three daily 200 mg/kg doses. Tissue samples were collected 6 h (end of the distribution phase) and 24 h (trough) after the third dose. The total number of observations and the concentrations of clarithromycin in plasma, uninvolved lung, cellular and necrotic lesions are shown in Figure 0.2A. In line with the high intracellular uptake in macrophages, total clarithromycin concentrations were 30 to 40-fold higher in uninvolved lung (devoid of macroscopic lesions but infiltrated with various immune cell types) than in plasma, and over 100-fold higher in cellular lesions than in plasma (Figure 0.2A). In caseum isolated from a large cavity at 24 h, clarithromycin was present at higher concentration than in plasma, but lower than average concentrations in cellular lesions. To confirm this initial observation and better describe the partitioning of clarithromycin at the interface between cellular rims and caseous (necrotic) foci, we reserved large necrotic lesions from the same animals for laser-capture microdissection (LCM) in thin tissue sections (46).

Concentrations in uninvolved lung and cellular rims matched the corresponding concentrations measured in lung tissue and cellular lesion homogenates (Figure 0.2B). We found the highest clarithromycin concentrations in cellular rims, decreasing as one moves inward into the caseum periphery and deep caseum, in line with the limited f_u -caseum measured in vitro. The trend of concentration gradients was similar at 6 and 24 h. However, clarithromycin appeared to gradually diffuse into deep caseum between 6 and 24 h, reducing the caseum/cellular concentration ratio (Figure 0.2B). To confirm this observation, we applied LCM to clinical lung samples resected from (i) a TB patient who had received clarithromycin 1,000 mg once daily (QD) for 5 weeks as salvage therapy, and (ii) an *M. abscessus* patient who had been on azithromycin 250 mg once daily (QD) for approximately 2 years. Resections took place 31 h and 24 h after the last macrolide dose, respectively. We found that drug concentrations measured at trough in lung and cellular rims were similar in these two subjects and in rabbits after three daily 200 mg/kg doses (Figure 0.2C). Interestingly, the decreasing drug concentration from the cellular rim into deep caseum was much shallower in these patients – who were in advanced steady state – than in rabbits after 3 doses. Specifically, clarithromycin partitioned evenly across all lesion compartments including deep caseum, while azithromycin was only 2- to 3-fold lower in caseum than in cellular regions (Figure 0.2C). This suggests that, as suspected, macrolides equilibrate slowly into non-vascularized caseum, and that steady state appears to be achieved in caseum after QD dosing for 5 weeks but not after three daily doses in rabbits.

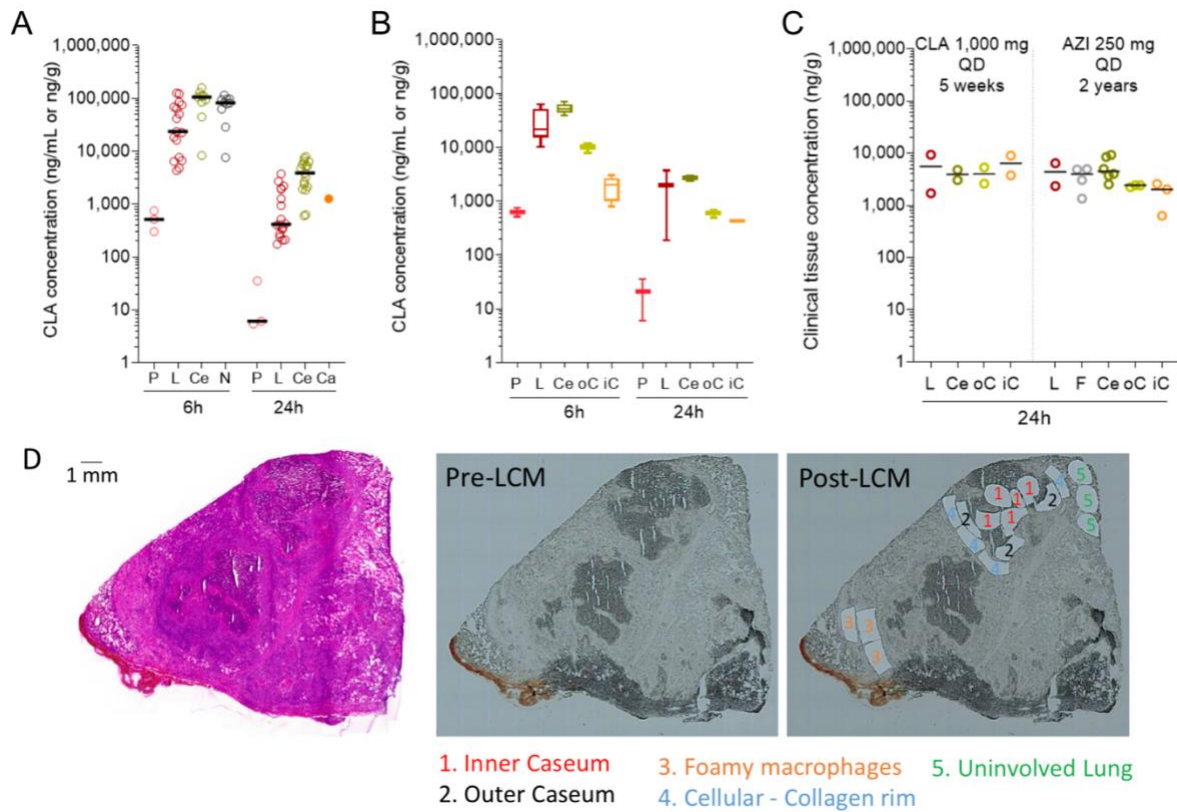


Figure 0.2. Distribution of clarithromycin from plasma into major pulmonary lesion compartments. (A) Clarithromycin concentrations in rabbit plasma, lung and whole lesion homogenates after 3 daily doses. P: plasma; L: uninvolved lung (devoid of macroscopically visible lesions); Ce: fully cellular lesion; N: partially necrotic lesion; Ca: cavity caseum. Each data point represents one individual plasma or tissue sample: $n = 3$ rabbits per time point. (B) Spatial quantitation of clarithromycin in large necrotic rabbit lesions by laser-capture microdissection: P: plasma; L: uninvolved lung; Ce: cellular rim; oC: outer edge of caseum adjacent to the cellular rim; iC: inner core of caseum. Lesions were collected from a subset of the animals shown in (A). (C) Spatial quantitation of clarithromycin and azithromycin in large lesions collected from the resected lung of a TB patient (left) and an *M. abscessus* disease patient (right), respectively. L: uninvolved lung; F: fibrotic cuff; Ce: cellular rim; oC: outer edge of caseum; iC: inner core of caseum. (D) Typical example of histology staining and laser capture microdissection (LCM) of thin human lesions sections. Two large necrotic lesions were collected from the resected lung tissue of human subject G-101 receiving CLA 1,000 mg QD. The adjacent lesion section was used for hematoxylin and eosin (H&E) staining (left) to guide LCM sample collection (right): 1. Inner caseum; 2. Outer caseum; 3. Cellular rim; 4. Uninvolved lung. Laser-dissected pieces belonging to the same tissue compartment were pooled for quantitation by LC-MS/MS.

To quantitatively describe the differential penetration of clarithromycin in mycobacterial lung lesions, we developed a multicompartiment nonlinear mixed effects PK model. The final plasma model was a two-compartment model with Weibull absorption – a flexible model function that better describes slow onset absorption with gradual acceleration (53) – and Michaelis-Menten

elimination. Infection status and weight were not identified as covariates of drug exposure. Replacing first-order absorption with Weibull absorption significantly improved model fit, with a delta objective function value (dOFV) of -52.743. Clarithromycin accumulated in regions of high cellularity (uninvolved lung and cellular lesions) with total AUC_{tissue} approximately 2 orders of magnitude higher than total AUC_{plasma} . Cellular lesions had the largest partition coefficient of 102. Necrotic areas including the outer caseum (the region adjacent to the cellular rim of the necrotic core) and inner caseum (the center of large necrotic lesions) of closed lesions and cavities also had high clarithromycin concentration relative to plasma with partition coefficients of 13.1 and 2.9, respectively (Table 0.3). Clarithromycin distribution to lesions – but not to uninvolved lung – was slow with concentrations peaking 2 to 4 hours after plasma C_{max} . Visual predictive checks indicated that the final model fit the data well (Figure 0.3).

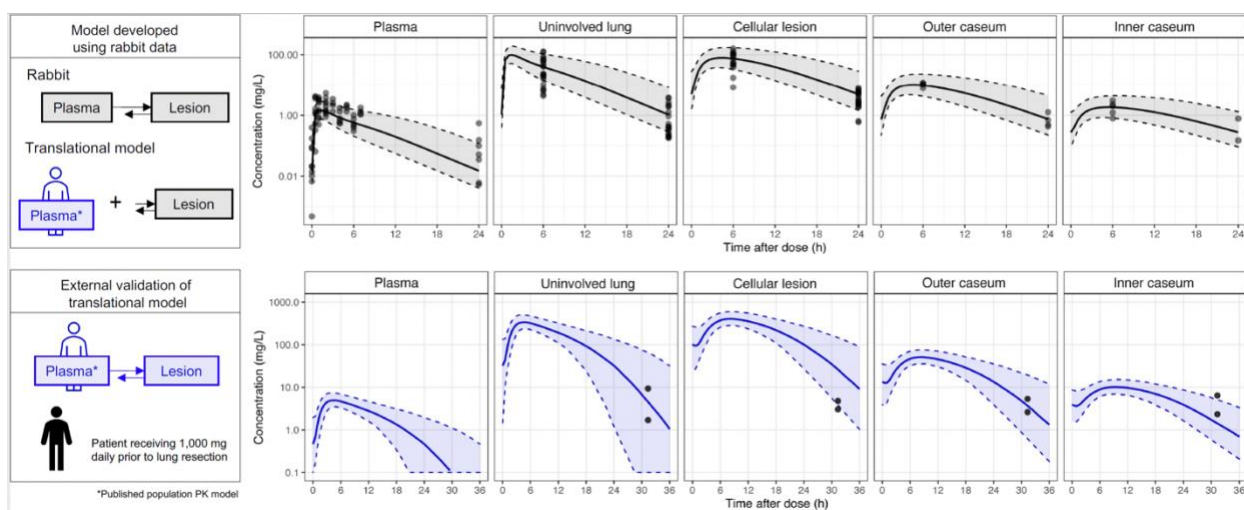


Figure 0.3. Visual predictive check of clarithromycin rabbit plasma-to-tissue multicompartment model.

Visual predictive check of clarithromycin rabbit plasma-to-tissue multicompartment model. The translational model was built by integrating a population PK model with lesion parameters estimated in rabbits. Top plots: observed clarithromycin concentrations (individual dots) in rabbits, with 500 simulations represented as median (solid line) and 5th and 95th percentiles (grey shaded area, dashed lines). To externally validate the model, we simulated clarithromycin penetration in 4 lesion compartments following a 1,000 mg daily dose to steady state (n=500) and compared with pulmonary drug levels of one patient who received 1,000 mg once-daily for 5 weeks prior to lung resection. Bottom plots: patient clarithromycin observations from two biopsies (individual dots) with 500 simulations represented as median (solid line) and 5th and 95th percentiles (blue shaded area, dashed lines).

Table 0.3. Plasma-to-tissue model parameters.

Compartment	Parameter	Value (RSE, %)
Plasma	V_{\max} (L/h)	88.72 (18.5)
	K_m (mg/L)	0.3862 (36.6)
	V	207.2 (26.4)
	K_w	0.1776 (145.9)
	λ	0.6028 (58.5)
	Q	157.5 (34.9)
	V2	393.4 (13.6)
	IIV F1	0.3311 (14.5)
	Additive Error (mg/L)	0.0071 (48.2)
Lung	Proportional Error (%)	45.66 (8.0)
	Partition coefficient	67.9 (35.6)
	Plasma to tissue rate constant (1/h)	10 (FIX)
Cellular lesion	Proportional Error (%)	108 (12)
	Partition coefficient	102 (16.2)
	Plasma to tissue rate constant (1/h)	0.283 (13.4)
Outer caseum	Proportional Error (%)	70.5 (16.2)
	Partition coefficient	13.1 (20.0)
	Plasma to tissue rate constant (1/h)	0.265 (14.2)
Inner caseum	Proportional Error (%)	39.6 (21.8)
	Partition coefficient	2.86 (9)
	Plasma to tissue rate constant (1/h)	0.174 (5.3)
	Proportional Error (%)	32.6 (24)

RSE: relative standard error; V_{\max} : maximum rate of clearance; K_m : Michaelis Menten constant; V: central volume of distribution; K_w : absorption rate constant; λ : shape parameter; Q: intercompartmental clearance; V2: peripheral volume of distribution; IIV: interindividual variability; F1: apparent bioavailability. FIX: parameter was fixed.

Clarithromycin exhibits differential pharmacokinetic-pharmacodynamic coverage of major lesion compartments

Clarithromycin inhibits growth of most replicating NTM strains below 1 mg/mL but has no bactericidal activity up to 20 to 256 mg/mL, depending on the strains and assay conditions (37; 71). To confirm these observations and place lesion concentrations of clarithromycin into pharmacodynamic context at the site of disease, we measured side-by-side (i) the MIC and MBC against representative clinical isolates of *M. abscessus* and *M. avium* in standard growth media (Table 0.4, Supplementary Figure 3.4A-D), and (ii) the concentrations required for growth inhibition and killing of intracellular *M. abscessus* and *M. avium* in macrophages (Supplementary Figure 3.5). Since *M. abscessus* and *M. avium* have been found in aggregates described as heaps (21), large clumps (72) or biofilms (20) in the lungs of NTM-PD patients, we

retrieved from the literature the concentrations required to inhibit biofilm formation and kill *M. abscessus* and *M. avium* in established biofilms and against non-replicating NTM bacteria (37; 39) (Table 0.4). We also confirmed that clarithromycin lacks bactericidal activity against planktonic *M. abscessus* and *M. avium* up to 25 mg/mL and exhibits limited bactericidal activity (approximately 5-fold kill) against intracellular *M. avium* only up to 25 mg/mL, without reaching the MBC₉₀ (Supplementary Figure 3.4 and 3.5). These potency values were used to simulate lesion PK-PD coverage in human lung lesions.

Table 0.4. In vitro potency of clarithromycin in representative growth inhibitory and bactericidal assays.

	<i>M. abscessus</i>	<i>M. avium</i>
Susceptibility breakpoints or ECOFF (epidemiological cutoff value) ⁽¹⁾	< 4 mg/mL susceptible 4-8 mg/mL intermediate > 8 mg/mL resistant (145)	< 2 mg/mL susceptible (146)
MIC₉₀ ⁽²⁾	0.2 to 1.2 mg/mL	0.15 to 1.2 mg/mL
MBC₉₀ (this work)	> 20 mg/mL	20 mg/mL
Intracellular IC₉₀	0.1 mg/mL ⁽³⁾	0.2 mg/mL ⁽³⁾ 0.05 mg/mL ⁽⁴⁾ (147)
Intracellular MBC₉₀ ⁽⁵⁾	> 25 mg/mL	> 20 mg/mL
Biofilm MIC₉₀	2.2 mg/mL (115)	2 mg/mL (148)
Biofilm MBC₉₀	> 75 mg/mL (115); 256 mg/mL (113)	> 20 mg/mL (149; 150)
Non-replicating nutrient starvation MBC₉₀	256 mg/mL (114)	n.d.

⁽¹⁾ against multiple subspecies and isolates

⁽²⁾ this work, 90% growth inhibition against a panel of susceptible reference strains

⁽³⁾ this work, 90% growth inhibition of *M. abscessus* subsp *abscessus* ATCC 19977 and *M. avium hominisuis* 11 in THP-1 macrophages

⁽⁴⁾ *M. avium* was grown in A549 lung epithelial cells

⁽⁵⁾ this work, bactericidal activity (90% kill) against *M. abscessus* ATCC 19977 and *M. avium* 11 in THP-1 macrophages

To predict concentrations within patient lungs and lesions, a published clinical model (56) was integrated with the rabbit plasma-to-lesion model, and a clinical dose of 500 mg administered twice daily was simulated. To assess the predictive ability of the translational

model, we simulated pulmonary tissue distribution following a 1,000 mg dose, reproducing a patient who underwent lung resection surgery after 5 weeks of clarithromycin treatment at 1,000 mg QD. Simulations adequately predicted the concentration in tissue with highest accuracy in lung and outer caseum (Figure 0.3). The model predictions were somewhat greater than the concentration measured in cellular lesions and somewhat lower than concentrations of inner caseum. This reflects the observation that macrolides slowly diffuse into non-vascularized caseum, and that achieving steady state in caseum requires more than the three daily doses required to achieve steady state in rabbit plasma. To select lesion-relevant pharmacodynamic targets, in vitro data were used that best represented the expected replication status and microenvironment of the compartment. Specifically, clarithromycin concentrations in lung and cellular lesions, where bacteria are essentially intracellular, were compared to intramacrophage potency values: concentrations that inhibit 90% growth (macIC_{90}) and minimum bactericidal concentration (macMBC_{90}). In these cellular and well perfused compartments, we simulated the concentration time profiles of total (bound and unbound) drug (Figure 0.4, dark grey shaded profile), as well as the free plasma concentrations to reflect passive diffusion of free drug from plasma to interstitial lung tissue (Figure 0.4, light grey shaded profile) (73). Even under the assumption that free plasma equilibrates with interstitial lung and cellular lesion, these free clarithromycin levels were above the macIC_{90} during the entire dosing interval, including in the lower 5th percentile of simulations, indicating high coverage for all patients. Under the scenario of free drug equilibration across compartments, the macMBC_{90} was not achieved in lung and cellular lesions. Using total clarithromycin concentrations in lung and cellular lesion, PD target achievement could not be firmly established due to the limited (less than 10-fold kill, i.e. MBC_{90} not reached) bactericidal activity at the highest concentration tested (Figure 0.4). Similar results have been reported by others (74). Clarithromycin concentrations measured by laser capture microdissection in outer and inner caseum, and in bulk cavity caseum, where bacteria are

extracellular, were compared to MIC₉₀ and MBC₉₀ against biofilms, revealing adequate static coverage throughout the dosing interval, but lack of bactericidal coverage. Because the highest concentration tested against *M. avium* biofilms (20 mg/mL), while inactive is within the range of concentrations achieved in the outer caseous rim, one cannot exclude that potentially bactericidal concentrations might be reached in caseous areas directly adjacent to the cellular rim, or in very small necrotic foci (Figure 0.4 and Table 0.4).

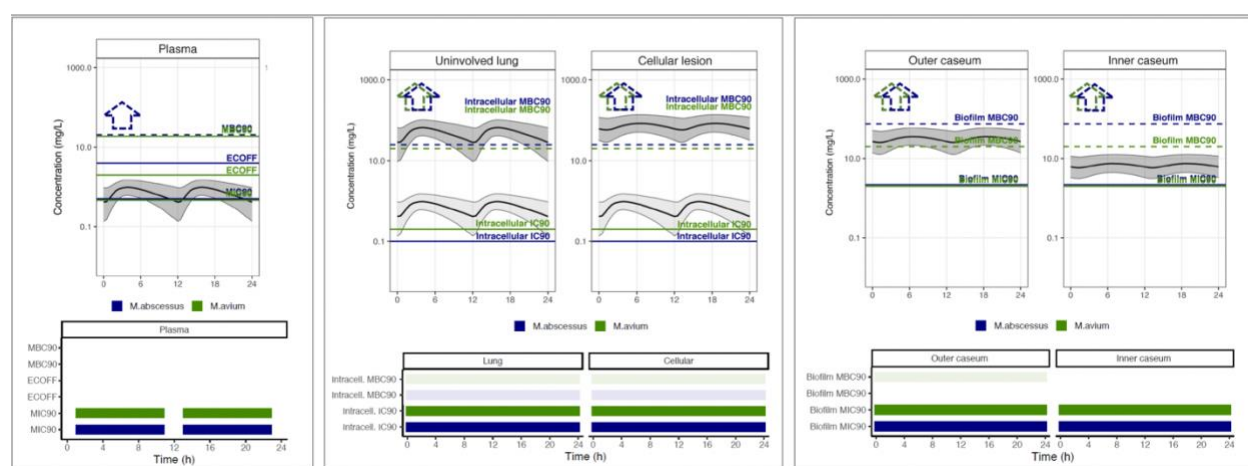


Figure 0.4. Clinical simulations of clarithromycin PK-PD coverage in plasma and four lung compartments.

Steady-state pharmacokinetic profiles are shown for one 24 h period following administration of 500 mg clarithromycin twice-daily. One thousand simulations were performed with the translational model and are represented as the median (solid black line) and 5th and 95th percentiles (thin black lines and gray shaded area). Plasma concentrations were corrected for protein binding ($f_u = 30\%$). In uninvolved lung and cellular lesions, the dark grey shaded profile was simulated using total clarithromycin tissue concentrations and the light grey shaded profile assumes passive diffusion of free drug from plasma to interstitial tissue. In vitro targets are represented as horizontal lines and colored by mycobacterial species (*M. abscessus*, blue; *M. avium*, green). Dotted lines accompanied by dotted line arrows indicate PD targets greater than the highest concentration tested in vitro. In PK-PD coverage plots shown under each concentration time profile, colored boxes indicate periods during which clarithromycin concentrations are above the corresponding in vitro PD target indicated on the left of each row (*M. abscessus*, blue; *M. avium*, green). The MIC₉₀ was set at 0.6 mg/mL or the average of the MIC₉₀ values measured against a panel of susceptible reference strains as part of this work. The ECOFF's (epidemiological cutoff values) or clinical susceptibility breakpoints were retrieved from (145; 146).

As a reference, plasma concentrations were compared to the MIC range published as epidemiological cut-off values or ECOFF, MIC₉₀ and MBC₉₀ against replicating bacterial populations in standard media (Table 0.4). Interestingly, differential PK-PD coverage was

observed in subjects with average PK profiles compared to subjects at the lower end (5th percentile) of drug exposure. Median plasma concentrations were above the MIC₉₀ against both species during most of the dosing interval, while plasma concentrations of subjects with suboptimal PK achieved the MIC₉₀ only during a limited fraction of the dosing interval.

To visualize target attainment across compartments in patients with average exposure or at the lower end of the drug exposure spectrum, we compiled the ratios between AUC and various PD parameters against *M. abscessus* and *M. avium* (Figure 0.5 and Supplementary Figure 3.6). Thus, across tissue compartments, clarithromycin was above growth inhibitory concentrations and below bactericidal concentrations against both *M. abscessus* and *M. avium*, and suboptimal PK exposure did not significantly impact target attainment against either pathogen, in line with lesion coverage being primarily driven by PD rather than PK.

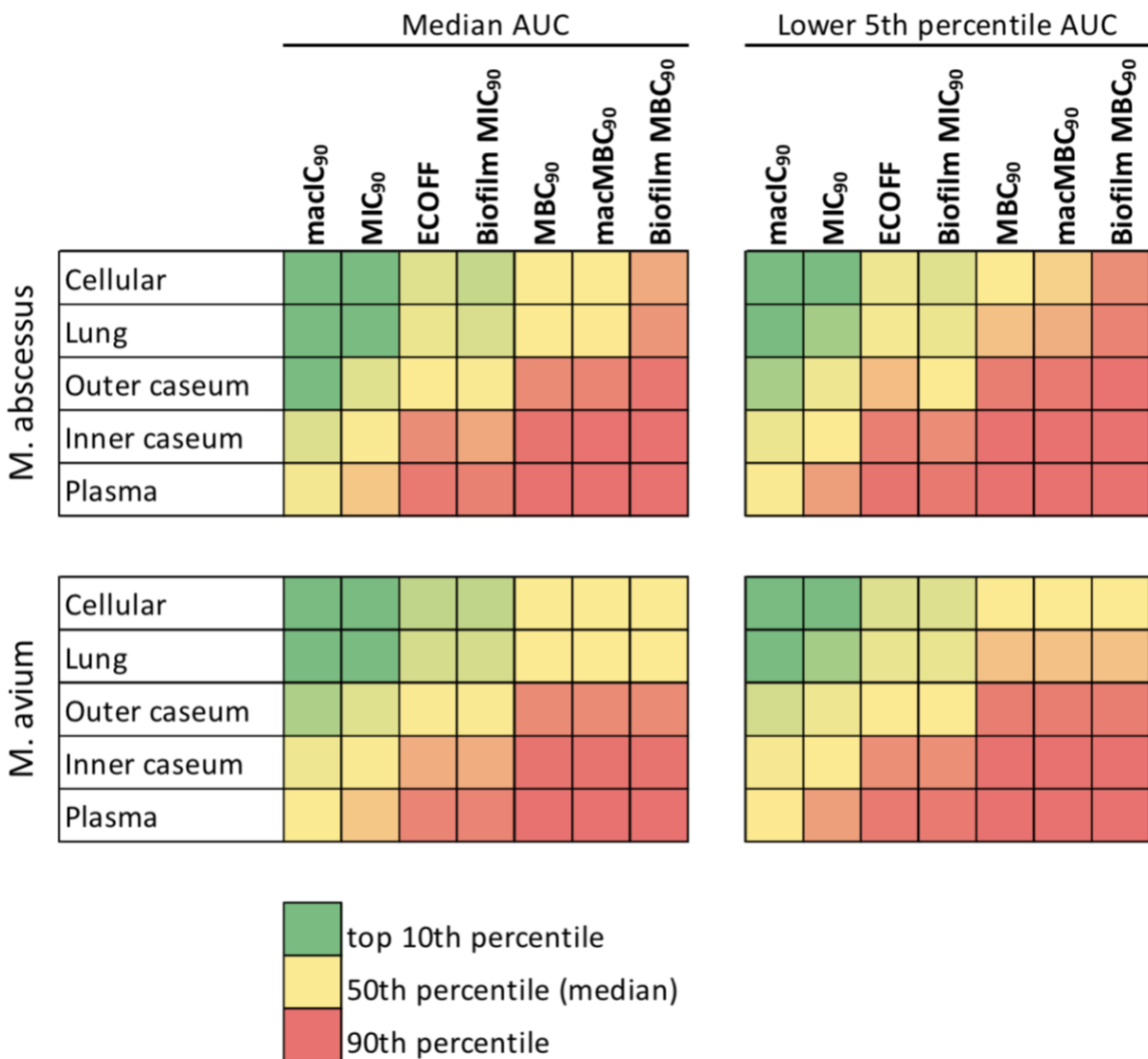


Figure 0.5. Predicted target attainment expressed as AUC/potency across compartments against *M. abscessus* and *M. avium* disease.

The analysis was performed for a range of bacteriostatic and bactericidal potency values and included simulated patients with either average clarithromycin exposure or at the lower end (5th percentile) of the drug exposure spectrum. Color coding spans from dark green (top 10th percentile of ratios or maximum coverage) to dark red (90th percentile or lower 10th percentile of ratios, indicating poor PK-PD coverage).

Discussion

Among the factors contributing to the poor success rates of the very long NTM-PD treatment with multiple antibiotics is the repurposed nature of all drugs in clinical use, which have not been developed to reach optimal PK-PD targets against NTM pathogens (75). Apart from a Phase II trial of inhaled amikacin completed in 2016 (76), no randomized controlled trial comparing antibiotic treatment of NTM lung infection has been conducted (77). In the case of *M. abscessus* disease, there is no reliable cure (78). In developed countries, the public health situation is significantly more dreadful for NTM-PD than for TB, owing to (i) the intrinsic drug resistance of NTM pathogens (78), (ii) the lack of bactericidal activity of most NTM antibiotics active against NTMs (79), and the ability of NTM pathogens to acquire a drug tolerant state in extracellular cords and biofilms (20; 39; 80). In common with TB is the role of the pulmonary pathophysiology in limiting drug penetration to the sites of disease.

Here we report the distribution and PK-PD of clarithromycin in lung lesions, using a rabbit model of NTM-PD-like pathology and a panel of relevant potency values. This is the first study focusing on the lesion PK-PD of an NTM drug, primarily due to the lack of an animal model of NTM disease presenting large, organized lesions adequate for drug quantitation in cellular and necrotic compartments. To validate the use of the active TB rabbit model for predicting antibiotic penetration in NTM-PD lesions, we showed that similar lesion types and lesion structure were found in resected lungs from a patient with *M. abscessus* disease, TB patients, and rabbits with chronic active TB. This finding was expected given the considerable overlap in immunopathology and radiographic features of pulmonary TB and NTM-PD (16-18). We found that growth inhibitory concentrations corrected for protein binding were exceeded throughout the dosing interval in cellular lesions and in moderately infiltrated lung tissue devoid of grossly visible lesions. In these pulmonary compartments, *M. avium* and *M. abscessus* are thought to reside within immune cells, mostly macrophages and neutrophils (18; 81), as well as

epithelial cells. Though clarithromycin showed favorable distribution across lesion compartments, it is expected to only inhibit growth of *M. avium* and *M. abscessus* given its lack of bactericidal activity against replicating and non-replicating bacterial populations, against intracellular bacteria in macrophages and against biofilm persisters found in lung lesions (39). Thus, clarithromycin's clinical activity at the site of infection appears to be PD- rather than PK-limited. Notably, free plasma concentrations were below the susceptibility breakpoints of 2 and 4 µg/mL for *M. avium* and *M. abscessus* respectively, during the entire dosing interval.

The high partitioning of clarithromycin in diseased lung and lesions matched the high uptake in PBMC-derived macrophages and foamy macrophages in vitro, with an enrichment factor of approximately 100-fold. Similarly high uptake has been reported for macrolides into monocytes and macrophages (82; 83), and even higher in polymorphonuclear leukocytes (25; 26; 84), which have been proposed to act as antibiotic Trojan horses (29; 31). In lung resections performed for other indications such as malignancy, favorable but lower (~ 30-fold) partitioning of clarithromycin was measured in healthy lung tissue relative to plasma (85), consistent with high penetration driven by the much higher abundance of immune cells in NTM- and TB-infected lung than in relatively healthier lung tissue. Collectively, results accumulated by our group with this and other drug classes (54; 86-88) indicate that intracellular-to-extracellular concentration ratios in the macrophage uptake assay are predictive of total cellular lesion-to-plasma concentration ratios in vivo. If we assume passive diffusion of unbound drug from plasma into interstitial pulmonary tissue and assume that unbound drug concentrations drive the pharmacological response, unbound clarithromycin remains above the MaIC_{90} in lung and lesions for the entire dosing interval, even in subjects with suboptimal drug exposure.

In cavity caseum and necrotic centers of large granulomas, we observed a decreasing concentration gradient after three daily doses in rabbits, but not in patients who were in advanced steady state. This slow diffusion of macrolides into non-vascularized caseum is likely driven by their high nonspecific binding to caseum macromolecules (Table 3.1). In addition,

foamy macrophages and other immune cells in which macrolides accumulate may act as a reservoir (26) from which the drugs are slowly released to gradually equilibrate at the caseum/cellular interface and into deep caseum. Based on the similar plasma PK (66), uptake in macrophages and foamy macrophages, and nonspecific binding to caseum macromolecules of azithromycin and clarithromycin, one would expect similar dynamics of partitioning between the cellular and necrotic lesion compartments for both drugs, as suggested by the sparse clinical data obtained here (Figure 3.2C). This needs to be confirmed with additional preclinical or clinical samples dosed with azithromycin.

What are the implications of these findings for NTM-PD treatment practice? Our in vitro and in vivo results consistently show high total concentrations within immune cells, in cellular lesions and minimally involved lung tissue. Although one can expect high nonspecific binding inside immune cells, the pharmacologically active fraction in this microenvironment is a function of the binding dynamics of the macrolides between their bacterial target and host cell macromolecules. The sustained presence of very high total intracellular concentrations, in excess of 100 mg/L, upon multi-month therapy may favor bactericidal activity. Recent work measuring the activity of clarithromycin over 7 and 14 days against replicating *M. abscessus* surprisingly revealed bactericidal activity at concentrations of 16 mg/L and above (38). In addition, the host- and pathogen-targeted anti-inflammatory properties of macrolides are beneficial in controlling harmful inflammatory responses during acute and chronic bacterial infections (89-91). Thus, subjects with minimal necrosis, mostly cellular nodules, consolidations, and miliary disease may respond better to macrolides. This type of immunopathology is more frequently seen in immunocompromised patients, a growing population due to increasing use of organ transplantation, stem cell transplants, and the widespread use of immunosuppressive therapies for patients with cancer and immune-mediated inflammatory disease (3). In caseum where bacteria are extracellular or within biofilm-like structures, the window between achieved free concentrations and inhibitory concentrations is much narrower than in cellular

compartments (Figure 3.4), potentially indicative of more limited activity. However, macrolides have been shown to prevent the production of factors involved in the formation of biofilm in both Gram-positive and Gram-negative bacteria (92) including at sub-inhibitory concentrations. Though this macrolide property has not been reported in NTM bacteria, it could contribute – if demonstrated – to the observed biofilm growth inhibitory effect (39; 93) and possibly weaken the dynamic life cycle of established biofilms. Indeed, macrolides are known to alter the structure and architecture of *Pseudomonas* and *Staphylococcal* biofilms via inhibition of polysaccharide synthesis (94; 95). A structurally impaired biofilm may allow for enhanced phagocytosis and clearance of bacteria (96). Considering these results as well as recent findings on the long-term bactericidal activity of clarithromycin against *M. abscessus* cultures (38), further investigations are warranted to better define the role of macrolides in patients with cavitary disease and determine whether patients would benefit from tailored regimens that take extent of disease pathology and presence of cavity into consideration.

The predicted human-equivalent dose of 200 mg/kg delivered slightly lower than expected exposure owing to the increased clearance in infected rabbits compared to uninfected. Modeling of the infected and uninfected plasma PK concentrations, we found that the 2-compartment model with Michaelis-Menten elimination and Weibull function absorption best fit the data. While the structural model appropriately matched the published model (56), there was uncertainty in estimating the absorption parameter (RSE = 145.9%), possibly due to the inherent variability of clarithromycin absorption in rabbits. Despite the uncertainty, the Weibull function provided appropriate model fit. Michaelis-Menten elimination is consistent with clarithromycin inhibiting its own metabolism via CYP3A4. We also acknowledge that human subjects undergo lung resection due to drug recalcitrant disease associated to severe pathology. Thus, the two subjects who contributed resected tissue may not be representative of the typical immunohistology and lesion distribution of mycobacterial lung disease. The small clinical sample size constitutes an additional limitation of the study. A prospective lesion

pharmacokinetic study (44) is required to quantify the diffusion kinetics of macrolides into large necrotic foci and cavity caseum.

In summary, we have leveraged the rabbit model of active chronic TB to quantify the penetration of NTM-PD antibiotics at the site of lung infection. The model encompasses the typical immunopathology seen in immune-compromised and immune-competent patients, namely cellular nodules, consolidations, necrotic lesions and cavities. By combining standard analytical quantitation with laser-capture microdissection, the methodology delivers spatial quantitation of the drugs of interest in complex lesions. Our results provide the first step towards the simulation of lesion PK-PD coverage by multi-drug combinations, to enable the prioritization of most promising regimens for clinical trials, an emerging paradigm in TB drug development (97).

References

1. Cowman S, van Ingen J, Griffith DE, Loebinger MR. 2019. Non-tuberculous mycobacterial pulmonary disease. *Eur Respir J* 54
2. O'Connell ML, Birkenkamp KE, Kleiner DE, Folio LR, Holland SM, Olivier KN. 2012. Lung manifestations in an autopsy-based series of pulmonary or disseminated nontuberculous mycobacterial disease. *Chest* 141:1203-9
3. Henkle E, Winthrop KL. 2015. Nontuberculous mycobacteria infections in immunosuppressed hosts. *Clin Chest Med* 36:91-9
4. Klein JL, Corbett EL, Slade PM, Miller RF, Coker RJ. 1998. *Mycobacterium kansasii* and human immunodeficiency virus co-infection in London. *J Infect* 37:252-9
5. Tomashefski JF, Jr., Stern RC, Demko CA, Doershuk CF. 1996. Nontuberculous mycobacteria in cystic fibrosis. An autopsy study. *Am J Respir Crit Care Med* 154:523-8
6. Swenson C, Zerbe CS, Fennelly K. 2018. Host Variability in NTM Disease: Implications for Research Needs. *Front Microbiol* 9:2901
7. Koh WJ, Hong G, Kim K, Ahn S, Han J. 2012. Pulmonary sequestration infected with nontuberculous mycobacteria: a report of two cases and literature review. *Asian Pac J Trop Med* 5:917-9
8. Merckx JJ, Soule EH, Karlson AG. 1964. The Histopathology of Lesions Caused by Infection with Unclassified Acid-Fast Bacteria in Man. Report of 25 Cases. *Am J Clin Pathol* 41:244-55
9. Smith MB, Molina CP, Schnadig VJ, Boyars MC, Aronson JF. 2003. Pathologic features of *Mycobacterium kansasii* infection in patients with acquired immunodeficiency syndrome. *Arch Pathol Lab Med* 127:554-60

10. Kim YK, Hahn S, Uh Y, Im DJ, Lim YL, et al. 2014. Comparable characteristics of tuberculous and non-tuberculous mycobacterial cavitary lung diseases. *Int J Tuberc Lung Dis* 18:725-9
11. Kim C, Park SH, Oh SY, Kim SS, Jo KW, et al. 2017. Comparison of chest CT findings in nontuberculous mycobacterial diseases vs. *Mycobacterium tuberculosis* lung disease in HIV-negative patients with cavities. *PLoS One* 12:e0174240
12. Miura K, Nakamura M, Taooka Y, Hotta T, Hamaguchi M, et al. 2020. Comparison of the chest computed tomography findings between patients with pulmonary tuberculosis and those with *Mycobacterium avium* complex lung disease. *Respir Investig*
13. Shah HH, Holland RH, Meador RS, Webb WR. 1969. The surgical variations of pulmonary infections caused by different species of *Mycobacteria*. *Ann Thorac Surg* 7:145-9
14. Yuan MK, Chang CY, Tsai PH, Lee YM, Huang JW, Chang SC. 2014. Comparative chest computed tomography findings of non-tuberculous mycobacterial lung diseases and pulmonary tuberculosis in patients with acid fast bacilli smear-positive sputum. *BMC Pulm Med* 14:65
15. Oshitani Y, Kitada S, Edahiro R, Tsujino K, Kagawa H, et al. 2020. Characteristic chest CT findings for progressive cavities in *Mycobacterium avium* complex pulmonary disease: a retrospective cohort study. *Respir Res* 21:10
16. Jeong YJ, Lee KS, Koh WJ, Han J, Kim TS, Kwon OJ. 2004. Nontuberculous mycobacterial pulmonary infection in immunocompetent patients: comparison of thin-section CT and histopathologic findings. *Radiology* 231:880-6
17. Kwon YS, Koh WJ. 2014. Diagnosis of pulmonary tuberculosis and nontuberculous mycobacterial lung disease in Korea. *Tuberc Respir Dis (Seoul)* 77:1-5
18. Jain D, Ghosh S, Teixeira L, Mukhopadhyay S. 2017. Pathology of pulmonary tuberculosis and non-tuberculous mycobacterial lung disease: Facts, misconceptions, and practical tips for pathologists. *Semin Diagn Pathol* 34:518-29

19. Crow HE, King CT, Smith CE, Corpe RF, Stergus I. 1957. A limited clinical, pathologic, and epidemiologic study of patients with pulmonary lesions associated with atypical acid-fast bacilli in the sputum. *Am Rev Tuberc* 75:199-222
20. Fennelly KP, Ojano-Dirain C, Yang Q, Liu L, Lu L, et al. 2016. Biofilm Formation by *Mycobacterium abscessus* in a Lung Cavity. *Am J Respir Crit Care Med* 193:692-3
21. Snijder J. 1965. Histopathology of pulmonary lesions caused by atypical mycobacteria. *J Pathol Bacteriol* 90:65-73
22. Griffith DE, Aksamit T, Brown-Elliott BA, Catanzaro A, Daley C, et al. 2007. An official ATS/IDSA statement: diagnosis, treatment, and prevention of nontuberculous mycobacterial diseases. *Am J Respir Crit Care Med* 175:367-416
23. Griffith DE, Aksamit TR. 2012. Therapy of refractory nontuberculous mycobacterial lung disease. *Curr Opin Infect Dis* 25:218-27
24. Diel R, Ringshausen F, Richter E, Welker L, Schmitz J, Nienhaus A. 2017. Microbiological and Clinical Outcomes of Treating Non-*Mycobacterium Avium* Complex Nontuberculous Mycobacterial Pulmonary Disease: A Systematic Review and Meta-Analysis. *Chest* 152:120-42
25. Bosnar M, Kelneric Z, Munic V, Erakovic V, Parnham MJ. 2005. Cellular uptake and efflux of azithromycin, erythromycin, clarithromycin, telithromycin, and cethromycin. *Antimicrob Agents Chemother* 49:2372-7
26. Wildfeuer A, Laufen H, Zimmermann T. 1996. Uptake of azithromycin by various cells and its intracellular activity under in vivo conditions. *Antimicrob Agents Chemother* 40:75-9
27. Labro MT. 1996. Intracellular bioactivity of macrolides. *Clin Microbiol Infect* 1 Suppl 1:S24-S30
28. Gladue RP, Bright GM, Isaacson RE, Newborg MF. 1989. In vitro and in vivo uptake of azithromycin (CP-62,993) by phagocytic cells: possible mechanism of delivery and release at sites of infection. *Antimicrob Agents Chemother* 33:277-82

29. Frank MO, Sullivan GW, Carper HT, Mandell GL. 1992. In vitro demonstration of transport and delivery of antibiotics by polymorphonuclear leukocytes. *Antimicrob Agents Chemother* 36:2584-8
30. Nakamura S, Yanagihara K, Araki N, Yamada K, Morinaga Y, et al. 2010. Efficacy of clarithromycin against experimentally induced pneumonia caused by clarithromycin-resistant *Haemophilus influenzae* in mice. *Antimicrob Agents Chemother* 54:757-62
31. Amsden GW. 2001. Advanced-generation macrolides: tissue-directed antibiotics. *Int J Antimicrob Agents* 18 Suppl 1:S11-5
32. Alffenaar JW, Martson AG, Heysell SK, Cho JG, Patanwala A, et al. 2021. Therapeutic Drug Monitoring in Non-Tuberculosis Mycobacteria Infections. *Clin Pharmacokinet*
33. Strydom N, Gupta SV, Fox WS, Via LE, Bang H, et al. 2019. Tuberculosis drugs' distribution and emergence of resistance in patient's lung lesions: A mechanistic model and tool for regimen and dose optimization. *PLoS Med* 16:e1002773
34. Choi GE, Shin SJ, Won CJ, Min KN, Oh T, et al. 2012. Macrolide treatment for *Mycobacterium abscessus* and *Mycobacterium massiliense* infection and inducible resistance. *Am J Respir Crit Care Med* 186:917-25
35. Richard M, Gutierrez AV, Kremer L. 2020. Dissecting erm(41)-Mediated Macrolide-Inducible Resistance in *Mycobacterium abscessus*. *Antimicrob Agents Chemother* 64
36. Yoshida S, Tsuyuguchi K, Kobayashi T, Inoue Y, Suzuki K. 2021. Comparison of drug-susceptibility patterns and gene sequences associated with clarithromycin and azithromycin resistance in *Mycobacterium abscessus* complex isolates and evaluation of the accumulation of intrinsic macrolide resistance. *J Med Microbiol* 70
37. Greendyke R, Byrd TF. 2008. Differential antibiotic susceptibility of *Mycobacterium abscessus* variants in biofilms and macrophages compared to that of planktonic bacteria. *Antimicrob Agents Chemother* 52:2019-26

38. Lee J, Ammerman N, Agarwal A, Naji M, Li SY, Nuermberger E. 2021. Differential In Vitro Activities of Individual Drugs and Bedaquiline-Rifabutin Combinations against Actively Multiplying and Nutrient-Starved *Mycobacterium abscessus*. *Antimicrob Agents Chemother* 65
39. Yam Y-K, Alvarez N, Go M-L, Dick T. 2020. Extreme Drug Tolerance of *Mycobacterium abscessus* “Persisters”. *Front Microbiol*
40. Obregon-Henao A, Arnett KA, Henao-Tamayo M, Massoudi L, Creissen E, et al. 2015. Susceptibility of *Mycobacterium abscessus* to antimycobacterial drugs in preclinical models. *Antimicrob Agents Chemother* 59:6904-12
41. Ordway D, Henao-Tamayo M, Smith E, Shanley C, Harton M, et al. 2008. Animal model of *Mycobacterium abscessus* lung infection. *J Leukoc Biol* 83:1502-11
42. Riva C, Tortoli E, Cugnata F, Sanvito F, Esposito A, et al. 2020. A New Model of Chronic *Mycobacterium abscessus* Lung Infection in Immunocompetent Mice. *Int J Mol Sci* 21
43. Maggioncalda EC, Story-Roller E, Mylius J, Illei P, Basaraba RJ, Lamichhane G. 2020. A mouse model of pulmonary *Mycobacteroides abscessus* infection. *Sci Rep* 10:3690
44. Prideaux B, Via LE, Zimmerman MD, Eum S, Sarathy J, et al. 2015. The association between sterilizing activity and drug distribution into tuberculosis lesions. *Nat Med* 21:1223-7
45. Tsenova L, Harbacheuski R, Ellison E, Manca C, Kaplan G. 2006. Aerosol Exposure System for Rabbits: Application to *M. Tuberculosis* Infection *Applied Biosafety* 11:7-14
46. Zimmerman M, Blanc L, Chen PY, Dartois V, Prideaux B. 2018. Spatial Quantification of Drugs in Pulmonary Tuberculosis Lesions by Laser Capture Microdissection Liquid Chromatography Mass Spectrometry (LCM-LC/MS). *J. Vis. Exp.* 134: e57402
47. Low JL, Wu ML, Aziz DB, Laleu B, Dick T. 2017. Screening of TB Actives for Activity against Nontuberculous *Mycobacteria* Delivers High Hit Rates. *Front Microbiol* 8:1539

48. Lefebvre AL, Dubee V, Cortes M, Dorchene D, Arthur M, Mainardi JL. 2016. Bactericidal and intracellular activity of beta-lactams against *Mycobacterium abscessus*. *J Antimicrob Chemother* 71:1556-63
49. Yee M, Klinzing D, Wei JR, Gengenbacher M, Rubin EJ, et al. 2017. Draft Genome Sequence of *Mycobacterium avium* 11. *Genome Announc* 5
50. Blanc L, Daudelin IB, Podell BK, Chen PY, Zimmerman M, et al. 2018. High-resolution mapping of fluoroquinolones in TB rabbit lesions reveals specific distribution in immune cell types. *Elife* 7
51. Sarathy JP, Liang HH, Weiner D, Gonzales J, Via LE, Dartois V. 2017. An In Vitro Caseum Binding Assay that Predicts Drug Penetration in Tuberculosis Lesions. *J Vis Exp*
52. Sarathy JP, Zuccotto F, Hsinpin H, Sandberg L, Via LE, et al. 2016. Prediction of Drug Penetration in Tuberculosis Lesions. *ACS Infect Dis* 2:552-63
53. Zhou H. 2003. Pharmacokinetic strategies in deciphering atypical drug absorption profiles. *J Clin Pharmacol* 43:211-27
54. Ernest JP, Sarathy J, Wang N, Kaya F, Zimmerman MD, et al. 2021. Lesion penetration and activity limit the utility of second-line injectable agents in pulmonary tuberculosis. *Antimicrob Agents Chemother*:AAC0050621
55. Rifat D, Prideaux B, Savic RM, Urbanowski ME, Parsons TL, et al. 2017. Using the rabbit cavitary disease model, site-of-disease PK to understand rifamycin trial results for tuberculosis. *Sci Transl Med* in press
56. Abduljalil K, Kinzig M, Bulitta J, Horkovics-Kovats S, Sorgel F, et al. 2009. Modeling the autoinhibition of clarithromycin metabolism during repeated oral administration. *Antimicrob Agents Chemother* 53:2892-901
57. Davey PG. 1991. The pharmacokinetics of clarithromycin and its 14-OH metabolite. *J Hosp Infect* 19 Suppl A:29-37

58. Chen RY, Xiang Yu, Bronwyn Smith, Xin Liu, Jingcai Gao, et al. 2021. Radiological and functional evidence of the bronchial spread of tuberculosis: an observational analysis. *The Lancet Microbe*
59. Wells G, Glasgowlb JN, Nargana K, Lumambaa, Madanseinc KR, et al. 2021. μ CT analysis of the human tuberculous lung reveals remarkable heterogeneity in 3D granuloma morphology. *American Journal of Respiratory and Critical Care Medicine*
60. Je S, Quan H, Na Y, Cho SN, Kim BJ, Seok SH. 2016. An in vitro model of granuloma-like cell aggregates substantiates early host immune responses against *Mycobacterium massiliense* infection. *Biol Open* 5:1118-27
61. Peyron P, Vaubourgeix J, Poquet Y, Levillain F, Botanch C, et al. 2008. Foamy macrophages from tuberculous patients' granulomas constitute a nutrient-rich reservoir for *M. tuberculosis* persistence. *PLoS Pathog* 4:e1000204
62. Prosser G, Brandenburg J, Reiling N, Barry CE, 3rd, Wilkinson RJ, Wilkinson KA. 2017. The bacillary and macrophage response to hypoxia in tuberculosis and the consequences for T cell antigen recognition. *Microbes Infect* 19:177-92
63. Chu S, Wilson DS, Deaton RL, Mackenthun AV, Eason CN, Cavanaugh JH. 1993. Single- and multiple-dose pharmacokinetics of clarithromycin, a new macrolide antimicrobial. *J Clin Pharmacol* 33:719-26
64. Chu SY, Sennello LT, Bunnell ST, Varga LL, Wilson DS, Sonders RC. 1992. Pharmacokinetics of clarithromycin, a new macrolide, after single ascending oral doses. *Antimicrob Agents Chemother* 36:2447-53
65. Chu SY, Wilson DS, Guay DR, Craft C. 1992. Clarithromycin pharmacokinetics in healthy young and elderly volunteers. *J Clin Pharmacol* 32:1045-9
66. Lebel M. 1993. Pharmacokinetic properties of clarithromycin: A comparison with erythromycin and azithromycin. *Can J Infect Dis* 4:148-52

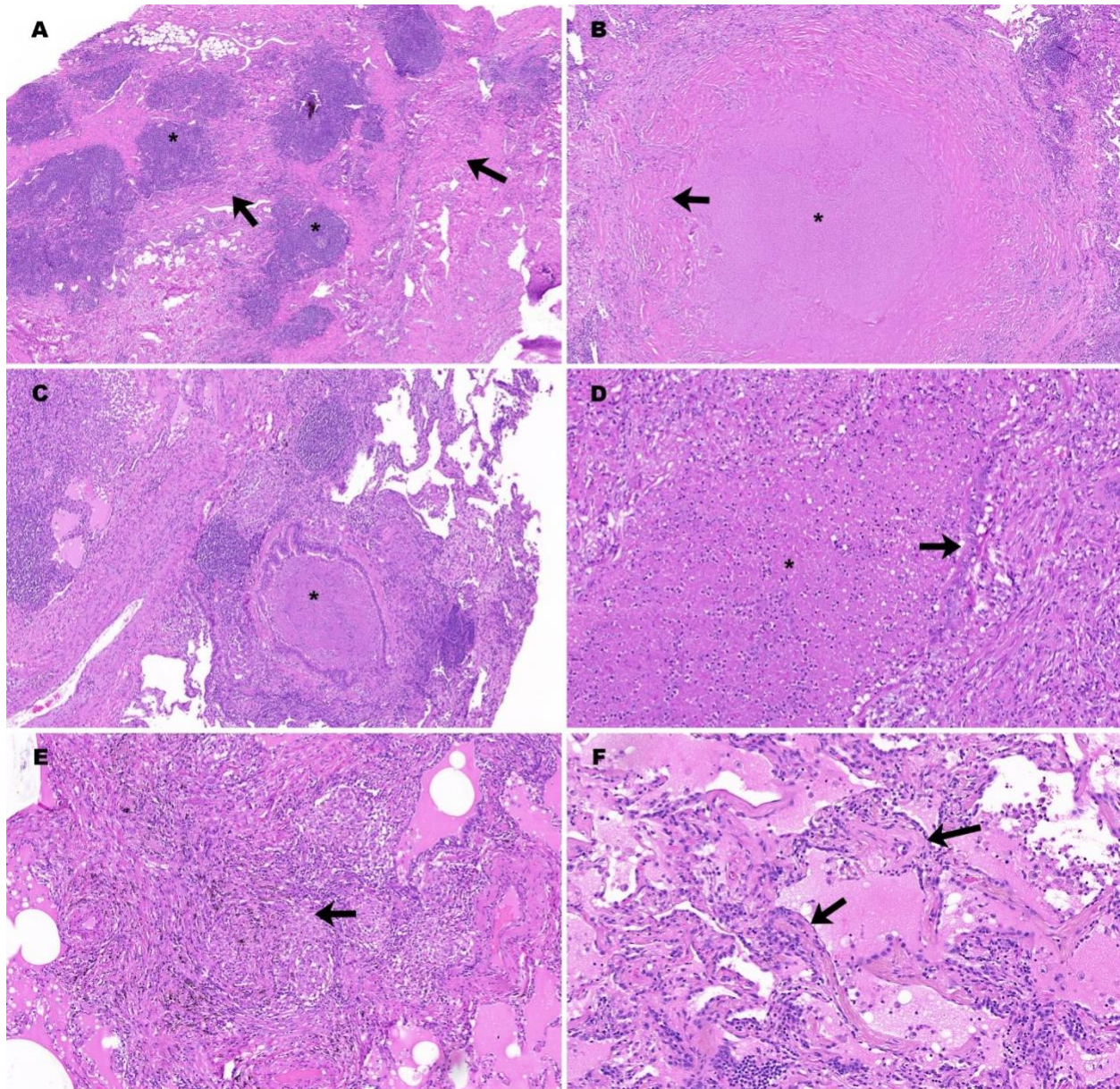
67. Rodvold KA. 1999. Clinical pharmacokinetics of clarithromycin. *Clin Pharmacokinet* 37:385-98
68. Van Bambeke F, Tulkens PM. 2001. Macrolides: pharmacokinetics and pharmacodynamics. *Int J Antimicrob Agents* 18 Suppl 1:S17-23
69. Eyler RF, Shvets K. 2019. Clinical Pharmacology of Antibiotics. *Clin J Am Soc Nephrol* 14:1080-90
70. Jacobs MR. 2001. Optimisation of antimicrobial therapy using pharmacokinetic and pharmacodynamic parameters. *Clin Microbiol Infect* 7:589-96
71. Aziz DB, Low JL, Wu ML, Gengenbacher M, Teo JW, et al. 2017. Rifabutin Is Active Against *Mycobacterium abscessus* Complex. *Antimicrob Agents Chemother*
72. Rodriguez G, Ortegon M, Camargo D, Orozco LC. 1997. Iatrogenic *Mycobacterium abscessus* infection: histopathology of 71 patients. *Br J Dermatol* 137:214-8
73. Smith DA, Rowland M. 2019. Intracellular and Intraorgan Concentrations of Small Molecule Drugs: Theory, Uncertainties in Infectious Diseases and Oncology, and Promise. *Drug Metab Dispos* 47:665-72
74. Molina-Torres CA, Tamez-Pena L, Castro-Garza J, Ocampo-Candiani J, Vera-Cabrera L. 2018. Evaluation of the intracellular activity of drugs against *Mycobacterium abscessus* using a THP-1 macrophage model. *J Microbiol Methods* 148:29-32
75. Kim HY, Sintchenko V, Alffenaar JW. 2019. Nontuberculosis mycobacteria infections: would there be pharmacodynamics without pharmacokinetics? *Eur Respir J* 54
76. Olivier KN, Griffith DE, Eagle G, McGinnis JP, 2nd, Micioni L, et al. 2017. Randomized Trial of Liposomal Amikacin for Inhalation in Nontuberculous Mycobacterial Lung Disease. *Am J Respir Crit Care Med* 195:814-23
77. Waters V, Ratjen F. 2012. Antibiotic treatment for nontuberculous mycobacteria lung infection in people with cystic fibrosis. *Cochrane Database Syst Rev* 12:CD010004

78. Johansen MD, Herrmann JL, Kremer L. 2020. Non-tuberculous mycobacteria and the rise of *Mycobacterium abscessus*. *Nat Rev Microbiol* 18:392-407
79. Wu M-L, Aziz DB, Dartois V, Dick T. 2018. NTM drug discovery: status, gaps and way forward. *Drug Discov Today* in press
80. Bernut A, Herrmann JL, Kissa K, Dubremetz JF, Gaillard JL, et al. 2014. *Mycobacterium abscessus* cording prevents phagocytosis and promotes abscess formation. *Proc Natl Acad Sci U S A* 111:E943-52
81. Malcolm KC, Caceres SM, Pohl K, Poch KR, Bernut A, et al. 2018. Neutrophil killing of *Mycobacterium abscessus* by intra- and extracellular mechanisms. *PLoS One* 13:e0196120
82. Olsen KM, San Pedro G, Gann LP, Gubbins PO, Halinski DM, Campbell GD, Jr. 1996. Intrapulmonary pharmacokinetics of azithromycin in healthy volunteers given five oral doses. *Antimicrob Agents Chemother* 40:2582-5
83. Iskandar I, Walters JD. 2011. Clarithromycin accumulation by phagocytes and its effect on killing of *Aggregatibacter actinomycetemcomitans*. *J Periodontol* 82:497-504
84. Liu P, Allaudeen H, Chandra R, Phillips K, Jungnik A, et al. 2007. Comparative pharmacokinetics of azithromycin in serum and white blood cells of healthy subjects receiving a single-dose extended-release regimen versus a 3-day immediate-release regimen. *Antimicrob Agents Chemother* 51:103-9
85. Fish DN, Gotfried MH, Danziger LH, Rodvold KA. 1994. Penetration of clarithromycin into lung tissues from patients undergoing lung resection. *Antimicrob Agents Chemother* 38:876-8
86. Egbelowo O, Sarathy JP, Gausi K, Zimmerman MD, Wang H, et al. 2021. Pharmacokinetics and Target Attainment of SQ109 in Plasma and Human-Like Tuberculosis Lesions in Rabbits. *Antimicrob Agents Chemother* 65:e0002421

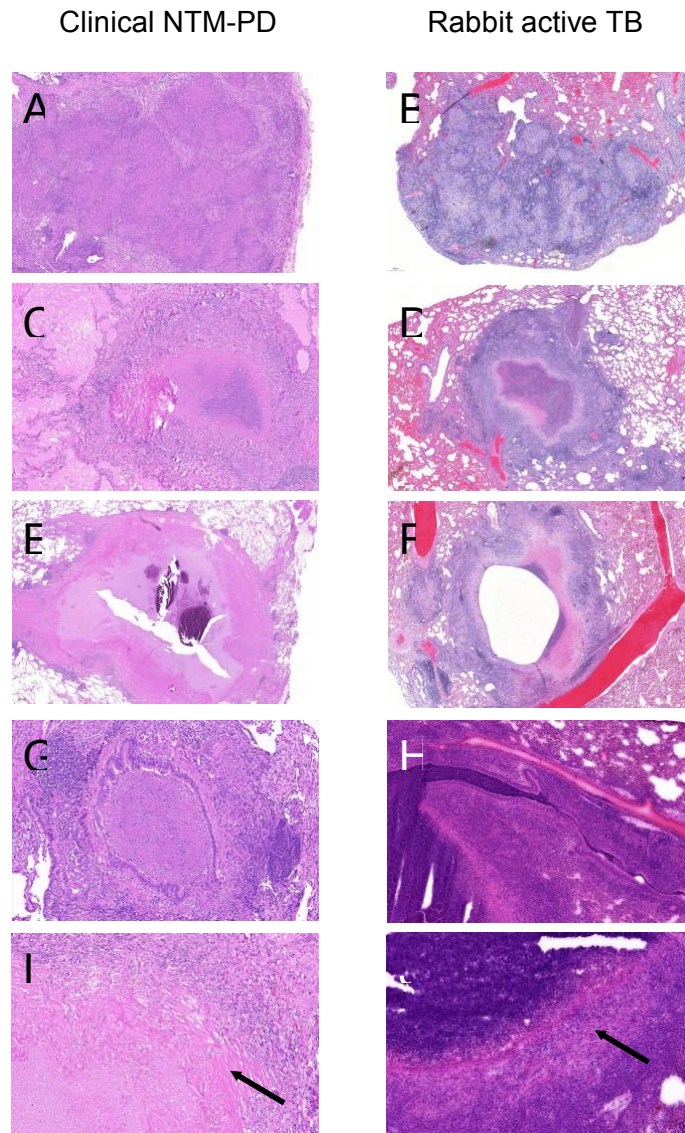
87. Sarathy J, Blanc L, Alvarez-Cabrera N, O'Brien P, Dias-Freedman I, et al. 2019. Fluoroquinolone Efficacy against Tuberculosis Is Driven by Penetration into Lesions and Activity against Resident Bacterial Populations. *Antimicrob Agents Chemother* 63
88. Gengenbacher M, Zimmerman MD, Sarathy JP, Kaya F, Wang H, et al. 2020. Tissue Distribution of Doxycycline in Animal Models of Tuberculosis. *Antimicrob Agents Chemother* 64
89. Steel HC, Theron AJ, Cockeran R, Anderson R, Feldman C. 2012. Pathogen- and host-directed anti-inflammatory activities of macrolide antibiotics. *Mediators Inflamm* 2012:584262
90. Altenburg J, de Graaff CS, van der Werf TS, Boersma WG. 2011. Immunomodulatory effects of macrolide antibiotics - part 1: biological mechanisms. *Respiration* 81:67-74
91. Amsden GW. 2005. Anti-inflammatory effects of macrolides--an underappreciated benefit in the treatment of community-acquired respiratory tract infections and chronic inflammatory pulmonary conditions? *J Antimicrob Chemother* 55:10-21
92. Parra-Ruiz J, Vidaillac C, Rybak MJ. 2012. Macrolides and staphylococcal biofilms. *Rev Esp Quimioter* 25:10-6
93. Carter G, Young LS, Bermudez LE. 2004. A subinhibitory concentration of clarithromycin inhibits *Mycobacterium avium* biofilm formation. *Antimicrob Agents Chemother* 48:4907-10
94. Yasuda H, Ajiki Y, Koga T, Kawada H, Yokota T. 1993. Interaction between biofilms formed by *Pseudomonas aeruginosa* and clarithromycin. *Antimicrob Agents Chemother* 37:1749-55
95. Yasuda H, Ajiki Y, Koga T, Yokota T. 1994. Interaction between clarithromycin and biofilms formed by *Staphylococcus epidermidis*. *Antimicrob Agents Chemother* 38:138-41

96. Takeoka K, Ichimiya T, Yamasaki T, Nasu M. 1998. The in vitro effect of macrolides on the interaction of human polymorphonuclear leukocytes with *Pseudomonas aeruginosa* in biofilm. *Chemotherapy* 44:190-7
97. Ernest J, Strydom N, Wang Q, Zhang N, Nuermberger E, et al. 2020. Development of New Tuberculosis Drugs: Translation to Regimen Composition for Drug-Sensitive and Multidrug-Resistant Tuberculosis. *Annu Rev of Pharmacol Toxicol* 61
98. Brown-Elliott BA, Vasireddy S, Vasireddy R, Iakhiaeva E, Howard ST, et al. 2015. Utility of sequencing the *erm(41)* gene in isolates of *Mycobacterium abscessus* subsp. *abscessus* with low and intermediate clarithromycin MICs. *J Clin Microbiol* 53:1211-5
99. Schon T, Chryssanthou E. 2017. Minimum inhibitory concentration distributions for *Mycobacterium avium* complex-towards evidence-based susceptibility breakpoints. *Int J Infect Dis* 55:122-4
100. Tomioka H, Sato K, Sano C, Sano K, Shimizu T. 2002. Intramacrophage passage of *Mycobacterium tuberculosis* and *M. avium* complex alters the drug susceptibilities of the organisms as determined by intracellular susceptibility testing using macrophages and type II alveolar epithelial cells. *Antimicrob Agents Chemother* 46:519-21
101. McNabe M, Tennant R, Danelishvili L, Young L, Bermudez LE. 2011. *Mycobacterium avium* ssp. *hominissuis* biofilm is composed of distinct phenotypes and influenced by the presence of antimicrobials. *Clin Microbiol Infect* 17:697-703
102. Rose SJ, Babrak LM, Bermudez LE. 2015. *Mycobacterium avium* Possesses Extracellular DNA that Contributes to Biofilm Formation, Structural Integrity, and Tolerance to Antibiotics. *PLoS One* 10:e0128772

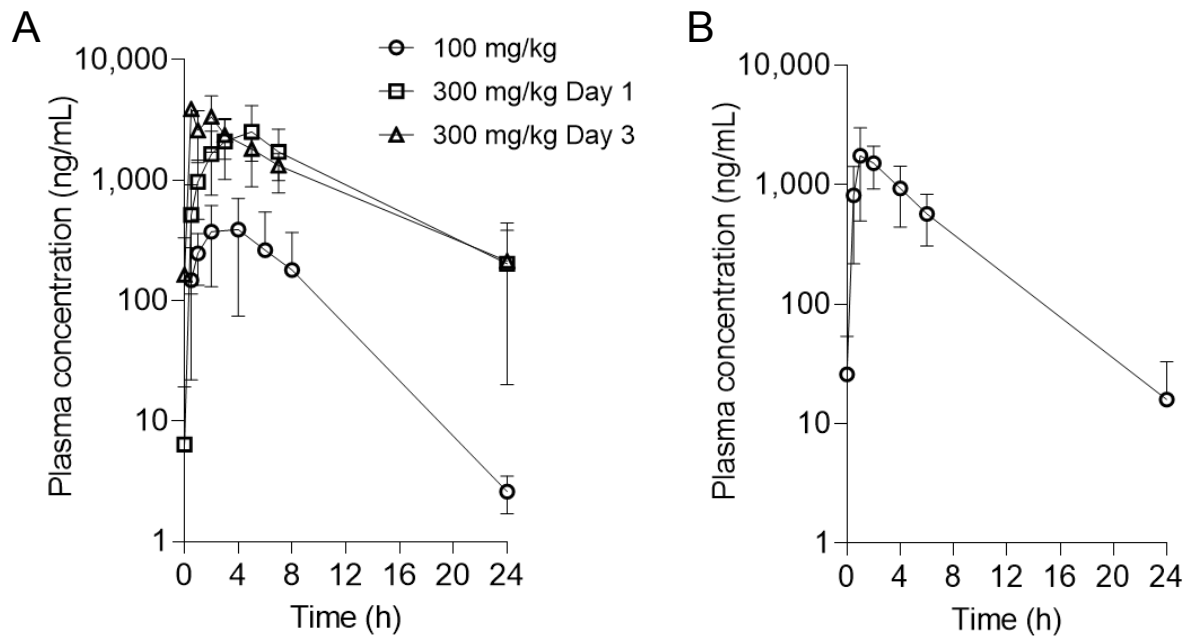
Supplementary Material



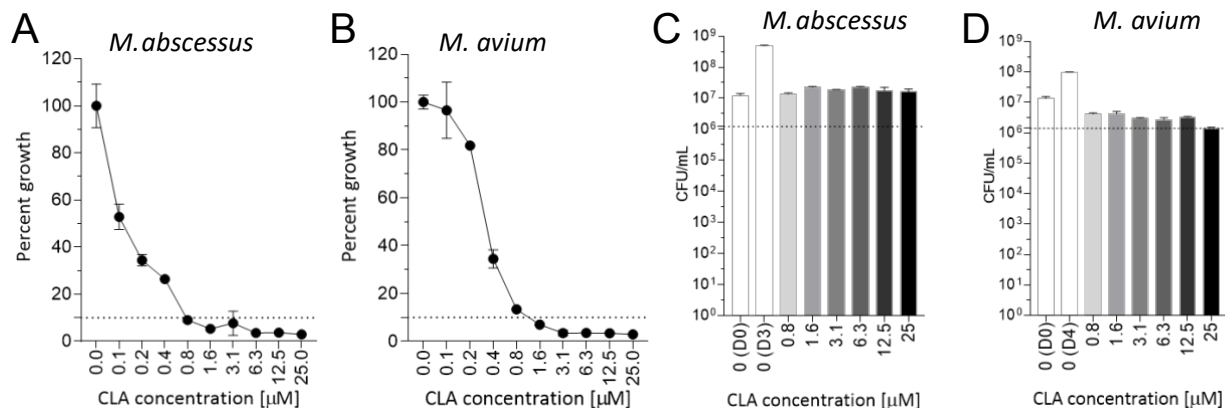
Supplementary Figure 0.1. Histopathological features of chronic NTM infection in human lung. (A) Extensive pulmonary and pleural fibrosis (arrows) with adhesion and numerous secondary lymphoid follicles (*). (B) Chronic fibrosis (arrow) and pauci-inflammatory response surrounding caseous necrosis (*). (C) Caseous debris filling an intact bronchiolar airway, indicative of bronchogenic spread (*). (D) Caseous debris and neutrophils fill an airway (*) with effaced epithelium and fibrosis (arrow). (E) Chronic fibrosis among solid macrophage dominated granulomas (arrows). (F) Chronic interstitial fibrosis with lymphocytic inflammation in alveolar tissue (arrow).



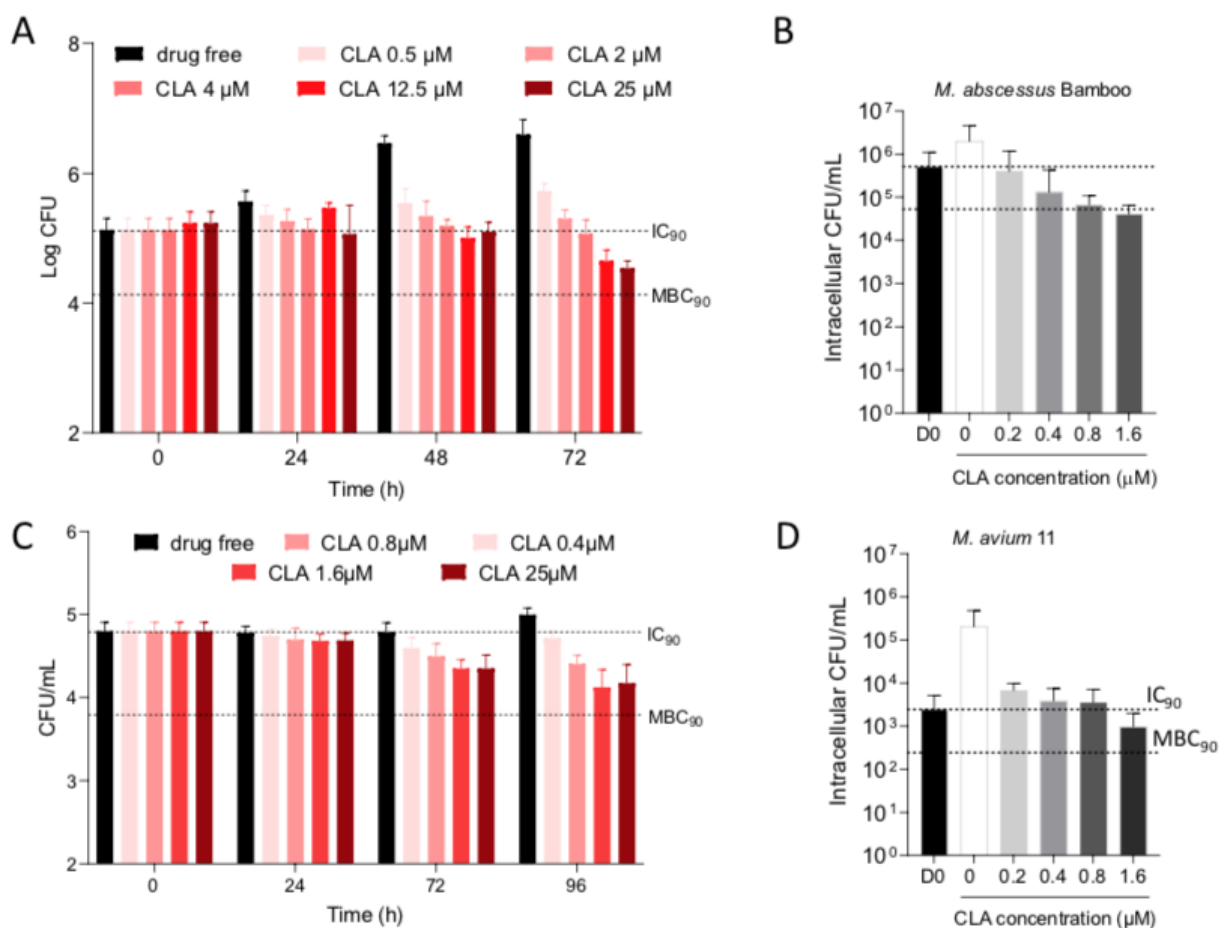
Supplementary Figure 0.2. Common histopathological features seen in human NTM-PD and active rabbit TB, shown side-by side. (A-B) Coalescing non-necrotic granulomas. (C-D) Necrotic granuloma with mixed cellularity seen in caseous foci. (E-F) Cavitating lesion. (G-H) Bronchiole filled with necrotic caseum (G) and cavity caseum oozing into a connected airway (H), both indicative of bronchogenic spread. (I-J) Areas of fibrosis (arrows) surrounding caseous necrosis. Sections shown in panel H and J are from flash-frozen lesions and appear slightly different from all other tissue sections, which are from formalin fixed tissues.



Supplementary Figure 0.3. Plasma pharmacokinetic profile of clarithromycin in rabbits. (A) Plasma concentration time profiles of clarithromycin dosed via the oral route to disease-naïve rabbits as indicated. (B) Plasma concentration time profile of clarithromycin after 3 oral daily doses of 200 mg/kg to TB-infected rabbits. Mean and SD (error bars) are shown (n = 6 rabbits except for the 24 h time point where n = 3).



Supplementary Figure 0.4. Dose-response activity of clarithromycin (CLA) against clinical isolates *M. abscessus* bamboo and *M. avium* 11. (A-B) Growth inhibition curves: mid-log phase cultures ($OD_{600} \sim 0.05$) were exposed to increasing concentrations of CLA for 3 days (*M. abscessus* bamboo) or 4 days (*M. avium* 11) in 96-well flat-bottom Corning Costar microplates in a final volume of 200 μ L. Percentage of growth was calculated relative to cell density in the drug-free culture. The dotted line indicates 90% growth inhibition compared to the untreated control. (C-D) Bactericidal activity: cultures were grown as described in (A-B). At the end of the experiment, 10 μ L were collected from the first clear well onward and plated at different dilutions on 7H10 agar for CFU enumeration. The MBC_{90} is the concentration of CLA that results in a 90% reduction in CFU/ml of the treated culture compared to untreated control at time zero (D0), indicated by the horizontal dotted line. D3 and D4 in (C) and (D) indicate the untreated control at the end of the drug incubation period. Each experiment was performed twice independently. The average and standard deviations of 3 technical replicates of one representative experiment are shown.



Supplementary Figure 0.5. Dose-response activity of clarithromycin (CLA) against intracellular *M. abscessus* bamboo (A-B) and *M. avium* 11 (C-D) in THP-1 derived macrophages. Differentiated THP-1 cells were infected with each strain at a multiplicity of infection of 1:5 for 2 h and treated with clarithromycin as indicated for 3 days (*M. abscessus*) and 4 days (*M. avium*) prior to CFU enumeration on solid medium. Concentrations in excess of 25 mg/mL were not tested due to the immunomodulatory activity of clarithromycin and macrolides in general at higher concentrations. The reported IC₉₀ is the concentration that reduced intracellular growth by 90% compared to untreated controls. Due to the poor intracellular growth of *M. avium* in panel C, the MacIC₉₀ was derived only from the data shown in panel D. The reported MBC₉₀ is the concentration that reduced intracellular Mtb viability by 90% compared to the starting inoculum on Day 0. Each experiment was performed twice independently. The average and standard deviations of 3 technical replicates (4 replicates in panel A) of one representative experiment are shown, except for panel C where both datasets were pooled.

Supplementary Table 0.1. Ratios between area under the concentration time curve (AUC) in tissue or plasma, and the bacteriostatic and bactericidal potency values. The analysis was performed for simulated *M. abscessus* and *M. avium* patients with either average pharmacokinetic exposure or at the lower end (5th percentile) of the drug exposure spectrum. Color coding spans from dark green (top 10th percentile of ratios) to dark red (90th percentile or lower 10th percentile of ratios).

M. abscessus - lower 5th percentile

	macIC ₉₀	MIC ₉₀	ECOFF	Biofilm MIC ₉₀	MBC ₉₀	Mac MBC ₉₀	Biofilm MBC ₉₀
Cellular	33274.0	6654.8	831.9	1512.5	166.4	133.1	44.4
Lung	22146.0	4429.2	553.7	1006.6	110.7	88.6	29.5
Outer caseum	4272.3	854.5	106.8	194.2	21.4	17.1	5.7
Inner caseum	932.7	186.6	23.3	42.4	4.7	3.7	1.2
Plasma	326.1	65.2	8.2	14.8	1.6	1.3	0.4

M. abscessus - median

	macIC ₉₀	MIC ₉₀	ECOFF	Biofilm MIC ₉₀	MBC ₉₀	Mac MBC ₉₀	Biofilm MBC ₉₀
Cellular	61359.9	12272.0	1534.0	2789.1	306.8	245.4	81.8
Lung	40855.8	8171.2	1021.4	1857.1	204.3	163.4	54.5
Outer caseum	7880.3	1576.1	197.0	358.2	39.4	31.5	10.5
Inner caseum	1720.2	344.0	43.0	78.2	8.6	6.9	2.3
Plasma	601.7	120.3	15.0	27.4	3.0	2.4	0.8

M. avium - lower 5th percentile

	macIC ₉₀	MIC ₉₀	ECOFF	Biofilm MIC ₉₀	MBC ₉₀	Mac MBC ₉₀	Biofilm MBC ₉₀
Cellular	16637.0	6654.8	1663.7	1663.7	166.4	166.4	166.4
Lung	11073.0	4429.2	1107.3	1107.3	110.7	110.7	110.7
Outer caseum	2136.1	854.5	213.6	213.6	21.4	21.4	21.4
Inner caseum	466.4	186.6	46.6	46.6	4.7	4.7	4.7
Plasma	163.1	65.2	16.3	16.3	1.6	1.6	1.6

M. avium - median

	macIC ₉₀	MIC ₉₀	ECOFF	Biofilm MIC ₉₀	MBC ₉₀	Mac MBC ₉₀	Biofilm MBC ₉₀
Cellular	30679.9	12272.0	3068.0	3068.0	306.8	306.8	306.8
Lung	20427.9	8171.2	2042.8	2042.8	204.3	204.3	204.3
Outer caseum	3940.2	1576.1	394.0	394.0	39.4	39.4	39.4
Inner caseum	860.1	344.0	86.0	86.0	8.6	8.6	8.6
Plasma	300.9	120.3	30.1	30.1	3.0	3.0	3.0

Chapter 4: Spatially and temporally resolved diffusion kinetics of bedaquiline and TBAJ-587 in hard-to-treat sites of tuberculosis disease

Abstract

In treatment of tuberculosis, patients with cavitation are considered among the hardest to treat. Diarylquinolines – bedaquiline (BDQ) and TBAJ-587 – are leading candidates for Phase II trials in drug-susceptible and multidrug-resistant TB. While they are lipophilic and predicted to penetrate hard-to-treat cavities, their small free fraction in caseum contributes to slow passive diffusion to the center of avascular caseum. In this work, we characterized the rate of diffusion into granulomas of TB-infected rabbits as a function of distance from the cellular rim and time from treatment initiation using a novel quantification method – laser capture microdissection – and multicompartment site-of-action modeling. The approach allowed, for the first time, micrometer resolution of the concentration gradients exhibited at the site of TB disease. Simulations revealed that BDQ and TBAJ-587 achieve therapeutic concentrations in patients up to 1,000 micrometers toward the lesion center. TBAJ-587 has effective concentration without extended residence time after treatment which may reduce the risk of resistance development compared to BDQ. The novel drug quantification method and novel spatiotemporal PK modeling offers a tool to assess drug penetration in hard-to-reach sites of disease, to select promising regimens, and to predict Phase 3 trial success.

Introduction

Cavitation is a risk factor for relapse and unfavorable outcome in the treatment of tuberculosis (TB) (1). Cavities and caseous lesions harbor slow, non-replicating bacteria that are extremely drug tolerant (2). Because these regions are largely avascular, drugs that are lipophilic and capable of passive diffusion through caseum are needed to reach bacteria at concentrations high enough to be therapeutic. At the same time, sufficient drug clearance is needed to avoid long windows of monotherapy that lead to resistance.

Bedaquiline (BDQ) is the first in a new class of drugs known as diarylquinolines. Conditionally approved in 2012, BDQ was recently approved in combination with pretomanid and linezolid for short-course six-month treatment of highly drug-resistant tuberculosis (3). BDQ is currently the backbone of most clinical trials in multidrug resistant- and drug susceptible-TB. TBAJ-587 is a next-generation diarylquinoline currently in Phase 1 of clinical development (ClinicalTrials.gov identifier NCT04890535). TBAJ-587 is more potent than BDQ in mice and may offer a wider therapeutic window than BDQ (4). Because bacterial loads are higher in caseum and found within all depths of large caseous lesions, whether and how quickly drugs penetrate these areas is needed to predict treatment duration and evaluate potential for resistance. Both BDQ and TBAJ-587 are active against bacteria in caseum, however their penetration kinetics into large caseous lesions is unknown.

Here, laser capture microdissection (LCM) was used to dissect caseous lesions into concentric sections (Figure 4.1). We performed a fully quantitative investigation of the spatial drug gradients from the cellular rim to the center of caseum for BDQ, TBAJ-587, and their active metabolites (BDQ-M2 and TBAJ-587-M3). We developed a multicompartment site-of-action model and performed simulations to determine lesion temporal and spatial coverage and drug residence after the end of treatment. Both BDQ and TBAJ-587 achieve therapeutic concentrations. While BDQ penetrates further into caseous center than TBAJ-587, TBAJ-587

clears quicker than BDQ. Our results indicate that TBAJ-587 has effective concentration without extended residence time after treatment that can lead to development of resistance relative to BDQ.

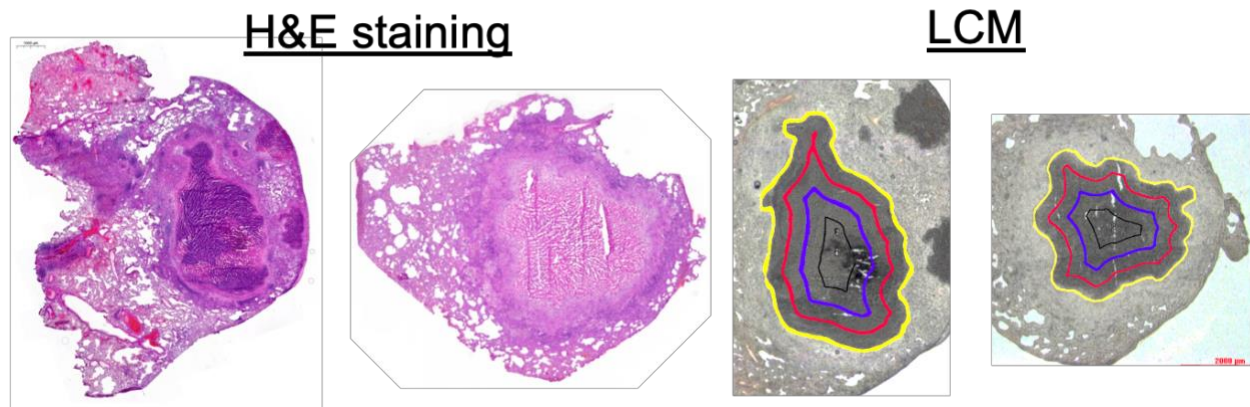


Figure 0.1. Representative images of caseous lesions from TB-infected rabbits. Hematoxylin and eosin (H&E) staining (left) used to guide dissection using laser capture microdissection (LCM, right). Colored borders represent outline of dissections.

Methods

Two studies were investigated in TB-infected rabbits: 1.) a loading-dose study to rapidly reach steady state concentrations: 400 mg and 300 mg for BDQ and TBAJ-587, respectively, dosed for three days, 2.) a long duration study to capture the rate of equilibration: 80 mg dosed for 1, 17, 26, 28 days for BDQ and 30 mg for 14 and 28 days for TBAJ-587. BDQ, BDQ-M2, TBAJ-587, and TBAJ-587-M3 were quantified. For caseum samples, the average distance from the caseum border in micrometers (μm) was calculated by creating a caseum 'mask' and processing it using the Exact Euclidean Distance Transform plugin of the ImageJ software.

The modeling analysis was performed in NONMEM 7.4.2. A site-of-action model was developed where a rate (k_{lesion}) and extent of partitioning (PC_{lesion}) were estimated (Eq. 4.1 and Figure 4.2) (5).

$$\frac{dC_{\text{lesion}}}{dt} = k_{\text{lesion}} \times (PC_{\text{lesion}} \times C_{\text{plasma}} - C_{\text{lesion}}) \quad \text{Eq. 4.1}$$

Distance from the cellular rim was tested as a covariate on PC_{lesion} and k_{lesion} . Multiple covariate relationships were tested including linear, loglinear, power, sigmoidal E_{max} , and inverse relationship. To predict patient lesion coverage, the lesion parameters were linked to a clinical PK model for BDQ (6) and allometric scaled for TBAJ-587. Simulations were compared to potency metrics in an ex vivo caseum assay (casMBC₉₀, minimum concentration to kill 90% bacteria) (2). Lesion coverage ($PK > \text{casMBC}_{90}$) as a function of distance was quantified.

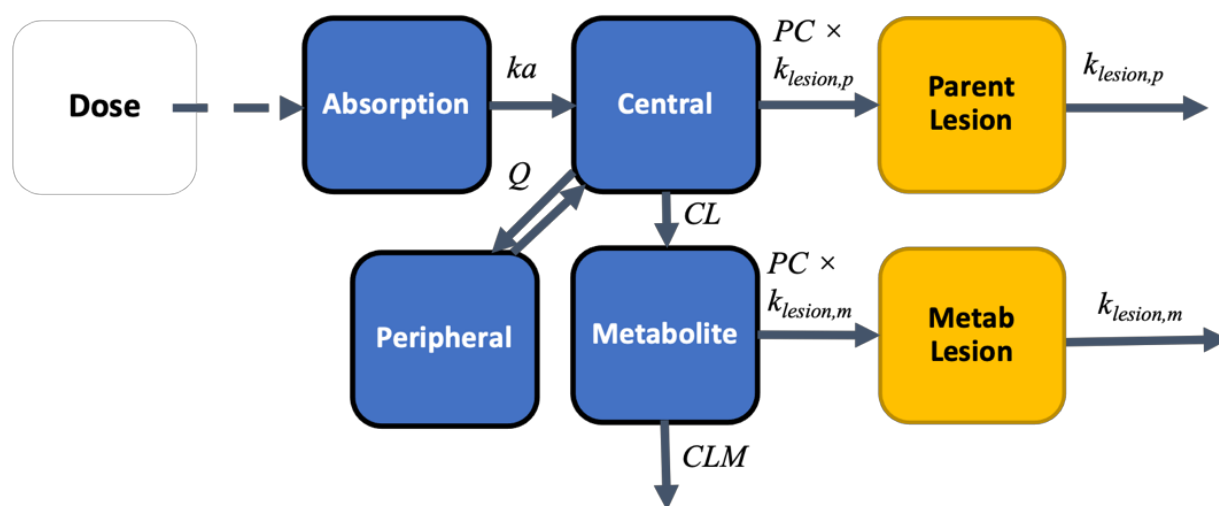


Figure 0.2. Model structure of parent-metabolite plasma-lesion multicompartment model.

Results

Overall, fifty five rabbits contributed 464 measurements from plasma and 140 from lesion for BDQ and BDQ-M2. Thirty five rabbits contributed 544 measurements from plasma and 155 from lesion for TBAJ-587 and TBAJ-587-M3 (Figure 4.3). Plasma PK were described by an oral two-compartment distribution model. The final model included a distance covariate on the partition coefficient described in Equation 4.2. Final model parameter estimates can be found in Table 4.1.

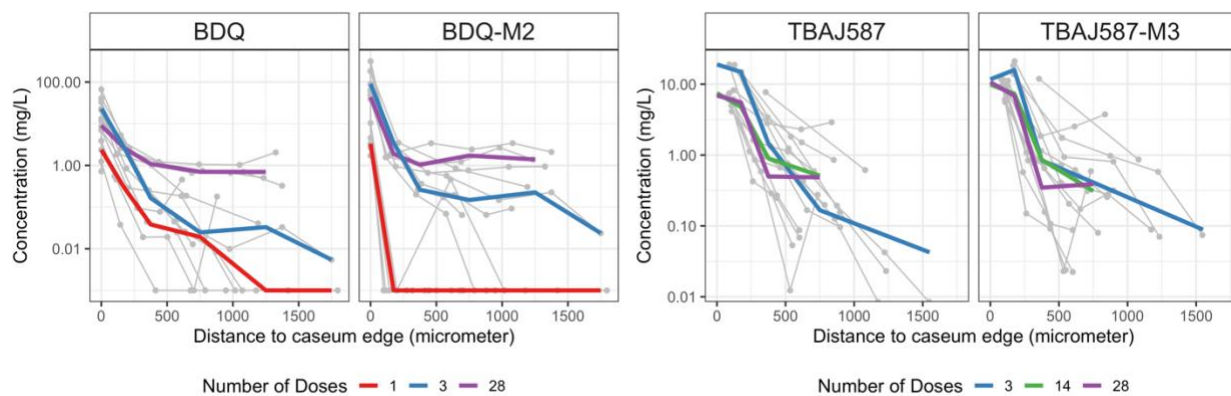


Figure 0.3. Spatial data available for BDQ, TBAJ-587, and their metabolites.

$$PC = \frac{\exp(MAX_{PC})}{DIST^{HILL}} \quad \text{Eq. 4.2}$$

Table 0.1. Final model parameter estimates.

Parameter	BDQ Value (RSE%)	TBAJ-587 Value (RSE%)
k_a (h^{-1})*	0.4106 (17.5)	0.2701 (25.2)
CL (L/h)	11.19 (9.8)	5.56 (17.9)
V (L)	257.3 (20.6)	68.95 (39.7)
Q (L/h)	26.03 (62.2)	28.77 (29.5)
V2 (L)	301.5 (34.3)	365.2 (20.9)
CL _m (L/h)	27.22 (10.6)	12.39 (14.6)
IIV F1 (%CV)	31.81 (25.2)	63.6 (27.1)
IIV V (%CV)	57.18 (16.0)	-
Prop.Err,p (%CV)	27.59 (7.8)	25.7 (12.0)
Prop.Err,m (%CV)	0.038 (15.8)	17.6 (19.0)
$K_{lesion,p}$ (h^{-1})	0.000394 (167)	0.007601 (22.9)
MAX _{PC,p}	7.022 (26.0)	12.61 (5.5)
HILL _p	0.8002 (10.3)	1.852 (7.7)
Prop.Err,p (%CV)	2.67 (39.2)	40.75 (39.0)
Add.Err,p (mg/L)	1.761 (13.6)	0.2726 (54.9)
$K_{lesion,m}$ (h^{-1})	0.002009 (110)	0.02106 (31.6)
MAX _{PC,m}	7.373 (14.9)	12.69 (6.6)
HILL _m	0.774 (9.8)	1.845 (8.4)
Prop.Err,m (%CV)	22.69 (77.9)	23.3 (38.1)
Add.Err,m (mg/L)	1.268 (17.4)	0.7374 (43.2)

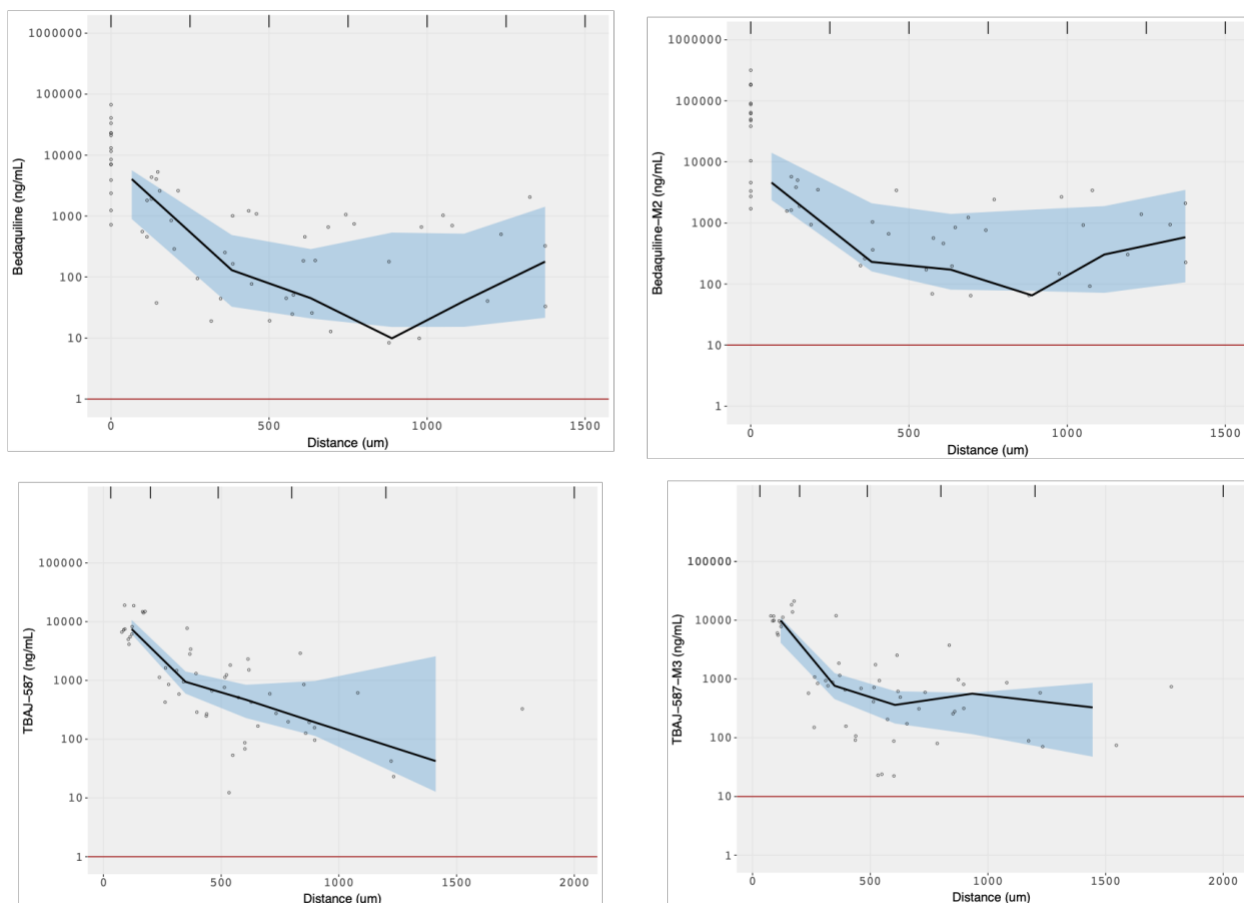


Figure 0.4. Visual predictive check of BDQ and TBAJ-587 spatial model.

Five hundred simulations of final models with observed data. Observed data represented as points with median (black, solid line). Simulated data represented as the 95% confidence interval of the median (blue shaded area). Lower limit of quantification represented as the red solid line.

BDQ concentrations in caseum were greatest near the edge of the rim. As dosing continued, the gradient flattened across the distance. The inverse covariate on distance best described the relationship and was used for simulations. For BDQ standard regimen, caseum concentrations were above the casMBC_{90} after 2 weeks of dosing at the caseum edge ($< 300 \mu\text{m}$). At the end of treatment, coverage was achieved at distances up to $1800 \mu\text{m}$ from the cellular rim. BDQ is predicted to remain in caseum for over two years after treatment end. BDQ-M2 had a slightly faster rate of penetration but a lower extent.

Steeper gradients were observed for TBAJ-587 than for BDQ yet was more potent in the caseum assay. Simulations of 400 mg QD produced TBAJ-587 concentrations above casMBC_{90}

as far as 600 μm . TBAJ-587-M3 metabolite present at effective concentrations up to 300 μm .

The concentration remained over the casMBC_{90} in caseum edges ($< 300 \mu\text{m}$) for about 3 weeks post-treatment and over the limit of quantification (1 ng/mL) for 7 weeks post-treatment.

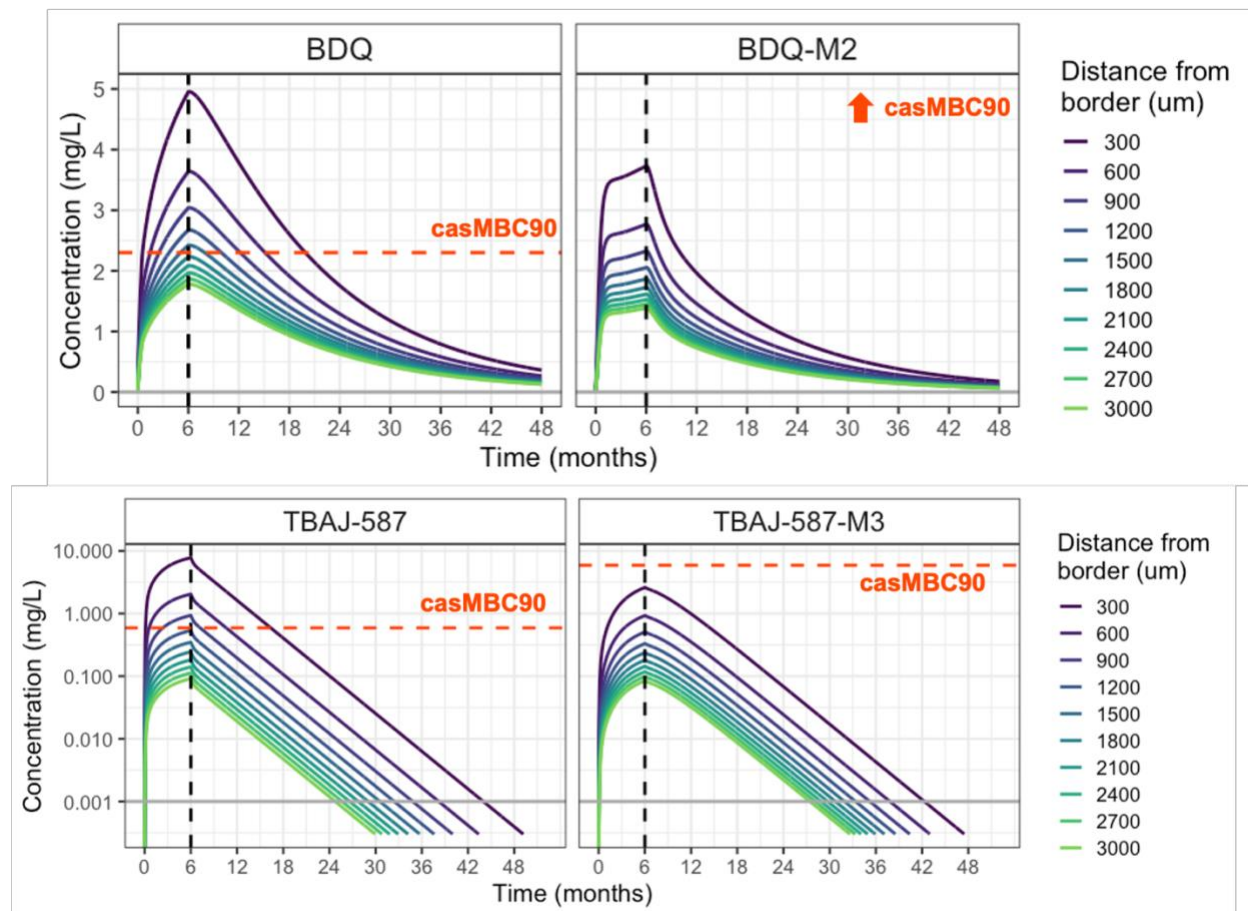
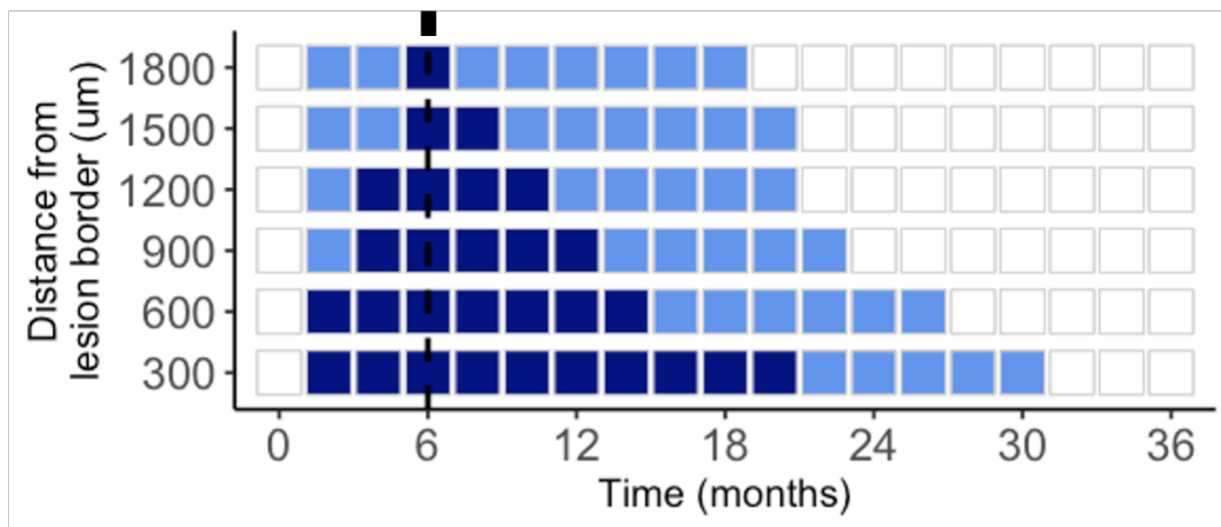


Figure 0.5. Clinical simulations at varying depths into lesions.

BDQ was dosed at 400 mg daily for 2 weeks and 200 mg thrice weekly for a total of 6 months (black dashed line). TBAJ-587 was dosed daily at 400 mg for 6 months. Both drugs never achieve steady state in caseum, however both achieve therapeutic concentrations with peak accumulation at the end of treatment. Drugs are above lower limit of quantification (LLOQ) for years after treatment. Red dashed line is the caseum MBC_{90} derived from the ex vivo caseum assay. Solid grey line is the LLOQ.

Bedaquiline



TBAJ-587

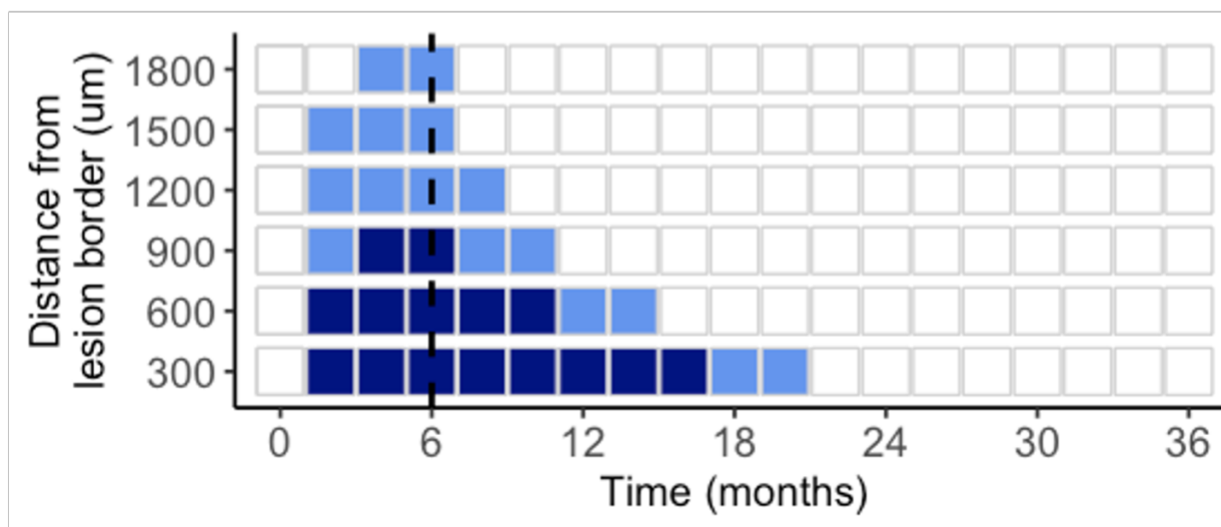


Figure 0.6. Predicted clinical lesion coverage.

Clinical lesion coverage (defined as PK greater than casMBC₉₀ (dark blue)) was predicted to depths of 1800 μm for BDQ and 900 μm for TBAJ-587. At a lower threshold of coverage (defined as PK greater than casMBC₅₀ (light blue)), BDQ was predicted to cover the outer most ring (< 300 μm) for up to 30 months after start of treatment and TBAJ-587 up to 19 months after start of treatment.

Discussion

In this study, a spatially resolved PK model that captures the movement of drug from plasma to centers of necrotic cores in hard-to-treat TB lesions was developed. BDQ penetrates to a greater extent compared to TBAJ-587. However, it is currently unknown the target depth of penetration that is linked to clinical outcome or what sites – the cellular rim or the center – are most important. Positron emission tomography and computerized tomography (PET-CT) imaging in patients such as those being performed in the ongoing PredictTB trial (ClinicalTrials.gov identifier NCT02821832) can better determine areas that are most vulnerable to relapse.

BDQ is predicted to exhibit sustained drug residence time in caseum beyond 2 years after end of treatment, which creates prolonged periods of monotherapy that may trigger resistance development. TBAJ-587 has effective concentration without extended residence time after treatment which may reduce the risk of resistance development compared to BDQ. However, whether its elimination is sufficiently fast enough to alleviate selective pressure causing resistance mutations is unknown. The novel drug quantification method and novel spatiotemporal PK modeling offers a tool to assess drug penetration in hard-to-reach sites of disease, to select promising regimens, and to predict Phase 3 trial success.

References

1. Imperial MZ, Nahid P, Phillips PPJ, Davies GR, Fielding K, et al. 2018. A patient-level pooled analysis of treatment-shortening regimens for drug-susceptible pulmonary tuberculosis. *Nat Med* 24:1708-15
2. Sarathy JP, Via LE, Weiner D, Blanc L, Boshoff H, et al. 2018. Extreme Drug Tolerance of *Mycobacterium tuberculosis* in Caseum. *Antimicrob Agents Chemother* 62
3. Conradie F, Diacon AH, Ngubane N, Howell P, Everitt D, et al. 2020. Treatment of Highly Drug-Resistant Pulmonary Tuberculosis. *The New England journal of medicine* 382:893-902
4. Xu J, Converse PJ, Upton AM, Mdluli K, Fotouhi N, Nuernberger EL. 2021. Comparative Efficacy of the Novel Diarylquinoline TBAJ-587 and Bedaquiline against a Resistant Rv0678 Mutant in a Mouse Model of Tuberculosis. *Antimicrob Agents Chemother* 65
5. Kjellsson MC, Via LE, Goh A, Weiner D, Low KM, et al. 2012. Pharmacokinetic evaluation of the penetration of antituberculosis agents in rabbit pulmonary lesions. *Antimicrob Agents Chemother* 56:446-57
6. Svensson EM, Dosne AG, Karlsson MO. 2016. Population Pharmacokinetics of Bedaquiline and Metabolite M2 in Patients With Drug-Resistant Tuberculosis: The Effect of Time-Varying Weight and Albumin. *CPT Pharmacometrics Syst Pharmacol* 5:682-91

Chapter 5: Translational predictions of phase 2a first-in-patient efficacy studies for bedaquiline and rifapentine

Abstract

A clinical early bactericidal activity (EBA) study of tuberculosis (TB) drugs is the first study in patients to evaluate the efficacy of novel anti-TB drugs, using the decrease of colony-forming units (CFU) counts of *Mycobacterium tuberculosis* in sputum samples for up to 14 days of treatment. We hypothesized that results from EBA trials can be reliably predicted from the preclinical in vivo mouse data using a model-based translational pharmacology approach. Rifapentine and bedaquiline were the focus of this analysis, however the compilation of the entire compiled database includes preclinical and clinical pharmacokinetics (PK) and longitudinal pharmacodynamics (PD) data for nine established anti-TB compounds (bedaquiline, delamanid, isoniazid, linezolid, moxifloxacin, pretomanid, pyrazinamide, rifampin and rifapentine). With these data, preclinical PK and PKPD models were developed, which included quantification of bacterial replication and kill, host immune effect, and quantification of in vivo PKPD relationships for each drug. Translational prediction of clinical EBA studies was performed using clinical PK models, estimated mouse PKPD relationships, and species-specific protein binding. Predicted daily decreases of CFU in the first 2 days of treatment and between day 2 and day 14 were consistent with clinical observations. This platform provides an innovative solution to inform and/or partially replace Phase 2a EBA trials, to bridge the gap between mouse efficacy studies and Phase 2b and Phase 3 trials, and to substantially accelerate drug development.

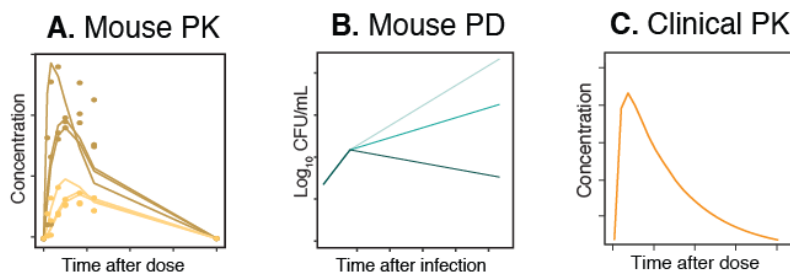
Introduction

Mycobacterium tuberculosis remains one of the deadliest infectious agents globally. Tuberculosis (TB) drug discovery and development activity has increased emphasis on shorter, more universal regimens to treat all TB cases independent of resistance status (1; 2). However, with an increasing number of new drugs and limited resources for clinical trials, further innovation of drug development is imperative to identify effective drugs and regimens with higher confidence (3). The mouse model has been used for over 50 years and efficacy in mice is regarded as the nonclinical model with highest predictive value (3; 4). Traditional translation of findings from mice includes matching a dose in humans that matches efficacious drug exposure in mice. However, given the different bacterial dynamics and host immune responses to infection, these methods are insufficient. Mechanistic mouse-to-human pharmacokinetic-pharmacodynamic (PKPD) models that describe the bacterial kill and PKPD relationships are better at predicting clinical results, including the results of late-stage trials (5-7).

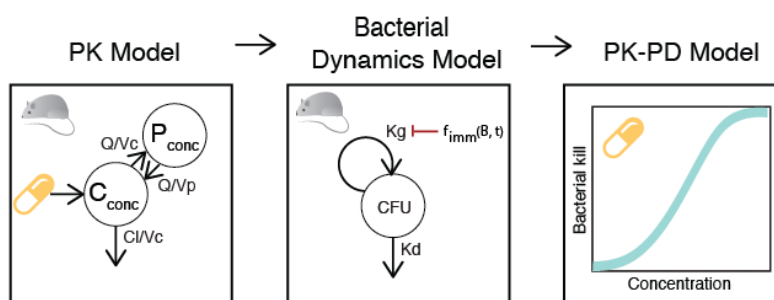
A Phase 2a early bactericidal activity (EBA) study is the first clinical evaluation of novel anti-TB drug efficacy in TB patients with the primary purpose of detecting the presence and magnitude of EBA and informing possible dose-response relationships (8). We hypothesized that using the wealth of PK and PD data available in mice and model-based methods, we could reliably predict results of EBA trials (Figure 5.1). Here, we compiled a comprehensive preclinical and clinical database of PK, PD, and baseline bacterial growth for nine compounds. The drugs used to develop our proposed platform were rifampin (RIF), isoniazid (INH), PZA, rifapentine (RPT), bedaquiline (BDQ), delamanid (DLM), pretomanid (PMD), moxifloxacin (MXF) and linezolid (LZD). The work presented in this dissertation focuses on two of the nine drugs, BDQ and RPT. We establish a relevant and robust model-based translational platform that can reliably link nonclinical to clinical drug development and predict early efficacy trials for anti-TB drugs across different compound classes.

The translational platform in the present study intends to increase the accuracy of preclinical to clinical translation by enabling quantitative prediction of clinical studies from preclinical outputs and serves as a foundation for model-informed TB drug discovery and development.

1.) Compile data. Collect dose-ranging preclinical data and clinical (if available) or scaled PK



2.) Build model. Estimate translatable efficacy parameters from preclinical data



3.) Predict clinical EBA. Simulate clinical PK and predict clinical CFU decline

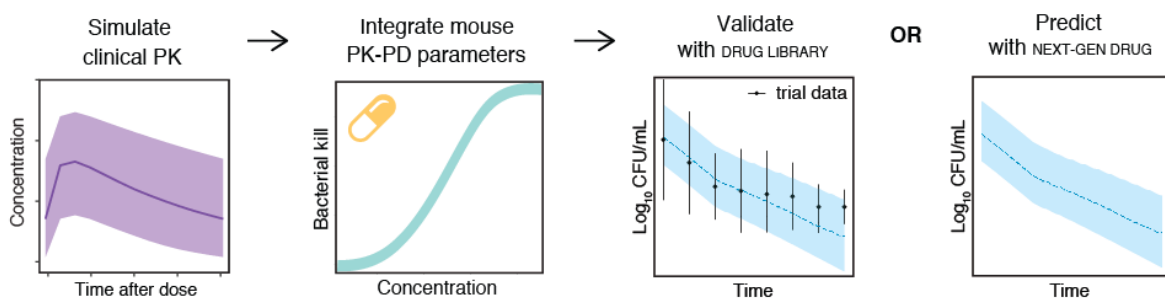


Figure 0.1. The translational pharmacology approach to predicting early bactericidal efficacy in patients.

Components necessary for translation include mouse PK-PD and clinical PK (actual or scaled). The estimated relationship between concentration and bactericidal kill is assumed to be portable after correction for protein binding and integrated with clinical PK. Using baseline bacterial burden from previous EBA trials as initial conditions, the early bactericidal efficacy is simulated with the translational model.

Methods

Drug dataset for model building and validation

Mouse experiments in the BALB/c mouse model using H37rv strain of TB were performed at Johns Hopkins University. Mouse PK, mouse PD, human population PK models and human clinical EBA data were collected. The data available are shown in Table 5.1 and Figure 5.2. Clinical PK data were simulated using published human population PK models (9; 10). CFU counts in sputum samples were collected or digitized from published clinical studies (11-13).

Table 0.1. Mouse PKPD data available for bedaquiline and rifapentine.

Mouse PK		
PK data	BDQ	RPT
Observations	90	69
Doses (mg/kg)	12.5, 25, single dose	5, 10, 20, daily for 16 days
Protein binding (f_u, Human/Mouse)	1.0*	0.422**
Mouse PD		
PD data	BDQ	RPT
Observations	75	55
Doses (mg/kg)	12.5, 25, 50	5, 10
Treatment duration (days)	70	56

*Reference 9

**Reference 15

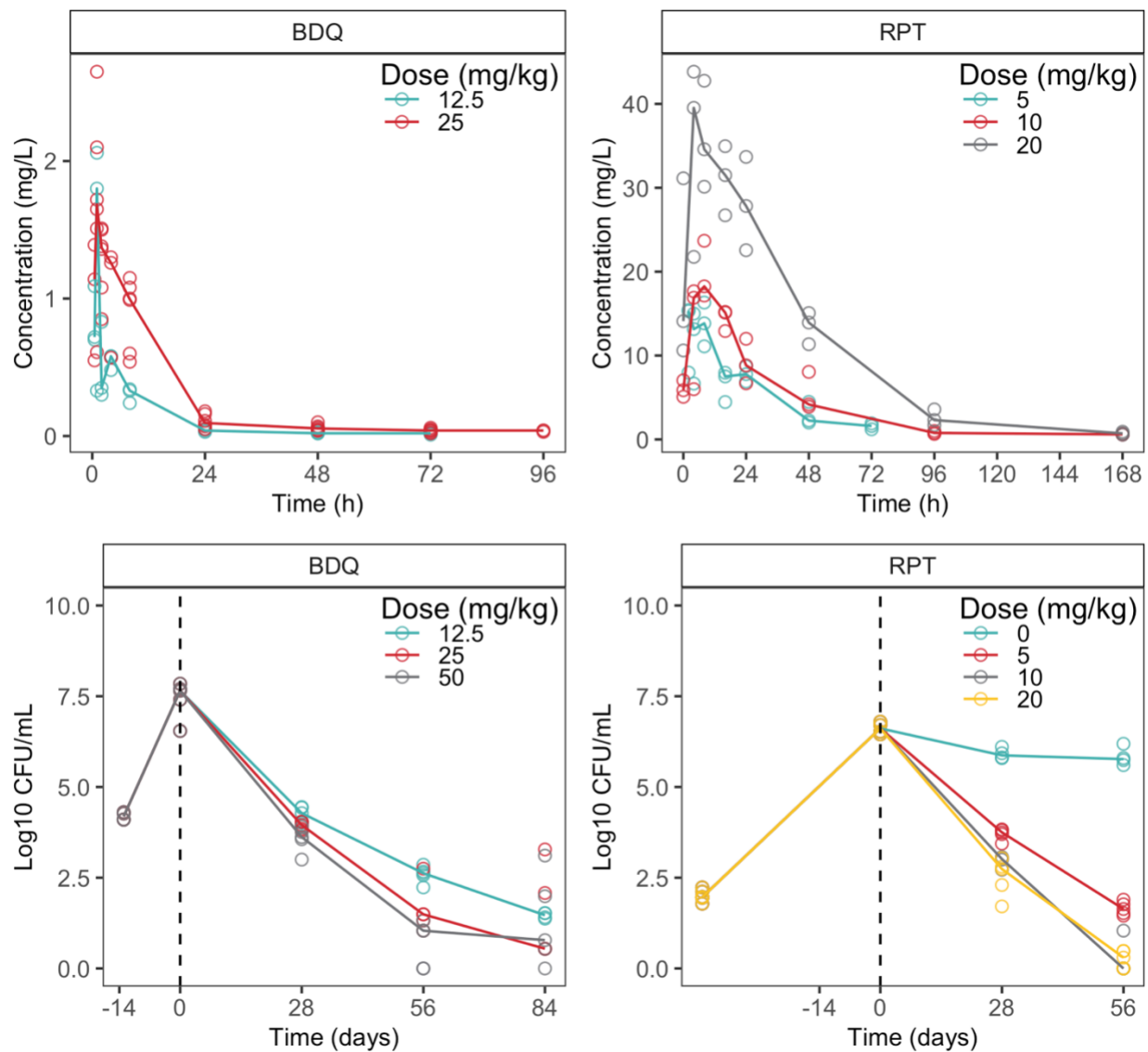


Figure 0.2. Mouse pharmacokinetic and pharmacodynamic data available for rifapentine and bedaquiline.

Table 0.2. Published population PK models and EBA trial information.

Drugs	PK Structure Model	Doses	References
BDQ	3-cmt model with transit absorption	400 mg p.o. daily for 14 days and 200 mg p.o. three times per week for 24 weeks	(9)
RPT	1-cmt PK model (saturable bioavailability, transit absorption and auto-induction)	300, 450, 600, 750, 900, 1050, 1200, 1350, 1500, 1650, 1800 mg once weekly up to twice daily for up to four months	(10)
Drugs	EBA trial doses	Baseline (log₁₀ CFU/mL)	References
BDQ	100, 200, 300 and 400 mg (with 200, 400, 500, 700 mg loading dose on first day and 100, 300, 400, 500 mg on second day, respectively)	6.302 (100 mg), 6.001 (200 mg), 6.071 (300 mg), 6.625 (400 mg)	(12)
BDQ	25, 100, 400 mg	6.66 (25 mg), 6.32 (100 mg), 6.82 (400 mg)	(13)
RPT	300, 600, 900, 1200 mg	N/A	(11)

Mouse PKPD model development

An integrated mouse PKPD model was developed for each drug. PK data was described using one or two compartment models with first order absorption with or without delay, and saturable elimination when necessary. Additive, proportional, and combination residual error models were tested to describe the error in the observed data. The bacterial growth dynamics without treatment was described using our previously published baseline model (Equation 5.1) (14). The baseline model captures the time- and bacteria-dependent immune control of bacterial growth rate over time. Drug effect was driven by plasma concentration and added as a separate term, EFF (Equation 5.2). PKPD relationships for drug effect were optimized by fitting the mouse PD data to linear, nonlinear, log linear, E_{max} and sigmoidal functions (Equation 5.3). A delay effect was tested to optimize the relationship between plasma exposures, time, and treatment response (Equation 5.4). In this case, drug effect was driven by A_{delay} . An additive error model was used to describe residual error for the mouse PKPD models.

$$\frac{dB}{dt} = K_g \times B \times \left(1 - \frac{K_B \times B^{\gamma_B}}{B_{50}^{\gamma_B} + B^{\gamma_B}}\right) \times \left(1 - \frac{K_T \times t^{\gamma_T}}{T_{50}^{\gamma_T} + t^{\gamma_T}}\right) - K_d \times B \quad Eq. 5.1$$

$$\frac{dB}{dt} = K_g \times B \times \left(1 - \frac{K_B \times B^{\gamma_B}}{B_{50}^{\gamma_B} + B^{\gamma_B}}\right) \times \left(1 - \frac{K_T \times t^{\gamma_T}}{T_{50}^{\gamma_T} + t^{\gamma_T}}\right) - K_d \times B - EFF \times B \quad Eq. 5.2$$

B : bacterial number

t : incubation time since inoculation

K_g : bacterial growth rate

K_d : bacterial natural death rate

K_B : bacterial number-dependent maximal adaptive immune effect

B_{50} : bacterial number that results in half of K_B

γ_B : steepness of bacterial number-dependent immune effect relationship

K_T : incubation time-dependent maximal adaptive immune effect

T_{50} : bacterial number that results half of K_T

γ_T : steepness of time-dependent immune effect relationship

EFF : bacterial killing rate

$$EFF = \frac{A_{delay}^\gamma \times E_{max}}{EC_{50}^\gamma + A_{delay}^\gamma} \quad Eq. 5.3$$

E_{max} : the maximal level of drug effect

EC_{50} : the delayed concentration that results in half of the maximal drug effect

γ : the steepness of the relationship between the delayed plasma concentration and drug effect

$$\frac{dA_{delay}}{dt} = K_{delay} \times \left(\frac{A_2}{V_1} - A_{delay} \right) \quad Eq. 5.4$$

A_{delay} : the delayed concentration level associated with drug effect

K_{delay} : the rate constant of delay between plasma concentration and drug effect

Prediction of the outcomes for clinical EBA studies

The PKPD relationship quantified in mice was used to predict the clinical EBA. Drug concentration in humans were simulated based on clinical population pharmacokinetic models (Table 5.2) to drive the concentration-effect relationship in the clinical predictions. Protein binding ratios between humans and mice ($f_{u_{mice}}^{humans}$) were used to convert unbound plasma drug concentrations from human to mouse to translate the mouse PKPD relationships (Table 5.1) (9; 15).

Clinical predictions were done by simulating CFU decline in 1000 virtual patients treated with the same dose as reported in the clinical EBA study. The baseline (Day 0) sputum values used were derived from the mean value for each arm reported in each study, and the variability in baseline bacterial burden between individuals used was the baseline variance among all

clinical studies. The net growth and death of bacteria without treatment was assumed to be zero (Equation 5.6).

$$\frac{dB}{dt} = K_{net} \times B - EFF \times B \quad Eq. 5.6$$

K_{net}: the net rate of change in bacterial number in the sputum of TB patients

Predictions were reported as the mean and standard deviation of the predicted time course of CFU decline. The observed data were overlayed for visual inspection. EBA values were calculated as the daily change of CFU counts. EBA for Day 0-2 and Day 2-14 were compared to the observed at all dose levels along a line of unity to assess predictive accuracy. Seven additional drugs not analyzed in this work were added for diagnostics of the translational platform.

Software and Statistical method

Preclinical and clinical PKPD modelling was performed in NONMEM (7.4.3) using PsN (4.8.1.). Models were developed following numerical and graphical diagnostics, assessing drop in objective function value through the likelihood ratio test and parameter precision, as well as goodness-of-fit plots, visual predictive checks, and pharmacological relevance. The first-order conditional estimation with interaction method (FOCE+I) was used. Data transformation and graphical output was performed in R (4.1.3) through the RStudio (2022.02.3) interface using the xpose4 and tidyverse packages.

Results

Large preclinical and clinical PK and PD database of nine TB drugs

We collated a rich longitudinal dataset of mouse PK (159 data points) and PD data (lung CFU counts, 126 data points), as well as human population PK models and human PD data (sputum CFU counts) (Table 5.3). PD experiments were done in mice infection models infected via aerosol with an inoculum size no less than $2 \log_{10}$ CFU/ml and incubation period of 14 days and 42 days prior to the start of treatment for BDQ and RPT, respectively.

Human PD data with a total of 260 human sputum CFU datapoints originating from Phase2a trials across 13 different studies ranging from 2 to 14 days were used to validate our Phase 2a EBA predictions.

Preclinical PK and PKPD models adequately described mouse data

The final PK and PKPD model parameter estimates are shown in Table 5.3. A 2-compartment model best described the mouse plasma data for BDQ. RPT was best described by a 1-compartment model with saturated clearance described via the Michaelis-Menten equation. Visual predictive checks of the final model for both mouse PK and PKPD data showed good fits (Figure 5.3 and Figure 5.4).

Table 0.3. Mouse PK and PKPD parameter estimates.

Drugs	BDQ	RPT
PK model	Oral 2-cmt model	Oral 1-cmt model with non-linear elimination
PK Model Parameters	$k_a = 3.24 \text{ (15.1\%)} \text{ h}^{-1}$ $CL = 0.0243 \text{ (5.9\%)} \text{ L/h}$ $V = 0.24 \text{ (11.4\%)} \text{ L}$ $V_p = 0.822 \text{ (29.3\%)} \text{ L}$ $Q = 0.0127 \text{ (11.5\%)} \text{ L/h}$	$k_a = 0.894 \text{ (31\%)} \text{ h}^{-1}$ $V = 0.0139 \text{ (6\%)} \text{ L}$ $k_m = 75.8 \text{ (31\%)} \text{ } \mu\text{g/mL}$ $V_{max} = 0.0333 \text{ (24\%)} \text{ } \mu\text{g/h}$
PKPD Model	Delayed E_{max} Function	Direct Sigmoidal Function
PKPD Model Parameters	$E_{max} = 0.295 \text{ (1\%)} \text{ day}^{-1}$ $EC_{50} = 0.173 \text{ (5\%)} \text{ mg/L}$ $K_d = 3.45 \text{ (10\%)} \text{ day}^{-1}$	$E_{max} = 0.299 \text{ (1\%)} \text{ day}^{-1}$ $EC_{50} = 6.02 \text{ (0\%)} \text{ mg/L}$ $\gamma = 2.36 \text{ (7\%)}$

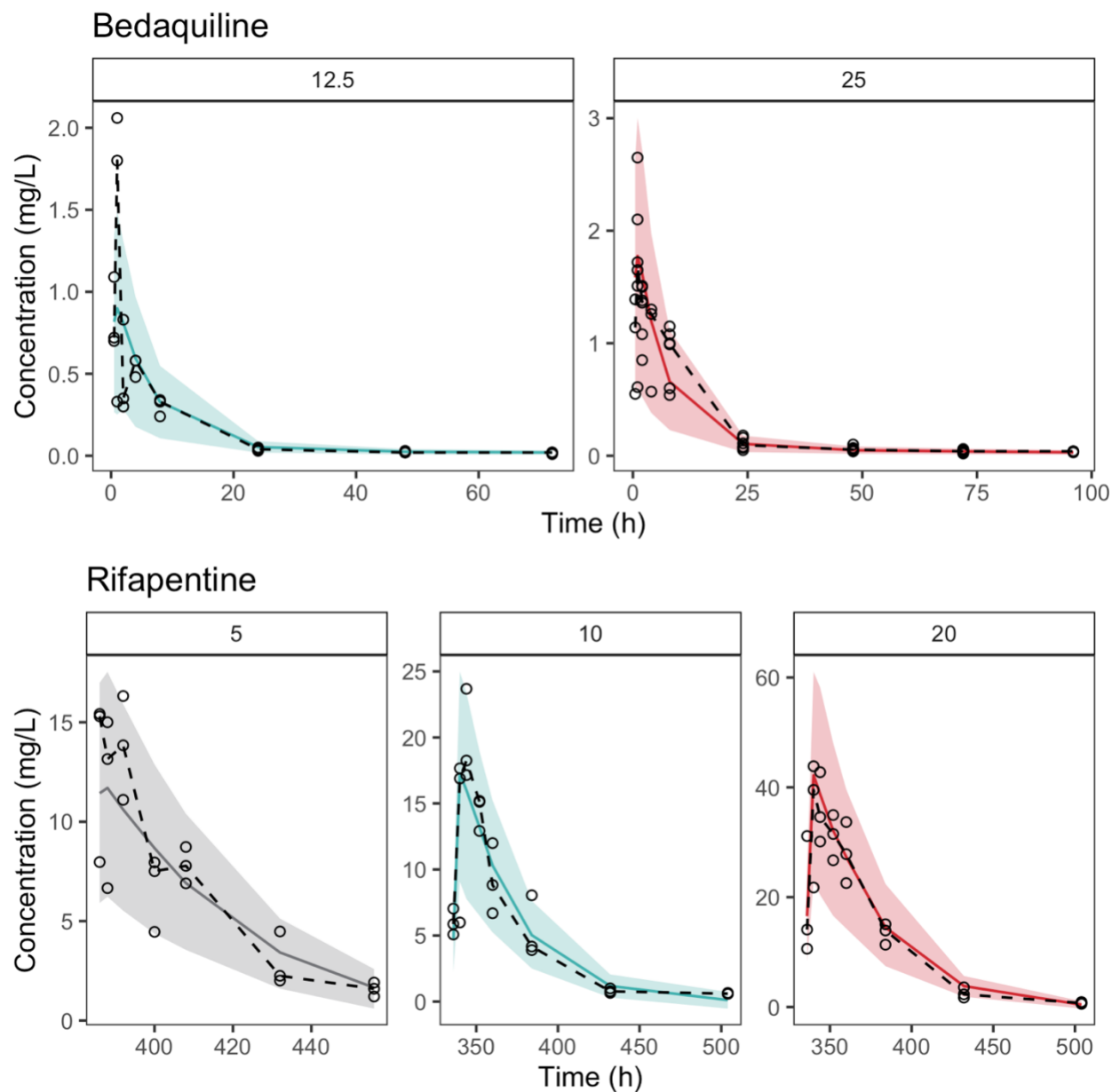


Figure 0.3. Visual predictive check of bedaquiline and rifapentine pharmacokinetics in mice. Observations represented as points and black dashed line (median). Solid colored line are median of 1,000 simulations and shaded areas are the prediction interval, or the middle 95th of simulations. Facet titles are the dose in mg/kg.

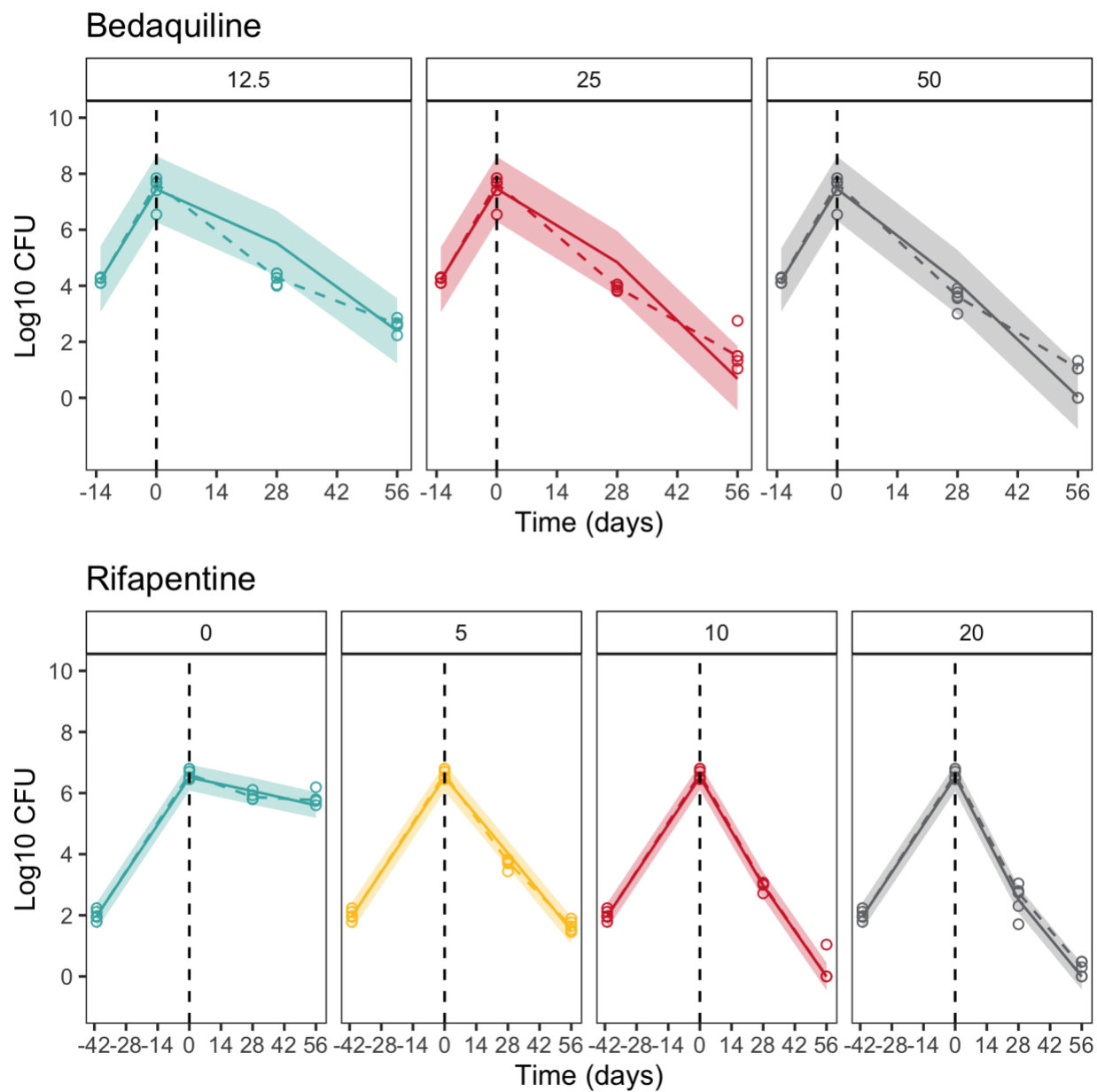


Figure 0.4 Visual predictive check of bedaquiline and rifapentine PKPD models in mice. Observations represented as points and black dashed line (median). Solid colored lines are median of 1,000 simulations and shaded areas are the prediction interval, or the middle 95th of simulations. Facet titles are the dose in mg/kg.

Clinical EBA well predicted by translational platform

Clinical CFU decline predictions are shown in Figure 5.5. RPT was underpredicted showing limited activity after a single dose. BDQ was slightly overpredicted at later timepoints. Agreement between predicted and observed quantitative change in CFU is shown in Figure 5.6 as a correlation plot for EBA at time intervals 0-2 days and 2-14 days. Predictions for seven other drugs using this platform are included (analysis not done in this work). Most of the predictions fell within $\pm 0.25 \log_{10}$ CFU/ml/day of the observed EBA as indicated by the line of unity and corresponding dotted lines. Predictions are overall consistent with the observed data in the clinical EBA studies for all nine drugs.

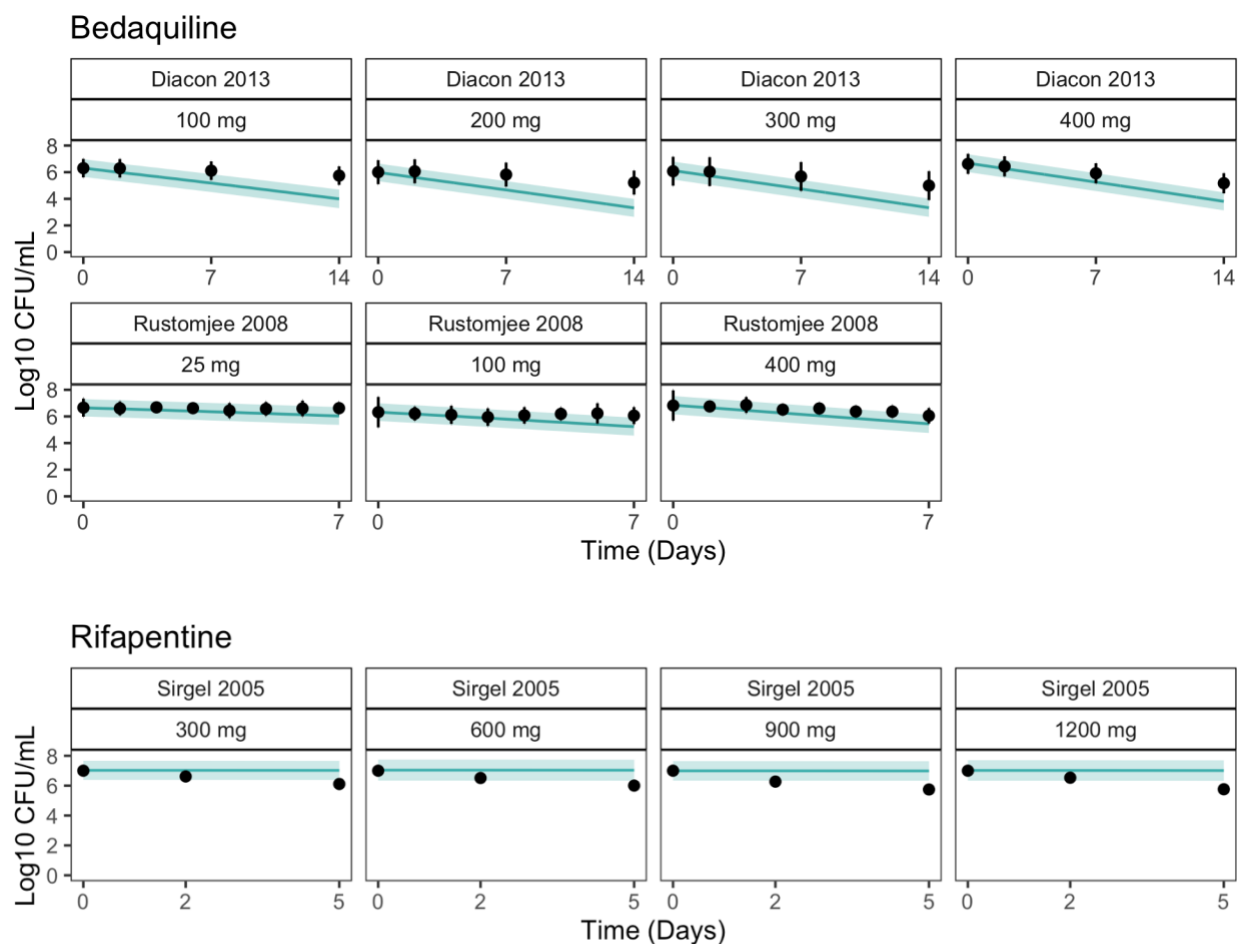


Figure 0.5. Clinical simulations using translational PKPD model and clinical observations. Mean and standard deviation from published EBA studies (black points and error bars) overlayed with mean (solid line) and standard deviation (shaded area) of 1,000 simulations using the translational PKPD model.

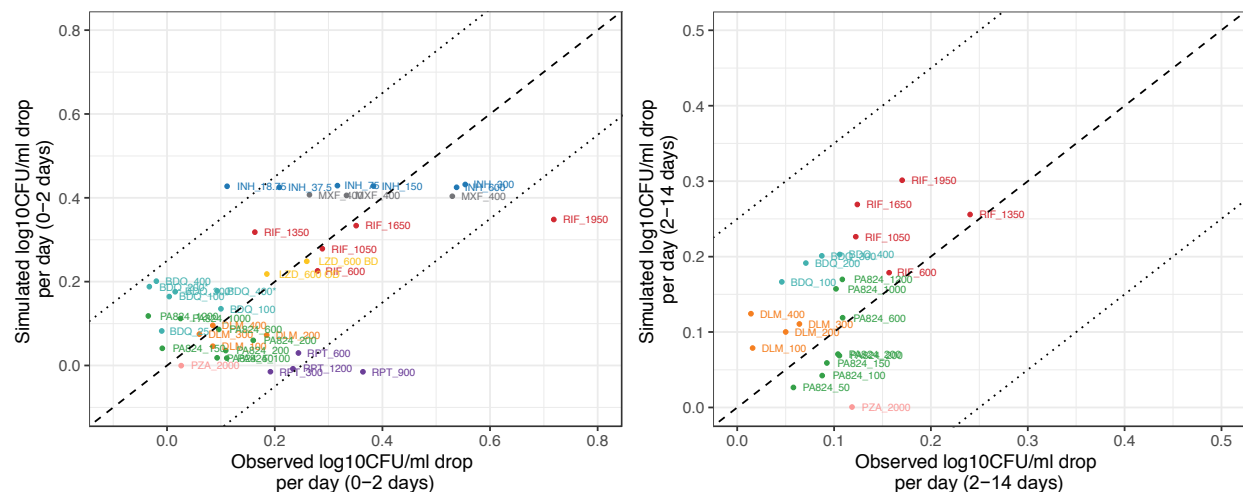


Figure 0.6. Model-based prediction of daily change in log10 CFU/mL correlates well with clinically observed daily change in log10 CFU/mL for nine TB drugs at multiple dose levels of monotherapy treatment between day 0 to 2 (left) and day 2 to 14 (right).

Line of unity (dashed line) ± 0.25 (dotted lines). BDQ = bedaquiline, DLM = delamanid, INH = isoniazid, LZD = linezolid, MXF = moxifloxacin, PMD = pretomanid, PZA = pyrazinamide, RIF = rifampin, RPT = rifapentin. *regimen contained a loading dose.

Discussion

We established a mouse-to-human translational platform by integrating a bacterial dynamics model, mouse PKPD relationships, clinical PK and species-specific drug plasma protein binding and validated the platform with clinical TB data (Figure 5.1). The change in sputum CFU counts over the first two days and Day 2-14 in TB patients receiving monotherapy with each of nine TB drugs over 13 clinical EBA studies were successfully predicted, except for RPT (Figure 5.3 and 5.4). Our human PK model indicated RPT was mostly cleared from the body two days after a single dose, but RPT's Phase 2a study showed RPT was still exerting bacterial kill at five days. It is possible that RPT had a post antibiotic effect that was not sufficiently captured by the model (16).

Murine TB models are routinely and often exclusively used as in vivo efficacy models in nonclinical TB drug development (4). As the inoculum size and incubation period for bacterial infection in the lung prior to treatment can affect drug response (14), we decided to standardize to the most common design with the incubation duration of 13-17 days and inoculum size to larger than $3.5 \log_{10}$ CFU/ml. Incubation durations outside this range were considered when data was not available which was the case for RPT in which 42-day, chronic infection data was used. In general, Day 2-14 was better predicted than Day 0-2. Acute infection models with less than 7 days infection may have greater ability to predict EBA in the first two days.

A key component to our model accuracy is the addition of the bacterial dynamics model. Mouse and human immune activation against TB infection differ significantly, therefore the underlying baseline of bacterial dynamics will differ. Subtracting the mouse immune effect on bacterial decline more accurately estimates the drug's contribution to CFU decline. Without such consideration, the clinical CFU decline is overpredicted. Despite inherent differences between species, sampling (whole lung homogenate versus sputum), and strain of bacteria, the relationship between drug effect on bacteria and the concentration to achieve the effect appear,

based on this analysis, to be portable between mice and patients. In addition, although the BALB/c mouse strain used in these studies models intracellular bacteria but not extracellular bacteria in caseous lesions, it still reflects the antibacterial characteristics of these drugs in a specific microenvironment. Other approaches or more information may need to be included to account for hard-to-treat microenvironments (17; 18).

Clinical EBA studies are the only acceptable way to evaluate a drug as monotherapy in TB patients despite its limitations on predicting long-term efficacy. In addition to detecting the presence of an EBA response, the trial can inform the dose-response curve. We have shown here that our translational platform can adequately predict these outcomes. With limited resources, this costly clinical study can be designed more efficiently or avoided altogether by using our approach to predict a reliable result regarding clinical dose-response effect, and to provide useful information about dose and/or drug candidate selection for further clinical development. The translational modeling platform minimizes the time and effort in early clinical development, and therefore, accelerates progress to trials that are more informative of long-term outcomes.

Building on our translational framework, efficacy of combination regimens of TB drugs tested nonclinically can be predicted in the future. This shows the principles of how nonclinical findings through a model-based translational framework can inform the design of clinical late-stage efficacy studies, such as Phase 2b studies. Future goals to improve the platform include characterizing PKPD relationships of combination regimens by accounting for PKPD drug-drug interactions, as well as characterizing lesion-specific PKPD relationships. Clinical TB disease (e.g., caseation necrosis and cavitation) will be represented in the translational platform to include infection and efficacy data in animal TB models with human-like necrotic lesions, such as C3HeB/FeJ mice and New Zealand white rabbits (18). Our translational platform may then be able to predict late-stage trials of combination regimens. As such, our platform cannot only

partially replace Phase 2a efficacy studies by predicting EBA, but also directly inform the design of Phase 2b and Phase 3 studies to assist clinical TB drug development.

In summary, we established a foundation for translating the results from mouse efficacy models to clinical EBA studies through establishing quantitative relationships involving mouse PK and PD, as well as drug dose response in vivo. In the future, our platform will be expanded to include combination regimens and longer durations of treatment by accounting for PKPD drug-drug interactions, and necrotic lesion penetration. This platform is an innovation to accelerate TB drug development as a good example of model-informed drug discovery and development.

References

1. Ginsberg AM. 2010. Drugs in development for tuberculosis. *Drugs* 70:2201-14
2. Ginsberg AM. 2010. Tuberculosis drug development: progress, challenges, and the road ahead. *Tuberculosis (Edinb)* 90:162-7
3. Nuermberger EL. 2017. Preclinical Efficacy Testing of New Drug Candidates. *Microbiol Spectr* 5
4. Dooley KE, Phillips PP, Nahid P, Hoelscher M. 2016. Challenges in the clinical assessment of novel tuberculosis drugs. *Adv Drug Deliv Rev* 102:116-22
5. Chen C, Ortega F, Rullas J, Alameda L, Angulo-Barturen I, et al. 2017. The multistate tuberculosis pharmacometric model: a semi-mechanistic pharmacokinetic-pharmacodynamic model for studying drug effects in an acute tuberculosis mouse model. *J Pharmacokinet Pharmacodyn* 44:133-41
6. Danhof M, de Jongh J, De Lange EC, Della Pasqua O, Ploeger BA, Voskuyl RA. 2007. Mechanism-based pharmacokinetic-pharmacodynamic modeling: biophase distribution, receptor theory, and dynamical systems analysis. *Annu Rev Pharmacol Toxicol* 47:357-400
7. Danhof M, de Lange EC, Della Pasqua OE, Ploeger BA, Voskuyl RA. 2008. Mechanism-based pharmacokinetic-pharmacodynamic (PK-PD) modeling in translational drug research. *Trends Pharmacol Sci* 29:186-91
8. Jindani A, Aber VR, Edwards EA, Mitchison DA. 1980. The early bactericidal activity of drugs in patients with pulmonary tuberculosis. *Am Rev Respir Dis* 121:939-49
9. Svensson EM, Dosne AG, Karlsson MO. 2016. Population Pharmacokinetics of Bedaquiline and Metabolite M2 in Patients With Drug-Resistant Tuberculosis: The Effect of Time-Varying Weight and Albumin. *CPT Pharmacometrics Syst Pharmacol* 5:682-91

10. Hibma JE, Radtke KK, Dorman SE, Jindani A, Dooley KE, et al. 2020. Rifapentine Population Pharmacokinetics and Dosing Recommendations for Latent Tuberculosis Infection. *Am J Respir Crit Care Med* 202:866-77
11. Sirgel FA, Fourie PB, Donald PR, Padayatchi N, Rustomjee R, et al. 2005. The early bactericidal activities of rifampin and rifapentine in pulmonary tuberculosis. *Am J Respir Crit Care Med* 172:128-35
12. Diacon AH, Dawson R, von Groote-Bidlingmaier F, Symons G, Venter A, et al. 2012. 14-day bactericidal activity of PA-824, bedaquiline, pyrazinamide, and moxifloxacin combinations: a randomised trial. *Lancet* 380:986-93
13. Rustomjee R, Diacon AH, Allen J, Venter A, Reddy C, et al. 2008. Early bactericidal activity and pharmacokinetics of the diarylquinoline TMC207 in treatment of pulmonary tuberculosis. *Antimicrob Agents Chemother* 52:2831-5
14. Zhang N, Strydom N, Tyagi S, Soni H, Tasneen R, et al. 2020. Mechanistic Modeling of Mycobacterium tuberculosis Infection in Murine Models for Drug and Vaccine Efficacy Studies. *Antimicrob Agents Chemother*
15. Egelund EF, Weiner M, Singh RP, Prihoda TJ, Gelfond JA, et al. 2014. Protein binding of rifapentine and its 25-desacetyl metabolite in patients with pulmonary tuberculosis. *Antimicrob Agents Chemother* 58:4904-10
16. Wicha SG, Clewe O, Svensson RJ, Gillespie SH, Hu Y, et al. 2018. Forecasting Clinical Dose-Response From Preclinical Studies in Tuberculosis Research: Translational Predictions With Rifampicin. *Clin Pharmacol Ther* 104:1208-18
17. Kramnik I, Beamer G. 2016. Mouse models of human TB pathology: roles in the analysis of necrosis and the development of host-directed therapies. *Semin Immunopathol* 38:221-37
18. Dartois V. 2014. The path of anti-tuberculosis drugs: from blood to lesions to mycobacterial cells. *Nat Rev Microbiol* 12:159-67

Chapter 6: Comparative efficacy of rifapentine alone and in combination with isoniazid for latent tuberculosis infection: a translational pharmacokinetic-pharmacodynamic modelling study*

Abstract

Rifapentine has facilitated treatment shortening of latent tuberculosis infection (LTBI) in combination with isoniazid once weekly for 3 months (3HP) or daily for 1 month (1HP) from 9 months of isoniazid monotherapy. We determine the optimal rifapentine dose for a 6-week monotherapy regimen (6wP) and predict clinical efficacy. Rifapentine and isoniazid pharmacokinetics were simulated in mice and humans. Mouse lung colony-forming unit data were used to characterize exposure-response relationships of 1HP, 3HP, and 6wP and translated to predict clinical efficacy. A 600 mg daily dose for 6wP delivered greater cumulative rifapentine exposure than 1HP or 3HP. The maximum regimen effect (E_{\max}) was 0.24 day^{-1} . The regimen potencies, measured as concentration at 50% of E_{\max} (EC_{50}), were estimated as 2.12 mg/L for 3HP, 3.72 mg/L for 1HP, and 4.71 mg/L for 6wP, suggesting that isoniazid contributes little to 1HP efficacy. Clinical translation predicted that 6wP reduces bacterial load at a faster rate than 3HP and a greater extent than 3HP and 1HP. 6wP (600 mg daily) is predicted to result in equal or better efficacy than 1HP and 3HP for LTBI treatment without the potential added toxicity of isoniazid. Results from ongoing and future clinical studies will be required to support these findings.

* Modified from the publication: Radtke KK, Ernest JP, *et al.* Comparative efficacy of rifapentine alone and in combination with isoniazid for latent tuberculosis infection: a translational pharmacokinetic-pharmacodynamic modeling study. *Antimicrobial Agents and Chemotherapy*. 2021. 65:12

Introduction

Treatment of latent tuberculosis infection (LTBI) has been facilitated by short-course regimens that range in duration from one to four months (1, 2). These short-course regimens have significantly shortened the length of treatment compared to the historical standard of 6-12 months of isoniazid monotherapy, which in turn has led to improved treatment completion rates (3). All current short-course regimens include a rifamycin (e.g., rifampin or rifapentine) either as monotherapy or in combination with isoniazid. Rifapentine is a newer rifamycin that has a longer elimination half-life than rifampin (15 hours vs. 4 hours) (4), making it an ideal candidate for shortened duration and/or less frequent dosing. Rifampin given daily for four months, and rifapentine in combination with isoniazid once weekly for 3 months (3HP) or daily for 1 month (1HP) have demonstrated non-inferior effectiveness compared to 9 months of daily isoniazid (9H) in preventing active TB disease (2, 5, 6).

Use of isoniazid is associated with significant dose-limiting toxicities, namely hepatotoxicity, which can be fatal (7, 8). Intermittent dosing of rifapentine and isoniazid, as in 3HP, has shown significantly less hepatotoxicity than with 9H (9), but when rifapentine and isoniazid were given daily, adverse effects were similar (2). Isoniazid may also contribute to the hypersensitivity reactions reported with 3HP use (10, 11). Eliminating isoniazid from LTBI treatment altogether could prove beneficial from a safety perspective and would reduce pill burden.

A novel regimen of daily rifapentine for 6 weeks is under investigation (ClinicalTrials.gov identifier NCT03474029). The optimal dose of rifapentine in the absence of isoniazid to prevent active TB disease is not well understood. In a murine model of LTBI, rifapentine monotherapy at 10 mg/kg of body weight daily (equivalent to 600 mg per day in humans) was similar or better than rifapentine plus isoniazid in reducing lung CFU and relapse rates when given for the same duration (12, 13).

However, differences in rifapentine pharmacokinetics (PK) between mice and humans must be considered. In humans, rifapentine exhibits concentration-dependent autoinduction of clearance, resulting in lower concentrations over time with daily dosing (14). Rifapentine autoinduction may also occur in mice but the relationships to drug concentration and dosing frequency have not been well characterized (15, 16). Additionally, rifapentine bioavailability is affected by HIV infection, dose, and fasting/meal conditions, and interpatient variability is high in humans (17, 18). To determine the optimal dose for rifapentine monotherapy to treat LTBI, both the pharmacokinetic and pharmacodynamic (PD) relationships need to be characterized.

The aim of this study was to characterize the PK and PD of rifapentine and to build a translational model that accounts for species-specific PK parameters, plasma protein binding, and host adaptive immunity in the context of LTBI to predict efficacy of a 6-week rifapentine monotherapy regimen in humans. To that end, we implemented a mechanistic model of murine immune response to *Mycobacterium tuberculosis* infection and used drug efficacy data and population PK models in mice and humans to compare drug exposure and clinical effectiveness of different rifapentine-containing regimens for the treatment of LTBI.

Methods

Clinical PK simulations

Rifapentine clinical PK were simulated using a population PK model published by Hibma *et al.* generated from an individual participant data meta-analysis of nine clinical PK studies (19). The model captures dose, HIV status, and meal effects on rifapentine bioavailability, and autoinduction of clearance as a function of rifapentine concentration. Simulations were performed to compare rifapentine PK of clinically tested rifapentine-based LTBI regimens with the PK of an experimental 6-week once-daily rifapentine monotherapy regimen (6wP) at various dose levels. For comparator regimens, we evaluated 1HP (300 mg isoniazid plus 600 mg rifapentine daily for one month) and 3HP (900 mg isoniazid plus 900 mg rifapentine once weekly for three months). For isoniazid-containing regimens (i.e., 1HP and 3HP), isoniazid clinical PK were also simulated with a population PK model (20). Simulations ($n=500$) were performed for an HIV-seronegative population receiving a low-fat meal (relative rifapentine bioavailability = 1) and with 50/50 slow/fast acetylator status for isoniazid. PK profiles were summarized as maximum concentration (C_{max}), area under the plasma concentration-time curve (AUC), and time above minimum inhibitory concentration (MIC). The rifapentine MIC was set to 0.06 mg/L (4).

Mouse PK simulations

Mouse PK models were built in NONMEM 7.4 for rifapentine and isoniazid. Modelling details and results are provided in the Supplemental Material. Rifapentine PK were simulated 500 times under different dosing conditions that matched clinical rifapentine regimens: 10 mg/kg once daily for 6 weeks (6wP regimen), 10 mg/kg once daily for 4 weeks (1HP regimen), and 15 mg/kg once weekly for 12 weeks (3HP regimen). Similarly, isoniazid PK was simulated 500 times with 10 mg/kg once daily for 4 weeks (1HP regimen) and 50 mg/kg once weekly for 12

weeks (3HP regimen). For daily regimens, mouse PK was simulated as dosing 5 days/week in accordance with the original studies.

PD Model

Mouse CFU data were acquired from two studies: ‘high-dose’ rifapentine (13) and ‘low-dose’ rifapentine (see Supplementary Material). All animal procedures were approved by the Institutional Animal Care and Use Committee of Johns Hopkins University unless otherwise specified from the original publication. Data were used to describe the in vivo exposure-response relationship of different rifapentine-based regimens. The baseline immune effect was determined by estimating the net bacterial growth/death without treatment (K_{NET}). A PK-PD model was developed using CFU data from treated mice by adding drug effect (EFF) to the baseline model (Eq. 1), where ‘B’ is the bacterial load. EFF was modeled as a function of rifapentine concentration (C_p). PK-PD relationships for the drug effect were optimized by fitting the mouse efficacy data to linear, nonlinear, loglinear, E_{max} and sigmoidal functions (Eq. 2–4). An additive error model was used to describe residual error for the mouse PK-PD models.

$$\frac{dB}{dt} = K_{NET} \times B - EFF \times B \quad \text{Eq. 1}$$

$$EFF = \text{slope} \times C_p + \text{intercept} \quad \text{Eq. 2}$$

$$EFF = \text{slope} \times \ln(C_p) + \text{intercept} \quad \text{Eq. 3}$$

$$EFF = \frac{C_p^Y \times E_{max}}{EC_{50}^Y + C_p^Y} \quad \text{Eq. 4}$$

Translational PK-PD

The clinical population PK model of rifapentine was linked to the PK-PD relationships established for three rifapentine-based regimens in the latent infection study. The clinical PK-PD relationship was assumed to be the same as the estimated murine PK-PD relationship after

correcting for the difference in unbound drug fraction. No murine protein binding information was available so the unbound fraction from Wistar rats was used instead; the estimated ratio of free fraction (human/mouse) was 0.422 (21, 22). The net bacterial growth (K_{NET}) in humans was assumed to be zero, representing the balance between immune-mediated killing and any bacterial growth. Other assumptions (eg, $K_{NET} < 0$ and $K_{NET} > 0$) were also tested. The drug effect (EFF) was incorporated as an additional effect inhibiting the bacterial growth. Simulations of the change in bacterial load following treatment were performed 500 times with each regimen (6wP, 3HP, and 1HP) with a baseline bacterial load of 2 to 4 \log_{10} CFU and variance of 0.1 (Eq. 1).

In silico clinical trial simulations

An *in silico* clinical trial was simulated based on our final model with 1000 individuals per arm: placebo, 3HP, 1HP, and 6wP. The baseline bacterial load was set to $2.5 \pm 0.5 \log_{10}$ CFU. Active TB was defined as $CFU \geq 4 \log_{10}$ as the lower limit of quantification of acid-fast smears is 10^4 CFU/mL (21). The number of individuals to develop active TB were determined over a 2-year period.

Software

All modeling and simulation analyses were conducted using NONMEM (version 7.4). Perl speaks NONMEM (PsN), R (version 3.5) statistical program, and the xpose4 and ggplot2 R packages were utilized for model diagnostics and data visualization. Survival analysis of *in silico* data was done with survival R package. The first-order conditional estimation with interaction method was used. Mouse PK and PK-PD models were developed and selected based on graphical (goodness of fit plots), statistical (significant change in objective function value), and simulation-based diagnostics (visual predictive checks).

Results

Clinical PK of rifapentine-based regimens

To determine the effective rifapentine dose for a 6-week daily monotherapy regimen (6wP), rifapentine exposures at various dose levels were compared to those of clinically tested regimens (i.e., 1HP and 3HP). After 300 mg daily for 6 weeks, the predicted total rifapentine cumulative AUC (cAUC) was similar to that following 900 mg once weekly for 3 months (i.e., 3HP) and 600 mg daily for 1 month (i.e., 1HP) (Figure 6.1). With 600 mg rifapentine daily for 6 weeks, rifapentine cAUC was predicted to be nearly double that of 3HP and approximately 1.5 times that of 1HP. A 900 mg daily dose delivered even higher rifapentine exposures.

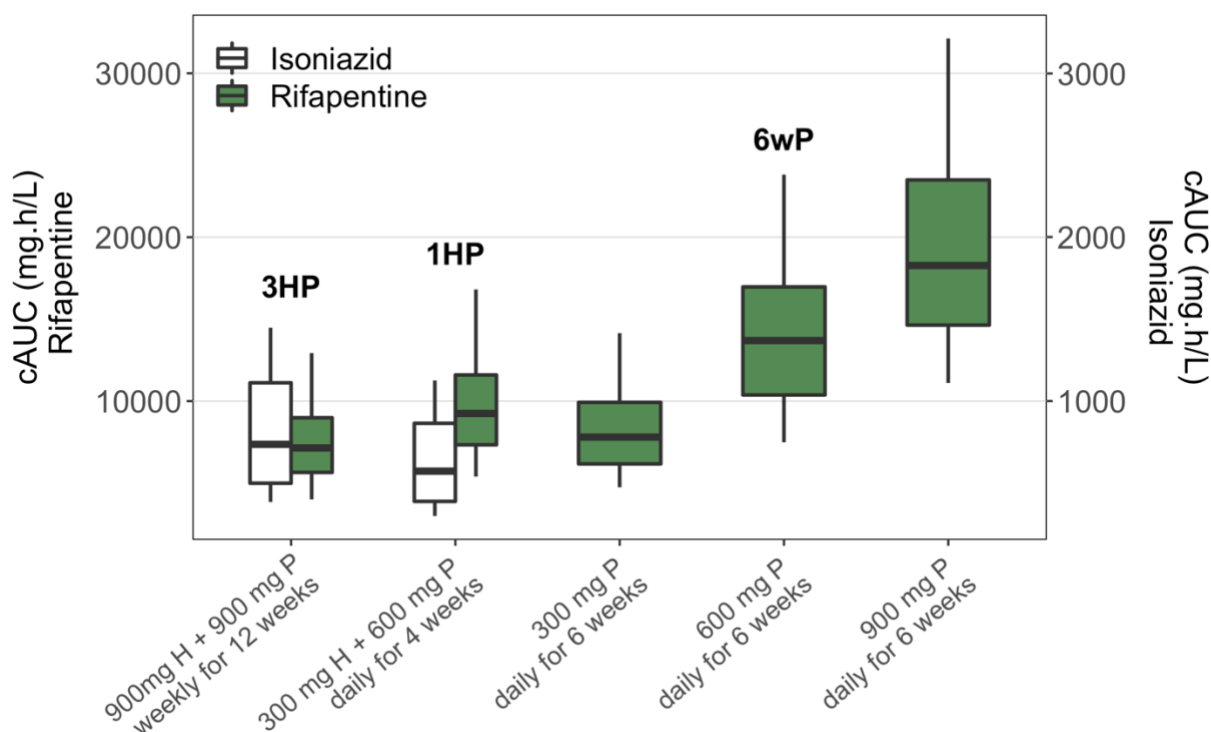


Figure 0.1. Predicted rifapentine exposure in patients.

Predicted rifapentine exposure in experimental 6-week rifapentine mono-therapy regimens at various dose levels compared to 3 months of weekly isoniazid plus rifapentine (3HP) and 1 month of daily isoniazid plus rifapentine (1HP). Based on 500 simulations. HIV-seronegative status was assumed for all regimens. cAUC = cumulative area under the curve for the complete regimen. H = isoniazid. P = rifapentine. 6wP = selected 6-week monotherapy regimen.

Given the favorable PK, the 600 mg dose for the daily 6-week regimen (i.e., 6wP) was chosen. Average daily total AUC/MIC and C_{\max} /MIC were comparable for 6wP and 1HP, which were higher than for 3HP (Table 6.1). The percentage of the treatment duration with concentrations above MIC was 100% for 1HP and 6wP (Table 6.1).

Isoniazid exposure over the full treatment course was slightly higher with 3HP than 1HP (Figure 6.1; Table 6.1). The 6-week rifapentine monotherapy regimens tested did not include isoniazid.

Table 0.1. PK/PD indices for rifapentine-containing LTBI regimens.

		3HP	1HP	6wP
Rifapentine				
Dose	Human	900 mg weekly	600 mg daily	600 mg daily
	Mouse	15 mg/kg weekly	10 mg/kg daily	10 mg/kg daily
cAUC (mg*h/L)	Human	7143 (3610-14281)	9248 (4838-19697)	13462 (7113-27736)
	Mouse	10130 (8783-11955)	7100 (5640-8927)	10677 (8485-13470)
AUC/MIC	Human	1405 (713-2796)	4972 (2640-10686)	5010 (2685-10365)
	Mouse	2011 (1743-2374)	4292 (3384-5449)	4280 (3385-5434)
C_{\max} /MIC	Human	318 (156-646)	390 (206-730)	388 (208-718)
	Mouse	333 (327-341)	311 (268-365)	313 (269-364)
Percentage of treatment duration above MIC	Human	99 (57-100)	100 (100-100)	100 (100-100)
	Mouse	93 (86-98)	100 (100-100)	100 (100-100)
Isoniazid				
Dose	Human	900 mg weekly	300 mg daily	NA
	Mouse	50 mg/kg weekly	10 mg/kg daily	NA
cAUC (mg*h/L)	Human	745 (343-1608)	579 (267-1250)	NA
	Mouse	667 (489 – 879)	156 (118 - 207)	NA

Values represent total drug (free + bound) and are based on 500 simulations. Data are expressed as median (2.5th-97.5th quantile range). cAUC = cumulative AUC. AUC/MIC = ratio of average daily AUC to MIC at steady state. C_{\max} /MIC = ratio of maximum concentration to MIC at steady state. NA = not applicable. MIC = minimum inhibitory concentration (0.06 mg/L). 3HP = 3 months weekly rifapentine and isoniazid. 1HP = 1-month daily rifapentine and isoniazid. 6wP = 6 weeks daily rifapentine.

Comparison of mouse and human PK

Rifapentine PK simulations in mouse and human are shown in Figure 6.2. A rifapentine dose in mice of 10 mg/kg given 5/7 days delivers similar concentration profiles to 600 mg once daily in humans and 15 mg/kg rifapentine once weekly (1/7) in mice has similar PK to 900 mg once weekly in humans (Figure 2). Clinical and murine PK/PD indices were similar (Table 6.1).

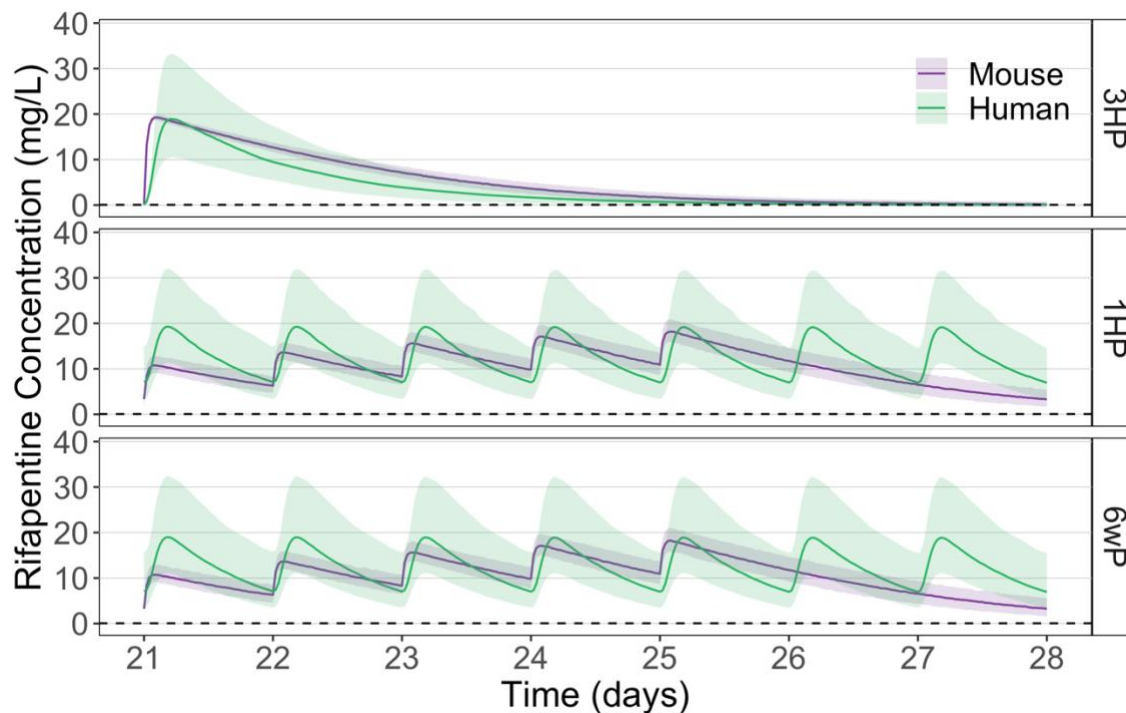


Figure 0.2. Steady state rifapentine pharmacokinetics in mice and humans.

Median (solid line) and 95% prediction interval (shaded area) based on 500 simulations. 3HP = three months of once weekly rifapentine and isoniazid. 1HP = one month of daily rifapentine and isoniazid. 6wP: 6 weeks of daily rifapentine (600 mg, human; 10 mg/kg, mouse) monotherapy.

PK-PD model

The bacterial growth rate constant for the baseline model describing the primary immune response in the latent infection mouse model was estimated to be -0.048 and 0.0151 day^{-1} for the high dose and low dose studies, respectively. In the PK-PD model, the net maximal rifapentine drug effect (E_{\max}) was estimated to be 0.24 day^{-1} for monotherapy (Table 6.2). The rifapentine concentration required to achieve half of the maximal effect (EC_{50}) was estimated to

be 4.71 mg/L for monotherapy (Table 6.2). For combination LTBI regimens (1HP and 3HP), the E_{\max} and EC_{50} of rifapentine were assumed to be the same. Isoniazid increased the potency of these regimens by decreasing the apparent EC_{50} by 21% in the 1HP regimen (an apparent EC_{50} of 3.72 mg/L) and 55% in the 3HP regimen (an apparent EC_{50} of 2.12 mg/L) (Figure 6.3; Table 6.2).

Visual predictive checks (VPCs) of 500 simulations indicated that the observed data were within the 95% prediction interval of the simulated CFU counts in the final PK-PD models (Supplementary Figure 6.2).

Table 0.2. Pharmacological parameters of rifapentine-containing regimens in latent TB mouse study.

Parameter	Description	Value (RSE, %)
$KNET_{HD}$ (day^{-1})	Net rate of bacterial growth without drug for high dose study	-0.048 (0%)
$KNET_{LD}$ (day^{-1})	Net rate of bacterial growth without drug for low dose study	0.0151 (0%)
E_{\max} (day^{-1})	Maximum efficacy of rifapentine monotherapy regimen	0.24 (20%)
γ	Steepness of the sigmoidal concentration-response relationship	1.62 (16%)
EC_{50_6WP} (mg/L)	Rifapentine concentration at 50% of E_{\max} in daily rifapentine monotherapy regimen	4.71 (36%)
EC_{50_1HP} (mg/L)	Rifapentine concentration at 50% of E_{\max} in daily rifapentine and isoniazid regimen	3.72 (59%)
EC_{50_3HP} (mg/L)	Rifapentine concentration at 50% of E_{\max} in weekly rifapentine and isoniazid regimen	2.12 (54%)

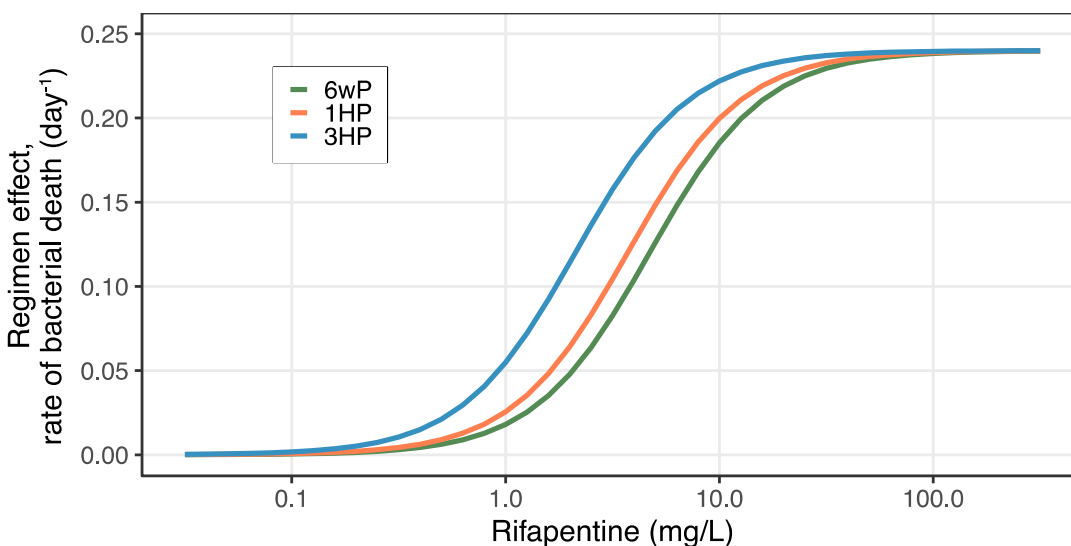


Figure 0.3. Concentration-response relationship of rifapentine-containing regimens.

3HP = 900 mg rifapentine plus isoniazid given once weekly for 3 months. 1HP = 600 mg rifapentine plus isoniazid given daily for 1 month. 6wP = 600 mg rifapentine monotherapy given daily for 6 weeks.

Clinical efficacy predictions

Simulated CFU profiles in humans showed median CFU reductions up to 1.5- \log_{10} with 1HP, 2- \log_{10} with 6wP and 3HP regimens at the end of treatment (Figure 6.4). 1HP had the fastest rate of decline in CFU but the highest remaining bacterial burden at the end of therapy. 6wP achieved greater or equal reduction in bacterial load from baseline compared to 3HP but at a much faster rate and shorter treatment duration. The predicted absolute CFU after treatment depended on the baseline bacterial load and the assumption of the balance between immune killing and bacterial growth (Supplementary Figure 6.3) and the interspecies ratio of the fraction unbound (Supplementary Figure 6.4). A lower baseline CFU, an immune kill rate higher than the bacterial growth rate, and an equal interspecies ratio of the fraction unbound each resulted in a lower bacterial burden at the end of treatment. The comparative efficacy remained consistent between regimens regardless of the assumption. The *in silico* clinical trial predicted that 12.8% of patients would develop active TB ($> 4 \log_{10}$ CFU) with placebo compared to 1.2% or less with

a rifapentine-based treatment regimen after 2 years (Figure 6.5). Notably, the predicted clinical efficacy was similar between rifapentine-based regimens in the *in silico* clinical trial.

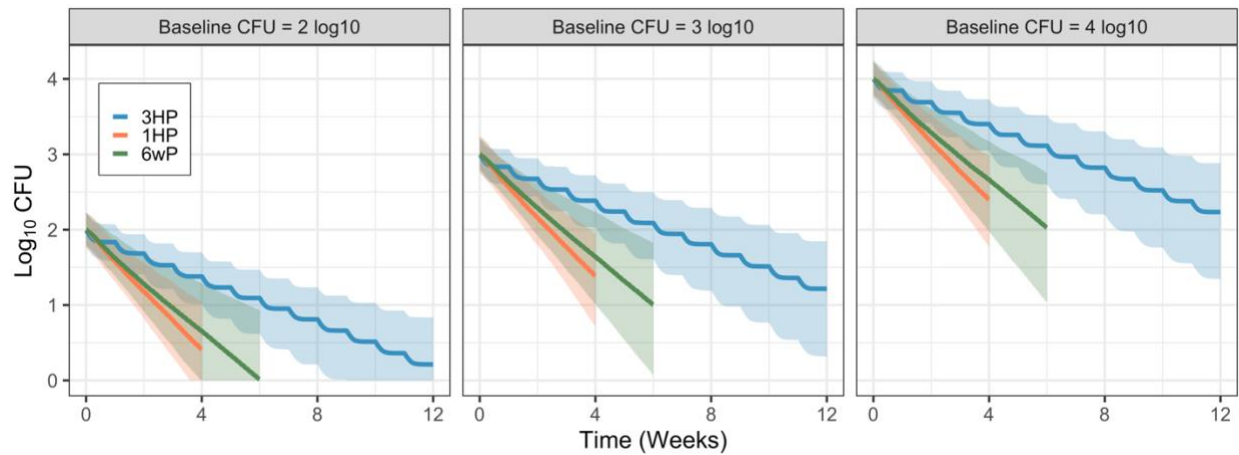


Figure 0.4. Predicted bacterial load over time in humans following LTBI treatment with rifapentine-containing regimens.

Panels represent different baseline bacterial loads of 2, 3, and 4 log₁₀ (left to right). Data show median (line) and 90% prediction interval (shaded area) based on 500 simulations for each regimen. CFU: colony forming unit.

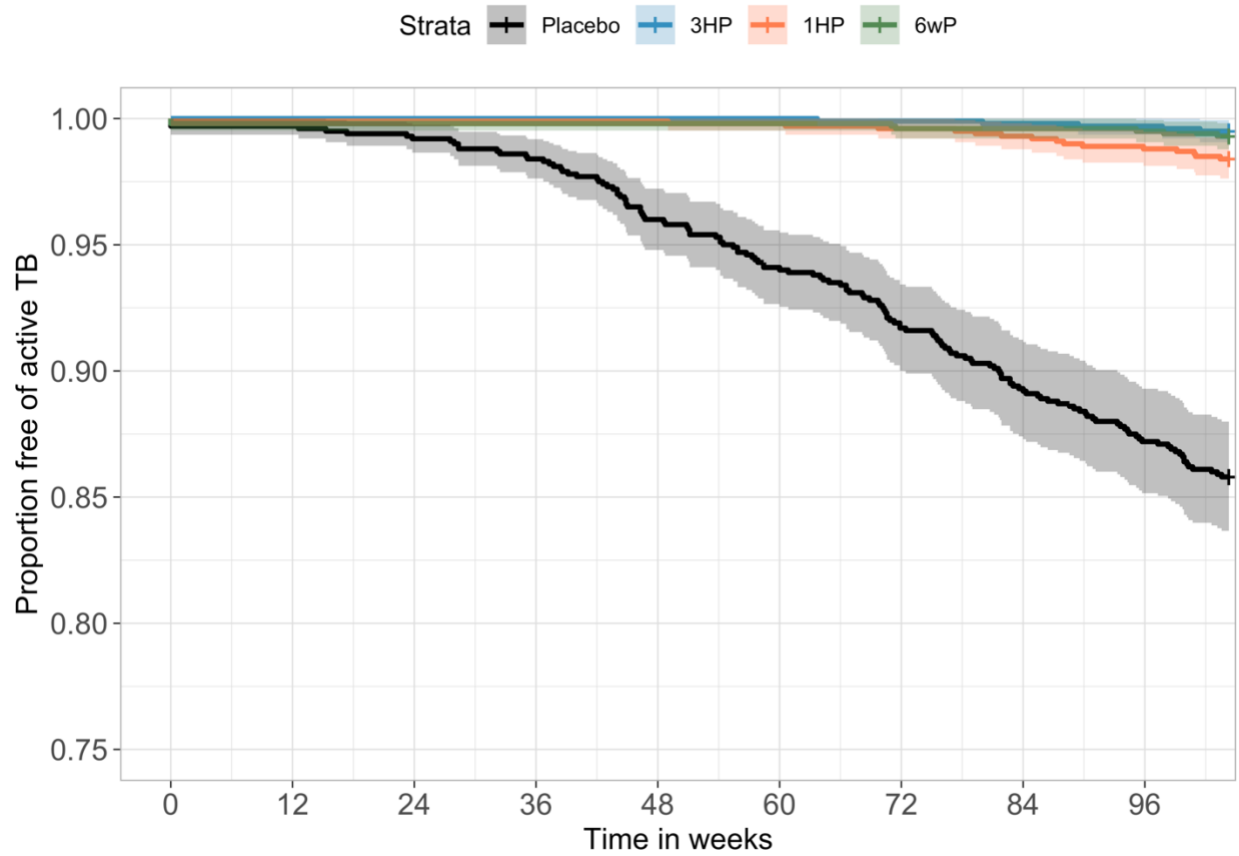


Figure 0.5. Kaplan-Meier plot.

Kaplan-Meier plot of *in silico* patients treated with rifapentine-based regimens or placebo for LTBI. Clinical trial simulations included 1000 patients per arm with baseline log CFU of 2.5 ± 0.5 . *In silico* patients were followed for 2 years. Active TB was defined as CFU $> 4 \log_{10}$.

Discussion

In this study, we predicted that a 600 mg daily dose of rifapentine monotherapy for 6 weeks delivered sufficient drug exposure for effective treatment of LTBI based on PK simulations of experimental and clinically approved regimens. The cumulative rifapentine drug exposure was greater with 600 mg 6wP than the clinically tested regimens of 1HP and 3HP. The translational PK-PD predictions showed that 6wP had similar efficacy to those of 1HP and 3HP, suggesting that clinical efficacy will be similar to that of either combination regimen.

Currently, there is no established PK-PD relationship or target for rifapentine in the treatment of LTBI. Rifamycins are believed to exhibit concentration-dependent killing, and the AUC/MIC ratio has been linked to efficacy against TB disease (24, 25). Our PK simulations demonstrated that 6wP had an AUC/MIC ratio equivalent to that of 1HP and a higher AUC/MIC ratio than that of 3HP. This trend was consistent across other PK/PD indices (e.g., C_{max} /MIC and time above MIC).

The role of isoniazid in the efficacy of rifamycin-containing LTBI treatment regimens is not well understood. Given the toxicity concerns with isoniazid, rifapentine monotherapy would be appealing if it were sufficiently effective. The PK-PD relationships in this study showed that adding isoniazid only slightly increased the potency of a daily rifapentine regimen (i.e., 21% lower EC_{50} with 1HP compared to 6wP) and comes with the cost of a cumulative isoniazid exposure of 156 mg·h /L over 4 weeks. Our predictions of bacterial burden showed similar bacterial burden at 4 weeks with 1HP and 6wP and similar bacterial burden at the end of treatment with 3HP and 6wP, which were lower than those with 1HP. Furthermore, the *in silico* clinical trial showed no difference in the probability of active TB between regimens. This suggests that the clinical efficacy of 6wP would likely be similar to those of 1HP and 3HP and promotes the elimination of isoniazid from ultrashort-course LTBI regimens.

The PK-PD relationship in the paucibacillary mouse model of LTBI was established with a few assumptions. The mouse PD data from which the PK-PD model was built is based on investigated regimens that mimicked rifapentine monotherapy and in combination with isoniazid, but dose-ranging was only available for rifapentine monotherapy. As such, a continuous concentration-response relationship could only be estimated for rifapentine monotherapy. The maximum effect (E_{\max}) of combination regimens was assumed to be equal to that estimated for rifapentine monotherapy from the dose-ranging data and only the EC_{50} (potency) differed by regimen. This assumption is reasonable as rifamycins are thought to drive bacterial killing. Another assumption was that the net bacterial growth rate (K_{net}) (in the absence of drug killing) was the same in untreated and treated mice. Despite these assumptions, the visual predictive checks and model diagnostics demonstrated good predictability of our mouse PD model.

The absolute bacterial burden at the end of treatment was dependent on the baseline bacterial load and the human immune effect assumption. Post-mortem examination of apparently healed tuberculous lesions and adjacent areas have found viable bacteria in smear-negative lesions suggesting that the bacterial burden in latent tuberculous lesions is less than 4 \log_{10} CFU/mL (21, 22), the lower limit of sensitivity of acid-fast smears for detection of *M. tuberculosis* (*Mtb*). As such, the median baseline bacterial load for clinical efficacy predictions was assumed to be 2, 3, or 4 \log_{10} CFU with active infection defined as > 4 \log_{10} CFU. While complete eradication of bacteria was only achieved with a baseline bacterial load of 2 \log_{10} CFU, all regimens showed <1.2% active patients at the end of a 2-year trial period, consistent with LTBI clinical trials. The true range and distribution of baseline bacterial load in individuals with LTBI is unknown. It is also unknown what end-of-treatment bacterial load is sufficient for clinical success of LTBI treatment, typically defined as lack of confirmed active TB after a 2-5 year follow up period. LTBI is diagnosed by immune response to *Mtb* antigen, and *Mtb* bacteria are undetectable in clinical samples else the individual is considered to have active disease (1). Further, we assumed that immune killing of bacteria was in equilibrium with bacterial growth.

While this is an accepted phenomenon, it is likely an oversimplification of reality. There is increasing recognition that tuberculosis is more heterogeneous than a two-state condition (i.e., active or latent) and likely exists on a spectrum from complete immune dominance (successful bacterium elimination but retained immune memory) to bacterial dominance (resulting in active disease) (27–30). Assuming modest immune dominance over bacterial growth ($K_{\text{net}} = -0.01 \text{ day}^{-1}$) and baseline bacterial load of $< 4 \log_{10} \text{ CFU}$, all regimens were predicted to have 90% of individuals with less than $1 \log_{10} \text{ CFU}$ at 1-year post-treatment start. As such, given the unknowns with LTBI, our clinical efficacy simulations are not contradictory to the Phase 3 clinical trial results for 1HP and 3HP. Importantly, our predictions showed that 6wP efficacy is within the efficacy range of 1HP and 3HP, implying that 6wP would perform equally well.

There were limitations of this study. First, there is a lack of good clinical PK or PK/PD targets for LTBI regimens linking rifapentine exposure to efficacy. We compared drug exposures and translational efficacy of the 600 mg 6wP experimental regimen with regimens that have demonstrated clinical efficacy (i.e., 1HP and 3HP). Second, assumptions were made with the translational PK-PD model. In addition to those already mentioned is that rifapentine protein binding in mice was equal to that of Wistar rats (another murine species). While this assumption would impact the extent of bacterial killing, the relative efficacy of the three regimens would remain consistent. The same is true for the other PK-PD assumptions and initial conditions. Both the nonclinical experiments and clinical simulation predictions support that 6wP will have non-inferior efficacy to both 1HP and 3HP.

With the above limitations noted, the following conclusions can be drawn. First, comparison of rifapentine clinical PK profiles indicate that 6wP would achieve comparable or superior exposure to previously studied regimens of 1HP and 3HP. Second, by quantifying a relationship between rifapentine concentration and bacterial kill in mice, we found that the relative efficacy of an experimental 6wP regimen at a 600 mg dose level is similar to those of 1HP and 3HP. Finally, we conclude that isoniazid's contribution to efficacy is minimal in ultrashort-course

regimens where rifapentine is administered daily. The comparison of PK profiles, nonclinical analysis and subsequent clinical simulations performed in this study indicate that 6wP is a promising regimen for LTBI and could serve as a safer, simpler solution for TB prevention.

References

1. World Health Organization. 2020. WHO operational handbook on tuberculosis. Module 1: Prevention- tuberculosis preventive treatment. Accessed
2. Swindells S, Ramchandani R, Gupta A, Benson CA, Leon-Cruz J, Mwelase N, Jean Juste MA, Lama JR, Valencia J, Omoz-Oarhe A, Supparatpinyo K, Masheto G, Mohapi L, da Silva Escada RO, Mawlana S, Banda P, Severe P, Hakim J, Kanyama C, Langat D, Moran L, Andersen J, Fletcher CV, Nuernberger E, Chaisson RE, Team BTAS. 2019. One Month of Rifapentine plus Isoniazid to Prevent HIV-Related Tuberculosis. *N Engl J Med* 380:1001-1011.
3. Horsburgh CR, Jr., Goldberg S, Bethel J, Chen S, Colson PW, Hirsch-Moverman Y, Hughes S, Shrestha-Kuwahara R, Sterling TR, Wall K, Weinfurter P. 2010. Latent TB infection treatment acceptance and completion in the United States and Canada. *Chest* 137:401-409.
4. Alfarisi O, Alghamdi WA, Al-Shaer MH, Dooley KE, Peloquin CA. 2017. Rifampin vs. rifapentine: what is the preferred rifamycin for tuberculosis? *Expert Rev Clin Pharmacol* 10:1027-1036.
5. Sterling TR, Villarino ME, Borisov AS, Shang N, Gordin F, Bliven-Sizemore E, Hackman J, Hamilton CD, Menzies D, Kerrigan A, Weis SE, Weiner M, Wing D, Conde MB, Bozeman L, Horsburgh CR, Jr., Chaisson RE. 2011. Three months of rifapentine and isoniazid for latent tuberculosis infection. *N Engl J Med* 365:2155-2166.
6. Menzies D, Adjobimey M, Ruslami R, Trajman A, Sow O, Kim H, Obeng Baah J, Marks GB, Long R, Hoepfner V, Elwood K, Al-Jahdali H, Gninafon M, Apriani L, Koesoemadinata RC, Kritski A, Rolla V, Bah B, Camara A, Boakye I, Cook VJ, Goldberg H, Valiquette C, Hornby K, Dion MJ, Li PZ, Hill PC, Schwartzman K, Benedetti A. 2018. Four Months of

- Rifampin or Nine Months of Isoniazid for Latent Tuberculosis in Adults. *N Engl J Med* 379:440-453.
7. Kopanoff DE, Snider DE, Jr., Caras GJ. 1978. Isoniazid-related hepatitis: a U.S. Public Health Service Cooperative Surveillance Study. *Am Rev Respir Dis* 117:991-1001.
 8. Snider DE, Jr., Caras GJ. 1992. Isoniazid-associated hepatitis deaths: a review of available information. *Am Rev Respir Dis* 145:494-497.
 9. Bliven-Sizemore EE, Sterling TR, Shang N, Benator D, Schwartzman K, Reves R, Drobeniuc J, Bock N, Villarino ME. 2015. Three months of weekly rifapentine plus isoniazid is less hepatotoxic than nine months of daily isoniazid for LTBI. *Int J Tuberc Lung Dis* 19:1039-103v.
 10. Sterling TR, Moro RN, Borisov AS, Phillips E, Shepherd G, Adkinson NF, Weis S, Ho C, Villarino ME, Tuberculosis Trials C. 2015. Flu-like and Other Systemic Drug Reactions Among Persons Receiving Weekly Rifapentine Plus Isoniazid or Daily Isoniazid for Treatment of Latent Tuberculosis Infection in the PREVENT Tuberculosis Study. *Clin Infect Dis* 61:527-35.
 11. Lee MR, Huang HL, Lin SW, Cheng MH, Lin YT, Chang SY, Yan BS, Kuo CH, Lu PL, Wang JY, Chong IW. 2019. Isoniazid Concentration and NAT2 Genotype Predict Risk of Systemic Drug Reactions during 3HP for LTBI. *J Clin Med* 8.
 12. Zhang T, Zhang M, Rosenthal IM, Grosset JH, Nuermberger EL. 2009. Short-course therapy with daily rifapentine in a murine model of latent tuberculosis infection. *Am J Respir Crit Care Med* 180:1151-7.
 13. Zhang T, Li SY, Williams KN, Andries K, Nuermberger EL. 2011. Short-course chemotherapy with TMC207 and rifapentine in a murine model of latent tuberculosis infection. *Am J Respir Crit Care Med* 184:732-7.
 14. Savic RM, Lu Y, Bliven-Sizemore E, Weiner M, Nuermberger E, Burman W, Dorman SE, Dooley KE. 2014. Population pharmacokinetics of rifapentine and desacetyl rifapentine

- in healthy volunteers: nonlinearities in clearance and bioavailability. *Antimicrob Agents Chemother* 58:3035-42.
15. Hosagrahara V, Reddy J, Ganguly S, Panduga V, Ahuja V, Parab M, Giridhar J. 2013. Effect of repeated dosing on rifampin exposure in BALB/c mice. *Eur J Pharm Sci* 49:33-8.
 16. Rosenthal IM, Williams K, Tyagi S, Peloquin CA, Vernon AA, Bishai WR, Grosset JH, Nuermberger EL. 2006. Potent twice-weekly rifapentine-containing regimens in murine tuberculosis. *Am J Respir Crit Care Med* 174:94-101.
 17. Savic RM, Weiner M, MacKenzie WR, Engle M, Whitworth WC, Johnson JL, Nsubuga P, Nahid P, Nguyen NV, Peloquin CA, Dooley KE, Dorman SE, Tuberculosis Trials Consortium of the Centers for Disease C, Prevention. 2017. Defining the optimal dose of rifapentine for pulmonary tuberculosis: Exposure-response relations from two phase II clinical trials. *Clin Pharmacol Ther* 102:321-331.
 18. Zvada SP, Van Der Walt JS, Smith PJ, Fourie PB, Roscigno G, Mitchison D, Simonsson US, McIlleron HM. 2010. Effects of four different meal types on the population pharmacokinetics of single-dose rifapentine in healthy male volunteers. *Antimicrob Agents Chemother* 54:3390-4.
 19. Hibma JE, Radtke KK, Dorman SE, Jindani A, Dooley KE, Weiner M, McIlleron HM, Savic RM. 2020. Rifapentine Population Pharmacokinetics and Dosing Recommendations for Latent Tuberculosis Infection. *Am J Respir Crit Care Med* 202:866-877.
 20. Wilkins JJ, Langdon G, McIlleron H, Pillai G, Smith PJ, Simonsson US. 2011. Variability in the population pharmacokinetics of isoniazid in South African tuberculosis patients. *Br J Clin Pharmacol* 72:51-62.
 21. Assandri A, Ratti B, Cristina T. 1984. Pharmacokinetics of rifapentine, a new long-acting rifamycin, in the rat, the mouse, and the rabbit. *J Antibiot* 37:1066-1075.
 22. US FDA. *Prifitin (rifapentine) Product Label*. US FDA, Silver Spring, MD. https://www.accessdata.fda.gov/drugsatfda_docs/label/2014/021024s011lbl.pdf.

23. Opie E, Aronson J. 1927. Tubercle bacilli in latent tuberculous lesions and in lung tissue without tuberculous lesions. *Arch Pathol Lab Med* 4:1–21.
24. Jayaram R, Gaonkar S, Kaur P, Suresh BL, Mahesh BN, Jayashree R, Nandi V, Bharat S, Shandil RK, Kantharaj E, Balasubramanian V. 2003. Pharmacokinetics-pharmacodynamics of rifampin in an aerosol infection model of tuberculosis. *Antimicrob Agents Chemother* 47:2118-24.
25. Gumbo T, Louie A, Deziel MR, Liu W, Parsons LM, Salfinger M, Drusano GL. 2007. Concentration-dependent *Mycobacterium tuberculosis* killing and prevention of resistance by rifampin. *Antimicrob Agents Chemother* 51:3781-8.
26. Canetti G. 1955. The tubercle bacillus in the pulmonary lesions of man. Springer, New York.
27. Behr MA, Edelstein PH, Ramakrishnan L. 2019. Is *Mycobacterium tuberculosis* infection life long? *BMJ* 367:l5770.
28. Behr MA, Edelstein PH, Ramakrishnan L. 2018. Revisiting the timetable of tuberculosis. *BMJ* 362:k2738.
29. O'Garra A, Redford PS, McNab FW, Bloom CI, Wilkinson RJ, Berry MP. 2013. The immune response in tuberculosis. *Annu Rev Immunol* 31:475-527.
30. Blumberg HM, Ernst JD. 2016. The Challenge of Latent TB Infection. *JAMA* 316:931-3.

Supplementary Material

Mouse PK model methods and results: rifapentine

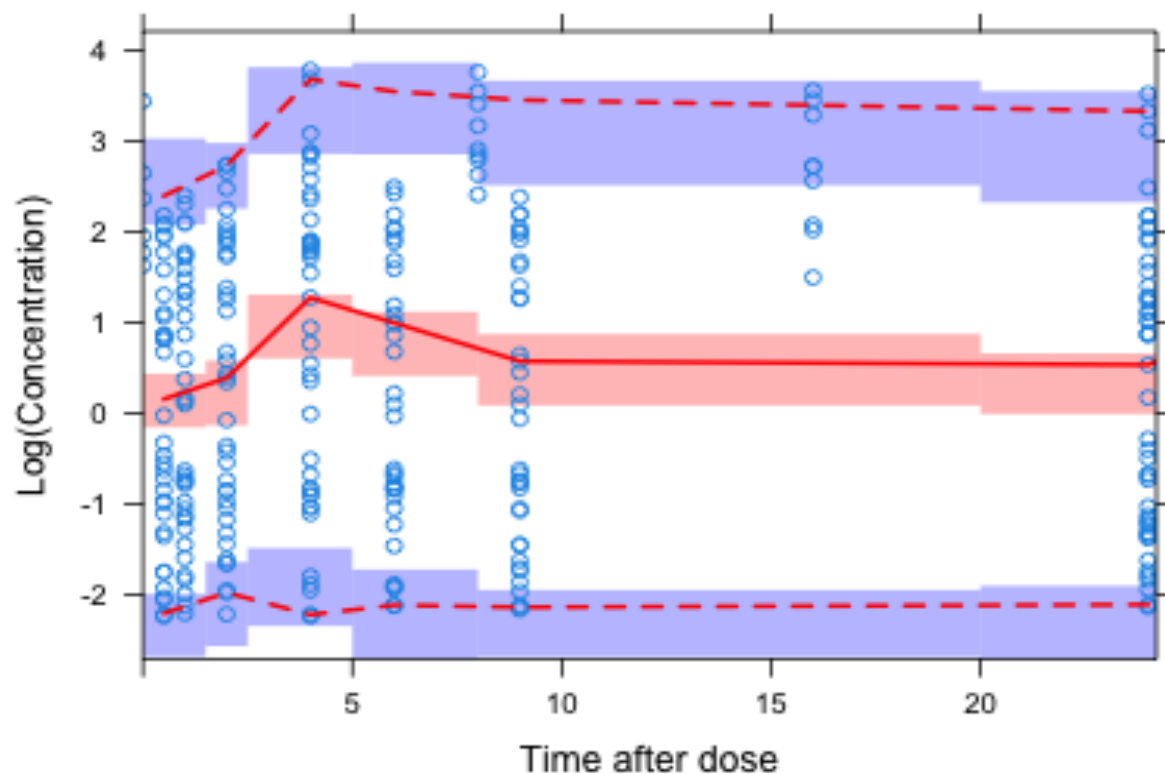
All animal procedures were approved by the Institutional Animal Care and Use of Committee of Johns Hopkins University unless otherwise specified from the original publication.

Plasma concentration data was acquired from three different studies which included oral rifapentine dosing as follows: once daily dosing with 5, 10, and 20 mg/kg (1, 2); once daily dosing ranging with 0.1 to 3 mg/kg for 10 days (low-dose PK study, unpublished); and twice daily dosing with 0.075 to 1.25 mg/kg for 3 weeks (low-dose PK-PD study, unpublished). For unpublished studies, mouse sourcing and husbandry (including ethical approvals), drug preparation and dosing, PK sampling, and plasma drug measurements were conducted as previously described (1, 3).

PK data were log-transformed and modelled in NONMEM 7.4. The data fit a one-compartment model with non-linear elimination. Estimating relative bioavailability for the two highest doses (10 and 20 mg/kg) improved the model fit. Inter-mouse variability was tested on all parameters and was best applied to the Michaelis-Menten rate constant (K_m). The final PK parameters are shown in Supplementary Table 6.1.

Supplementary Table 0.1. Rifapentine pharmacokinetic parameters in the mouse model.

Parameter	Description	Value (RSE)
V (L)	Volume of distribution	15.0 (0.051)
V_{max} (L)	Maximum velocity	10.0 (0.549)
k_m (µg/mL)	Michaelis-Menten constant	18.4 (0.628)
KA (hr⁻¹)	Absorption rate constant	2.15 (0.196)
F_10	Relative bioavailability of 10 mg/kg dose	0.603 (0.178)
F_20	Relative bioavailability of 20 mg/kg dose	0.533 (0.304)
IIV_KM (%CV)	Inter-individual variability on Michaelis-Menten constant	13.6 (0.268)
ADD (mcg/L)	Additive residual error	0.373 (0.051)



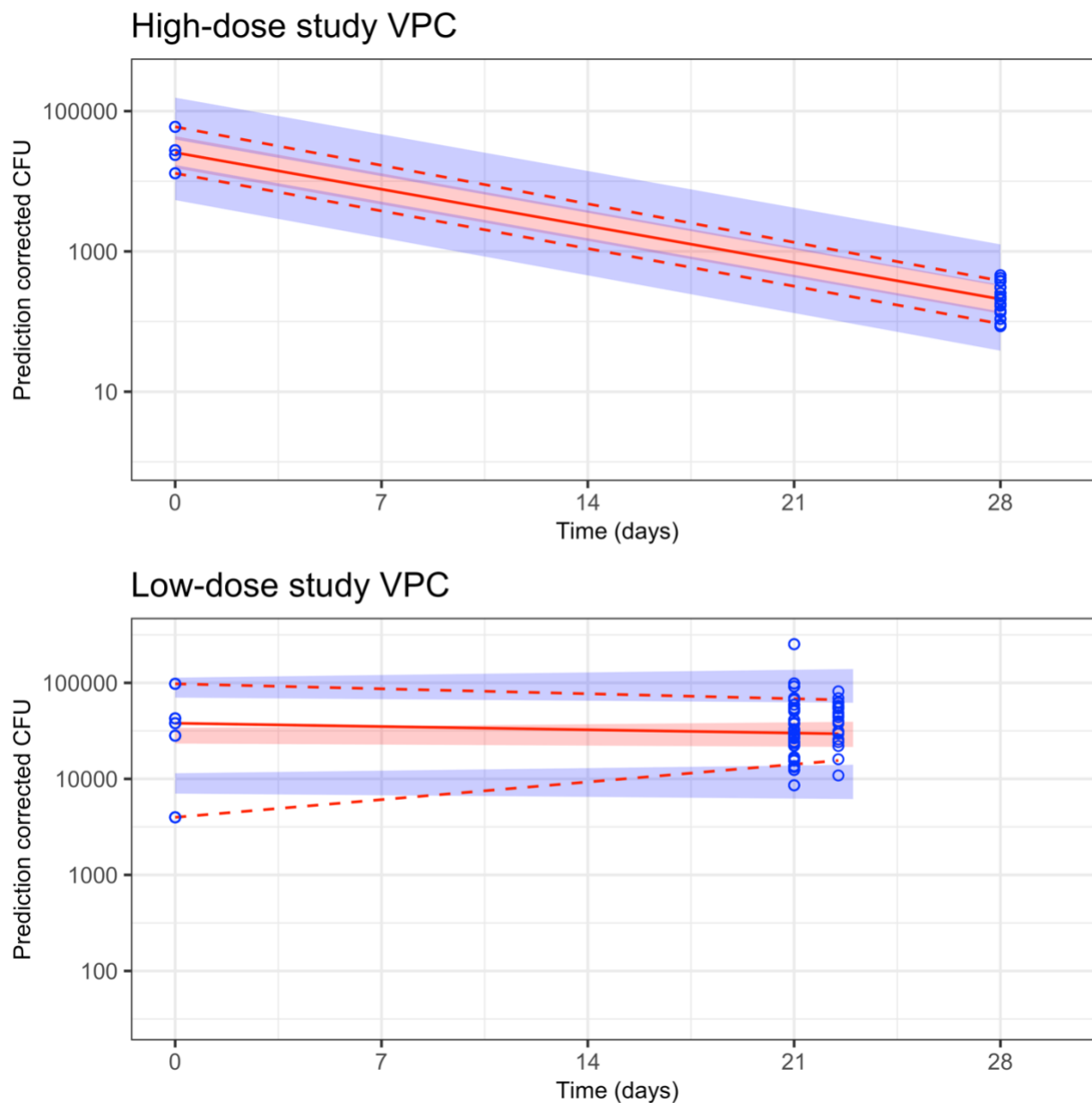
Supplementary Figure 0.1. Prediction-corrected visual predictive check of mouse rifapentine pharmacokinetic model. The blue circles are the observed, prediction-corrected, log-transformed, rifapentine concentrations ($\log[\text{mg/L}]$). The solid and dashed red lines represent the median, 5th and 95th percentiles of observed prediction-corrected data. The shaded areas represent the simulation-based prediction-corrected 95% confidence interval for the median (red) and 5th and 95th percentiles (blue).

Mouse PK model methods & results: isoniazid

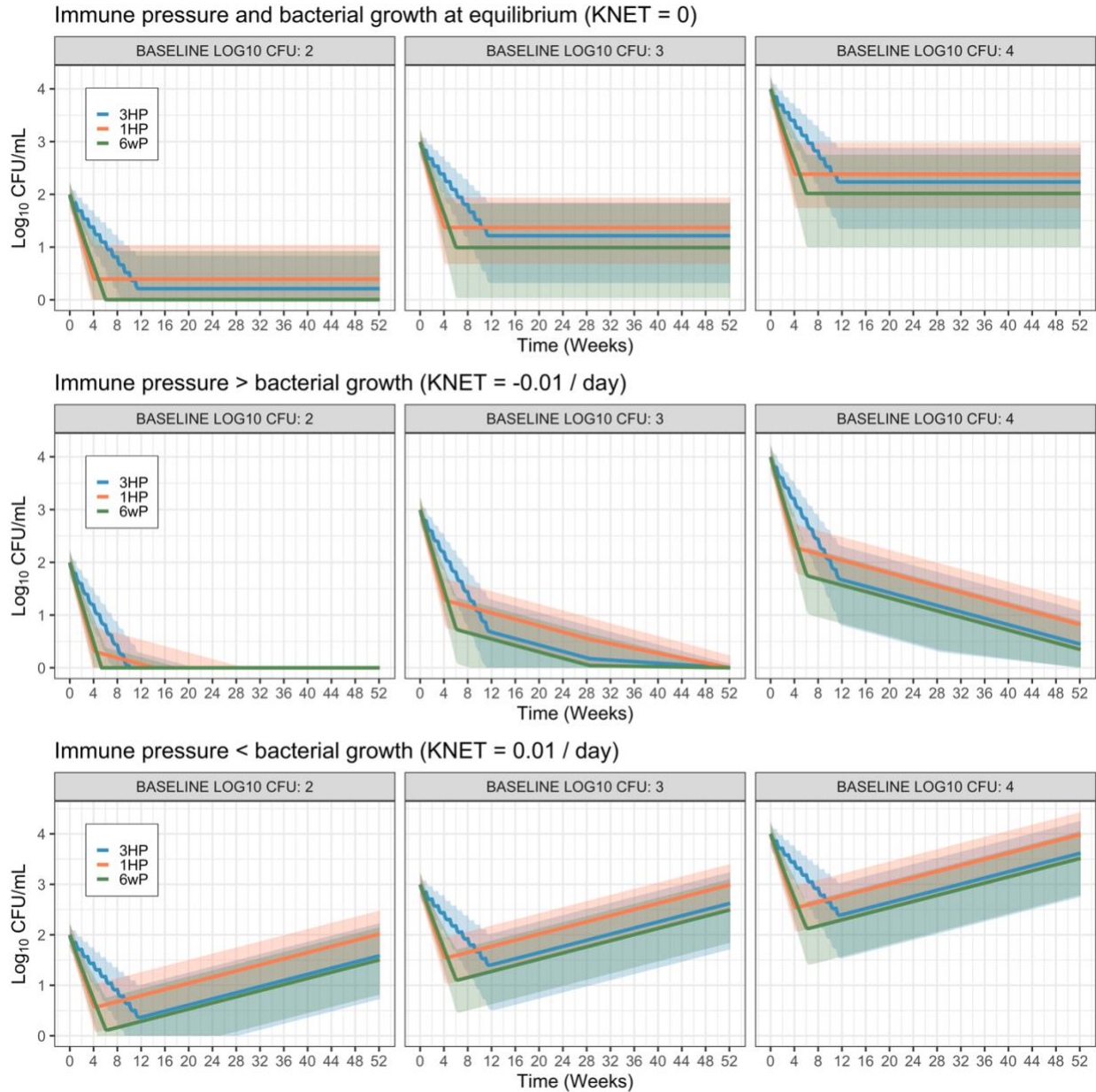
Plasma concentration data was acquired from a study of mice orally treated with a single dose of isoniazid at 1.56, 6.25 and 25 mg/kg (4). Extensive sampling was conducted by drawing blood samples at 15 min, 30 min, 1, 2, 4, and 8 hours post-dose. PK data was modelled in NONMEM 7.4. Model building procedures and results were described previously (2).

Low-dose mouse PK-PD study methods

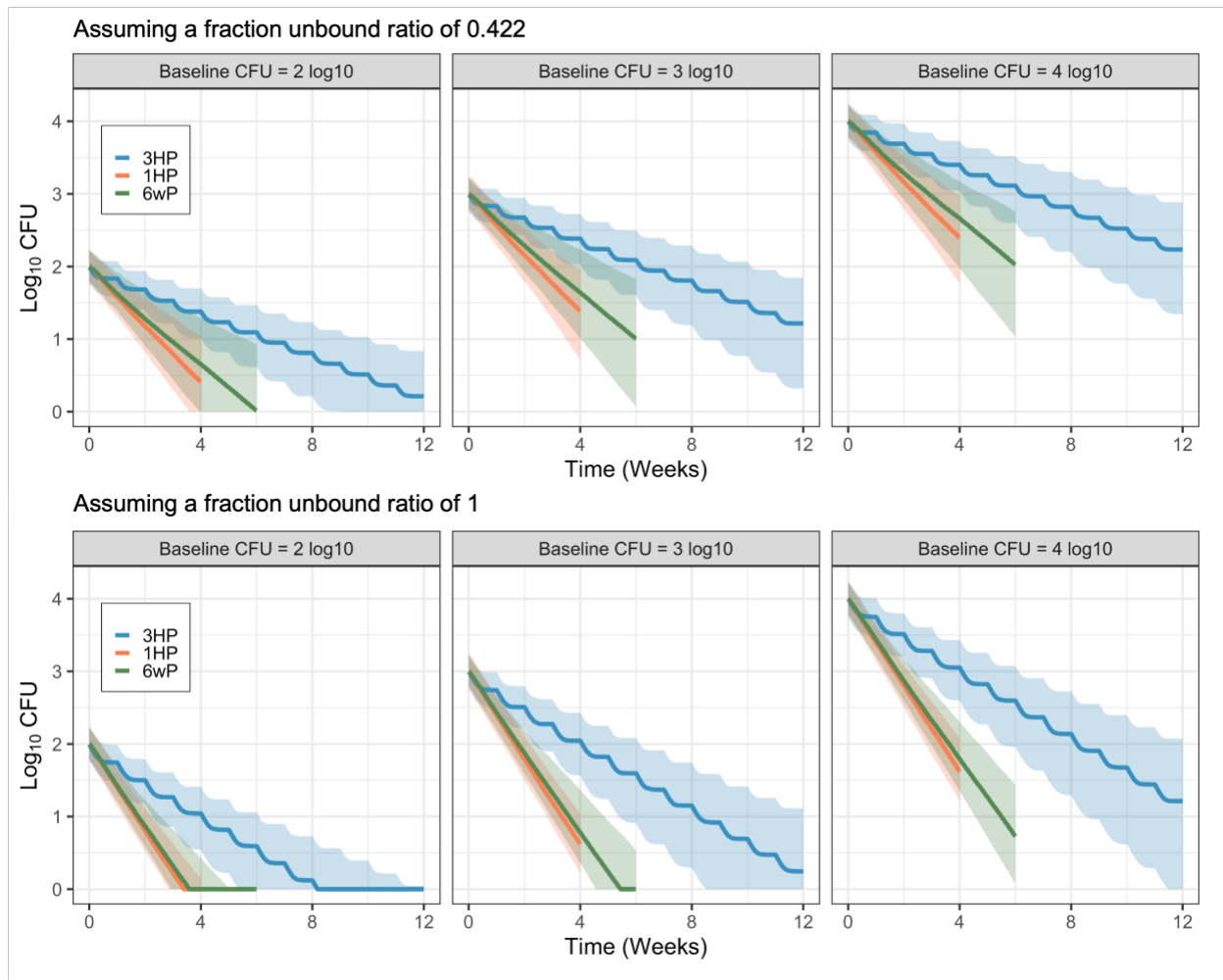
Low-dose, oral rifapentine regimens, with twice daily dosing at 0.075 to 1.25 mg/kg, administered for 3 weeks, were evaluated in a validated mouse model of TB preventive therapy, as previously described [5, 6]. Mouse procedures, rifapentine dosing, and PK methods are described above in “Mouse PK model methods & results: rifapentine.” For PD data, lung CFU were determined after infection and at the start (baseline) and end of treatment, as previously described [5, 6].



Supplementary Figure 0.2. Prediction-corrected visual predictive check of the latent tuberculosis pharmacodynamic model. The blue circles are the observed CFU and the solid and dashed red lines represent the median, 10th, and 90th percentiles of observed CFU, respectively. Observed data were prediction-corrected according to Bergstrand *et al.* (7) given large dose range. The shaded areas represent the simulation-based 95% confidence interval for the median (red) and the 10th and 90th prediction intervals (blue) following 500 simulations.



Supplementary Figure 0.3. Clinical efficacy predictions under different immune effect assumptions. The top row assumes equilibrium between bacterial growth and immune pressure. The middle row assumes immune dominance with a negative net growth adding to drug effect ($K_{net} = -0.01 \text{ day}^{-1}$). The bottom row assumes bacterial proliferation with a positive net growth counteracting drug effect ($K_{net} = 0.01 \text{ day}^{-1}$). Data show median (line) and 90% prediction interval (shaded area) based on 500 simulations for each regimen. CFU = colony forming unit.



Supplementary Figure 0.4. Predicted bacterial load overtime under different assumptions of the interspecies ratio of fraction unbound. The top panel depicts results under the assumption that protein binding in mice is the same as Wistar rats, resulting in an unbound ratio of 0.422. The bottom panel depicts results under the assumption that protein binding in mice is equal to humans. Data show median (line) and 90% prediction interval (shaded area) based on 500 simulations for each regimen. CFU = colony forming unit.

References

1. Rosenthal IM, Tasneen R, Peloquin CA, et al. Dose-ranging comparison of rifampin and rifapentine in two pathologically distinct murine models of tuberculosis. *Antimicrob Agents Chemother* 2012; 56(8): 4331-40.
2. Zhang N, Strydom N, Wang Q, Ernest J, Nuermberger E, Savic R. Predicting the early bactericidal activity (EBA) of tuberculosis (TB) drugs for the phase IIA first-in-patients studies. In: *Clinical Pharmacology and Therapeutics*, 2020:S83-S.
3. Bigelow KM, Deitchman AN, Li SY, et al. Pharmacodynamic Correlates of Linezolid Activity and Toxicity in Murine Models of Tuberculosis. *J Infect Dis* 2020.
4. Almeida D, Nuermberger E, Tasneen R, et al. Paradoxical effect of isoniazid on the activity of rifampin-pyrazinamide combination in a mouse model of tuberculosis. *Antimicrob Agents Chemother* 2009; 53(10): 4178-84.
5. Zhang T, Zhang M, Rosenthal IM, Grosset JH, Nuermberger EL. Short-course therapy with daily rifapentine in a murine model of latent tuberculosis infection. *Am J Respir Crit Care Med* 2009; 180(11): 1151-7.
6. Zhang T, Li SY, Williams KN, Andries K, Nuermberger EL. Short-course chemotherapy with TMC207 and rifapentine in a murine model of latent tuberculosis infection. *Am J Respir Crit Care Med* 2011; 184(6): 732-7.
7. Bergstrand M, Hooker AC, Wallin JE, Karlsson MO. Prediction-corrected visual predictive checks for diagnosing nonlinear mixed-effects models. *AAPS J* 2011; 13(2): 143-51.

Chapter 7: Conclusions

The work presented in this dissertation establishes a basis for nonclinical-clinical translation in TB drug development through development of data-driven models evaluating the ability of drugs to penetrate lesions and to kill bacteria in active and latent infection. The model frameworks integrated a compendium of experimental data to predict clinical efficacy and to contribute toward development of model-based translation methods.

The review of current animal models and translational approaches available illustrated that it is not lack of data, but lack of data *integration* that is needed for accurate translation into the clinic. Translational models, both empirical and mechanistic, provide solutions to integrate data from varying sources in a quantitative way and to increase predictive accuracy. Here, two frameworks are applied to transform nonclinical data to portable learnings of pharmacology and to aid in clinical decision-making.

The hallmark of tuberculosis is immune infiltrate that form granulomas, and in mature states, necrotic centers. The rabbit model of tuberculosis recapitulates the hallmarks of pulmonary tuberculosis disease seen in humans. Using PK data collected from systemic circulation and heterogenous lung pathology in rabbits, models describing the kinetics of drug from absorption in the gut to distribution to sites of action were developed and integrated with available clinical population PK models to predict the concentration at the site of action in humans. In vitro and ex vivo potency values were used to assess whether therapeutic concentrations were achieved. Using this approach, we predicted drug lesion penetration and calculated PK/PD indices in diverse lesion microenvironments for two aminoglycosides, kanamycin and amikacin, and a macrolide, clarithromycin.

Kanamycin and amikacin are second-line injectables used in multidrug-resistant TB. However, there has been limited evidence of their clinical utility in large retrospective studies and meta-analyses. In addition, their introduction and widespread use occurred without rigorous assessment in the currently available tools and before drug concentration data was regularly

collected. In this work, kanamycin and amikacin were quantified in rabbit uninvolved lung, cellular lesions, caseous lesions, and caseum after a dose equivalent to an intramuscular dose of 1,000 mg in humans. Overall, amikacin exposures were greater than kanamycin in all lesion compartments. When integrated with clinical population PK models, the predicted lesion concentrations were less than expected to have an effect. The finding confirms the clinical observation that adding aminoglycosides to multidrug regimens has little benefit and suggests a basis for the limited utility of these two long-standing, widely used aminoglycosides. Importantly, these frameworks are currently being used to assess high-priority drugs in Phase 1 and 2 and to construct untested multidrug regimens.

Clarithromycin is the cornerstone of treatment in non-tuberculous mycobacteria pulmonary disease (NTM-PD) infections. Two species of NTM were included in the study – *Mycobacterium avium*, the most prevalent worldwide, and *Mycobacterium abscessus*, for which cure is not guaranteed in all patients. While minimum inhibitory concentration (MIC) is low, high concentrations are needed to induce a bactericidal effect. Leveraging the pathological similarities to TB, the rabbit model of active TB was used to assess site of action PK-PD. Concentrations expected to inhibit growth of bacteria were achieved in all compartments for both species of NTM even when corrected for the unbound drug concentration. However, concentrations expected to kill bacteria were not achieved despite the high accumulation in tissue compared to plasma. The findings indicate 1) clarithromycin's limited ability to produce reliable cure may be due to pharmacodynamic rather than pharmacokinetic deficits, and 2) commonly used metrics such as indexing plasma concentration to MIC may not be the most accurate measure of efficacy. Importantly, this approach can be implemented to evaluate other drug candidates for NTM-PD.

Chapter 4 extends the site-of-action model to describe with high resolution the diffusion of drug from the cellular rim of necrotic lesions into avascular caseum. Using a new method, laser capture microdissection, caseum was dissected into concentric sections and drug was

quantified in each sample using liquid chromatography coupled to tandem mass spectrometry. Our findings revealed that two diarylquinolines, BDQ and TBAJ-587, achieve therapeutic concentrations within avascular caseum at depths of over 1,000 micrometers. TBAJ-587 may have a more favorable profile due to the faster clearance out of the lesion compared to BDQ which is expected to persist for over two years after the end of treatment. The findings could explain, in part, the slow onset of BDQ efficacy and provide a rationale for the rapidly growing body of evidence of BDQ resistance.

The nonclinical model with the largest database of in vivo efficacy data for TB drugs is the BALB/c mouse infected with wild-type strain H37Rv *Mycobacterium tuberculosis*. Drugs are given orally after infection and response is usually measured as lung CFU counts at one- and two-months post-treatment. We developed a translational modeling platform that leverages this database and uses baseline infection, immune-dependent bacterial growth kinetics, and drug-dependent bactericidal effect to estimate portable efficacy parameters. We illustrate that our model can accurately predict the outcome of 14 clinical trials for nine different drugs. The platform serves to inform, or even replace Phase 2a EBA trials, to better link drug response between species, and to substantially accelerate drug development.

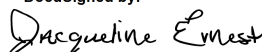
Chapter 6 applies a similar methodology as the Phase 2a translational model to compare efficacy of three rifapentine-containing regimens for latent tuberculosis. We estimate that daily rifapentine alone taken for 6 weeks has similar efficacy to approved rifapentine-isoniazid combination regimens (3HP and 1HP). Results of the ASTERoid trial (ClinicalTrials.gov identifier NCT03474029) testing the novel therapy against 3HP are expected December 2023.

In summary, we applied model-based approaches to improve the translation of nonclinical findings to support regimen prioritization for TB clinical trials. The presented work establishes the basis for future evaluation of drugs in development and in bringing effective short-course therapeutics to combat the TB global health crisis.

Publishing Agreement

It is the policy of the University to encourage open access and broad distribution of all theses, dissertations, and manuscripts. The Graduate Division will facilitate the distribution of UCSF theses, dissertations, and manuscripts to the UCSF Library for open access and distribution. UCSF will make such theses, dissertations, and manuscripts accessible to the public and will take reasonable steps to preserve these works in perpetuity.

I hereby grant the non-exclusive, perpetual right to The Regents of the University of California to reproduce, publicly display, distribute, preserve, and publish copies of my thesis, dissertation, or manuscript in any form or media, now existing or later derived, including access online for teaching, research, and public service purposes.

DocuSigned by:

AFB972A9F3B9412... Author Signature

12/14/2022
Date